Ab Initio Electronic Transport in Single-Molecule Junctions: Quantum Interference Effects and Spin-Orbit Torque

Dissertation

zur Erlangung des
Doktorgrades der Naturwissenschaften (Dr. rer. nat.)
der Fakultät für Physik der Universität Regensburg

vorgelegt von

María Camarasa Gómez

aus Salamanca, Spanien

im Jahr 2020

Promotionsgesuch eingereicht am: 13.05.2020
Die Arbeit wurde angeleitet von: Prof. Dr. Ferdinand Evers

Prüfungsausschuss:

Vorsitzender:	Prof. Dr. Christoph Strunk
Erstgutachter:	Prof. Dr. Ferdinand Evers
Zweitgutachter:	Prof. Dr. Jaroslav Fabian
weiterer Prüfer:	Prof. Dr. Vladimir Braun

Termin Promotionskolloquium: 10.09.2020

A Daniel,
mi interferencia constructiva

Contents

Introduction **xiii**
Challenges for numerics . . . xv
Spin-orbit torque in molecular spintronics . . . xvi
Quantum interference in single-molecule junctions . . . xvii
Molecular insulators in single-molecule junctions . . . xvii
Structure of this thesis . . . xix

I Basic elements of *ab initio* transport calculations **1**

1 Theoretical foundations and methods **3**
1.1 Non-relativistic density functional theory . . . 3
1.1.1 Hohenberg-Kohn theorems . . . 3
1.1.2 Kohn-Sham formalism . . . 5
1.1.3 Basis sets . . . 6
1.1.4 Approximations for exchange-correlation functionals . . . 7
1.2 Quantum transport . . . 8
1.2.1 Green's function approach to quantum transport . . . 8
1.2.2 Absorbing boundary conditions . . . 9
1.2.3 Transmission function . . . 10
1.3 Quantum transport with spin-orbit coupling . . . 11
1.3.1 Origin of spin-orbit coupling . . . 11
1.3.2 Transmission function in the presence of spin-orbit coupling . . . 14
1.4 *Ab initio* spin-orbit torque . . . 16
1.5 Density matrix . . . 18
1.5.1 Equilibrium density matrix with spin-orbit coupling . . . 18
1.5.2 Non-equilibrium density matrix with spin-orbit coupling . . . 19

2 Self-consistent calculations at finite bias with spin-orbit coupling: Methodology and validation **23**
2.1 DFT-NEGF self-consistent cycle with spin-orbit coupling . . . 23
2.1.1 How the DFT-NEGF cycle works . . . 23
2.1.2 Reconstruction of the Kohn-Sham Hamiltonian . . . 26
2.1.3 Self-energy parametrization and charge neutrality condition . . . 27

2.1.4 Application of an external bias voltage . . . 28
2.1.5 Calculation of observables: spin-orbit torque . . . 29
2.1.6 Approximations for the self-consistent cycle . . . 29
2.2 Validation: Test calculations . . . 29
2.2.1 Spin-orbit coupling in FHI-aims . . . 30
2.2.2 First test case: Bipyridine-gold without spin-orbit coupling . . . 31
2.2.3 Second test case: bipyridine-gold crosscheck with TURBOMOLE . . . 34
2.2.4 Third test case: BDT-copper and -gold with spin-orbit coupling . . . 34
2.3 Summary of this chapter . . . 38

II Electronic transport studies in single-molecule junctions 41

3 Spin-orbit torque in vanadocene single-molecule junctions 43
3.1 Why is spin-orbit torque interesting? . . . 43
3.2 Brief overview of spin torque in spintronics . . . 44
3.3 Vanadocenes: a test case study of spin-orbit torque . . . 45
3.3.1 Choice of the system . . . 45
3.3.2 Electronic structure of vanadocene . . . 47
3.3.3 Choice of the electrodes and geometry of the molecular junction . . . 48
3.3.4 Non-equilibrium electronic transport . . . 49
3.4 Magnetic properties of copper-vanadocene junctions . . . 50
3.4.1 Total magnetization . . . 50
3.4.2 Projected magnetization per atomic species . . . 52
3.4.3 Local magnetization at the metallic center . . . 54
3.5 Spin-orbit torque in vanadocene single-molecule junctions . . . 54
3.5.1 Spin-orbit torque from *ab initio* . . . 54
3.5.2 Comparison to torkance calculations . . . 57
3.6 Summary of this chapter . . . 59

4 Mechanically-tunable quantum interference in ferrocene-based molecular junctions 61
4.1 Why quantum interference in ferrocene? . . . 61
4.2 Transport simulations in ferrocene-based junctions . . . 63
4.2.1 *Ab initio*-based transport characteristics . . . 63
4.2.2 Conductance control by ferrocene ring rotation . . . 63
4.3 Model-based analysis of quantum interference . . . 70
4.3.1 Interference terms in transmission trace formula . . . 70
4.3.2 Effective three-level model for ferrocene junctions . . . 72
4.4 Relation to experimental measurements . . . 75
4.4.1 Conductance and displacement measurements . . . 75
4.4.2 Pull-push measurements . . . 77
4.5 Summary of this chapter . . . 77

5 Molecular insulators 79
5.1 Why molecular insulators? . . . 80
5.2 Silane-based single-molecule junctions . . . 81
5.2.1 Motivation . . . 81

5.2.2 Transport calculations for silane junctions . . . 83
5.2.3 Impact of relativistic kinetic energy corrections on transmission . . . 85
5.2.4 Impact of spin-orbit coupling on transmission . . . 86
5.2.5 Summary of this section . . . 86
5.3 Imidazole-based single- and stacked-molecular junctions . . . 88
5.3.1 Imidazole as an anchor group . . . 88
5.3.2 Transport calculations for imidazole-terminated alkanes . . . 90
5.3.3 Summary of this section . . . 93
5.4 Metallocene-based linkers in single-molecule junctions . . . 93
5.4.1 Metallocenes as linkers . . . 93
5.4.2 Theoretical analysis of binding and transport properties . . . 95
5.4.3 Summary of this section . . . 97

Summary and conclusions **99**

Outlook **103**

Appendices **107**

A Structure of the transport module and computational performance **107**
A.1 Scheme of the code structure of the AITRANSS module with spin-orbit coupling . . . 107
A.2 Computational performance of AITRANSS module with spin-orbit coupling 107

B Practical guide for spin-orbit dependent calculations with FHI-aims and AITRANSS **111**
B.1 Step 0: Optimization of the molecular junction geometry . . . 111
B.2 Step 1: Parametrization of the self-energy . . . 111
B.3 Step 2: Finite bias calculation . . . 113
B.4 Step 3: Spin density, spin-orbit torque, transmission function . . . 113
B.4.1 Spin-orbit torque and magnetization . . . 114
B.4.2 Transmission function . . . 114
B.4.3 Current . . . 114
B.5 Non-self consistent transmission with spin-orbit coupling . . . 115

C Sample input files and parameters for spin-orbit torque calculations **117**
C.1 Parameters for figures in chapter 2 . . . 117
C.2 Parameters for figures in chapter 3 . . . 120

D Additional calculation details for ferrocene-based molecular junctions **123**
D.1 Computational details for *ab initio* calculations . . . 123
D.2 Impact on transmission of the functionalized linker rotations . . . 124
D.3 Isosurface plots of relevant gas-phase orbitals . . . 125
D.4 Model parametrization . . . 127

E Quantum interference in ferrocene molecular junctions **129**
E.1 Energetics of ring rotations of gas-phase SMe-Fe . . . 129
E.2 Conductance control by ring rotation . . . 129
E.3 Impact of the anchor group in the quantum interference . . . 131

F The scanning tunneling microscope-based break junction technique 133

G Theoretical calculation details for silane, imidazole and metallocene-based molecular junctions 135
G.1 Silane-based molecular junctions 135
G.1.1 Computational details 135
G.1.2 Relevant scattering states involved in charge transport 136
G.2 Imidazole-based molecular junctions 137
G.2.1 Computational details 137
G.3 Metallocene-based linkers in single-molecule junctions 137
G.3.1 Experimental two-dimensional conductance-displacement histogram of 1,1'-M metallocenes 137
G.3.2 Computational details 138

Bibliography 139

List of publications 151

List of programs 153

Acknowledgements 155

List of Figures

1 Molecular junction: Au-S-silicon-based wire-S-Au xviii

1.1 Scheme of the extended molecule concept 8

2.1 Scheme of the self-consistent (DFT-NEGF) procedure 25
2.2 Benchmark for SO coupling in FHI-aims and TURBOMOLE in gold clusters 30
2.3 Differences in the impact of SO coupling between FHI-aims and TURBOMOLE for gold clusters 31
2.4 Validation of the self-consistent cycle for bipyridine-Au junctions (I) 32
2.5 Validation of the self-consistent cycle for bipyridine-Au junctions (II) 33
2.6 Validation of the self-consistent cycle for bipyridine-Au junctions (III) . . . 35
2.7 Validation of the implementation: impact of non-self-consistent SO interaction 36
2.8 Validation of self-consistent cycle for the benzenedithiol-copper junction with SO interaction 39

3.1 Geometry of pristine vanadoce 46
3.2 Qualitative molecular orbital diagram of pristine vanadocene 47
3.3 Geometry of the vanadocene-copper molecular junction 49
3.4 I-V characteristics of the vanadocene-copper molecular junction 50
3.5 Magnetization of the vanadocene-copper junction against voltage for different Zeeman fields 51
3.6 Projected magnetization per atomic species of the vanadocene-copper junction against voltage for large Zeeman fields 53
3.7 Projected magnetization per atomic species of the vanadocene-copper junction against voltage for small Zeeman fields 55
3.8 Local magnetization at the vanadium atom as a function of the bias voltage 56
3.9 Local SOT at the vanadium atom as a function of the bias voltage 58

4.1 Molecular orbital diagram and electronic structure of ferrocene 62
4.2 Geometries and transmission curves for $1,1$'-Fe, $1,3$-Fe and P_3 64
4.3 Sketch of rotation of the carbon-based rings in ferrocene 65
4.4 Energy cost for 1,1'-Fe "scissor mode" 66
4.5 Geometries and transmission curves for 1,1'-Fe 67
4.6 Isosurface plots for the Kohn-Sham states at $\varphi \in \{\pi/6, \pi/2, 2\pi/3\}$ 69

4.7 Change in the nodal structure of selected gas-phase Kohn-Sham states upon rotation . . . 70
4.8 Sketch of the minimal model for the three-level Hamiltonian. . . . 71
4.9 Transmission function obtained for the three-level model . . . 74
4.10 1D-conductance histograms and plateaus lengths for 1,1'-Fe, 1,3-Fe and P_3 . 75
4.11 Sketch of the compression and elongation mechanism of 1,1'-Fe in a STM-BJ 76
4.12 Experimental results for pull-push in 1,1'-Fe using STM-BJ . . . 78

5.1 Sketch of silane-based junctions with different anchors and contact materials. 81
5.2 Conductance histograms of SH- and NH_2-terminated silanes and corresponding β parameter. . . . 82
5.3 Transport calculations and relaxed geometries for NH_2-Si_4-NH_2 junctions and SH-Si_7-SH with Au and Ag contacts . . . 84
5.4 Impact of different implementations of scalar relativistic effects on the theoretical transport calculations . . . 85
5.5 Comparison of silane transport characteristics with and without SO interaction 87
5.6 Imidazole structural formula . . . 88
5.7 Structure of im-N-im series and experimental results . . . 89
5.8 *Ab initio* based results for the single imidazole molecular junctions . . . 91
5.9 Experimental and theoretical results for the $\pi - \pi$ stacked imidazole dimer junctions . . . 92
5.10 Chemical structure for 1,1'-M and 1-M metallocenes, M = Fe, Ru, Os . . . 94
5.11 One-dimensional conductance histograms of 1,1'-M and 1-M junctions, M = Fe, Ru, Os . . . 95
5.12 Transmission function for 1,1'-M and 1-M junctions, M = Fe, Ru, Os . . . 96
5.13 Comparison of transmission functions for different binding configurations of 1-Fe molecular junction . . . 97

A.1 Scheme of the AITRANSS module with spin-orbit coupling . . . 109
A.2 CPU time for different number of threads . . . 110

D.1 Transmission calculation for constrained and free 1,1'-Fe geometries . . . 124
D.2 Isosurface plots of Kohn-Sham states for $\varphi \simeq 5\pi/6$ . . . 125
D.3 Isosurface plots of 1,1'-Fe gas phase orbitals for relevant rotational angles . 126

E.1 Energy cost of the "scissor mode" for SMe-Fe . . . 130
E.2 Selected geometries of SMe-ferrocene and transmission plots . . . 131
E.3 Impact of NH_2 and SMe anchor groups on transmission . . . 132

F.1 STM-based break-junction technique . . . 134

G.1 HOMO and LUMO scattering states of silane-based junctions . . . 136
G.2 Two-dimensional conductance-displacement length histograms of 1,1'-M metalocenes, M = Fe, Ru, Os . . . 137

List of Tables

2.1 Benchmark of the self-energy in the absence of SO coupling 33
2.2 Benchmark of the chemical potential: new module compared to pre-existing AITRANSS 34
2.3 Frontier orbital energies with and without SO coupling for Au/Cu-BDT-Au/Cu 36
2.4 Benchmark for benzenedithiol junction: self-consistent vs non-self-consistent, SO interaction vs no SO interaction 37

3.1 Vanadocene frontier orbitals with SO coupling for different Zeeman energies. 48

4.1 Phase-shifts of Kohn-Sham states for different rotation angles 73

A.1 Walltime benchmark needed for the self-consistent calculations 108

D.1 *Ab initio* numerical data used in the three-level model 127

Introduction

There have been always visionaries in science. One of them was, undoubtedly, Richard Feynman, who in December of 1959 during the annual American Physical Society meeting at Caltech gave one of his most inspiring lectures titled *"There's plenty of room at the bottom"* [1]. There, he challenged scientists to explore how to control or manipulate individual atoms and molecules by improving the existing technology to make this endeavor happen. Although he never mentioned the words "nanotechnology" or "nanoelectronics" in that lecture, he envisioned some of the achievements realized only in recent decades.

Despite Feynman's motivating speech, the proposal of a molecular-based electronic device had to wait until 1974, when Aviram and Ratner put forward the first theoretical design of a single-molecule rectifier [2]. From the experimental side, advancements such as the invention of the scanning tunneling microscope (STM) in 1981 [3] became a game changer. The combination of this type of theoretical and experimental advances marked the first successful attempt of measuring the conductance of a single molecule [4] and set the beginning of *molecular electronics*. In this field, one of the original driving forces was the idea of using individual molecules as functional building blocks for electronics, thus exploiting their electronic (transport) properties to develop and integrate nanoelectronic devices into conventional electronics following a bottom-up approach. Although this goal has been only partially achieved, the field has become an excellent platform to study quantum mechanical effects at the molecular scale with no counterpart in condensed matter physics.

From an experimental perspective, wiring individual molecules between macroscopic metallic leads has become a routinary procedure thanks mainly to three different techniques: electromigration [5], mechanically controlled break junction [6] and scanning tunneling microscope-based break junction (STM-BJ) [7]. The enormous advances in these techniques has allowed the experimental studies to achieve fabulous control and reproducibility of the conductance measurements. Thanks to this, transport associated phenomena have been further studied in a reliable manner. Among them, we find spin-related [8] or quantum interference (QI) effects [9, 10], which play a significant role in this thesis.

The control and manipulation of the spin in molecules has given rise to a prolific research branch of molecular electronics. We refer here to "molecular spintronics" [11, 12, 13, 14]. This field exploits the spin and the electronic degrees of freedom in molecules to manipulate the current. Similar to molecular electronics, the ultimate goal of this field is the miniaturization of spintronics devices down to a very small magnetic unit: a molecule. The magnetic nature of the molecule depends on its closed or open-shell electronic structure and it can be diamagnetic or paramagnetic.

Systems which have been on the spotlight of molecular spintronics are organic-based molecules, which may contain transition metal atoms. These atoms normally have partially filled d-orbitals. In the presence of the organic environment (ligand), the degeneracy of the d-levels is lifted by the ligand field [15]. This results into a $e_g - t_{2g}$ splitting, which determines the spin density and the local distribution of magnetic moments, and thus, the magnetic nature of the molecule. In other words, the ligand environment of the molecule and the possibility of presenting spin-orbit (SO) coupling make the system anisotropic.

For example, double-decker carbon-based compounds containing transition metals, such as iron, niobium or tantalum, present magnetic moments localized in the metallic atoms. Importantly, the SO takes an important role that cannot be neglected in the calculations. The switch of the magnetization direction of the magnetic moments has been traditionally performed by applying external magnetic fields. However, the spin degree of freedom might be manipulated using a different approach: exploiting SO coupling while using conventional electronic current [16]. Therefore, an interesting question arises: can we switch the magnetization direction of the magnetic moments in a molecule by means of the SO coupling? And, how large the SO coupling has to be in order to manipulate magnetic moments in molecules when a current flows through the molecule?

Another important transport phenomenon, investigated in this thesis, is QI. This is a purely quantum mechanical effect related to the wave nature of the electron. Mathematically, it comes from the simple statement that the wavefunction amplitude must be first added when computing the probabilities. QI appears in many contexts in condensed matter physics, for example in the Aharanov-Bohm effect [17] occurring in mesoscopic metallic rings, where the interference patterns can be tuned by applying external magnetic fields, or in superconducting quantum interference devices (SQUIDS). In the latter, the interference features are extremely sensitive to magnetic fields and can be used as field sensors.

QI effects also take place, not surprisingly, in single-molecule junctions. In experiments, very low value of the conductance of the molecule sandwiched between the contacts have been often attributed to this physical effect. QI is a direct manifestation of the connection between structure and electronic features of the molecule, emerging as the electron propagates through the junction. For this reason, it gives rise to strong and robust features in transport observables which persist under thermal fluctuations. In general, the prediction of the existence of quantum interference in an arbitrary molecule is a complicated task. Over the past fifteen years different methods have been developed to gain further understanding in how the interference is produced and its consequences for observables [18, 19, 20, 21].

For instance, a "sum over paths" approach has been applied to multibranched structures [22], where the molecule offers the electron two or more possible transport paths. The interference effects in this case are similar to those that can be observed in mesoscopic rings. Another example are the so-called "orbital rules", which are valid for molecules with π-orbitals and sublattice symmetry, such as benzoids. However, in arbitrary molecules with more complicated chemical structure the previous methods cannot be employed to predict the presence of QI. This situation happens in the aforementioned double decker compounds, which can contain a transition metal atom sandwiched between carbon-based rings. Their chemical structure does not present sublattice symmetry and the π-system of the carbon ring hybridizes strongly with d-orbitals of the metallic atom giving rise to

non-trivial interference effect. In this case, an analysis based on the Green's function, which describes how the electron propagates across the junction is necessary.

Since QI is commonly present in molecules, it is interesting to predict when it arises and whether it can be manipulated in order to control the flow of current across the molecule. In molecular junctions, tuning of QI may be achieved by changing the overlap of the molecular orbitals in a controlled (mechanical) manner. For instance, in double decker structures made of π-π stacked dimers without metal atom, the displacement of the metallic contacts produces the upper part of the π-π stack to slide with respect to the lower part. As a consequence of the motion of the contacts, the overlap between the two subsystems is altered and affects the nodal structure of the molecular orbitals involved in the QI [23, 24]. If we now turn our attention to double decker compounds in which a metallic atom is sandwiched between the upper part and the lower part of the stack, the sliding of the carbon rings with respect to each other is not longer possible. What is the nature of the QI in this compounds? Is there another mechanical degree of freedom in the molecular structure of the double decker that can be exploited to control the interference? What is the role of the interplay of the d-orbitals with the π-system of the carbon rings? All of these points will be considered in this thesis.

Challenges for numerics

To answer these questions, a theoretical description of steady-state electronic transport in molecular junctions, in particular in the presence of SO interaction, is needed. This task is not simple and it represents a challenging problem in condensed matter physics and quantum chemistry [21]. The employed formalism must be able to take into account a variety of effects, among them non-linearities in the I-V characteristics, the variability of molecule-electrode binding motifs *etc.*. The correct description of the electronic structure is also crucial, as the molecular states are fundamental pieces of the scattering wave-function involved in transport. The coupling to electrodes (which act as macroscopic reservoirs) must be also taken into account.

Ab initio descriptions are useful in the endeavor of dealing with large electronic systems and incorporate appropriate geometrical and microscopic information, as well as exchange and correlation effects, into the scattering states. Although many-body methods such as GW allow for a very precise characterization of the electronic structure of gas phase molecules or bulk materials, at the moment of writing this thesis only DFT can deal microscopically with open quantum systems (where energy and particles can be exchanged between the molecule and the reservoirs). The reason is that, as opposed to many-body techniques, DFT deals with a single-particle description of the transport problem. At the same time, it provides a good qualitative description of weakly correlated states in molecular junctions. Sufficiently large in this context means that the electronic structure of the extended molecule (the molecule and part of the metal atoms that belong to the electrodes obtained after *partitioning* the system) [21, 25] can be approximately obtained. This extended molecule captures the hybridization of the orbitals from the molecule with the leads.

The transport problem is commonly addressed using the non-equilibrium Green's func-

tion formalism (NEGF). The Green's function of the extended molecule coupled to the reservoirs describes how the electron propagates across the junction. It can be constructed by employing the single-particle Hamiltonian of this system (from the DFT) and the self-energies from the leads. The self-energy can be modeled [26] or calculated explicitly by means of iterative approaches [27]. When employing model self-energies, the expressions become accurate only when a sufficient number of atoms from the leads are considered. Due to the imaginary part, the self-energy produces that the original states of the molecule acquire a finite lifetime (broadening). This simply describes the fact that after scattering, the electrons can be absorbed in the macroscopic reservoirs and leave the scattering region.

This combination of DFT and NEGF has become the common workhorse used to compute transport properties of molecular junctions in the linear response regime. NEGF can be also employed for the calculation of transport properties outside of the linear regime at even higher bias voltages. When a voltage is applied, there is a redistribution of the charges in the junction. In addition, the molecule can be polarized and a molecular dipole field can be created. All of these effects change the scattering potential, which itself is a functional of the density matrix (and therefore the density given by its diagonal part). The correct theoretical description requires to incorporate self-consistently the effects of the bias in the density matrix. This can be achieved through a self-consistent iteration of the DFT-NEGF cycle. In this thesis, we have first extended the existing transport code AITRANSS incorporate SO coupling. Then, we have employed this module in the self-consistent cycle to compute SO torques. This is to the best of our knowledge the only code which can compute SO torque in a self-consistent fashion in molecular junctions.

Spin-orbit torque in molecular spintronics

As anticipated above, the control of magnetic moments in solid-state devices has traditionally been performed by applying external magnetic fields. More recently, spin torques (such as SO torque) have been considered for the magnetization control as they allow for the manipulation of magnetic moments by means of conventional electric currents.

In this thesis, we embark on the investigation of SO torques in a vanadocene-based molecular junction. This molecule has a double decker chemical structure sandwiching a vanadium atom between two carbon rings. The metal center has localized magnetic moments. This molecule has been recently shown to act as a spin-filter to generate spin-polarized current in single-molecule junctions [28]. As a first application of our extension of AITRANSS with SO coupling, we study whether the SO torque at the metallic center is sufficiently large to manipulate the local magnetic moment. Since SO torque is a non-equilibrium phenomenon, we drive the system to a non-equilibrium state through a voltage bias, using our module in a self-consistent DFT-NEGF cycle. The results will be put in context with previous linear response calculations of the SO torque in metallic heterostructures.

Quantum interference in metallocene single-molecule junctions

Metallocenes, as the aforementioned vanadocene, are double-decker sandwich compounds with a metallic unit between cyclopentadienyl (Cp) carbon rings. In the case of a ferrocene, the metal center is iron. Ferrocenes are known to have a low energy barrier for the rotation of the Cp rings. The fact that the rings can rotate easily opens the possibility to mechanically change the interference properties of these junctions. This degree of freedom has never been used before to tune QI. Practically, the rotation can be achieved by elongating and compressing the junction once the molecule has bound to the contacts.

Motivated by the conformational flexibility of metallocenes we embark upon the study of QI interference in ferrocene-based single-molecule junctions using density functional theory-based quantum transport calculations. We find that destructive QI of the Fano-type is responsible for the low conductance properties of these junctions. Furthermore, we show that the destructive QI features can be tuned mechanically by near-rotation of the Cp rings. Rotation of the rings affects the hybridization between the π-system of the carbon-based ligands and the d-orbitals of the metallic center. This way, the nodal structure of the interfering molecular orbitals is altered and the interference can become constructive. As a consequence, the conductance of the junction is increased substantially. We will provide a simplified model that describes this phenomenon and whose basic ideas can be applied to the study of interference in any type of molecular junctions. Our theoretical calculations will be compared and used to successfully interpret experimental measurements performed at L. Venkataraman's group in Columbia University.

Molecular insulators in single-molecule junctions

In the context of our collaboration with the group of Columbia, we were also motivated to investigate other molecules in the context of single-molecular junctions. This has given rise to several side projects in this thesis related to molecular insulators. These are molecules which fully suppress the electronic transmission. As a consequence, their conductance is smaller than the conductance of a vacuum layer as wide as the length of the molecule. Traditionally, it has been considered that carbon-based wires such as alkanes or more recently siloxanes, which consist of repeating Si-O units, were good molecular insulators. However, their conductance was always larger than the vacuum layer associated to the length of the molecules [29]. In L. Venkataraman's group, it has been observed that silicon-based wires with *cis*-configuration for the Si-Si bond can act as ideal molecular insulators. In them, the conductance is smaller than the conductance through the vacuum layer due to destructive QI effects. Interestingly, these molecular wires behave as insulators even at distances smaller than 1 nm. This is surprising, since tunneling of electrons normally take place for tunnel barriers of this length.

Motivated by this, in one of these projects, we have studied the transport properties of silicon-based wires in *trans*-configuration, see Fig. 1. These wires present an important technological interest as they connect the world of semiconductor electronics, where conventional electronic devices are made from silicon, to molecular electronics [30]. The miniaturization of silicon-components to the single-molecule level poses also fundamental questions related to the scaling: how does charge transfer in silicon occurs at the molecular

level? In this project, we investigate a surprising observation for these wires: their conductance is larger when attached through thiol (S) anchors to silver electrodes compared to gold. This behavior is apparently contradictory when looking at the work function trends (smaller in silver compared to gold). The trend is, however, reversed compared to thiol if the linkers employed are amines (NH_2). Using quantum transport calculations based on DFT, we will explain the origin of these results.

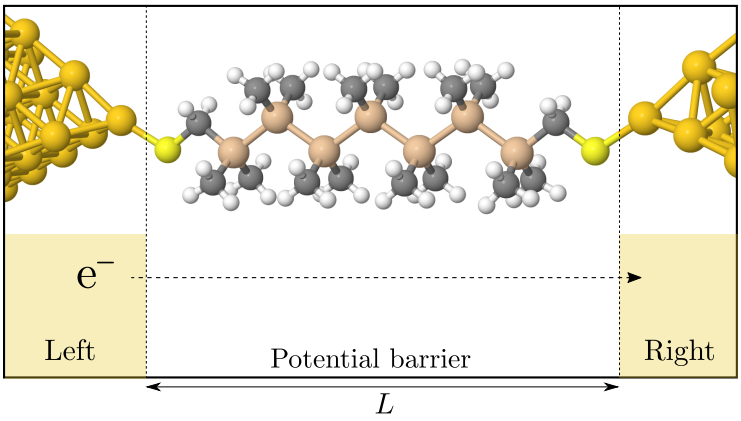

Figure 1 – Top part: Geometry of a model molecular junction Au-S-silicon-based wire-S-Au in *trans*-configuration. Au electrodes have a prototypical pyramidal shape. The anchor groups are thiols. The molecular bridge is the silane wire, saturated with methyl groups. Bottom part: Representation of the potential (tunnel) barrier where an electron e^- is scattered from the left to the right reservoirs (yellow areas) through the barrier. The potential barrier has a width, L, equivalent to the molecular length.

With an eye on bio-nanoelectronics, it is of large interest to be able to bind macromolecular insulators to metallic leads. Usually, these biochemical complexes are more difficult to bind to gold contacts. One way to overcome this situation is to use precursors, which are part of the biomolecule and can act as linkers. With this in mind, we focus on the imidazole anchor. It is an diazole heterocyclic organic ring part of many biochemical compounds. In this project we investigate how the imidazole-metallic lead binding happens, how imidazole binds to other molecules and how this linker affects the transport properties of the molecules.

Other molecules, which also act as linkers are metallocenes, as the ones we employ to study SO torque and QI. Interestingly, these molecules can directly bind to electrodes through the metallic center. Molecules employed in molecular junctions usually are terminated with anchor groups of the p-block of the periodic table, such as nitrogen or sulfur. The metal-metal bond formed with transition metals opens the possibility of controlling the binding through the oxidation state of the metal center of the molecule *in situ*. In other words, by applying specific bias voltage across the junction, the oxidation state of the metal changes, binding the molecule just for specific voltages [1]. In this project, we focus on ferrocenes, osmocenes and ruthenocenes to answer the question of how these metallocenes bind to gold electrodes and how the substitution of the metallic centers affect the binding and transport properties of these molecules.

1. Private communication from Dr. Michael S. Inkpen.

Structure of this thesis

In **Chapter 1** we set the scene and provide a general overview of the basic theory needed to perform and understand *ab initio* electronic transport calculations. We briefly introduce the basic notions of DFT and do a succinct derivation of the main NEGF formulae that are used in our *ab initio* transport calculations. We also derive the necessary expressions later employed in the calculation of SO torque in single-molecule junctions.

In **Chapter 2** we provide the details of the numerical extension of the DFT-NEGF self-consistent cycle in the transport module AITRANSS to incorporate SO interaction. The methodology will be explained and numerical checks shown in order to ensure the correctness of our implementation.

In **Chapter 3**, the first calculation of SO torque in single-molecule junctions using the methods presented in chapter 2 is shown. We discuss why vanadocene (double decker molecule with a vanadium core) is a good candidate for this computation and we calculate the bias-dependent SO torque at the metal center. The results obtained in this pioneering calculation are later put in context with previous linear response calculations in the linear response regime.

In **Chapter 4**, we study quantum transport properties of single-molecule ferrocene-based junctions. We show that these junctions can have non-trivial quantum transport characteristics due to quantum interference effects and demonstrate how and why destructive quantum interference can be mechanically controlled in the junction.

In **Chapter 5**, three transport studied on molecular insulators are presented. First, we embark upon the investigation of the transport properties of silicon-based molecular insulators attached to leads of different metallic nature. We will see that SO coupling and the nature of the molecular anchor groups are related to the unexpected experimental results obtained in L. Venkataraman's group in Columbia University. Next, also in collaboration with L. Venkataraman's group, we explore the paradigmatic case of alkane single molecule junctions bound to gold leads through imidazole linkers. Finally, we study the how metal-electrode binding can occur in metallocene-based junctions of group 8 (Fe, Ru, Os), how the different metal substitutions impacts both binding and transport features.

Part I

Basic elements of *ab initio* transport calculations

Chapter 1

Theoretical foundations and methods

In this chapter, we provide the theoretical framework and methods that will be used in the rest of this thesis. In the first part of the chapter, we do a short and concise review of density functional theory. In the second part of the chapter, we derive the basic formalism of quantum transport expressed in the language of Green's functions. This formalism allows for the calculation of transport properties of interest such as electrical current or conductance. In the last section, we provide the basic formulae that allow for the calculation of non-equilibrium spin-orbit torque using ab initio methods. Starting from non-collinear density functional theory, we show how to construct the two fundamental objects to compute the non-equilibrium spin-orbit torque: the torque operator and the [non-collinear] non-equilibrium density matrix.

1.1 Non-relativistic density functional theory

1.1.1 Hohenberg-Kohn theorems

Although the many-body Hamiltonian of a system of N non-relativistic electrons interacting through the Coulomb force [in a non-magnetic potential] created by N_I ions of

charge Z_I is well-known [1], in practical terms it is of little use as the many-body Schrödinger equation cannot be solved for a macroscopic number of degrees of freedom ($N_{\rm A} \sim 10^{23}$ atoms and / or electrons). Therefore, it is needed to reduce the number of degrees of freedom in systems made of hundreds or thousands of electrons and ions in order to simulate and understand the properties of matter. Density functional theory (DFT) is an extremely successful attempt to realize such a reduction. It provides a theoretical framework that allows to reformulate the many-body problem, characterized by $3N$ degrees of freedom of the complex scalar many-body wavefunction [2], in terms of the scalar particle density $n(\mathbf{r})$, which possesses only 3. Once the ground state density, $n_0(\mathbf{r})$, is known, different ground state properties can be reconstructed. This discovery, formulated on the basis of the famous Hohenberg-Kohn theorems [31] (the proofs can be found in any standard DFT book, see *i.e.* Ref. [32]), has lead to one of the most successful breakthroughs in condensed matter theory in the last century.

First Hohenberg-Kohn theorem: *Given a system of N interacting particles, the external potential, $v_{\rm ext}(\mathbf{r})$, is uniquely determined by the ground state density, $n_0(\mathbf{r})$, up to a trivial additive constant.*

The theorem states a non-trivial fact: the ground state of an interacting system can be described only by the particle density. Note that the reciprocal relation, $v_{\rm ex}(\mathbf{r}) \Rightarrow n_0(\mathbf{r})$, is always trivially true. Therefore, the theorem actually states that there exists a one-to-one correspondence between the external potential and the ground state density of the system of N interacting particles (electrons). A straightforward consequence of this theorem is that the expectation value of any observable, $\hat{O}$, in the ground state is a functional of the exact ground state density, $\langle \hat{O} \rangle = O[n_0(\mathbf{r})]$. The calculation of the ground state density can be done, in principle, using the second Hohenberg-Kohn theorem:

1. In the Born-Oppenheimer approximation, the many-body Hamiltonian can be written as

$$\hat{\mathcal{H}}(\{\mathbf{r}\},\{\mathbf{R}\}) = \hat{T}(\{\mathbf{r}\}) + \hat{V}_{\rm int}(\{\mathbf{r}\}) + \underbrace{\sum_{i=1}^{N} \hat{v}_{\rm ext}(\mathbf{r}_i,\{\mathbf{R}\})}_{\hat{V}_{\rm ext}(\{\mathbf{r}\},\{\mathbf{R}\})}, \tag{1.1}$$

where $\hat{T}(\{\mathbf{r}\})$ is the electronic kinetic energy

$$\hat{T}(\{\mathbf{r}\}) = -\frac{\hbar^2}{2m}\sum_{i=1}^{N} \Delta_{\mathbf{r}_i}, \tag{1.2}$$

the term $\hat{V}_{\rm int}(\{\mathbf{r}\})$ is the Coulomb interaction between electrons

$$\hat{V}_{\rm int}(\{\mathbf{r}\}) = \frac{e^2}{2}\sum_{i=1}^{N}\sum_{j\neq i}^{N} \frac{1}{|\mathbf{r}_i - \mathbf{r}_j|}, \tag{1.3}$$

and the third term, $\hat{V}_{\rm ext}(\mathbf{r},\{\mathbf{R}\})$ is the external potential which describes the interaction between the electrons and the ions located at fixed positions $\{\mathbf{R}\}$

$$\hat{v}_{\rm ext}(\mathbf{r},\{\mathbf{R}\}) = -e^2\sum_{i=1}^{N_I} \frac{Z_I}{|\mathbf{r} - \mathbf{R}_i|}. \tag{1.4}$$

Because the ions are considered to be "frozen", we shall drop the parametric dependence on its positions, $\{\mathbf{R}\}$ in the rest of the chapter.

2. For simplicity, we exclude the spin degree of freedom at this point.

Second Hohenberg-Kohn theorem *Given a system of N interacting particles, there exists a universal functional, $\mathcal{F}[n] = \langle\Psi[n]|\hat{T} + \hat{V}_{\rm int}|\Psi[n]\rangle$ where Ψ is the many-body wavefunction, which is uniquely determined once $\hat{T}$ and $\hat{V}_{\rm int}$ have been defined. The functional*

$$E[n] = \mathcal{F}[n] + \int d\mathbf{r}\, n(\mathbf{r}) v_{\rm ext}(\mathbf{r}), \tag{1.5}$$

is minimized for the ground state density.

The universal Hohenberg-Kohn functional $\mathcal{F}$ only depends on the kinetic energy and the electron-electron interaction, with all the specific details of the system being relegated to $v_{\rm ex}$. Note, however, that the form of $\mathcal{F}$ is not known, and thus the practical application of these ideas is limited.

1.1.2 Kohn-Sham formalism

In 1965, Kohn and Sham developed the Kohn-Sham formalism which provides a practical recipe to put the Hohenberg-Kohn theorems into practice. As opposed to the more abstract Hohenberg-Kohn theorems, the Kohn-Sham approach introduces a set of single-particle wavefunctions (Kohn-Sham orbitals, $\psi_l(\mathbf{r}) = \langle\mathbf{r}|\psi_l\rangle$ with corresponding occupation numbers f_l) obtained from an effective single-particle Hamiltonian such that the particle density

$$n(\mathbf{r}) = \sum_l f_l |\psi_l(\mathbf{r})|^2, \tag{1.6}$$

is the same that the density of the interacting system.

In the Kohn-Sham formulation of DFT, the functional (1.5) is first rewritten as

$$E[n] = T_s[n] + E_{\rm H}[n] + \int d\mathbf{r} n(\mathbf{r}) v_{\rm ext}(\mathbf{r}) + E_{\rm xc}[n], \tag{1.7}$$

where

$$T_s[n] = -\frac{\hbar^2}{2m} \sum_l \int d\mathbf{r} \psi_l^* \Delta_{\mathbf{r}} \psi_l(\mathbf{r}), \tag{1.8}$$

is the single-particle kinetic energy,

$$E_{\rm H} = \frac{e^2}{2} \int d\mathbf{r} \int d\mathbf{r}' \frac{n(\mathbf{r}) n(\mathbf{r}')}{|\mathbf{r} - \mathbf{r}'|}, \tag{1.9}$$

is the Hartree potential, the third term in Eq. (1.5) represents the contribution of the external potential and the last term is the so-called exchange-correlation energy. Note that all the terms except the last term are now explicitly written in terms of the single-particle Kohn-Sham orbitals or the density (which itself is written in terms of ψ_l, see Eq. (1.6)). The exchange correlation energy, $E_{\rm xc}[n]$, is an unknown unique functional of the density and must be approximated (see section 1.1.4). This is due to the fact that it incorporates not only the electron-electron exchange (in the Hartree-Fock sense) and correlations but also the part of kinetic energy that is due to interactions. Formally, we can write it as $E_{\rm xc}[n] = (V_{\rm int}[n] - E_{\rm H}[n]) + (T[n] - T_s[n])$. Note that the "exchange" part included here implicitly should take care of the self-interaction of the charge density with itself that occurs in the Hartree part of the functional (1.9).

The variational problem $\delta E[n]/\delta n(\mathbf{r}) = 0$ can be solved under the constraints of wavefunction orthogonality and fixed particle number

$$\langle \psi_l | \psi_l \rangle = \delta_{l,l'} \qquad \text{and} \qquad N = \int d\mathbf{r} n(\mathbf{r}), \tag{1.10}$$

to obtain the famous Kohn-Sham equations [33]. In real space these equations read

$$\hat{\mathcal{H}}^{\mathrm{KS}}(\mathbf{r})\psi_l(\mathbf{r}) = \left[-\frac{\hbar^2}{2m}\Delta_{\mathbf{r}} + v_{\mathrm{eff}}(\mathbf{r}) \right] \psi_l(\mathbf{r}) = \epsilon_l \psi_l(\mathbf{r}), \tag{1.11}$$

where ϵ_l are the corresponding Lagrange multipliers (Kohn-Sham eigenenergies) and the effective potential

$$v_{\mathrm{eff}}(\mathbf{r}) = \int d\mathbf{r}' \frac{n(\mathbf{r}')}{|\mathbf{r} - \mathbf{r}'|} + v_{\mathrm{xc}}(\mathbf{r}) + v_{\mathrm{ext}}(\mathbf{r}), \tag{1.12}$$

with $v_{\mathrm{xc}}(\mathbf{r}) = \delta E_{\mathrm{xc}}[n]/\delta n(\mathbf{r})$ the so-called exchange-correlation functional.

Eqs. (1.11)-(1.12) constitute the final result of the Kohn-Sham approach. It provides an impressive result as it reduces the N-particle many-body Schrödinger equation (1.1) to a set of auxiliary single-particle Schrödinger [Kohn-Sham] equation (1.11). We note that the Kohn-Sham potential (1.12) depends on the density and as a consequence, the Kohn-Sham equations have to be solved self-consistently. Also, we stress here that, in general, the Kohn-Sham eigenenergies are not the "true" energy levels of the many-body interacting system but only Lagrange multipliers resulting from the constrained variational problem. Nevertheless, they themselves and the corresponding Kohn-Sham wavefunctions offer important information regarding, *i.e.*, symmetries of the system, nodal structure of the states. We shall make the loose identification of the set $\{\epsilon_l\}$ with the system (single-particle) energies.

1.1.3 Basis sets

In order to solve Kohn-Sham equations practically, we must first define a basis to expand the Kohn-Sham wavefunctions $\psi_l(\mathbf{r})$. Note that, practically, the projection happens in a finite-dimensional space of dimension N_{basis}

$$\psi_l(\mathbf{r}) = \sum_{j=1}^{N_{\mathrm{basis}}} c_{jl}\varphi_j(\mathbf{r}). \tag{1.13}$$

In other words, the size of each vector is fixed by the number of basis functions. This introduces numerical errors, which can be reduced by increasing the size of N_{basis}.

In this thesis, we mostly use the FHI-aims *ab initio* molecular simulation package [34] in which $\varphi(\mathbf{r})$ are numeric atom-centered orbitals (NCAOs). However, we note that the basis set is not unique and other basis functions can be used - such as contracted Gaussian orbitals (TURBOMOLE [35, 36]) or plane-waves (Quantum Espresso or Wien2K [37, 38]). The NCAOs used in FHI-aims are hydrogenic-like states of the form $\varphi(\mathbf{r}) = R_{nl}(r)Y_l^m(\Omega)$, where $R_{nl}(r) = u_{nl}(r)/r$ correspond to a radial part and $Y_l^m(\Omega)$ are the

spherical harmonics. Note that the set of NCAOs is not an orthogonal set of vectors. Therefore, the Kohn-Sham equation (1.11) in the orbital representation reads

$$\sum_j \left[\mathcal{H}_{ij}^{\mathrm{KS}} - \epsilon_l S_{ij}\right] c_{jl} = 0, \tag{1.14}$$

where the matrix elements are defined as

$$\mathcal{H}_{ij}^{\mathrm{KS}} = \int d\mathbf{r}\varphi_i^*(\mathbf{r})\mathcal{H}_{ij}^{\mathrm{KS}}(\mathbf{r})\varphi_j(\mathbf{r}) \qquad \text{and} \qquad S_{ij} = \int d\mathbf{r}\varphi_i^*(\mathbf{r})\varphi_j(\mathbf{r}). \tag{1.15}$$

Here, S is the so-called overlap matrix. If $\{\varphi_j\}$ is an orthogonal set, then $S = \mathbb{1}$.

We finally mention here that FHI-aims comes with predefined basis defaults for each atomic species that may be used in a calculation. These defaults go under the names `light`, `tight` or `really_tight` (in order of accuracy) and they possess tested parameters for the basis functions that can be used to check for convergence of our results. These parameters are, among others,

— Basis set size (number of orbitals per atom).
— Cut-off radius for the tails of the radial part of the NCAO (this trick allows to reduce the computational cost due to small finite overlaps between the orbitals far from nuclei).
— Integration grid used to compute the real-space integrals in Eq. (1.15).

1.1.4 Approximations for exchange-correlation functionals

We briefly mentioned in section 1.1.2 that the exact form of the exchange-correlation potential, $v_{\mathrm{xc}}(\mathbf{r})$ which derives from the exchange correlation-energy, is not known and has to be approximated. A natural first approximation inspired from the results of the homogeneous electron-gas [39] is to assume that $v_{\mathrm{xc}}(\mathbf{r})$ is a local function of the density

$$E_{\mathrm{xc}}^{\mathrm{LDA}}[n] = \int d\mathbf{r} n(\mathbf{r})\varepsilon_{\mathrm{xc}}^{\mathrm{LDA}}(n(\mathbf{r})), \tag{1.16}$$

where $\varepsilon_{\mathrm{xc}}^{\mathrm{LDA}}(n(\mathbf{r}))$ is the exchange-correlation energy (normalized to each particle) of a homogeneous electron gas with local density $n(\mathbf{r})$. Albeit its simplicity, this approximation is remarkably good for solids (metals, covalent insulators) although worse for molecules where it tends to overestimate binding energies and underestimate bond lengths [40].

One can improve on LDA by including derivatives of the local density [41] to get a semi-local exchange correlation functional

$$E_{\mathrm{xc}}^{\mathrm{GGA}}[n] = \int d\mathbf{r} n(\mathbf{r})\varepsilon_{\mathrm{xc}}^{\mathrm{GGA}}(n(\mathbf{r}), |\nabla n(\mathbf{r})|, \Delta n(\mathbf{r})). \tag{1.17}$$

These non-empirical approximate functionals are known by the name of generalized gradient approximations (GGA). A popular GGA functional is the PBE (Perdew-Burke-Ernzerhof) [42] which is mostly used in this thesis.

Finally, we mention that GGA functionals can also be improved empirically by replacing part of the exchange in GGA by a fraction of the exact Hartree-Fock exchange,

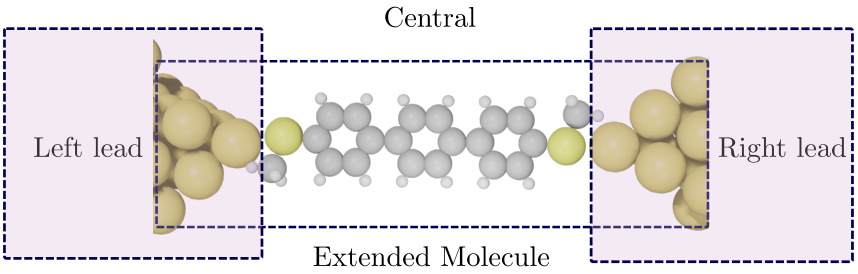

Figure 1.1 – The metallic electrodes/leads are represented by the external shadowed boxes of the molecular junction. Part of the atoms of the electrode at the interface between the molecule and the lead, together with the molecule, form the extended molecule. The self-energy is only applied to the outermost layers of the molecule-metal interface.

$E_{\mathrm{xc}}(\alpha) = \alpha E_x^{\mathrm{HF}} + (1-\alpha)E_x^{\mathrm{GGA}} + E_c^{\mathrm{GGA}}$. This fraction of Hartree-Fock exchange can be altered to fit to experimental results. These functionals are called *hybrid* functionals and they are very widespread in molecular electronics and quantum chemistry. Although in the context of this thesis they have not been employed, we just want to mention that one is B3LYP [43, 44] (Becke-3-parameter-Lee-Yang and-Parr functional), in which the fraction of exact exchange is fixed to be 20%.

1.2 Quantum transport

1.2.1 Green's function approach to quantum transport

In this section, we provide a short overview of the theory of quantum transport based on Green's functions. Most of the results can be found on standard literature [45, 46]. Our typical transport setup consists of a point contact or molecular junction with some arbitrary geometry in the stationary limit (*steady state*). Three parts can be distinguished in the system: a central region (C) where scattering takes place and two semi-infinite leads - left (L) and right (R). The leads act as reservoirs in which the electrons are at equilibrium [which are defined by a temperature T_α and chemical potential μ_α ($\alpha \in \{L, R\}$)]. A schematic of this type of two-terminal transport setup is provided in Fig. 1.1. Note that the separation into these three subsystems (called *partitioning*) is somewhat arbitrary. Normally, some of the atoms of the metallic electrodes forming the interface with the molecule are included into the central region. They, together with the molecule, form the so-called extended molecule, see Fig. 1.1. The usefulness of this concept will be explained in section 1.2.2.

The (time-independent) Schrödinger equation for a system partitioned like in Fig. 1.1 adopts a block form

$$\begin{pmatrix} \hat{\mathcal{H}}_L & \hat{t}_{LC} & 0 \\ \hat{t}_{LC}^\dagger & \hat{\mathcal{H}}_C & \hat{t}_{RC}^\dagger \\ 0 & \hat{t}_{RC} & \hat{\mathcal{H}}_R \end{pmatrix} \begin{pmatrix} |\psi_L\rangle \\ |\psi_C\rangle \\ |\psi_R\rangle \end{pmatrix} = E \begin{pmatrix} |\psi_L\rangle \\ |\psi_C\rangle \\ |\psi_R\rangle \end{pmatrix}, \tag{1.18}$$

where $|\psi_L\rangle, |\psi_C\rangle, |\psi_R\rangle$ are single-particle states that belong to the left, central and right subsystems respectively and we denote the couplings between left-center and center-right

parts by $\hat{t}_{RC} = \hat{t}_{CR}^{\dagger}$ and $\hat{t}_{CL} = \hat{t}_{LC}^{\dagger}$. Introducing the bare [retarded] Green's function

$$\hat{G}_{\alpha}(E) = (E - \hat{\mathcal{H}}_{\alpha} + i0^{+})^{-1}, \tag{1.19}$$

where 0^{+} is an infinitesimal positive quantity. By defining the *self-energy* operators by $\hat{\Sigma}_{\alpha}(E) := \hat{t}_{C\alpha}\hat{G}_{\alpha}(E)\hat{t}_{\alpha C}$, it is a straightforward task to rearrange Eq. (1.18) into a single equation for an effective energy-dependent Hamiltonian $\hat{\mathcal{H}}_{\text{eff}}(E)|\psi_C\rangle = E|\psi_C\rangle$ where $\hat{\mathcal{H}}_{\text{eff}}(E) = \hat{\mathcal{H}}_C + \hat{\Sigma}_L(E) + \hat{\Sigma}_R(E)$. Using the effective Hamiltonian, we can define the Green's function of the coupled system as

$$\hat{G}(E) = [E - \hat{\mathcal{H}}_C + \hat{\Sigma}(E)]^{-1}, \tag{1.20}$$

with $\hat{\Sigma}(E) = \sum_{\alpha}\hat{\Sigma}_{\alpha}(E)$. This [self-energy dressed] Green's function describes electron propagation in the molecular system in the presence of the electrodes.

The self-energies, $\hat{\Sigma}_{\alpha} := \hat{\Sigma}_{\alpha}(E)$, describe the influence (due to coupling) of the leads on the central (scattering) region. They thus contain information about the electronic structure of the reservoirs. Note that the self-energy operator is not Hermitian: the Hermitian part contains information about shifts in the energies of $\hat{\mathcal{H}}_C$ while the anti-Hermitian part,

$$\hat{\Gamma}_{\alpha} := i\left[\hat{\Sigma}_{\alpha} - \hat{\Sigma}_{\alpha}^{\dagger}\right], \tag{1.21}$$

broadens the resonances produced by the [molecular] energy levels. In the time-domain, this is equivalent to introducing a finite lifetime (or decay rate) for the electron in the system which can therefore leave the central region as it is absorbed by the electrodes in the scattering process.

1.2.2 Absorbing boundary conditions

The precise form that $\hat{\Sigma}_{\alpha}$ takes depends on the specific coupling of the central device to the reservoirs, and the calculation can be computationally demanding for large electrodes. We thus consider here the absorbing boundary conditions (ABC) scheme introduced in Refs. [47, 48] and again considered in [49]. This approach considers the self-energy of the reservoirs to be energy-independent (Markovian) and characterized by a local but spatially varying leakage rate

$$\Sigma_{\alpha}(\mathbf{r}, \mathbf{r}') := \langle \mathbf{r}|\hat{\Sigma}_{\alpha}|\mathbf{r}'\rangle = i\eta(\mathbf{r})\delta(\mathbf{r} - \mathbf{r}'). \tag{1.22}$$

In the orbital basis we have

$$\hat{\Sigma}_{\alpha} = i\sum_{p\in\mathcal{S}_{\alpha}}\sum_{j\in O_{\alpha,p}}\eta_p|p,j\rangle\langle p,j|, \tag{1.23}$$

where $\mathcal{S}_{\alpha}$ is the atomic subspace (of lead α) where the electrons can be absorbed, with basis functions $O_{\alpha,p}$ associated to the atoms in $\mathcal{S}_{\alpha}$. The leakage rate $\eta(\mathbf{r})$ acquires non-zero values only at the "surface regions" of the extended molecule; in this way one takes into account that in a realistic situation absorption can only occur far from the molecule. For our specific self-energy model, we choose a value η for the outermost metallic layer of atoms between $\eta \in [0.05, 0.1]$ Hartree. The next layer is given the value $\eta/2$, if there is an eventual third layer, $\eta/4$ *etc.* The value of the leakage has to be adjusted in such a way

that the transmission curves are (largely) invariant under smooth moderate changes of η. In other words, tuning slightly η must not influence the transport properties of the system. Therefore, it is clear that the choice of η is not arbitrary but should adequately describe the smooth and finite density of states of the metallic leads close to the Fermi energy.

Finally, let us mention the important advantages of the Markovian approximation employed in the ABC framework. First, and most importantly, transport properties can be computed as if infinite leads were used in the calculation. Second, this approach leads to an important reduction of the computational effort as only *ab initio* calculations in finite systems have to be performed. And third, substantial simplification of the numerical calculations can be done as described, *i.e.* for the transmission function or the density matrix (see Secs. 1.3.2 and 1.5).

1.2.3 Transmission function

We come now to the transport problem in which an isolated system (the molecule) is connected across a junction to two metal contacts (acting as a "battery" with an electron "source" and a "sink"). The complicated system is modeled as an open system where the central part of the junction is connected to two reservoirs. Each of the reservoirs is assumed to be in equilibrium [characterized by a chemical potential μ and inverse temperature $\beta = 1/(k_B T)$] and with occupation numbers given by Fermi-Dirac distributions $f(E - \mu_\alpha) = \{\exp[\beta_\alpha(E - \mu_\alpha)] + 1\}^{-1}$ where we recall that $\alpha \in \{L, R\}$. The non-equilibrium phenomenae can be introduced by considering that each reservoir has different chemical potentials while assuming the electrodes to be roughly at the same temperature T; the difference $\mu_L - \mu_R = eV_{\text{bias}}$ yields the voltage bias across the whole junction [3]. For example, if $V_{\text{bias}} > 0$ ($\mu_L > \mu_R$), electrons enter the molecule from the left lead into the junction and leave it at the right lead where they are absorbed.

Within the Landauer-Büttiker approach [46, 50, 51, 52], the total stationary current can be expressed by an integral

$$I(V_{\text{bias}}) = \frac{2e}{h} \int_{-\infty}^{+\infty} dE \, [f(E - \mu_L) - f(E - \mu_R)] \, T(E, V_{\text{bias}}), \tag{1.24}$$

where the factor of 2 comes from the spin-degeneracy and we have introduced the bias-dependent transmission function $T(E, V_{\text{bias}})$. The transmission function is a central object in the interpretation of transport in nanoscale systems. It can be understood as the probability for an electron that is injected with energy E at V_{bias} to propagate from one contact to the other. It therefore contains information about the occupied states from the source electrode, the empty states on the drain electrode and the available transport channels in the molecule [53]. Due to this, transport can be ballistic, enhanced or suppressed due to interference [4] or backscattering. The transmission function can be computed from the self-energy dressed Green's function of the central subsystem by a trace formula

$$T(E) = \text{Tr}\left[\hat{\Gamma}_L \hat{G}_C \hat{\Gamma}_R \hat{G}_C^\dagger\right], \tag{1.25}$$

3. Thermoelectrics effects would result if the temperatures of the reservoirs are different.

4. Destructive quantum interference on ferrocene-based molecular junctions will be the subject of chapter 4 of this thesis.

where $\hat{\Gamma}_{L/R}$ is given by Eq. (1.21), the Green's function is given by Eq. (1.20) and, importantly, the trace is taken over the degrees of freedom of the central part only. For small bias compared to the energy barrier across the molecular junction (*i.e.* HOMO-LUMO gap), the transmission function is largely independent of the bias voltage, $T(E, V_{\text{bias}}) \simeq T(E)$. Furthermore, considering the limit of zero temperature for which $f(E-\mu_\alpha) = \theta(E-\mu_\alpha)$ with $\mu_L = E_{\text{F}} + eV_{\text{bias}}$ and $\mu_R = E_{\text{F}}$, it can be easily checked that Eq. (1.24) reduces to

$$I \underbrace{\rightarrow}_{T\to 0} \frac{2e}{h} \int_{\mu_R}^{\mu_L} dE T(E) \underbrace{\rightarrow}_{V_{\text{bias}}\to 0} G_0 T(E_{\text{F}}) V_{\text{bias}}, \tag{1.26}$$

where $G_0 = 2e^2/h$ is the quantum of conductance. We therefore obtain as an important result that the conductance $G = dI/dV_{\text{bias}} = G_0 T(E_{\text{F}})$ is given by the value of the transmission function at the Fermi energy, a result that is very commonly used in molecular electronics.

1.3 Quantum transport with spin-orbit coupling

1.3.1 Origin of spin-orbit coupling

As this thesis is partially devoted to investigate the impact of spin-orbit (SO) coupling into electronic and spin properties of molecular junctions, we provide here a short discussion of its origin. A full description of the relativistic dynamics of a single electron of mass m and spin $s = 1/2$ in vacuum was done in the early days of quantum mechanics by P. A. Dirac [54], who derived his well-known equation,

$$[c\boldsymbol{\gamma} \cdot \hat{\mathbf{p}} + mc^2 \mathbb{1}]\Psi = i\hbar\gamma^0 \partial_t \Psi. \tag{1.27}$$

Here, the vector $\boldsymbol{\gamma} = (\gamma_1, \gamma_2, \gamma_3)$ and γ^0 correspond to the Dirac [gamma] matrices, $\mathbf{p}$ the linear momentum, c the velocity of light, $\mathbb{1}$ the 4×4 identity matrix and Ψ a four-component spinor. The Dirac matrices are 4×4 matrices whose form depend on the particular representation. For example, in the so-called Pauli representation they read

$$\gamma^0 = \begin{pmatrix} \sigma_0 & 0 \\ 0 & -\sigma_0 \end{pmatrix}, \text{ and } \gamma^j = \begin{pmatrix} 0 & \sigma_j \\ -\sigma_j & 0 \end{pmatrix}, \tag{1.28}$$

where $j = 1, 2, 3$, σ_0 is the 2×2 identity matrix and $\boldsymbol{\sigma} = (\sigma_1, \sigma_2, \sigma_3) = (\sigma_x, \sigma_y, \sigma_z)$ are the Pauli matrices [5]. The block form of the matrices (1.28) suggests that we can decouple this equation into two coupled equations for [two-component] spinors. We therefore write the 4-component spinor as

$$\Psi = \begin{bmatrix} \psi_1 \\ \psi_2 \end{bmatrix}, \tag{1.30}$$

where ψ_1 is sometimes called the "large" component (describing electronic-like solutions at low energies), and ψ_2 is the "small", component (describing the positronic-like solutions).

5. We recall the definition of the Pauli matrices

$$\sigma_x = \begin{pmatrix} 0 & 1 \\ 1 & 0 \end{pmatrix}, \qquad \sigma_y = \begin{pmatrix} 0 & -i \\ i & 0 \end{pmatrix}, \qquad \sigma_z = \begin{pmatrix} 1 & 0 \\ 0 & -1 \end{pmatrix}. \tag{1.29}$$

We further consider in what follows the stationary problem by doing the usual replacement $i\hbar\partial_t \to E$ and assume that the electron interacts with an external electromagnetic field incorporated via the minimal coupling rule, $\mathbf{p} \to \boldsymbol{\pi} = \mathbf{p} + e\mathbf{A}(\mathbf{r})$ and $E \to E - V(\mathbf{r})$. We find the coupled equations

$$c\boldsymbol{\sigma}\cdot\hat{\boldsymbol{\pi}}\psi_1 = [E - mc^2 - V(\mathbf{r})]\sigma_0\psi_2, \tag{1.31a}$$

$$c\boldsymbol{\sigma}\cdot\hat{\boldsymbol{\pi}}\psi_2 = [E + mc^2 - V(\mathbf{r})]\sigma_0\psi_1. \tag{1.31b}$$

If $V(\mathbf{r})$ is a self-consistent scalar potential Eqs. (1.31a)-(1.31b) are known as the "Dirac-Kohn-Sham equations" [55]. From Eq. (1.31b), we have $\psi_2 = \boldsymbol{\sigma}\cdot\boldsymbol{\pi}\hat{K}\psi_1$ (this relation is sometimes called "kinetic balance" [55]) where

$$\hat{K} := \frac{c}{E + 2mc^2 - V(\mathbf{r})}, \tag{1.32}$$

so that we can easily find an equation involving only the two-component spinor ψ_1

$$c\boldsymbol{\sigma}\cdot\hat{\boldsymbol{\pi}}\hat{K}\boldsymbol{\sigma}\cdot\hat{\boldsymbol{\pi}}\psi_1 = [E - V(\mathbf{r})]\sigma_0\psi_1. \tag{1.33}$$

Here, we have also shifted the energy $E - mc^2 \to E$ so that E gives the difference to the energy of the particle in the rest frame. Note that Eq. (1.33) is not a usual eigenvalue equation and that ψ_1 is also not a normalized spinor.

The non-relativistic limit of Eq. (1.27), known as Pauli equation, can be obtained by expanding Eq. (1.32) in Taylor series for the small parameter $[E - V(\mathbf{r})]/2mc^2$ under the assumptions $E, |V(\mathbf{r})| \ll mc^2$. Note that because at low energies we have $E \simeq mv^2/2 + V(\mathbf{r})$ this Taylor expansion is in reality an expansion in powers of $v/c \ll 1$.

At lowest order, $\hat{K} \simeq \mathbb{1}/(2mc)$, and using the relation [6]

$$(\boldsymbol{\sigma}\cdot\hat{\boldsymbol{\pi}})^2 = \hat{\boldsymbol{\pi}}^2\sigma_0 + \frac{e\hbar}{c}\boldsymbol{\sigma}\cdot\mathbf{B}, \tag{1.34}$$

we straightforwardly obtain the well-known non-relativistic Schrödinger equation with Zeeman term

$$\left[\frac{\boldsymbol{\pi}^2}{2m} + \frac{e\hbar}{2m}\boldsymbol{\sigma}\cdot\mathbf{B} + V(\mathbf{r})\right]\psi_1 = E\psi_1. \tag{1.35}$$

This important result shows that the electron has an intrinsic magnetic moment given by the Bohr's magneton, $\mu_B = e\hbar/2m$, that can couple to an external magnetic field by a term of the form $\mu_B\boldsymbol{\sigma}\cdot\mathbf{B}$.

Keeping terms up to order $(v/c)^2$ in the expansion of $\hat{K}$ we find, after some rearrangements, the Pauli equation *in its full glory* [56]

$$\left[\underbrace{\frac{\hat{\boldsymbol{\pi}}^2}{2m^*} + V(\mathbf{r})}_{\text{NR Hamiltonian}} + \underbrace{\frac{e\hbar}{2mc}\boldsymbol{\sigma}\cdot\mathbf{B}}_{\text{Zeeman term}} - \underbrace{\frac{\hat{\mathbf{p}}^4}{8m^3c^2}}_{\text{KE corr.}} + \underbrace{\frac{e\hbar^2}{8(mc)^2}\nabla_{\mathbf{r}}\hat{\mathbf{E}}(\mathbf{r})}_{\text{Darwin term}} - \underbrace{\frac{e\hbar}{4(mc)^2}\boldsymbol{\sigma}\cdot[\hat{\mathbf{p}}\times\hat{\mathbf{E}}(\mathbf{r})]}_{\text{Spin-orbit coupling}}\right]\psi = E\psi, \tag{1.36}$$

6. Here we employed the following vector identity $(\mathbf{a}\cdot\boldsymbol{\sigma})(\mathbf{b}\cdot\boldsymbol{\sigma}) = (\mathbf{a}\cdot\mathbf{b})\mathbb{1} + i\boldsymbol{\sigma}\cdot[\mathbf{a}\times\mathbf{b}]$ as well as the constitutive relation between the magnetic field and the vector potential, $\mathbf{B} = \nabla_{\mathbf{r}}\times\mathbf{A}(\mathbf{r})$.

where $\mathbf{E}(\mathbf{r}) = \nabla_{\mathbf{r}} V(\mathbf{r})$, we have identified the "large" component with the well-known two-component Schrödinger-like spinor [7], $\psi_1 \simeq \psi$, and neglected corrections to the Zeeman interaction term. In Eq. (1.36), we obtain three corrections to Eq. (1.35): the scalar kinetic energy (mass-velocity) corrections, the Darwin term and the SO interaction. The corrections to the kinetic energy and the Darwing term (the latter mostly important only close to atomic nuclei) are characterized by an energy scale of ~ 0.01 meV, substantially smaller than the SO coupling with typical energies $\sim 1 - 100$ meV [56]. We note that the Darwin correction and the SO interaction are terms that appear due to the non-commutativity of the canonical momentum $\hat{\mathbf{p}}$ and the scalar potential operator $\hat{V}$, in a similar way as the Zeeman coupling arises from the non-commutativity of the kinetic momentum and the vector potential.

The SO interaction term, which plays a crucial role in this thesis, can be written for a spherical hydrogenic potential $V(\mathbf{r}) = V(r) = -Z/r$

$$\hat{\mathcal{H}}_{\mathrm{SOC}} = -\frac{e\hbar}{4m^2c^2}\frac{\partial V(r)}{r\partial r}\boldsymbol{\sigma}\cdot(\mathbf{r}\times\hat{\mathbf{p}}) = \frac{Ze}{2m^2c^2r^3}\hat{\mathbf{L}}\cdot\hat{\mathbf{S}}, \tag{1.39}$$

where $\mathbf{L} = \mathbf{r}\times\mathbf{p}$ is the orbital angular momentum and $\hat{\mathbf{S}} = \hbar\boldsymbol{\sigma}/2$ the spin operator. It is therefore immediately clear that the SO interaction has to be large in heavy atoms (in particular for core electrons) and smaller in the case of lighter elements. Note that, nevertheless, there might be situations where SO coupling becomes unexpectedly large and does not follow this rule, for example graphene ribbons with defects or ad-atoms [58, 59].

Spin-orbit interaction in density functional theory

We now focus on how SO interaction is dealt with in DFT and briefly discuss how the correction is treated in FHI-aims and TURBOMOLE codes.

FHI-aims. The FHI-aims code [34] (version `171221`) uses the so-called non-self consistent *second-variational method* to deal with SO interaction. This technique essentially starts from a converged self-consistent calculation where scalar relativistic corrections have been included at the atomic ZORA level [60] and rebuilds explicitly the Hamiltonian with a SO interaction term [55]. Therefore, the spin blocks of the Hamiltonian read

$$\mathcal{H}_{ij}^{\sigma\sigma'} = \langle\sigma,\varphi_i|\hat{\mathcal{H}}_{\mathrm{SR}}[n] + \hat{\mathcal{H}}_{\mathrm{SOC}}|\sigma',\varphi_j\rangle, \tag{1.40}$$

where $|\sigma,\varphi_j\rangle = |\sigma\rangle\otimes|\varphi_j\rangle$. The SO-corrected eigenenergies and spinors are obtained from exact diagonalization of this Hamiltonian, a matrix of dimension $2N\times 2N$ with N being the

7. Note that because the conservation of probability applies to the full four-dimensional spinor only

$$\langle\Psi|\Psi\rangle = \langle\psi_1|\psi_1\rangle + \langle\psi_2|\psi_2\rangle = 1, \tag{1.37}$$

one has to be careful when identifying the "large" component ψ_1 with the non-relativistic spinor if higher order corrections in $(v/c)^2$ are considered [57]. Indeed, to avoid some probability being "lost" into ψ_2, we need to redefine ψ_1 according to

$$\psi_1 \to \left[1 + \frac{1}{8m^2c^2}\left(\hat{\boldsymbol{\pi}}^2 + \frac{e\hbar}{c}\boldsymbol{\sigma}\cdot\mathbf{B}\right)\right]\psi_1. \tag{1.38}$$

This normalization enters to correct prefactors the SO term in Eq. (1.36)

number of spinless orbitals. This method has been claimed to offer performance advantages with respect to full self-consistent two-component or four-components implementations as it is similarly precise (in terms of accuracy) and diagonalization of the Hamiltonian with SO interaction occurs only once.

TURBOMOLE. Unlike FHI-aims, TURBOMOLE (version 7.1) [35, 36, 61, 62] aims to explicitly deal with the full four-component spinor using an exact decoupling of the "large" and "small" two-component spinors parts. This can by done by finding a suitable representation of the operator $\hat{K}$ and a proper unitary transformation that decouples the Dirac equation into the two Dirac-Kohn-Sham equations (1.31a)-(1.31b) in an exact way. In a nutshell, one calculates exactly a matrix, dubbed $\mathbb{W}$, with matrix elements given by $\mathbb{W}_{ij} = \langle\psi_i|\boldsymbol{\sigma}\cdot\mathbf{p}\hat{v}\boldsymbol{\sigma}\cdot\mathbf{p}|\psi_j\rangle$ where $\{\psi_i\}$ are two-component spinors and $\hat{v}$ the single-particle potential operator. This matrix can be written in terms of four real matrices $\{W^i\}_{i=0}^3$ as

$$\mathbb{W} = \begin{pmatrix} W^0 + iW^3 & iW^1 + W^2 \\ iW^1 - W^2 & W^0 - iW^3 \end{pmatrix}, \tag{1.41}$$

where $W^0_{ij} = \langle\psi_i|p_x\hat{v}p_x + p_y\hat{v}p_y + p_z\hat{v}p_z|\psi_j\rangle$ contains information about scalar-relativistic corrections and the off-diagonal blocks, $W^l = \epsilon_{lmn}\langle\psi_i|p_m\hat{v}p_n - p_n\hat{v}p_m|\psi_j\rangle$ where ϵ_{lmn} is the antisymmetric tensor, deal with the coupling of the "$\uparrow$" and "$\downarrow$" spins. The eigenvalue problem for the four component spinor is then reduced, by a so-called X2C transformation, into an effective problem $\hat{\mathcal{H}}_{\text{eff}}(W,S,v)C = SC$ (here S is the overlap matrix and C is the matrix of coefficients) for the electronic-like two-component spinor.

1.3.2 Transmission function in the presence of spin-orbit coupling

We describe now how to calculate in an efficient way the zero-bias transmission function in the presence of SO interaction. We again consider the standard setup for electron transport in molecular electronics where a "device" region (molecule) is coupled to two (semi-infinite) leads as presented in section 1.2. If the system has broken spin rotation symmetry, the spin-dependent zero-bias generalized transmission function at energy E, noted $T_{\sigma,\sigma'}(E)$ can be expressed as [50]

$$T_{\sigma,\sigma'}(E) = \text{Tr}\left[\hat{\Gamma}^{\sigma}_{L}\,\hat{G}^{\sigma,\sigma'}\hat{\Gamma}^{\sigma'}_{R}[\hat{G}^{\dagger}]^{\sigma',\sigma}\right]. \tag{1.42}$$

Here, we remind that $\hat{G} \equiv \hat{G}(E)$ is the Green's function of the finite cluster (*extended molecule*) with spin-blocks σ,σ' and $\hat{\Gamma}^{\sigma}_{\alpha} = i\left[\hat{\Sigma}^{\sigma}_{\alpha} - (\hat{\Sigma}^{\sigma}_{\alpha})^{\dagger}\right]$ is the anti-Hermitian part of the self-energy at lead $\alpha \in \{L,R\}$ with spin projection σ. Note that in Eq. (1.42) the trace is taken over orbital degrees of freedom only.

The total transmission function is given by the sum over the spin-resolved transmission components, *i.e.* the sum over the spin-conserved, $T_{\sigma,\sigma}(E)$, and spin-flip, $T_{\sigma,\bar{\sigma}}(E)$, transmission functions

$$T(E) = \sum_{\sigma,\sigma'} T_{\sigma,\sigma'}(E). \tag{1.43}$$

The spin-flip transmission, $T_{\sigma,\bar{\sigma}}(E)$ can be non-zero due to the presence of spin-orbit interaction or due to exchange coupling between local spins in the device region [58].

For simplicity, we now assume spin-unpolarized closed shell leads, with vanishing SO coupling, the extension to spin-polarized electrodes being trivial. This implies that spin, σ, is a good quantum number in the leads and therefore:

— the self-energy is spin-block diagonal;

— the self-energy is spin-independent, *i.e.* $\hat{\Sigma}_\alpha^\sigma = \hat{\Sigma}_\alpha^{\bar{\sigma}} \equiv \hat{\Sigma}_\alpha$ (so that $\hat{\Gamma}_\alpha^\sigma = \hat{\Gamma}_\alpha^{\bar{\sigma}} \equiv \hat{\Gamma}_\alpha$).

The single-particle retarded Green's function of the extended molecule given by Eq. (1.20) is written as

$$\hat{G}(E) = (E\mathbb{1} - \hat{\mathcal{H}}^{\mathrm{KS}} - \mathbb{1}_2 \otimes \hat{\Sigma})^{-1}, \tag{1.44}$$

with $\mathbb{1}$ and $\mathbb{1}_2$ being respectively the $2N \times 2N$ and 2×2 identity matrices, $\hat{\mathcal{H}}^{\mathrm{KS}}$ the Kohn-Sham Hamiltonian. Due to SO coupling, the Kohn-Sham Hamiltonian and therefore the Green's function (1.44) have non-zero entries in the off-diagonal blocks labeled by the spin indices $\sigma, \bar{\sigma}$. The matrix elements of the Kohn-Sham Hamiltonian are expressed in the basis $|\sigma, \varphi_j\rangle$ with $j = 1, \ldots, N$ (here, we recall that N is the number of spin resolved orbitals as well as the number of the spin-resolved basis functions). We further assume that the set of atom-centered real basis functions $\{\varphi_j(\mathbf{r})\}_{j=1}^N$ are orthogonal, obtained after Löwdin orthogonalization [63] of the basis functions used in the underlying density-functional theory calculation. The matrix elements of the Hamiltonian read [8]

$$(\mathcal{H}^{\mathrm{KS}})_{ij}^{\sigma\sigma'} = \langle \sigma, \varphi_i | \hat{\mathcal{H}}^{\mathrm{KS}} | \sigma', \varphi_j \rangle = \int \mathrm{d}\mathbf{x}\, \varphi_i(\mathbf{r}) (\hat{\mathcal{H}}^{\mathrm{KS}})^{\sigma,\sigma'}(\mathbf{r}) \varphi_j(\mathbf{r}). \tag{1.47}$$

We take advantage of the Markovian approximation for the self-energies (see section 1.2.2) and perform a change of basis into the basis that diagonalizes the complex-valued non-Hermitian matrix $\hat{\mathcal{H}}_\Sigma = \hat{\mathcal{H}}^{\mathrm{KS}} + \mathbb{1}_2 \otimes \hat{\Sigma}$. The advantage of using this basis, is that the retarded Green's function (1.44) is also diagonal. Indeed, if the (right) solution to the complex eigenvalue problem $\hat{\mathcal{H}}_\Sigma B = BZ$ is known [where $Z = \mathrm{diag}(z_1, \ldots, z_{2N})$ with $z_i \in \mathbb{C}$ is the eigenvalue matrix and B is a matrix whose columns correspond to the right eigenvectors], then it is straightforward to show that the Green's function can be expressed as

$$\hat{G}(E) = B \underbrace{\frac{1}{E\mathbb{1} - Z}}_{\hat{\mathcal{G}}(E)} B^{-1}. \tag{1.48}$$

Note that because the self-energy given in Eq. (1.22) is energy-independent, there is no need to invert a large matrix for each value of E, but the eigenvalue problem is solved once and the matrix inversion becomes trivial.

We now perform the block-matrix multiplication to obtain the relevant matrix blocks in spin-space

$$\hat{G}^{\sigma\sigma'}(E) = B^\sigma \hat{\mathcal{G}}(E) ([B^{-T}]^\sigma)^T, \tag{1.49}$$

with $B^{-T} = (B^{-1})^T$. Here, we noted by B^σ the $N \times 2N$ matrix extracted from B which results from projecting each eigenvector into the spin subspace labeled by σ. Inserting

8. Here we used the orthonormality and completeness of the basis $|\sigma, \mathbf{r}\rangle \equiv |\sigma\rangle \otimes |\mathbf{r}\rangle$, *i.e.*

$$\langle \sigma | \sigma' \rangle = \delta_{\sigma,\sigma'} \quad \text{and} \quad \langle \mathbf{x} | \mathbf{x}' \rangle = \delta(\mathbf{x} - \mathbf{x}'), \tag{1.45}$$

$$\mathbb{1}_2 \otimes \mathbb{1} = \sum_\sigma |\sigma\rangle \langle\sigma| \otimes \int \mathrm{d}\mathbf{x}\, |\mathbf{x}\rangle \langle\mathbf{x}|, \tag{1.46}$$

as well as the locality of the Hamiltonian in real space.

(1.49) into Eq. (1.42) we find

$$T_{\sigma,\sigma'}(E) = \mathrm{Tr}[\tilde{\Gamma}_L^{\sigma}\hat{\mathcal{G}}\tilde{\Gamma}_R^{\sigma'}\hat{\mathcal{G}}^*], \tag{1.50}$$

where we have introduced the following matrices

$$\tilde{\Gamma}_L^{\sigma} = (B^{\sigma})^{\dagger}\,\Gamma^L B^{\sigma}, \tag{1.51a}$$

$$\tilde{\Gamma}_R^{\sigma} = \left([B^{-T}]^{\sigma}\right)^T \Gamma_R^{\sigma}[(B^{-1})^{\dagger}]^{\sigma}. \tag{1.51b}$$

where $\left([B^{-T}]^{\sigma}\right)^T$ denotes the last N columns of the matrix B.

It is straightforward to check that in the limit of vanishing SO interaction we recover the standard expression for the open-shell transmission function. Indeed, if the Kohn-Sham Hamiltonian does not contain any off-diagonal blocks, $(\hat{\mathcal{H}}^{\mathrm{KS}})^{\sigma,\bar{\sigma}} = 0$, and the inverse of a block-diagonal matrix is given by the inverse of the diagonal blocks, the propagator of the extended molecule is $\hat{G}^{\sigma,\bar{\sigma}}(E) = 0$. Similarly, it is easy to be convinced that the matrix $\hat{\mathcal{H}}_{\Sigma}$ is given by the direct sum of the matrix with the $\sigma = \sigma'$ blocks so that the eigenvectors are the eigenvectors of the blocks correspondingly filled by zeros. In other words, the sectors labeled by σ decouple and we recover the expression given in Ref. [49].

1.4 *Ab initio* spin-orbit torque

We now provide a simple derivation of our main observable: the (SO) torque operator. Within the framework of non-collinear DFT, the single-particle Kohn-Sham Hamiltonian can be written as [64, 65, 66, 67]

$$\hat{\mathcal{H}}^{\mathrm{KS}}(\mathbf{r}) = \hat{\mathcal{H}}^{(0)}(\mathbf{r}) \otimes \mathbb{1}_2 + \boldsymbol{\sigma}\cdot\hat{\mathbf{B}}_{\mathrm{xc}}(\mathbf{r}), \tag{1.52}$$

where $\boldsymbol{\sigma}$ is a vector whose components are the Pauli matrices , $\boldsymbol{\sigma} = (\sigma_x, \sigma_y, \sigma_z)$; $\mathbb{1}_2$ is the 2×2 identity matrix, $\mathbf{B}_{\mathrm{xc}}$ is the exchange-correlation field and

$$\hat{\mathcal{H}}^{(0)}(\mathbf{r}) = \hat{T} + \hat{v}_{\mathrm{H}}(\mathbf{r}) + \hat{v}_{\mathrm{xc}}(\mathbf{r}) + \hat{v}_{\mathrm{ext}}(\mathbf{r}), \tag{1.53}$$

represents the spin-diagonal part of the Hamiltonian. Here, $\hat{T}$ is the single-particle kinetic energy operator, $\hat{v}_{\mathrm{H}}(\mathbf{r})$, $\hat{v}_{\mathrm{ext}}(\mathbf{r})$, $\hat{v}_{\mathrm{xc}}(\mathbf{r})$ are respectively the Hartree, external and diagonal parts of the exchange-correlation potential. The latter has been formally defined as the functional derivative of the exchange correlation energy with respect to the density $n(\mathbf{r})$

$$v_{\mathrm{xc}}(\mathbf{r}) = \frac{\delta E_{xc}[n(\mathbf{r}),\mathbf{m}(\mathbf{r})]}{\delta n(\mathbf{r})}. \tag{1.54}$$

The exchange-correlation field is therefore obtained as the functional derivative of the exchange-correlation energy with respect to the magnetization (or spin) density $\mathbf{m}(\mathbf{r})$ (the direction of $\hat{\mathbf{m}} = \mathbf{m}/|\mathbf{m}|$ defines the local spin quantization axis)

$$\mathbf{B}_{\mathrm{xc}}(\mathbf{r}) = \frac{\delta E_{xc}[n(\mathbf{r}),\mathbf{m}(\mathbf{r})]}{\delta \mathbf{m}(\mathbf{r})}. \tag{1.55}$$

This quantity plays the role of an internal "magnetic" field that couples to the electronic spin degree of freedom formally similar to the Zeeman coupling introduced in section 1.3.1.

Each of the components of the exchange-correlation field is readily obtained from the full Kohn-Sham Hamiltonian

$$B_{\mathrm{xc}}^{x} = (\hat{\mathcal{H}}^{\mathrm{KS}})^{\uparrow\downarrow} + (\hat{\mathcal{H}}^{\mathrm{KS}})^{\downarrow\uparrow} \tag{1.56a}$$

$$B_{\mathrm{xc}}^{y} = i[(\hat{\mathcal{H}}^{\mathrm{KS}})^{\uparrow\downarrow} - (\hat{\mathcal{H}}^{\mathrm{KS}})^{\downarrow\uparrow}] \tag{1.56b}$$

$$B_{\mathrm{xc}}^{z} = (\hat{\mathcal{H}}^{\mathrm{KS}})^{\uparrow\uparrow} - (\hat{\mathcal{H}}^{\mathrm{KS}})^{\downarrow\downarrow}. \tag{1.56c}$$

The non-collinear density matrix can be decomposed in spin-space in a similar way as the Hamiltonian potential

$$\rho(\mathbf{r}) = \frac{1}{2}[n(\mathbf{r}) \otimes \mathbb{1}_2 + \boldsymbol{\sigma} \cdot \mathbf{m}(\mathbf{r})] = \frac{1}{2}\begin{bmatrix} n(\mathbf{r}) + m_z(\mathbf{r}) & m_x(\mathbf{r}) - im_y(\mathbf{r}) \\ m_x(\mathbf{r}) + im_y(\mathbf{r}) & n(\mathbf{r}) - m_z(\mathbf{r}) \end{bmatrix}, \tag{1.57}$$

where the non-collinear components of the magnetization density enters directly in the off-diagonal elements of the density matrix. We note that, in collinear DFT, the off-diagonal elements vanish, and when SO interaction is not very large they are expected to be small.

The SO-induced torque operator [65] can be obtained from its definition as the rate of change of the spin density due to the local exchange field, $\hat{\mathbf{T}} = d\hat{\mathbf{S}}/dt$ where $\hat{\mathbf{S}} = (\hbar/2)\boldsymbol{\sigma}$. Using the Heisenberg's equation of motion, we find

$$\hat{\mathbf{T}} = \frac{1}{2i}[\boldsymbol{\sigma}, \hat{\mathcal{H}}^{\mathrm{KS}}] = \frac{1}{2i}[\boldsymbol{\sigma}, \boldsymbol{\sigma} \cdot \mathbf{B}_{\mathrm{xc}}] = \boldsymbol{\sigma} \times \mathbf{B}_{\mathrm{xc}}. \tag{1.58}$$

As with any other observable, both at equilibrium and non-equilibrium, we can obtain the expectation value of the torque through a trace of the operator with the density matrix (respectively at equilibrium or non-equilibrium), $O \equiv \langle \hat{O} \rangle = \mathrm{Tr}[\hat{\rho}\,\hat{O}]$. Therefore, we have

$$\mathbf{T} \equiv \langle \hat{\mathbf{T}} \rangle = \mathrm{Tr}\left[\hat{\rho}(\boldsymbol{\sigma} \times \mathbf{B}_{\mathrm{xc}})\right]. \tag{1.59}$$

The explict components of this vector in terms of the blocks of the density matrix and the exchange field are given by

$$T_x = \mathrm{Tr}[(\rho^{\downarrow\downarrow} - \rho^{\uparrow\uparrow})B_{\mathrm{xc}}^{y} + i(\rho^{\uparrow\downarrow} - \rho^{\downarrow\uparrow})B_{\mathrm{xc}}^{z}], \tag{1.60a}$$

$$T_y = \mathrm{Tr}[(\rho^{\uparrow\uparrow} - \rho^{\downarrow\downarrow})B_{\mathrm{xc}}^{x} - (\rho^{\uparrow\downarrow} + \rho^{\downarrow\uparrow})B_{\mathrm{xc}}^{z}], \tag{1.60b}$$

$$T_z = \mathrm{Tr}[(\rho^{\uparrow\downarrow} + \rho^{\downarrow\uparrow})B_{\mathrm{xc}}^{y} - i(-\rho^{\downarrow\uparrow} + \rho^{\uparrow\downarrow})B_{\mathrm{xc}}^{x}]. \tag{1.60c}$$

Some important observations are now in order. First, if the exchange-correlation field is smooth at the scale of variation of magnetization the SO torque would follow from the magnetization, $\langle \mathbf{T} \rangle \simeq \langle \boldsymbol{\sigma} \rangle \times \mathbf{B}_{\mathrm{xc}}$. This is however not the case neither for the heterostructures nor the single-molecule junctions, which are the objects of interest in this thesis, since the exchange-correlation field is not smooth at the atomic scale. In this situation, we must use Eq. (1.59). Second, it is also straightforward to show from Eq. (1.59) that we can decompose in a unique way the total torque as sum over the components at each atomic site

$$\mathbf{T} = \sum_{p=1}^{N_{\mathrm{at}}} \mathbf{T}_p. \tag{1.61}$$

This expression can be used to analyze locally the origin of the torque in a molecular junction, in which the current exerts a torque at the local spin for a given atom through the SO interaction.

1.5 Density matrix

As already mentioned above, the second fundamental object that participates in our calculations is the density matrix. We need to distinguish two different scenarios: on the one hand, we have the density matrix at equilibrium (DFT-density matrix); on the other hand, the non-equilibrium density matrix which appears due to the coupling of the central system (molecule) to the reservoirs. The equilibrium density matrix is associated to an isolated system (no exchange of energy or particles) and can be constructed from the Kohn-Sham states obtained in DFT. When the isolated system is connected to reservoirs (characterized by a temperature T and chemical potential μ), due to exchange of particles and energy we need to make use of the non-equilibrium Green's function (NEGF) formalism. Once the non-equilibrium density matrix for a steady-state is known, it can be used to compute the expectation value of any observable, as mentioned in section 1.4. We provide the derivation of the non-equilibrium density matrix in the presence of SO interaction and ABC in this section, extending the results from Refs. [49, 68] for cluster calculations.

1.5.1 Equilibrium density matrix with spin-orbit coupling

The density operator $\hat{\rho}$ for a given quantum system in a finite-dimensional Hilbert space can be written as

$$\hat{\rho} = \sum_l f_l \left|\Psi_l\right\rangle \left\langle\Psi_l\right|, \tag{1.62}$$

where $0 \leq f_l \leq 1$ and $l = 1, \ldots N_{\text{states}}$. The numbers f_l are the occupation of the energy level E_l associated to the quantum state $|\Psi_l\rangle$, therefore at zero-temperature

$$f_l = \begin{cases} 1 & \text{if occupied state,} \\ 0 & \text{if empty state.} \end{cases} \tag{1.63}$$

When SO interaction is present in a non-collinear magnetic system, the single-particle states $|\Psi_l\rangle$ forming the basis of the Kohn-Sham system can be represented by two-component spinors

$$\left|\Psi_l\right\rangle = \sum_\sigma \left|\sigma\right\rangle \otimes \left|\Psi_l^\sigma\right\rangle \equiv \begin{bmatrix} \left|\Psi_l^\uparrow\right\rangle \\ \left|\Psi_l^\downarrow\right\rangle \end{bmatrix}, \tag{1.64}$$

where $|\Psi_l^\sigma\rangle = \sum_{k=1}^{N} c_{kl}^\sigma |\varphi_l\rangle$ can be expanded basis of spinless states ($N_{\text{states}} = 2N$).

Using Eqs. (1.62) and (1.64), the equilibrium density matrix with SO interaction can be written in block form, with blocks given by

$$\rho^{\sigma\sigma'} = c^\sigma \mathfrak{f} (c^{\sigma'})^\dagger. \tag{1.65}$$

Here, $\mathfrak{f}$ is a diagonal matrix of dimension $2N \times 2N$ with the occupation numbers in the diagonal and zero elsewhere, *i.e.* $\mathfrak{f}_{\mu\nu} = f_\mu \delta_{\mu\nu}$. The matrix elements of each block of the density matrix at equilibrium can be explicitly written as

$$\rho_{ij}^{\sigma\sigma'} = \sum_\mu f_\mu c_{i\mu}^\sigma (c^{\sigma'})_{j\mu}^*, \tag{1.66}$$

that is

$$\rho_{ij} = \sum_{\mu} f_{\mu} \begin{pmatrix} c^{\uparrow}_{i\mu}(c^{\uparrow})^{*}_{j\mu} & c^{\uparrow}_{i\mu}(c^{\downarrow})^{*}_{j\mu} \\ c^{\downarrow}_{i\mu}(c^{\uparrow})^{*}_{j\mu} & c^{\downarrow}_{i\mu}(c^{\downarrow})^{*}_{j\mu} \end{pmatrix}. \tag{1.67}$$

The total particle number can be easily determined by a trace over the density matrix

$$N = \mathrm{Tr}(\hat{\rho}) = \sum_{i}\sum_{\sigma} \rho^{\sigma\sigma}_{ii} = \sum_{i\mu}\sum_{\sigma} f_{\mu}|(c^{\sigma})_{i\mu}|^2, \tag{1.68}$$

while the magnetization (spin density) of the system can be obtained through a trace of the density matrix with each of the Pauli matrices, $\mathbf{m} = \mathrm{Tr}(\hat{\rho}\boldsymbol{\sigma})$, *i.e.*

$$m_x = \sum_{i\mu} f_{\mu}\left[c^{\downarrow}_{i\mu}(c^{\uparrow})^{*}_{i\mu} + c^{\uparrow}_{i\mu}(c^{\downarrow})^{*}_{i\mu}\right], \tag{1.69a}$$

$$m_y = i\sum_{i\mu} f_{\mu}\left[c^{\downarrow}_{i\mu}(c^{\uparrow})^{*}_{i\mu} - c^{\uparrow}_{i\mu}(c^{\downarrow})^{*}_{i\mu}\right], \tag{1.69b}$$

$$m_z = \sum_{i\mu} f_{\mu}\left[c^{\uparrow}_{i\mu}(c^{\uparrow})^{*}_{i\mu} - c^{\downarrow}_{\mu}(c^{\downarrow})^{*}_{i\mu}\right]. \tag{1.69c}$$

1.5.2 Non-equilibrium density matrix with spin-orbit coupling

We now turn to the non-equilibrium case in which the isolated (central) system is connected to macroscopic reservoirs and therefore, we deal with an open quantum system. As a consequence of the differences in the chemical potentials of the source and drain, the voltage drop across the junction produces an electrical current and a redistribution of the electronic density in the scattering region. We focus on the steady-state regime and not on transient states (which require to deal with a time-dependent problem).

The non-equilibrium density matrix calculated in this section will enter in our calculations in two ways. First, as we discussed in section 1.4, we compute expectation values of observables such as the torque or the magnetization by tracing the density matrix with the corresponding density operator. Second, we will use this density matrix to update our Kohn-Sham Hamiltonian and obtain self-consistency during the non-equilibrium cycle in chapter 2. Because we are employing the NEGF, we can apply any voltage bias in the junction - not being limited to a narrow voltage window. This would be the case in the linear response regime [69, 70]. Finally, the use of absorbing boundary conditions in our formulation provides us with enormous flexibility in the consideration of the geometry of our single-molecule junction (not being restricted geometries with special symmetries, as it is the case for some self-consistent implementations of DFT-NEGF cycles [68]).

Within the NEGF, our object of interest is the non-equilibrium density matrix $\hat{\rho}$, which can be obtained from energy integration of the lesser Green's function, $\hat{G}^{<} := \hat{G}^{<}(E)$,

$$\hat{\rho} = \frac{1}{2\pi i}\int_{-\infty}^{+\infty} dE\hat{G}^{<}(E). \tag{1.70}$$

The particle density is readily obtained from $\hat{\rho}$ by a trace; for example, in real space representation using the basis $|\sigma, \mathbf{r}\rangle$, the density is given as

$$n(\mathbf{r}) = \sum_{\sigma} \rho^{\sigma\sigma}(\mathbf{r}, \mathbf{r}), \tag{1.71}$$

where $\rho^{\sigma\sigma}(\mathbf{r},\mathbf{r}') = \langle\sigma,\mathbf{r}|\hat{\rho}|\sigma',\mathbf{r}'\rangle$.

The lesser Green's function can be computed using Keldysh equation,

$$\hat{G}^{<}(E) = \hat{G}(E)\hat{\Sigma}^{<}(E)\hat{G}^{\dagger}(E), \tag{1.72}$$

where $\hat{G}(E)$ is the retarded Green's function and $\hat{\Sigma}^{<} := \hat{\Sigma}^{<}(E)$ is the lesser self-energy operator

$$\hat{\Sigma}^{<}(E) = i\sum_{\alpha} f(E-\mu_\alpha)\hat{\Gamma}_\alpha(E). \tag{1.73}$$

Here, we recall that $f(E-\mu_\alpha)$ is the Fermi-Dirac distribution function of lead $\alpha \in \{L,R\}$ with chemical potential μ_α and $\hat{\Gamma}(E)$ is the anti-Hermitian piece of the self-energy, see Eq. 1.21. In the presence of SO interaction, the spin is not a good quantum number. However, in what follows, we shall consider that the leads are made from a material which has small SO interaction compared to the central region and assume that the lesser self-energy is diagonal in spin space. We will still keep in the general derivation the self-energy of the reservoirs labeled by a spin index σ, *i.e.* $\hat{\Sigma}^{\sigma,\sigma'}(E) = \hat{\Sigma}^{\sigma}(E)\delta_{\sigma,\sigma'}$ [and therefore, in Eq. (1.73) the lesser self-energy is also diagonal in spin space], and thus allowing the possibility of having spin polarized currents in our expressions.

From Eq. (1.72), we compute explicitly the block-matrix product

$$\hat{G}^{<} = \begin{pmatrix} G^{\uparrow\uparrow} & G^{\uparrow\downarrow} \\ G^{\downarrow\uparrow} & G^{\downarrow\downarrow} \end{pmatrix} \begin{pmatrix} \Sigma^{<,\uparrow} & 0 \\ 0 & \Sigma^{<,\downarrow} \end{pmatrix} \begin{pmatrix} [G^{\dagger}]^{\uparrow\uparrow} & [G^{\dagger}]^{\uparrow\downarrow} \\ [G^{\dagger}]^{\downarrow\uparrow} & [G^{\dagger}]^{\downarrow\uparrow} \end{pmatrix} \tag{1.74a}$$

$$= \begin{pmatrix} G^{\uparrow\uparrow}\Sigma^{<,\uparrow}[G^{\dagger}]^{\uparrow\uparrow} + G^{\uparrow\downarrow}\Sigma^{<,\downarrow}[G^{\dagger}]^{\downarrow\uparrow} & G^{\uparrow\uparrow}\Sigma^{<,\uparrow}[G^{\dagger}]^{\uparrow\downarrow} + G^{\uparrow\downarrow}\Sigma^{<,\downarrow}[G^{\dagger}]^{\downarrow\downarrow} \\ G^{\downarrow\uparrow}\Sigma^{<,\uparrow}[G^{\dagger}]^{\uparrow\uparrow} + G^{\downarrow\downarrow}\Sigma^{<,\downarrow}[G^{\dagger}]^{\downarrow\uparrow} & G^{\downarrow\uparrow}\Sigma^{<,\uparrow}[G^{\dagger}]^{\uparrow\downarrow} + G^{\downarrow\downarrow}\Sigma^{<,\downarrow}[G^{\dagger}]^{\downarrow\downarrow} \end{pmatrix}. \tag{1.74b}$$

which can be recast into compact form as

$$G^{<,\sigma,\sigma'} = \sum_{\sigma_1} G^{\sigma\sigma_1}\Sigma^{<,\sigma_1}[G^{\dagger}]^{\sigma_1\sigma'}, \tag{1.75}$$

where the energy dependence is kept implicit.

Now, and in the context of absorbing boundary conditions presented in 1.2.2, we assume that the self-energy is Markovian (energy-independent) and parametrized by a local function in real space. As it happens with the transmission function, this allows us to transform the (retarded) Green's function into the basis that diagonalizes the non-Hermitian Hamiltonian incorporating the open boundary conditions in the extended molecule, $\hat{\mathcal{H}}_\Sigma = \hat{\mathcal{H}}^{\mathrm{KS}} + \Sigma$,

$$G^{<,\sigma,\sigma'} = \sum_{\sigma_1} B^{\sigma}\hat{\mathcal{G}}([B^{-T}]^{\sigma_1})^T\hat{\Sigma}^{<,\sigma_1}[(B^{-1})^{\dagger}]^{\sigma_1}\hat{\mathcal{G}}^{*}(B^{\sigma'})^{\dagger}, \tag{1.76}$$

where we recall that $\hat{\mathcal{G}} := \hat{\mathcal{G}}(E)$ is a complex-valued diagonal matrix of dimension $2N\times 2N$ with matrix elements $\mathcal{G}_{\mu\nu}(E) = \delta_{\mu\nu}(E-Z_\mu)^{-1}$, $Z_\mu = \mathrm{Re}Z_\mu + i\mathrm{Im}Z_\mu$ are the eigenvalues of $\hat{\mathcal{H}}_\Sigma$ and B the matrix whose columns are its right-eigenvectors, see also section 1.3.2. Substituting Eq. (1.76) into (1.70), using Eq. (1.73) and assuming the zero-temperature limit in which the Fermi-Dirac distribution function reduces to the Heaviside function

$$f(E-\mu_\alpha) \to \theta(E-\mu_\alpha) = \begin{cases} 1 & \text{if } E \le \mu_\alpha, \\ 0 & \text{if } E > \mu_\alpha, \end{cases} \tag{1.77}$$

we find

$$\rho^{\sigma\sigma'} = \sum_{\alpha} B^{\sigma} \left\{ \frac{1}{2\pi} \int_{-\infty}^{\mu_\alpha} dE\, \hat{\mathcal{G}}(E) \sum_{\sigma_1} \left[([B^{-T}]^{\sigma_1})^T \hat{\Gamma}_{\alpha}^{\sigma_1} ([B^{-1}]^{\dagger})^{\sigma_1} \right] \hat{\mathcal{G}}^*(E) \right\} (B^{\sigma'})^{\dagger}. \quad (1.78)$$

Note that the integral in the brackets does not depend on the spin index.

In order to recast Eq. (1.78) into a more familiar expression that can be related to the equilibrium density matrix, we define $\hat{\tilde{\Gamma}}_{\alpha} := \sum_{\sigma} ([B^{-T}]^{\sigma})^T \hat{\Gamma}_{\alpha}^{\sigma} ([B^{-1}]^{\dagger})^{\sigma}$ so that each of the spin-blocks of the non-equilibrium density matrix is written as

$$\rho^{\sigma\sigma'} = B^{\sigma} J (B^{\sigma'})^{\dagger}. \quad (1.79)$$

Here, the matrix $\hat{J} := \sum_{\alpha} \hat{J}_{\alpha}$, where $\hat{J}_{\alpha}$ is given by the integral

$$\hat{J}_{\alpha} = \frac{1}{2\pi} \int_{-\infty}^{\mu_\alpha} dE\, \hat{\mathcal{G}}(E) \hat{\tilde{\Gamma}}_{\alpha} \hat{\mathcal{G}}^*(E), \quad (1.80)$$

which can be evaluated analytically using contour integration taking advantage of the Markovian approximation for the self-energy. We do not enter into the details of this calculation, as it is identical to the case without SO interaction and we refer the reader to Ref. [49] for details. The final result for the matrix elements is

$$(J_{\alpha})_{\mu\nu} = (\tilde{\Gamma}_{\alpha})_{\mu\nu} F_{\mu\nu}(\mu_{\alpha}) \qquad \mu, \nu = 1, \ldots, 2N, \quad (1.81)$$

with

$$F_{\mu\nu}(\mu_) = \frac{1}{2\pi} \frac{1}{(\epsilon_\mu - \epsilon_\mu) + i(\eta_\mu - \eta_\nu)} \Big[-2\pi i + \frac{1}{2} \ln \left(\frac{\epsilon_\mu^2 + \eta_\mu^2}{\epsilon_\nu^2 + \eta_\nu^2} \right) - i \arctan \left(\frac{\eta_\mu}{\epsilon_\mu} \right) - i \arctan \left(\frac{\eta_\nu}{\epsilon_\nu} \right) \Big], \quad (1.82)$$

and $\epsilon_\mu = \mu - \mathrm{Re} Z_\mu$ and $\eta_\mu = \mathrm{Im} Z_\mu$.

Comparison of Eq. (1.79) to Eq. (1.65) allows us to give an interpretation of the matrix $\hat{J}$: this matrix is the non-equilibrium equivalent of the occupation numbers. Note that J is no longer diagonal unlike the matrix $\mathfrak{f}$ that contains the occupation numbers at equilibrium.

Chapter 2

Self-consistent calculations at finite bias with spin-orbit coupling: Methodology and validation

In this chapter, we explain the numerical methodology later employed in the calculation of SO torques in single-molecule junctions. We explain how the self-consistent DFT-NEGF cycle is implemented in the AITRANSS module for a two-terminal junction setup. We detail how self-consistent calculations that take into account the dependence of the potential on the density are performed, allowing us to go beyond the linear response regime in the calculation of electronic or spin related observables. The numerical validation of the methodology for different testbed systems is provided in great detail.

Calculations in Figures 2.2, 2.3 and 2.6 were done in collaboration with Dr. Vladislav Pokorný of Dr. Richard Korytár's group at Charles University, who obtained the TURBOMOLE data shown in those Figures. The numerical data shown in subsection 2.2.2 corresponding to the pre-existing AITRANSS code were obtained by Dr. Alexej Bagrets and Paul Schnaebele of Prof. Ferdinand Evers' group.

2.1 DFT-NEGF self-consistent cycle with spin-orbit coupling

2.1.1 How the DFT-NEGF cycle works

In chapter 1, we introduced the two fundamental quantities needed for the calculation of SO torque. On the one hand, the Kohn-Sham Hamiltonian in the presence of SO interaction which contains the information about the exchange-field. On the other hand, the non-equilibrium density matrix. The latter contains all the information of the non-equilibrium redistribution of the charge density in the junction once the molecule is connected to the leads and a bias voltage is subsequently applied. The two quantities are obtained within a DFT-NEGF self-consistent (SC) loop in which the density calculated from the non-equilibrium density matrix is used to update the Kohn-Sham Hamiltonian in the DFT. In turn, the DFT code provides the updated Kohn-Sham states, which are used in the construction of a new density matrix. Once the cycle is converged, observables can be computed from the non-equilibrium density matrix. The fundamental reason why this

cycle is necessary for finite-bias calculations is simple to understand: the scattering potential in the junction when a bias is applied is itself a functional of the density matrix. Under finite bias, a fixed amount of charge moves from one side of the junction to the other. The bias-induced charge reorganization has to be fed back to the scattering potential through the density matrix, so that the capacitor-like fields are well-incorporated into the scattering potential. We mention here that this idea of a SC procedure has been already used before (see, for instance, Refs. [26, 48, 49, 71]) and the purpose of this chapter is to validate the extension to systems with SO coupling. The method will be later employed for the calculation of SO torques in single-molecule junctions.

We give in Fig. 2.1 the general scheme of the SC DFT-NEGF cycle. In any SC DFT-NEGF calculation, we first start from an optimized geometry for the molecular junction obtained by the usual procedures [1]. Hence, once a given optimized geometry is given, we perform a first SC DFT-NEGF cycle. In this cycle, we make use of two different codes that have been interfaced for this purpose: FHI-aims is used as DFT-workhorse code, while the quantum transport package AITRANSS [26] takes care of the construction of the non-equilibrium density matrix, as detailed in section 1.5.2. The usage of two independent codes allows for greater versatility of our method, since our quantum tranport package can also be straightforwardly interfaced with other DFT codes using localized orbital basis sets (*e.g.* TURBOMOLE). As briefly mentioned above, the general idea is as follows: the DFT code provides the Kohn-Sham states $|\Psi_\mu\rangle$ and energies ϵ_μ where $\mu = 1, \dots 2N$ obtained from the diagonalization of the single-particle Kohn-Sham Hamiltonian (1.52). These states are first used to reconstruct the Kohn-Sham Hamiltonian in AITRANSS. Together with the model self-energies that introduce the coupling to the semi-infinite leads, the non-equilibrium density matrix of the extended molecule is then obtained. We take care that at each step of the cycle the total number of electrons N is fixed when the extended molecule is connected to reservoirs by appropriately shifting the energy levels (see section 1.5.2 for specific details). The density matrix at step n is linearly admixed with the density matrix at step $n-1$ to improve convergence. At each step, we check for convergence by calculating the Schur's norm of the matrix $\delta\hat{\rho} = \hat{\rho}_n - \hat{\rho}_{n-1}$ and the cycle stops if the condition

$$\frac{1}{N}\sqrt{\sum_{i,j=1}^{N} |\delta\rho_{ij}|^2} \leq \xi \tag{2.1}$$

is satisfied for a given ξ. In the next phase of the cycle, the density matrix is fedback to the DFT code and used to update the density (and the Kohn-Sham Hamiltonian). This way, the redistribution of the charge due to the coupling to the contacts is self-consistently taken into account while preserving charge neutrality. The whole iterative process is controlled by a shell script. In a second step, a bias voltage can be applied to the junction, which requires a new SC cycle similar to the first one (also controlled by a shell script and with convergence determined by the parameter ξ). Finally, after achieving convergence of the second cycle, any observable can be computed in a post-processing step by tracing the density matrix with the corresponding Hermitian operator.

1. We note that for the specific calculation of SO torque we need to ensure that the magnetic single-molecule junction presents broken inversion symmetry, see also chapter 3. In order to ensure this condition, we can choose a molecule with unpaired electrons and relax the junction minimizing the forces so that no inversion symmetry is present. In that system, SO interaction then appears and the coupling of the spin to the orbital degrees of freedom from the electrical current leads to the emergence of SO torques on the localized spins.

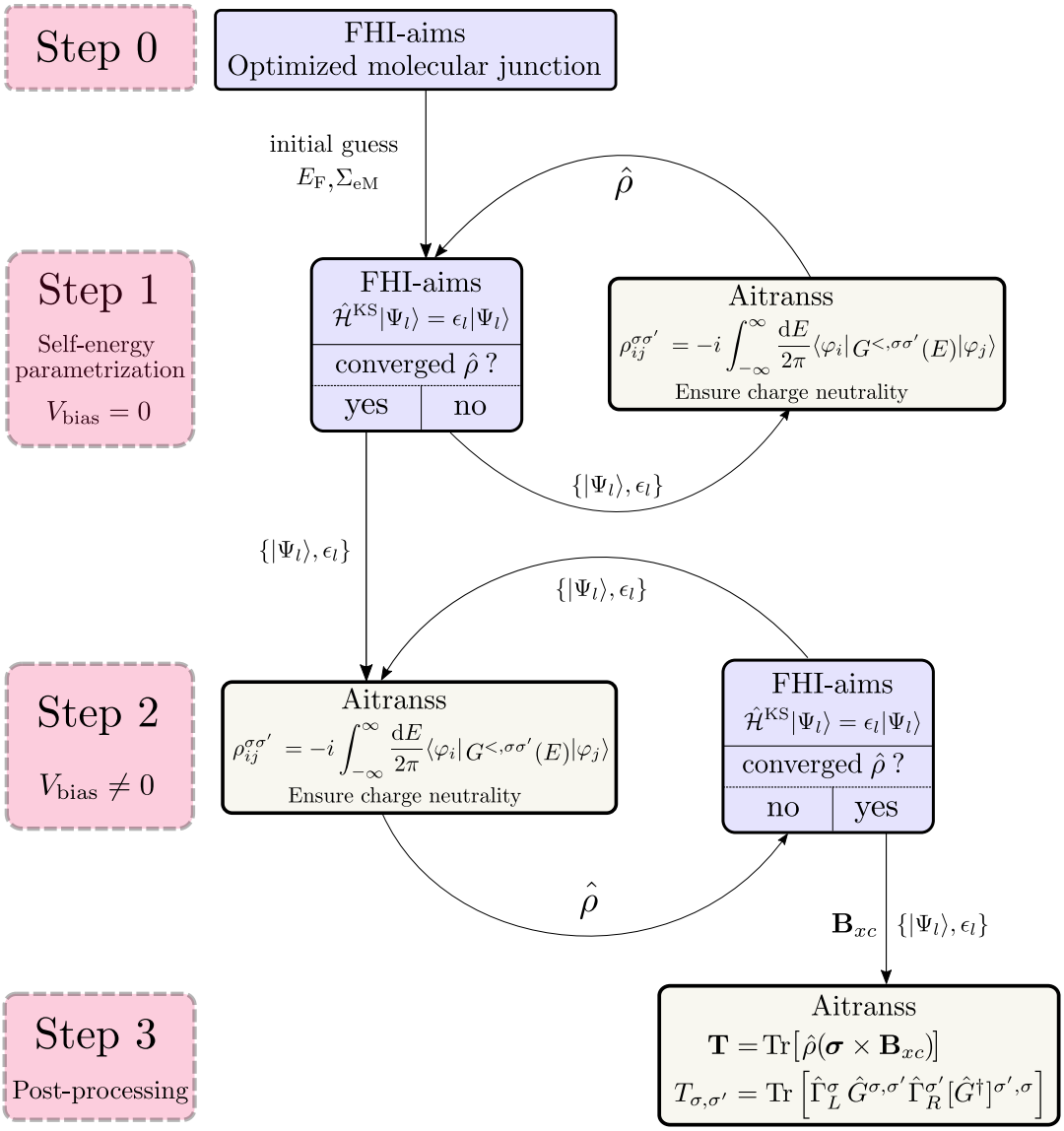

Figure 2.1 – Scheme of the SC DFT-NEGF cycle with SO interaction. The calculation procedure consists in four steps during which two SC loops between FHI-aims and AITRANSS take place. Once the self-energy is parametrized and a voltage bias V_{bias} is applied, we obtain the SC non-equilibrium density matrix to be used in the forthcoming calculation of physical observables of interest (such as SO torque) or in the calculation of transmission characteristics at finite bias, $T(E, V_{\mathrm{bias}})$.

2.1.2 Reconstruction of the Kohn-Sham Hamiltonian

We now briefly describe the (technical) details in the reconstruction of the Kohn-Sham Hamiltonian in our transport package extension, necessary for the computation of the Green's function and the non-equilibrium density matrix. In our simulation tool, we read as the output of FHI-aims the Kohn-Sham states (molecular orbitals), $\psi_\mu(\mathbf{r}) = \langle \mathbf{r}|\psi_\mu\rangle := \langle \mathbf{r}|\mu\rangle$ with $\mu = 1, \cdots 2N$, given by the spinor

$$\psi_\mu(\mathbf{r}) = \begin{bmatrix} \psi_\mu^\uparrow(\mathbf{r}) \\ \psi_\mu^\downarrow(\mathbf{r}) \end{bmatrix} = \sum_{j=1}^{N} \begin{pmatrix} c_{\mu j}^\uparrow \\ c_{\mu j}^\downarrow \end{pmatrix} \varphi_j(\mathbf{r}), \tag{2.2}$$

where $\varphi_j(\mathbf{r}) = \langle \mathbf{r}|\varphi_j\rangle := \langle \mathbf{r}|j\rangle$ are the basis functions and $c_{\mu j}^\sigma$ the Kohn-Sham coefficients projected on each spin component. In general, the distinction between spin up and down in the matrix of coefficients is not necessary, so we typically write the Kohn-Sham states as

$$\psi_\mu(\mathbf{r}) = \sum_{\nu=1}^{2N} B_{\nu\mu}\varphi_\nu(\mathbf{r}), \tag{2.3}$$

with B a complex quadratic matrix of dimension $2N \times 2N$.

Once the molecular orbitals have been read out from a file, we construct the Kohn-Sham Hamiltonian as

$$\mathcal{H}^{\mathrm{KS}} = \sum_{\mu=1}^{2N} |\psi_\mu\rangle \epsilon_\mu \langle \psi_\mu| = \sum_{\mu=1}^{2N} \sum_{\nu,\nu'=1}^{2N} |\nu\rangle B_{\nu\mu}\epsilon_\mu [B^*]_{\mu\nu'} \langle \nu'|. \tag{2.4}$$

Because the atomic basis $\varphi_j(\mathbf{r}, \sigma) = |\sigma\rangle \otimes \langle \mathbf{r}|\varphi_j\rangle$ is non-orthogonal in real space, we also construct the real-valued overlap matrix, S, with matrix elements

$$S_{\nu\nu'} = \langle \nu|\nu'\rangle = \begin{cases} \langle \varphi_\nu|\varphi_{\nu'}\rangle \text{ if } \nu, \nu' \leq N \text{ and } \sigma = \sigma' = \uparrow, \\ \langle \varphi_{\nu-N}|\varphi_{\nu'-N}\rangle \text{ if } \nu, \nu' \geq N \text{ and } \sigma = \sigma' = \downarrow . \end{cases} \tag{2.5}$$

This is a symmetric matrix diagonal in spin space

$$S = \begin{bmatrix} S_\varphi & 0 \\ 0 & S_\varphi \end{bmatrix}, \tag{2.6}$$

with S_φ the overlap matrix of the basis $\{\varphi_j(\mathbf{r})\}_{j=1}^N$.

Using Eq. (2.6), we perform a Löwdin orthogonalization [63] from the non-orthogonal atomic basis into an orthonormal one so that every basis relates mostly to one, and only one, atom

$$|\tilde{\nu}\rangle = \sum_{\nu'=1}^{2N} S_{\nu',\nu}^{-1/2} |\nu'\rangle, \tag{2.7}$$

or

$$|\nu'\rangle = \sum_{\nu'=1}^{2N} S_{\nu',\nu}^{1/2} |\tilde{\nu}'\rangle. \tag{2.8}$$

Combining Eqs. (2.4) and (2.7) we obtain the Hamiltonian in the orthonormal basis by a simple product

$$\hat{\mathcal{H}}^{\mathrm{KS}} = \sum_{\mu=1}^{2N} \sum_{\nu,\nu'=1}^{2N} \sum_{\tilde{\nu},\tilde{\nu}'=1}^{2N} |\tilde{\nu}\rangle S^{1/2}_{\tilde{\nu}\nu} B_{\nu\mu} \epsilon_{\mu} [M^*]_{\mu\nu'} S^{1/2}_{\nu'\tilde{\nu}'} \langle\tilde{\nu}'|, \tag{2.9}$$

or, in matrix form, $\hat{\mathcal{H}}^{\mathrm{KS}} = S^{1/2} B \boldsymbol{\epsilon} B^{\dagger} S^{1/2}$, where $\boldsymbol{\epsilon}$ is a diagonal matrix with the Kohn-Sham energies in the diagonal.

2.1.3 Self-energy parametrization and charge neutrality condition

In order to perform *ab initio* transport calculations in single-molecule junctions we must take into account the size of the metallic clusters that form part of the extended molecule. If there is enough number of metallic atoms in the leads, we add the self-energy using the absorbing boundary condition (ABC) scheme introduced in section 1.2.2. Since the Fermi energy provided by the DFT calculation is already close the Fermi energy of the bulk metal, it is not necessary to introduce a real part of the self-energy to shift the orbital energies in the system (and therefore fix the Fermi energy of the lead). If the number of metal atoms included is large enough, the results (for the transport properties) should coincide with those obtained using semi-infinite leads in the thermodynamic limit. We note that this type of calculation is limited to $V_{\mathrm{bias}} = 0$.

Under finite bias $V_{\mathrm{bias}} \neq 0$ or if the number of lead atoms included in the extended molecule is not large enough (so that the bulk electronic structure is not properly captured), the Fermi energy needs to be adjusted. Note that this is the case in the presence of SO interaction. For them, due to the computational costs, the non-equilibrium calculations will always be performed with a reduced number of metal atoms in the contact clusters.

As for the closed-shell calculations without SO interaction [49], there is no *a priori* knowledge of the value of the Fermi energy, E_{F}. The initial value for E_{F} is taken to be (close to) its value for the DFT solution of the isolated system. Given a value for the Fermi energy and fixed the imaginary part of the self-energy (according to the ABC independent parametrization for the chosen metal), we compute the real part of the self-energy by adjusting its value in a SC calculation. This is done by employing a local self-energy of the general form [49]

$$\Sigma^{\sigma}_{\alpha} = \sum_{i,j\in\mathcal{S}_{\alpha}} |i\rangle \left[\delta\epsilon_{\sigma} - i\eta\right] \delta_{ij} \langle j| \,, \tag{2.10}$$

where, in general, $\delta\epsilon_{\sigma} = \delta\epsilon + \sigma\Delta$. In our case, the leads are non-magnetic so we have that the exchange splitting vanishes, $\Delta = 0$. An extension to account for ferro- or antiferromagnetic contacts in the presence of SO interaction can be done trivially. The density matrix for the open system is constructed using Eq. (1.79) and Eq. (1.78). It, therefore, depends parametrically on $\delta\epsilon$ via the self-energy $\hat{\Sigma}$. At each step, n, we ensure that the charge neutrality condition in the extended molecule is satisfied (in the grand-canonical

sense [2]), $N = \mathrm{Tr}[\hat{\rho}(\delta\epsilon_n)]$, within some user-defined tolerance, *i.e.*

$$|N - \sum_{i=1}^{N} \sum_{\sigma} \rho_{ii}^{\sigma\sigma}(\delta\epsilon_n)| \leq \zeta N. \tag{2.11}$$

A safe value for the tolerance is $\zeta = 10^{-4}$. After convergence of the SC calculation, we find $\hat{\rho}(\delta\epsilon_\infty)$, reflecting the energy level shifts due to the coupling of the extended molecule to the contacts.

Next, we take into account that due to the small size of the metal clusters that belong to the extended molecule the excess charge at the boundaries is not properly screened. Indeed, unphysical charge can accumulate at the outermost layers of the metal leads. For that reason, we first obtain for each SC calculation (with E_F and associated shift $\delta\epsilon_\infty$) the excess charge at the interface

$$\delta Q^{\mathrm{outer}} = \sum_{i \in \mathcal{S}_\alpha} \sum_{\sigma} \rho_{ii}^{\sigma\sigma} - Q^{\mathrm{ref}}, \tag{2.12}$$

where $Q^{\mathrm{ref}} = N_{\mathcal{S}_\alpha} Z_{\mathcal{S}_\alpha}$ with $N_{\mathcal{S}_\alpha}$ the number of atoms at the contact region and $Z_{\mathcal{S}_\alpha}$ the charge per atom. These charges are computed by a standard Löwdin population analysis. The excess charge $\delta Q^{\mathrm{outer}}$ is a function of E_F (and therefore $\delta\epsilon_\infty$) and, for a general $\delta\epsilon_\infty$, we have $\delta Q^{\mathrm{outer}} \neq 0$. It has been shown in previous works [49] that the optimal value of the self-energy occurs when such parameters minimize the excess charge at the boundaries of the extendend molecule interfacing with the left/right reservoirs, $\delta Q^{\mathrm{outer}}(\delta\epsilon^*) = 0$. We, therefore, choose $\delta\epsilon^*$ and the corresponding Fermi energy $E_\mathrm{F}^*(\delta\epsilon^*)$ for the subsequent non-equilibrium calculations 2.8.

Finally, once the Fermi energy is obtained, we perform a SC calculation in which the values of $\delta\epsilon_\infty^*$ and E_F^* are fine tuned. This final calculation leads to very small changes in both quantities (of the order of 10^{-4} eV for the Fermi energy) but in our experience they have proved to be crucial in the computation of sensitive observables such as SO torques.

2.1.4 Application of an external bias voltage

After the self-energies have been parametrized, their values $\delta\epsilon^*$ and η are fixed and a bias voltage, V_{bias}, can be applied in the junction.The voltage is given by the difference between the chemical potentials of the left/right reservoirs, $\mu_L - \mu_R = V_{\mathrm{bias}}$ such that, by definition, $\mu_L > \mu_R$. Note that the individual values of the chemical potentials are not kept fixed, so that we have the freedom to change $\bar{\mu} = (\mu_L + \mu_R)/2$ such that the charge neutrality condition is satisfied within a given precision N_ζ. Here, as a difference to section 2.1.3, the convergence $|\mathrm{Tr}[\hat{\rho}(\bar{\mu})] - N| < N_\zeta$ is achieved faster for a strong convergence criteria of $N_\zeta = 10^{-7}$ electrons.

2. We remind the reader that once the isolated central system is connected to semi-infinite leads, the stationary quantum system is open and the number of electrons present in the extended molecule is only known in average for a given chemical potential (Fermi energy).

2.1.5 Calculation of observables: spin-orbit torque

Once the non-equilibrium density matrix is known at a given bias voltage, we can proceed with the calculations of different (non-equilibrium) observables by a simple trace [3]. In this thesis, we focus on the change of magnetic properties induced by currents in matter with SO coupling and will be mostly interested in SO torque (1.59). Note that, because we are interested in the response of an observable to an external perturbation (in the form of a current density), the computation of the proper quantity that does not contain equilibrium (spurious) contributions requires the substraction of the density matrix at zero-bias from the total one calculated at a given bias, $\delta\hat{\rho}(V_{\text{bias}}) = \hat{\rho}(V_{\text{bias}}) - \hat{\rho}(0)$. Using the change in the density matrix, we compute the response in the torque to application of a bias voltage V_{bias}, $\delta\mathbf{T}(V_{\text{bias}})$, using Eq. (1.59) with $\mathbf{B}_{\text{xc}}$ obtained from a calculation at V_{bias}. Alternatively, following Ref. [69] we can compute the change in the exchange-field $\delta\mathbf{B}_{\text{xc}}(V_{\text{bias}})$ due to the current and trace the operator with the density matrix at zero-bias. The response of the system given by $\delta\mathbf{T}(V_{\text{bias}})$ has to be the same. In general, we stress that any quantity that has a non-zero expectation value in equilibrium must always be subtracted from the final result since it will be not observed in a transport experiment. Typical examples of this phenomenon are spin currents in time-reversal invariant systems [72].

2.1.6 Approximations for the self-consistent cycle

Although the basic expressions presented in chapter 1 and the methodology shown here are fully general, we are forced to take certain approximations in our SC cycle due to the characteristics of the software used in this thesis. Here, we use as the main DFT package FHI-aims. As discussed in 1.3.1, it can only perform non-self consistent calculations with SO interaction. In other words, during the update of the density matrix, the Kohn-Sham Hamiltonian which is a functional of the density matrix, is only updated by using the real part of the diagonal blocks. One of the main achievement of this thesis is to show that, given this approximation, one is able to compute non-equilibrium SO-induced properties (magnetization, torques).

Another important point specific for SO torque is related to the fact that the magnetization needs to be able to point in any spatial direction. With the SO treatment offered by FHI-aims this is not a problem since in every step of the SC cycle the SO interaction is incorporated into the Hamiltonian, even though the update only takes into account the particle density. We shall see in chapter 3 that this scheme provides for the right order of magnitude of the SO interaction in a molecular junction.

2.2 Validation: Test calculations

As an appetizer, we first benchmark the implementation of SO coupling in FHI-aims against the full self-consistent non-collinear TURBOMOLE code. Next, we turn to the validation of the implementation of SO interaction in the extended module of AITRANSS. To

3. In the case of the transmission function, an additional trivial step is necessary (extraction of the eigenvalues from a last diagonalization of the Kohn-Sham Hamiltonian) in order to reconstruct the retarded Green's function that appears in the transmission formula (1.42).

begin with, we compare the zero-bias SC transmission function of a bipyridine-gold molecular junction with previous results obtained with AITRANSS in absence of SO interaction. Next, we compare SC calculations performed with the extended module of AITRANSS interfaced against FHI-aims with results where the same transport module has been interfaced with TURBOMOLE. Finally, we compute a self-consistent transmission function of benzenedithiol (BDT) connected to gold and copper leads, both in the presence and absence of SO interaction, and conclude the correctness of the AITRANSS extension to be used in chapter 3.

2.2.1 Spin-orbit coupling in FHI-aims

As we mentioned in section 1.3.1, SO coupling is implemented in FHI-aims as a post-processing step once the convergence of density is achieved. This is different to TURBOMOLE, which performs non-collinear self-consistent calculations in the presence of SO interaction. Here, we provide a benchmark for the SO implementation and compare between results from these two codes in order to evaluate the accuracy of the SO implementation in FHI-aims against a non-collinear self-consistent scheme.

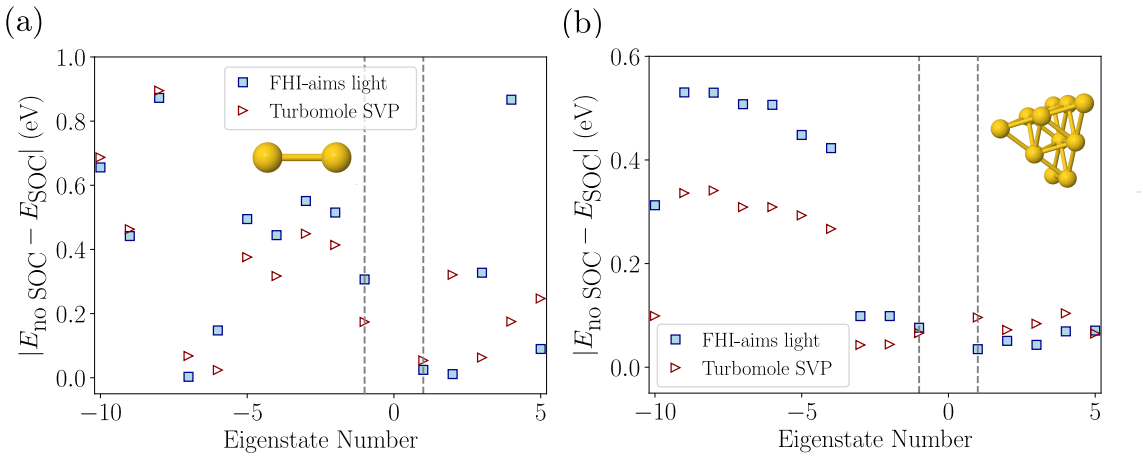

Figure 2.2 – Eigenenergies differences with and without SO coupling for FHI-aims and TURBOMOLE in gold clusters. (a) Difference for a gold dimer (inset) for equivalent light and double-ζ basis sets of FHI-aims (blue square dots) and TURBOMOLE (red triangle dots), respectively, in an all-electron fashion. HOMO and LUMO energies are indicated by dashed lines. (b) Same as in (a) but for a pyramidal gold cluster grown in (111) direction, see inset. The trend of the energies is similar in both panels except for energy values of the gold dimer above the LUMO orbitals. However, in general, deviations up to ~ 0.4 eV are observed for eigenenergies below the HOMO orbital.

In Fig. 2.2 we show the cluster geometries employed: (a) a gold dimer and (b) a gold pyramid made of 11 atoms and cut from a gold (111) surface. We plot for each code (FHI-aims, blue squares and TURBOMOLE, red triangles) the energy difference of the Kohn-Sham eigenvalues between a closed-shell calculation and a SO coupling calculation. We employ for FHI-aims the "light" settings for the basis set while for TURBOMOLE we use the double-ζ in a full electron calculation. The HOMO and LUMO energies are

indicated by dashed vertical lines (-1 for HOMO, 1 for LUMO) [4].

For each code, we find that the differences between the energies in the closed shell and SO coupling calculations can be as big as 1.0 eV, the impact of SO interaction is not negligible. Comparing both codes, the eigenvalue series follow the same trend, especially for the occupied states. The deviations can be as big as 0.1 eV for the gold dimer and even 0.4 eV in the case of the pyramid, the latter having larger number of gold atoms. We show the difference between the FHI-aims and TURBOMOLE Kohn-Sham energies with SO interaction in Fig. 2.3. Observe that for the non-occupied states, the differences become smaller as the number of gold atoms in the cluster increases. Based on this, we might expect that in transport calculations the SO interaction might have a quantitative effect in the position of the transport resonances but not a qualitative effect. Qualitative effects can occur if different metallic species are compared, as it was seen in chapter 5.

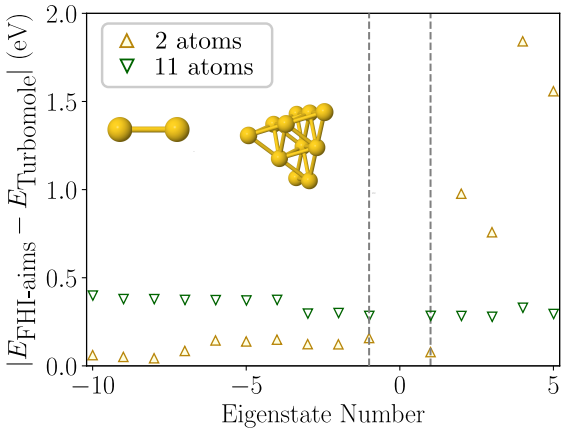

Figure 2.3 – Eigenenergy difference of all-electron calculations performed with SO coupling using light and double-ζ basis sets for FHI-aims and TURBOMOLE, correspondingly. Differences up to 0.4 eV are observed for the pyramidal cluster. For energies lower than the HOMO energy, the differences for the dimer are smaller than for the pyramid. The situation changes drastically for the empty states.

2.2.2 First test case: Bipyridine-gold without spin-orbit coupling

For our first test, we check the implementation of the SC cycle in the extended AITRANSS module by computing the transport characteristics of a bipyridine-gold molecular junction in the absence of SO interaction. We compare with previous results for the same system [5]. The extended molecule consist of the bipyridine molecule attached to two pyramidal gold clusters of 11 atoms. The gold pyramids are cut from a gold surface grown in the (111) direction.

Starting from a previously optimized geometry (see inset in Fig. 2.4), we first check the convergence during the SC cycle. This is done by direct inspection of the Kohn-Sham

4. Note that in the SO coupling calculation we have twice as many eigenvalues compared to the closed-shell calculation. Due to time-reversal symmetry, these eigenenergies come in pairs (Kramers' degeneracy) and for the comparison half of them are not necessary.

5. These results were obtained by P. Schnäbele and A. Bagrets at F. Evers' group.

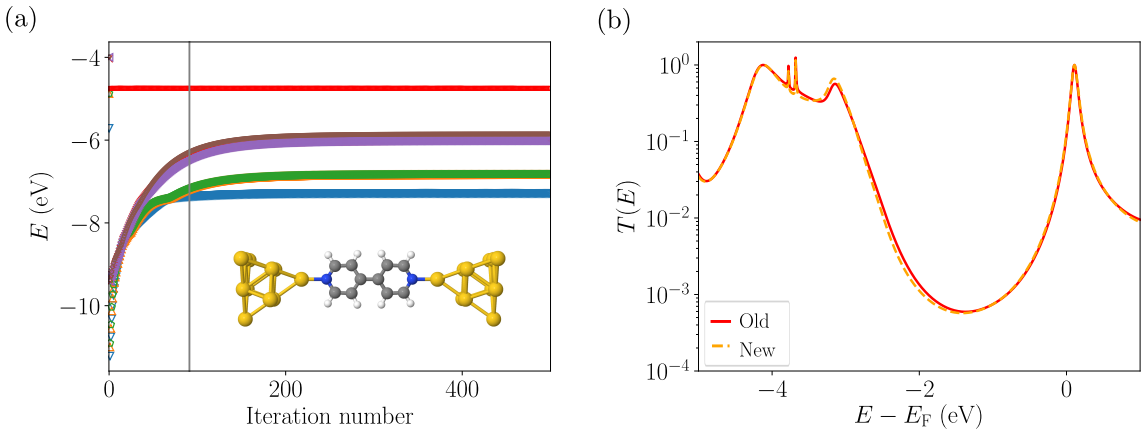

Figure 2.4 – (a) Evolution of the Kohn-Sham eigenvalues closest to the Fermi energy as a function of the number of iterations for the SC cycle adjusting the real part of the self-energy. The horizontal red line marks the value of the Fermi energy, E_{F}. The vertical line corresponds to the iteration for which the convergence criteria $\xi \leq 3 \cdot 10^{-4}$ has been satisfied. Inset: bipyridine-gold geometry used in our calculation. (b) Comparison between the zero-bias transmission functions obtained using the pre-existing AITRANSS in the SC cycle and the present module which accounts for SO interaction.

eigenvalues in each iteration step. In Fig. 2.4 (a), we show the evolution of the Kohn-Sham energies closest to the Fermi energy in the SC cycle that adjusts the real part of the self-energy (step 1 in Fig. 2.1). These energies are obtained from exact diagonalization of the Kohn-Sham Hamiltonian, after the reconstruction following Eq. (2.9). After ~ 400 iterations, we find that the flow of the eigenenergies becomes stable, with the difference for each of them (between consecutive cycles) smaller than 0.01 meV. We note, however, that a typical value for the convergence criteria, $\xi \leq 3 \cdot 10^{-4}$, is not strict enough in this system to achieve converged eigenenergies. Indeed, the iteration for which this criteria is satisfied is shown in Fig. 2.4 by a vertical line at around 90 iterations. Therefore, smaller values for the convergence parameters ξ will be used in our calculations to ensure totally converged values for the Kohn-Sham energies (for ~ 500 iterations we have used the very strict value $\xi = 10^{-6}$).

In table 2.1 we give the comparison between the self-energies obtained with new AITRANSS module, which incorporates SO coupling, and the pre-existing AITRANSS package. In both cases, a leaking rate of $\eta = 0.5 \cdot 10^{-1}$ Ha was used. We find for the real part of the self-energy that the results are qualitatively consistent. The difference is attributed to the improvement in the basis sets used in different versions of the DFT code. For a Fermi energy of $E_{\mathrm{F}} = -4.75$ eV, we find a value of $\delta\epsilon_{\infty} = 1.68$ eV, which is comparable to 1.67 eV for the first layer obtained with the pre-existing AITRANSS package. Respectively, for the second layer, we get $\delta\epsilon_{\infty} = 0.814$ eV with the new module and 0.838 eV with the pre-existing one. The deviation between both values is around $\sim 10^{-2}$ eV. The control file used in order to obtain the plot is given in appendix C.

As explained above, we compute the transmission function using Eq. (1.42) employing the a converged Kohn-Sham Hamiltonian to reconstruct the retarded Green's function.

Parameters	New module	Pre-existing AITRANSS
$\mathrm{Re}(\Sigma_1)$ (Ha)	0.0597	0.0616
$\mathrm{Im}(\Sigma_1)$ (Ha)	0.0500	0.0500
$\mathrm{Re}(\Sigma_2)$ (Ha)	0.0299	0.0308
$\mathrm{Im}(\Sigma_2)$ (Ha)	0.0250	0.0250

Table 2.1 – Benchmark of the self-energies (closed shell, no SO coupling): new module compared to pre-existing AITRANSS. $\mathrm{Re}(\Sigma_i)$ with $i \in \{1, 2\}$ stands for the real part of the self-energy for layer i, while $\mathrm{Im}(\Sigma_i)$, is the imaginary part.

We show the resulting transmission function in Fig. 2.4 (b) comparing to a previously obtained transmission function with the pre-existing AITRANSS package. As expected, we find excellent agreement between both results. This could already be expected due to the very good quantitative agreement between the values of the real part of the self-energy. The tiny discrepancies in the height of the resonances are attributed to small differences in the basis functions for the metallic atoms existing between different versions of the DFT package and the slightly tighter convergence criteria used in our calculations.

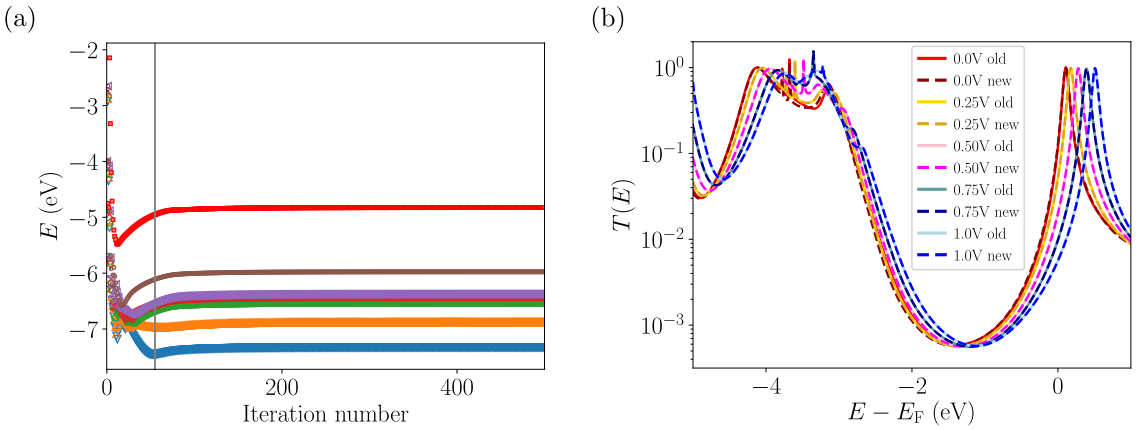

Figure 2.5 – (a) Evolution of the Kohn-Sham eigenvalues closest to the Fermi energy as a function of the number of iterations for the SC cycle adjusting chemical potential. The horizontal red line marks the value of the average chemical potential, $\bar{\mu}$. The vertical line corresponds to the iteration for which the criteria $\xi \leq 3 \cdot 10^{-4}$ has been satisfied. Inset: geometry used in the calculation. (b) Comparison between the zero-bias transmission functions obtained using a previous implementation of this SC cycle and the present implementation for different values of the bias voltage.

We now turn to the calculation of a transmission function at finite bias, $T(E, V_{\mathrm{bias}})$ by performing a SC that adjusts the chemical potential while keeping the system charge neutral. As in Fig. 2.4, Fig. 2.5 (a) shows the evolution of the Kohn-Sham energies as a function of the number of iterations in the SC cycle when adjusting the chemical potential for $V_{\mathrm{bias}} = 1$ V.Comparing with Fig. 2.4 (a), we observe that the convergence of the individual Kohn-Sham energies with the number of iterations occurs faster than in the process of adjusting the real part of the self-energy. Note that, nevertheless, the

strict criteria for ξ leads to a large number of iterations. We mark with a grey vertical line the iteration for $\xi = 3 \cdot 10^{-4}$. The value for the chemical potentials obtained after the SC calculation, using the parameters indicated in appendix C and a sample input file described in appendix B are given in table 2.2.

V_{bias}(V)	New module, E_{F} (Ha)	Pre-existing AITRANSS, E_{F} (Ha)
0.0	−0.17559	−0.17457
0.25	−0.17499	−0.17501
0.50	−0.17571	−0.17571
0.75	−0.17649	−0.17650
1.0	−0.17731	−0.17731

Table 2.2 – Benchmark of the chemical potential without SO coupling: new module compared to pre-existing AITRANSS.

In Fig. 2.5 (b), we compare the resulting transmission functions for different bias voltages (0.0 V, 0.25 V, 0.5 V, 0.75 V and 1.0 V). As above, we have employed the new module (that can account for SO coupling) and compared with pre-existing AITRANSS results. The agreement is excellent and we quantitatively recover the previous transmission function for the different voltages. We also find the expected behavior for the transmission function under bias voltages: shift of resonances together with appearance and/or suppressions of the existing resonances present at zero bias due to the Stark effect [26].

2.2.3 Second test case: bipyridine-gold crosscheck with TURBOMOLE

As a second test example for the AITRANSS module with SO interaction, we compare the transmission functions obtained using as DFT codes FHI-aims and TURBOMOLE [6]. Although we use the full implementation detailed in section 2.1, we still consider only scalar relativistic effects (whose effect in the transmission have been shown to be almost equivalent between both codes, see chapter 1) and neglect SO interaction. The comparison between the transmission characteristics is shown in Fig. 2.6: (a) for $V_{\text{bias}} = 0$ V and (b) for $V_{\text{bias}} = 0.5$ V. We use in both cases the geometry, convergence criteria characterized by ζ, N_ζ and ξ, and Fermi energy employed in section 2.2.2. Both transmission curves show a high degree of overlap with small quantitative deviations in the position and width of the resonances. We attribute the discrepancies to the differences between the basis sets in each code.

2.2.4 Third test case: BDT-copper and -gold with spin-orbit coupling

In this last section, we finally perform a calculation in which SO interaction is taken into account. For simplicity, we choose a system in which the SO coupling is small in

6. We remind the reader that both codes use localized basis sets; FHI-aims employs NCAOs while TURBOMOLE uses contracted Gaussians.

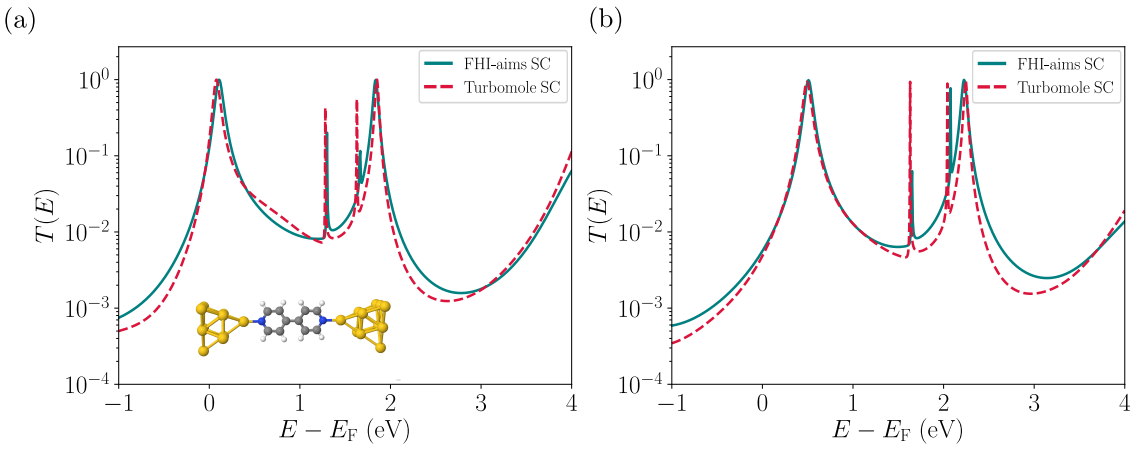

Figure 2.6 – (a) Transmission function for the bipyridine-gold molecular junction at zero bias. We compare both FHI-aims (blue-continuous line) and the TURBOMOLE results (red dashed line). (b) Same as in panel (a) but at $V_{\text{bias}} = 0.5$ V.

the molecular bridge and essentially only relevant in the atoms at the interface with the reservoirs.

To begin with, we consider a non-self consistent calculation of the zero-bias transmission function for benzenedithiol attached to copper and gold leads. These two lead materials are considered as they give us important information about the role of SO interaction. Both should have similar electronic structure since they are located in the same column of the periodic table but the impact of the relativistic effects can be very different (gold, with $Z = 79$ being substantially heavier than copper, $Z = 29$). We also note that both materials are relevant from the point of view of molecular electronics, being typically used as contacts in realistic experimental setups.

We show the results for the transmission function[7] in Fig. 2.7 (a) for copper (b) for gold leads grown in the (100) crystal direction (see geometry in the inset). We compare three different scenarios obtained with our implementation of the transport code with SO interaction: closed shell (dashed blue line), open-shell (or spin-polarized, dubbed here two-component no SO coupling) and SO coupling. First, we realize for both metals that the closed shell and two-component transmissions (spin-polarized calculation) overlap perfectly. This is expected because benzene is a non-magnetic molecule. In both situations, we find that the molecule is HOMO conducting, as it is well known [49]. Much more interesting is the trace for the SO interacting case obtained by adding all spin-conserved and spin-flip components, as defined in Eq. (1.43). For the BDT-copper, the SO interaction has a reduced impact; the resonances that can be attributed to the frontier orbitals are barely affected (deviations being smaller than 0.1 meV). We find that, only at energies around 2 eV below the Fermi energy, the trace with SO interaction deviates from the transmission characteristic obtained in the closed-shell calculation. This deviation is due to the d-orbitals of copper whose electrons might be more affected by the SO coupling compared to the s- and p-orbitals, since the orbital angular momentum $\mathbf{L}$ is larger compared to the

7. Observe that because here the objective is to monitor the impact of SO interaction in the transmission, the calculation need not to be converged with respect to the size of the metallic clusters.

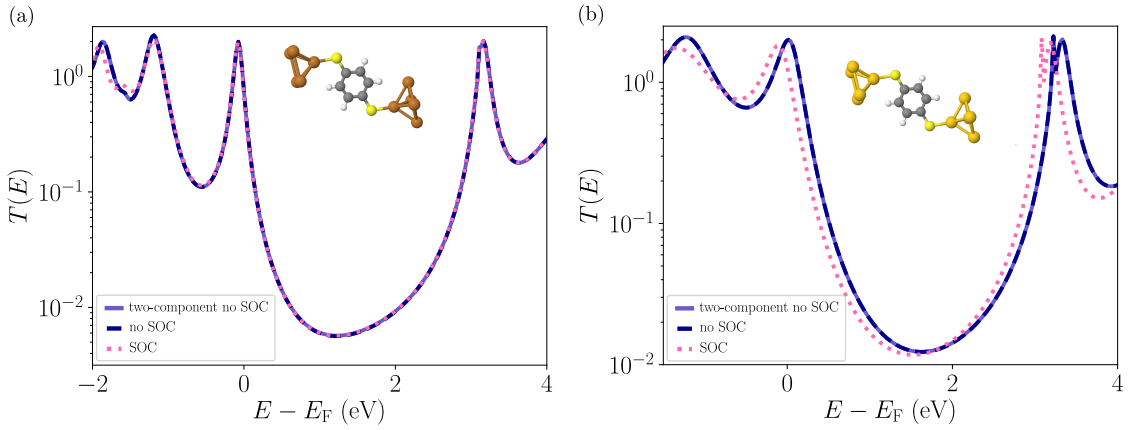

Figure 2.7 – (a) Transmission function obtained for BDT-copper junction for three non-selfconsistent calculations: closed shell (no SO coupling, dashed blue line), open-shell (two-component no SO coupling, solid violet line) and SO (SO coupling, dotted pink line). (b) Same as in (a) but for a BDT-gold junction where the metallic cluster have the same lattice spacing as in copper.

former electrons. For the BDT-gold junction, the situation is drastically different because SO coupling is stronger. Indeed, all the resonances are shifted to lower energies due to the large value of the SO interaction by ~ 100 meV. Note that the effect of SO interaction manifests even with a small number of gold atoms included in the extended molecule. In table 2.3 we provide the energy values close to the Fermi energy, E_F, of the spectrum with and without SO interaction, for gold and copper. In these calculations we have considered just one layer with imaginary part of the self-energy $\eta = 2.72$ eV. We observe that for values close to the Fermi energy E_F, the impact of the SO coupling for gold is larger than copper. For the former, the splitting in energy is noticeable at the second decimal place in the energies, while in the case of gold, we observe the difference in the energy spectrum at the level of the first decimal place. The parameters used for the calculations are given in appendix C and the transmission curves were obtained as indicated in appendix B.

	Cu		Au	
States	E (eV) no SO	E (eV) SOC	E (eV) no SOC	E (eV) SOC
HOMO−2	−4.5399	−4.5390	−5.2679	−5.2868
HOMO−1	−4.5302	−4.5361	−5.2546	−5.1864
HOMO	−4.5175	−4.5021	−5.2186	−5.0017
LUMO	−4.3381	−4.3351	−4.9310	−4.8434

Table 2.3 – Energy spectrum of the BDT molecular junction with Au and Cu. For Au, the impact of the energy value is larger than for Cu, since for the first one the impact of SO coupling (SOC) is notorious already at the first decimal place compared to values without SOC. For Cu, the impact of the SOC is noticeable at the second decimal place.

We therefore conclude that to minimize the effect of SO interaction in the junction properties, copper contacts are the material of choice. We therefore stick to this material for the calculation of the SO torque in single-molecule junctions.

We now proceed as final check of our code with a self-consistent calculation of the transmission function for the copper(111)-BDT molecular junction. We show the geometry, convergence checks and final results in Fig. 2.8. For the geometry given in Fig. 2.8 (a), we first perform step one of our methodology as given in Fig. 2.1. This consists on a SC search of the real part of the self-energy, $\delta\epsilon$. The evolution of the Kohn-Sham energies for a sample of states close to the frontier orbitals is shown in Fig. 2.8 (b), together with the Fermi energy (dashed red line kept fixed in the calculation). We observe that for a small number of metal layers in the cluster, the shift due to the real part of the self-energy is substantial. Indeed, after 600 iterations (which are needed to satisfy the convergence criteria given by $\zeta = 1.5 \cdot 10^{-4}$) we find that $\delta\epsilon_\infty = 0.378\,\text{eV} \sim 0.4$ eV. This value is consistent with the shift of the Kohn-Sham energies after convergence.

The calculation is done for several Fermi energies $E_\text{F} = -4.35, -4.40, -4.45, -4.50$ eV and we monitor the excess (Löwdin) charge accumulated at the boundaries of the extended molecule. As anticipated above in section 2.1.3, we find that the excess charge is almost a linear function of the Fermi energy, see Fig. 2.8 (c). By performing a linear fit $\delta Q^\text{outer} = aE_\text{F} + b$, being $a = -0.0706 \pm 0.0001|e|$ and $b = -0.3102 \pm 0.0006(1/V)$, and setting $\delta Q^\text{outer} = 0$ we find the value of the Fermi energy that minimizes the excess charge at the boundaries. We obtain $E_\text{F} = -4.40$ eV.

Next, we proceed with the second step of the calculation as explained in Fig. 2.1. We choose $\delta\epsilon$ and E_F to be the optimized values and introduce a bias voltage as the chemical potential difference between left and right electrodes. After proceeding as indicated in Fig. 2.1 we find the self-energies given in table 2.4 [8].

$V_\text{bias} = 50$ meV	SC closed-shell	SC open-shell	SC SOC	no SC closed-shell
$\text{Re}(\Sigma_1)$ (Ha)	-0.013903	-0.013904	-0.013889	0.0
$\text{Im}(\Sigma_1)$ (Ha)	0.01	0.01	0.01	0.01
E_F (Ha)	-0.161694	-0.161698	-0.161697	-0.142700

Table 2.4 – Values of the real and the imaginary part of the self-energy, as well as the chemical potential, obtained for self-consistent and no self-consistent calculations when $V_\text{bias} = 50$ meV is applied through a three-layered Cu-BDT-Cu molecular junction. We study the system under three different treatments: closed-shell and open-shell in the absence of SOC, and BDT with self-consistent SOC. The values of real part-part of the self energy differ at the order of 10 μeV. The chemical potential obtained once the bias voltage is applied also differs at the order of 10 μeV. In the case of the closed-shell non-self-consistent calculation, the chemical potential is not adjusted and, as a consequence, the chemical potential shifts by ~ 550 meV. This is expected, since the copper cluster is small.

As an example, we show in Fig. 2.8 (d) the evolution of the Kohn-Sham energies and the average chemical potential (which can also be adjusted to satisfy charge neutrality) as

8. For additional technical information on how the transmission has been obtained see appendix B for the detailed steps and appendix C for parameters and sample input files.

a function of the number of iterations in the SC cycle for $eV_{\text{bias}} = \mu_L - \mu_R = 50$ meV. We note that, compared to panel (b), the convergence occurs much faster, as only ~ 170 iterations are now needed to achieve convergence for the parameter $N_\zeta = 10^{-7}$ electrons. Finally, in Fig. 2.8 (e) the zero-bias transmission function for the copper-BDT junction is represented. We compare between non-self-consistent closed shell (dashed-dotted orange line), self-consistent closed shell (continuous pink line), self-consistent open-shell (dotted blue line) and self-consistent SO coupling (dashed-dotted green line) transmission characteristics. The non-selfconsistent calculation does not make the correction for the value of the Fermi energy while the other self-consistent calculation does. For the size of the clusters considered here, this correction leads to a shift of the Fermi energy of ~ 0.5 eV, which does not manifest in Fig. 2.8 (e) because the Fermi energy is chosen as reference value. As expected, we find small deviations between the non-selfconsistent and the self-consistent traces and a good overlap for the three self-consistent transmission functions. Similarly to Fig. 2.7 (a), we also find that the effect of SO interaction manifests in the transmission function at around -2 eV. Observe that due to the fact that the cavity is symmetric, spurious modes appear in the HOMO-LUMO gap region. This effect has no importance for the benchmark between the different implementations for the calculation of the transmission function which is of interest in this section.

2.3 Summary of this chapter

In this chapter, we have presented the methodology necessary to perform self-consistent calculations in molecular junctions at finite-bias. We have discussed in detail the practical steps and benchmarked the new AITRANSS module, which incorporates SO interaction, against previous results obtained for simple testbed systems.

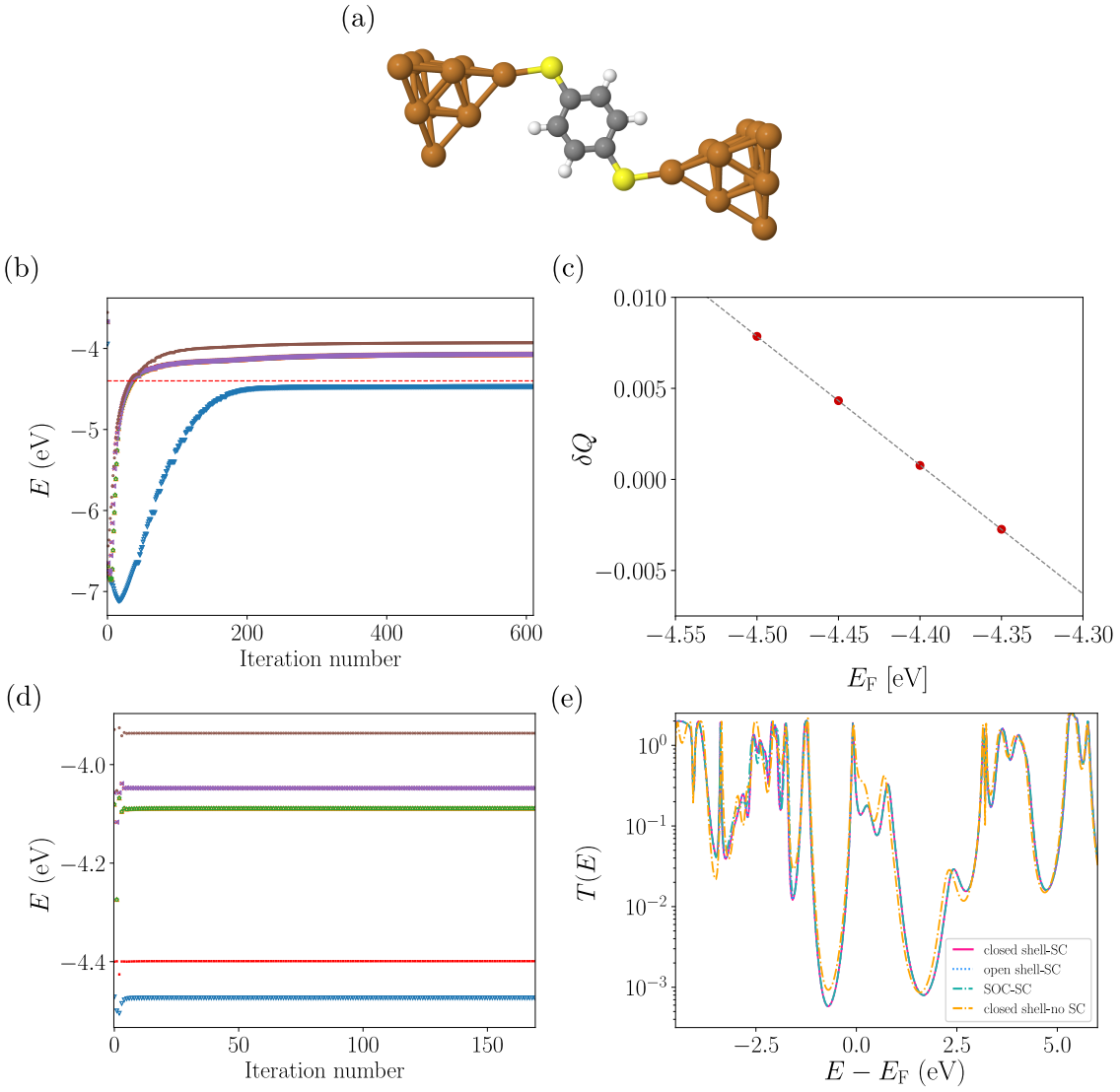

Figure 2.8 – (a) Optimized geometry for the BDT-copper junction. (b) Evolution of the Kohn-Sham energies as a function of the number of iterations in the SC cycle that searches for $\delta\epsilon_\infty$ for a fixed Fermi energy (dashed red line). (c) Excess of charge, δQ^{outer} in the contact region as a function of the Fermi energy. The value $\delta Q^{\text{outer}}(E_{\text{F}}^*) = 0$ and the corresponding $\delta\epsilon^*$ are chosen for the subsequent calculations at finite bias. The coefficients of the fit are $a = -0.0706 \pm 0.0001|e|$ and $b = -0.3102 \pm 0.0006(1/V)$(d) Evolution of Kohn-Sham energies closer to the frontier orbitals as a function of the number of iterations for the SC cycle with an applied voltage $V_{\text{bias}} = 50$ meV. (e) Comparison between the transmission functions for BDT-copper. Non-self-consistent closed shell (dashed-dotted orange line), self-consistent closed shell (continuous pink line), self-consistent open-shell (dotted blue line) and self-consistent SO coupling (dashed-dotted green line) transmission functions are shown.

Part II

Electronic transport studies in single-molecule junctions

Chapter 3

Spin-orbit torque in vanadocene single-molecule junctions

In this chapter, we show our results for the spin-orbit (SO) torque (SOT) obtained from first principles in a single-molecule junction (Cu-NH_2-vanadocene-NH_2-Cu junction). These results are, to the best of our knowledge, the first calculation of this observable in a single-molecule junction context. Following the formalism detailed in previous chapters 1 and 2, we provide an estimation of the order of magnitude of this quantity. The calculated value of SOT is compared to the torque values that can be obtained in extended heterostructures.

3.1 Why is spin-orbit torque interesting?

The calculation of spin torques has been a very active sub-field of spintronics over the past years [64, 65, 69, 73, 74, 75, 76, 77, 78, 79, 80, 81, 82, 83, 84, 85, 86, 87, 88, 16]. There the magnetization of extended heterostructures is controlled by (spin-polarized) electrical currents without applying external magnetic fields. Typically, spin-transfer torque (STT) mechanisms occur when spin-polarized current transfers angular momentum to a ferromagnetic layer to change the direction of the magnetization. Recently, the attention turned into SO-induced torques in heterostructures, [16] which can be used to induce a change in the magnetization direction of a material exploiting the intrinsic SO interaction. In other words, we can produce magnetization switching with non-polarized currents without external magnetic fields. An additional practical advantage of SOT is that the high current density (and electrical power) needed in STT schemes is no longer necessary. This reduces the deterioration of the heterostructures and opens the door for their usage as memory storage devices [89, 90, 91, 92, 93, 94].

We also remind that miniaturization has become increasingly important for modern technological applications. As presented in the introduction of the thesis, this was the driving force of molecular electronics when the field was founded by [2]. Nowadays, molecular junctions form the perfect testbed to study and understand quantum-mechanical phenom-

ena at the nanoscale. Combination of spintronics ideas and molecular electronics led to the field of molecular spintronics [13, 14, 95], paving a way to downscale spintronics devices to the single molecule level. We here propose and present a calculation from *first principles* in which we would like to investigate whether the SOT is large enough to change the magnetization direction of single molecules.

3.2 Brief overview of spin torque in spintronics

In spintronics, spin torques have been extensively studied since J. C. Slonczewski [96] and L. Berger [97] independently predicted the change in the magnetization direction of a ferromagnet placed in a heterostructure by means of spin polarized electric currents. STT in heterostructures became a popular effect studied both theoretically and experimentally [74, 75, 76, 77, 78, 79, 80, 81, 82, 83, 84, 85, 86, 87]. This effect has been studied especially in ferromagnetic-normal metal heterostructures in order to control their magnetization in such a way that no external magnetic fields are needed.

The possibility of switching magnetic moments in heterostructures using conventional electric currents without external magnetic fields has thus allowed for a miniaturization of components in which the switching is required; for example, in memory storage devices (STT-magnetic random access memories). Unfortunately, the necessary high currents produce the fatigue of the materials used in such memories. Thus, STT-MRAMs currently still require an important compromise between magnetoresistance, heterostructure cross section and current density. For this reason, much attention has been devoted to find alternative solutions, a natural one being SOT as the source of magnetization dynamics. The former has come with additional advantages. First, non-polarized currents can also be employed. Second, it requires smaller current densities, allowing for a more effective miniaturization of the components.

The first experimental observation of magnetization switching due to SOT was in Refs. [98, 99]. Since then, it has led to a considerable amount of theoretical and experimental research, mostly in periodic and asymmetrically layered heterostructures [16, 100]. More recent studies have considered topological systems (for instance, surface currents of topological insulators where the torque is induced at the interface of the hybrid heterostructure, see Ref. [16]) or light-induced SO-related switch [101]. Microscopic calculations of spin torques normally require the use of a non-collinear formulation of the transport problem applied to heterostructures [16, 102], while the macroscopic formulation is mostly based on effective dynamical equations for the (macroscopic) spin density [known as the Landau-Lifschitz-Gilbert (LLG) equation]. From the *ab initio* perspective, the theoretical calculation of SOT in heterostructures has been reviewed in Ref. [16]. Most notably, in Ref. [73] a density-matrix based formalism was developed for STT and applied to metals; later, Refs. [69, 70] apply these ideas to compute *ab initio* SOT in the linear response regime in ferromagnetic structures. Only very recently, the non-equilibrium Green's function formalism and *ab initio* have been combined to compute STT and SOT in multilayer periodic systems [65]. This approach has been used to obtain SOT in a Van der Waals heterostructures; the result being later employed in the LLG to study the spin dynamics [100].

3.3 Vanadocenes: a test case study of spin-orbit torque

3.3.1 Choice of the system

We begin by discussing previous considerations about the system in which the SOTs are going to be calculated. This is an important point, as we first need to carefully choose a molecule able of forming stable junctions with metallic leads and with the appropriate electronic (and spin) structure. We will see through this thesis that many organic molecules fulfill the stability requirement, and specifically we will later focus our attention onto carbon-based and silicon-based molecules with a variety of anchor groups (thiols, diamines or even molecules, see chapters 5 and 4). To overcome the small SO interaction of carbon and silicon, we look for molecules with an organic backbone that also contain (heavy) metallic atoms. These atoms will also provide for the localized magnetic moments. An archetypical molecular system of this kind is transition-metal phthalocyanines, which have been widely studied in the last years, both theoretical and experimentally [103, 104, 105, 106, 107, 108, 109, 110, 111]. Unfortunately, they are big molecules and, as a result, have too many degrees of freedom. Therefore, we turn our attention to smaller systems, for example, metal-organic double-decker molecules (metallocenes).

Metallocenes contain a metallic atom "sandwiched" between the carbon-based rings (Cp). The metal atom can be from different transition metals. This characteristic enables the possibility of obtaining a large set of candidate molecules within this family of molecular stacks. They can form multidecker structures which enhance the magnetization of the molecular compounds [112, 113, 114, 115, 116, 117, 118, 119]. A well-known metallocene is ferrocene which has two different electronic structures depending on the oxidation state of the iron atom: Fe^{2+} gives rise to a closed-shell configuration as seen in 4.1, while Fe^{3+} is open-shell. Unfortunately, none are suitable candidates because Cp_2Fe with Fe^{2+} does not present any magnetic moment and Cp_2Fe with Fe^{3+} is charged [1]. By considering these requirements, natural choices for the transition metal in the metallocene are found, for instance, in the fifth column of the periodic table (V, Nb, Ta).

The three metallocenes derived V, Nb, Ta (vanadocene, niobiocene and tantalocene) have magnetic moments localized at the metal atom. All the candidate molecules have uniaxial anisotropy (they have only one easy axis) with the easy magnetization axis located in the $\hat{\mathbf{z}}$-direction, as indicated in Fig. 3.1 (perpendicular to the plane of the Cp rings). The hard axis is located in a plane perpendicular to the easy axis. The magnitude that determines how stable is the magnetization is the so-called magnetoanisotropy energy (MAE). SO interaction is the main source of the MAE. It thus quantifies the cost of changing the magnetization direction from the easy to a hard axis and therefore large MAE means that a device is difficult to demagnetize.

We have computed with TURBOMOLE [35, 36] the MAEs [2] of vanadocene, niobiocene and tantalocene by fixing the spin quantization axis in the $\hat{\mathbf{z}}$ (easy axis) and $\hat{\mathbf{x}}$ (hard axis) directions (see the coordinate system in Fig. 3.1) and substracting both total energies. We find that the MAEs are 21 meV, 1.77 meV and almost 0 meV, for tantalocene, nio-

1. Here, we would like to study neutral molecules in order to prevent from additional effects that may impact the SOT in a non-controlled way.
2. Obtained in collaboration with Dr. Jan Wilhelm from Prof. F. Evers'group.

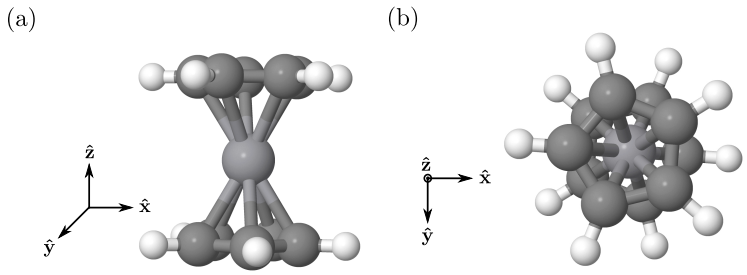

Figure 3.1 – Geometry of vanadocene in its staggered configuration. (a) Side-view of the molecule. The molecule is oriented with the axis perpendicular to the Cp rings oriented in the $\hat{\mathbf{z}}$–direction. (b) Top view of the vanadocene molecule showing the staggered rings in the $x-y$ plane.

biocene and vanadocene, respectively. These values qualitatively agree with values found in literature [117] and are consistent with MAEs calculated for other sandwich compounds [112, 118]. Based on this quantities we conclude that, in principle, the most suitable candidates to study SOT in a metallocene single-molecule junction are niobiocene and tantalocene, as the spin density will change smoothly under a small enough bias voltage.

We would like now to remind the reader of the approximations that were performed in chapter 2 in the SC cycle. In this case, the DFT code includes SOC non-self consistently and, therefore, the off-diagonal blocks as well as the imaginary part of the diagonal blocks of the density matrix are not used to update the Kohn-Sham Hamiltonian. The approximation needs to be treated carefully if the order of magnitude of the neglected matrix elements becomes comparable to those kept in this step of the SC cycle. This happens if the SO interaction is sufficently large. We have found that for Schur's norm computed for the off-diagonal blocks of the density matrix larger than 10^{-3} - as it happens for niobiocene and tantalocene - the SC calculation becomes challenging to be converged. For vanadocene, the SC converges smoothly and we find a Schur's norm of the order of $\sim 10^{-3}$. Consistently with the Schur's norm, the level splitting induced by the SOC is of the order of $\sim 10^{-3}$ eV for vanadocene. For niobiocene and tantalocene the level splitting is of the order of $\sim 10^{-2} - 10^{-3}$ eV and $\sim 10^{-1} - 10^{-2}$ eV, respectively, for the eigenenergies close to the Fermi energy E_{F}.

Finally, as we have pointed out above, the MAE is a relevant factor, which indicates how difficult is to demagnetize a system. A non-zero value of the MAE (which is small and close to zero for vanadocene) may prevent oscillations in the direction of the spin density when the electric current goes across the molecule in the calculation of the SOT. For vanadocene, MAE is almost negligible and the spin density direction rotates very easily. We overcome this situation by using the following "trick": we add a local Zeeman term at the vanadium atom in order to ensure the stability of the spin density direction in the SOT calculations. The local Zeeman field is simply added to the Hamiltonian of the isolated molecule, $\hat{\mathcal{H}}^{\mathrm{KS}}$, which is replaced by $\hat{\mathcal{H}} = \hat{\mathcal{H}}^{\mathrm{KS}} + \hat{\Sigma}_Z$. The value of the Zeeman term is considered to be small so that is acts as a perturbation to the molecular part of the Hamiltonian, shifting the eigenenergies of the Hamiltonian. In the MO basis, this term is easily written as

$$\Sigma_Z^{\sigma\sigma'} = \sigma\delta_{\sigma,\sigma'}\Delta_Z \sum_{p\in\mathcal{A}}\sum_{j\in\mathcal{O}_{\mathcal{A}}} |p,j\rangle\langle p,j|\,, \tag{3.1}$$

where $\mathcal{A}$ is the set of atoms in which the Zeeman term is applied, $\mathcal{O}$ the set of corresponding

orbitals and Δ_Z is referred to as the Zeeman energy. The physical effect of the Zeeman term is to align the spins along the easy axis (set to be the $\hat{\mathbf{z}}$ direction) of the paramagnetic vanadocene molecule. We point out that, although the Zeeman term is introduced locally in the vanadium atom, it affects the whole junction. For the rest of this chapter we will consider only vanadocene molecular junctions.

3.3.2 Electronic structure of vanadocene

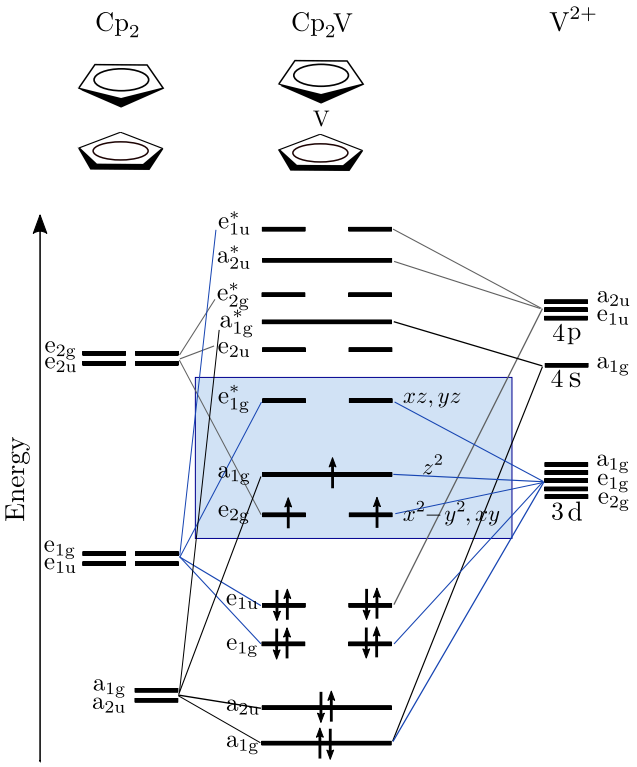

Figure 3.2 – Qualitative molecular orbital (MO) diagram of vanadocene. Here, the left column represents the energy levels of the Cp-rings while the right column corresponds to the (atomic) energy levels of the V^{2+} cation. The combined MO of vanadocene are given in the central column. Here, a stands for non-degenerate orbitals while e is used for doubly degenerate orbitals. The subindex g indicates an even (or inversion symmetric, *gerade*) orbital while u stands for odd (non-inversion symmetric, *ungerade*) orbital. The symbol $*$ refers to the antibonding nature of the MO. The energy levels of the different MOs are arranged from bottom (lower energy) to top (higher energy). The resulting vanadocene molecule is an octahedral complex. Vanadocene presents neutral open-shell metallocene with d-electrons distributed as marked in the blue area of the diagram due to the corresponding ligand field.

We now want to briefly discuss the electronic structure of pristine vanadocene in more detail and analyze the effect of SOC and the Zeeman term. As stated before, vanadocene is an open-shell metallocene with a single vanadium atom sandwiched in a double-decker structure. We show its qualitative molecular orbital (MO) diagram in Fig. 3.2. The distribution of the energy levels results from the combination of the left part of the diagram, that presents the distribution of the energy levels corresponding to the Cp rings, and the right part, where the energy levels of the isolated vanadium V^{2+} cation are shown. The levels are arranged for increasing energy value from bottom to top. In the center of the diagram, the resulting distribution of the MO and the electronic configuration of pristine vanadocene is given. The blue shaded area indicates the MO that derive from atomic d orbitals.

The electronic configuration and the distribution of the energy levels of vanadocene can be explained using ligand field theory [120]. In vanadocene, the role of the ligands is taken by the Cp rings, and together with the vanadium, the molecule conforms an octahedral

complex that lifts the five-fold degeneracy of the d shell from the isolated metallic cation. The occupied d-derived levels appear in a $e_{2g}+a_{1g}$ configuration with $E_{e_{2g}} < E_{a_{1g}}$ and they are occupied according to Hund's rule since the splitting between e_{2g} and a_{1g} is small. The molecule therefore presents three unpaired electrons with expected total magnetic moment of 3.0 a.u. confirmed by DFT calculations, using PBE functional.

In table 3.1, we reproduce the DFT energy values of the relevant MOs of vanadocene. The first two columns correspond to the Zeeman-field free case, with and without SOC. In the absence of SO interaction, the occupied HOMO, HOMO−1 and HOMO−2 levels follow the expected distribution from Fig. 3.2, with the degeneracy between the pair of levels e_{2g} weakly lifted. Adding SOC shifts the Kohn-Sham energies by $0.1 - 1$ meV, thus the SO coupling is small but not negligible. We also present in table 3.1 the impact of adding a local Zeeman field in the vanadium atom [3]. This Zeeman term has been incorporated in a SC cycle in which the equilibrium density matrix, in Eqs. (1.67), is constructed to add the effect of $\hat{\Sigma}_Z$ into the Hamiltonian. We observe that for $\Delta_Z = 1.0$ eV (resp. $\Delta_Z = -1.0$ eV) the energy levels are shifted downwards (resp. upwards) in energy. This result is consistent with our implementation of the Zeeman term, as $\hat{\mathcal{H}}^{\mathrm{KS}}$ for vanadocene and $\hat{\Sigma}_Z$ have each of them a ground state with opposite spin density.

	$\Delta_Z = 0.0\,\mathrm{eV}$		$\Delta_Z = -1.0\,\mathrm{eV}$		$\Delta_Z = -1.0\,\mathrm{eV}$	
	No SOC (eV)	SOC (eV)	No SOC (eV)	SOC (eV)	No SOC (eV)	SOC (eV)
HOMO−4	−4.8809	−4.8808	−4.8361	−4.8360	−4.9322	−4.9322
HOMO−3	−4.7445	−4.7444	−4.7539	−4.7538	−4.7272	−4.7271
HOMO−2	−3.7618	−3.7625	−3.5449	−3.5454	−3.8665	−3.8688
HOMO−1	−3.7168	−3.7187	−3.4979	−3.4997	−3.8471	−3.8473
HOMO	−3.5860	−3.5837	−3.3572	−3.3552	−3.7214	−3.7191
LUMO	−1.8668	−1.8676	−1.6289	−1.6294	−2.1145	−2.1155
LUMO+1	−1.6314	−1.6311	−1.3698	−1.3696	−1.9012	−1.9006

Table 3.1 – Energy levels of the relevant MO orbitals of vanadocene marked by a blue rectangle in Fig. 3.2. We show the energy values with and without SO interaction for three relevant local Zeeman energies $\Delta_Z = 0.0, \pm 1.0$ eV. These values are obtained from a SC calculation at equilibrium using (1.62). We also include the values of the deeper energy levels HOMO−3 and HOMO−4 which should be slightly more sensitive to the SO interaction. The level splitting observed is of the order of meV. This is qualitatively consistent with the typical SOC energy splitting of the hydrogenic-like atom of $Z = 23$ electrons [121], which is 10 times larger. The energies of the d-derived MO change (increasing or decreasing for negative and positive Δ_Z, respectively) by roughly 100 meV due to the Zeeman field.

3.3.3 Choice of the electrodes and geometry of the molecular junction

We now consider the junction that will be used for the single-molecule calculation of SOT. First, we add anchor groups to our metallocene. We consider diamine (NH_2) linkers

3. Clearly, even if the Zeeman term is added locally all the MO are affected due to hybridization between the orbitals of vanadium and the molecular junction.

as thiol anchor groups can be magnetic due to the presence of non-bonding electrons pairs. In order to ensure that the system always lacks inversion symmetry, we always perform a pre-optimization of the geometry under strict criteria for the residual force per atom (below 10^{-2} eV/Å). The resulting structure is attached to pyramidal copper leads growth in (111) direction.

The reader might be tempted to ask why copper has been chosen as electrode material. There are several reasons: first, copper is a material with weak SO interaction [121, 122]; second, the empirical model for the absorbing boundary conditions used for the self-energy has been well-tested [4] with a known value of the parameter η, and, finally, copper is a realistic metal for experiments. This way we consider a setup which can pave the way for possible future experiments in realistic scenarios.

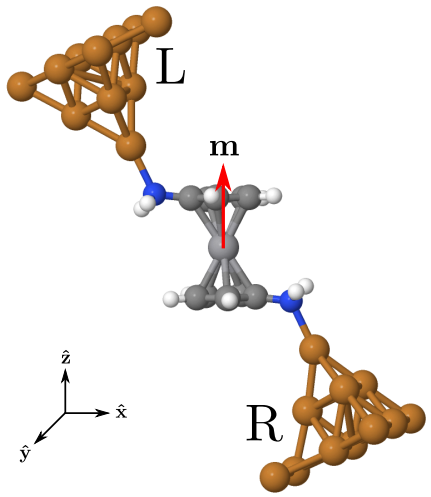

Figure 3.3 – Molecular geometry of the vanadocene-copper molecular junction used in our self-consistent calculations. Here, L and R stands for left and right electrodes, characterized by the chemical potential μ_L and μ_R, respectively, such that $\mu_{\rm L} - \mu_{\rm R} = eV_{\rm bias}$. The main molecular axis and the magnetization, $\mathbf{m}$, of the molecule is mostly oriented in the $\hat{\mathbf{z}}-$direction perpendicular to the plane containing the Cp rings. In contact with the copper leads, the junction Cu-NH_2-vanadocene-NH_2-Cu presents a magnetization carried by the 3 unpaired electrons from the vanadocene a_{1g} and e_{2g} levels with d orbital symmetry z^2, xy and x^2-y^2 (see Fig. 3.2).

In Fig. 3.3 we display the geometry of the full vanadocene-based molecular junction used for the study of the magnetic properties and SOT in vanadocene. We have checked by using DFT calculations that, when the molecule is brought in contact with copper leads, it still has 3 unpaired spins (total magnetization 3.0 a.u.) as observed in the bare molecule. After chosing the system, we now proceed with the calculation of the spin density and the SOT following the details given in Chapt. 2 and summarized in Fig. 2.1. We provide the numerical parameters used in the calculations in Appendix C. As a side remark, as a difference to what happens in other DFT codes, such as TURBOMOLE [36] and SIESTA [123], FHI-aims does not allow to change the spin quantization axis in the calculation [55]. This axis is set by default to be $\hat{\mathbf{z}}$ as indicated in Fig. 3.3. Consequently, we also choose to orient the easy magnetization axis of vanadocene along that axis.

3.3.4 Non-equilibrium electronic transport

Before diving into the magnetic properties of the vanadocene-copper junction we first inspect the I-V characteristic. We show the results in Fig. 3.4 for different values of the Zeeman field. We find that except for $\Delta_Z = \pm 5.0$ eV, the current-voltage curve

4. This is the reason why another metal such as sodium, with smaller SO coupling than copper has been discarded as investigation and parametrization of semi-empirical self-energies is not the main goal of this thesis.

present a linear response regime in a wide range of voltage. This is consistent with the large HOMO-LUMO gap, ~ 2 eV, of vanadocene. The only exception is $\Delta_Z = \pm 5.0$ eV for which the redistribution of the energy levels due to the Zeeman term has strongly altered the electronic structure of the molecular junction and therefore, the voltage range characterizing the linear response regime is reduced.

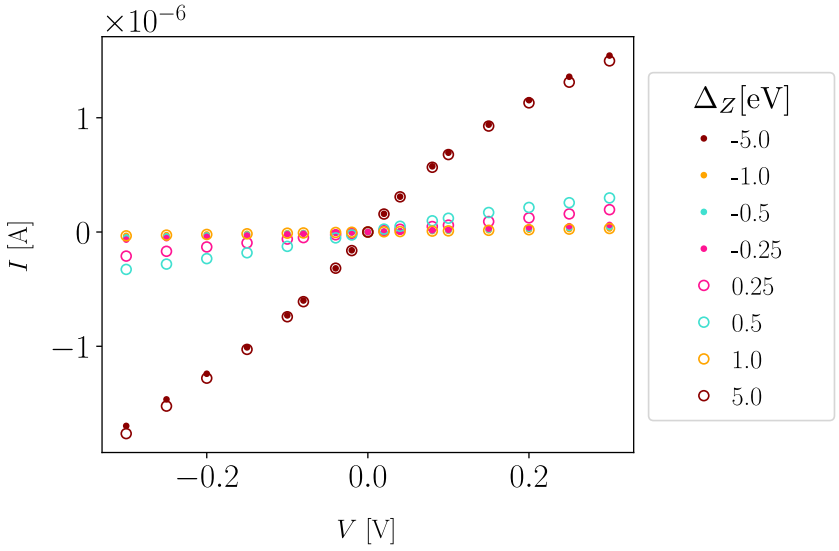

Figure 3.4 – Current-voltage characteristics of the vanadocene-copper molecular junction for different Zeeman fields, Δ_Z. A linear response regime is clearly visible. The range of bias voltage for which the junction is in this regime is a function of the Zeeman field. Notably, the I-V curve for $\Delta_Z = \pm 5.0$ eV shows much stronger nonlinearities due to the dramatic changes in the energy spectrum of the molecule for large local Zeeman fields in the vanadium atom.

3.4 Magnetic properties of copper-vanadocene junctions

3.4.1 Total magnetization

We now proceed with the study of the magnetization properties of the vanadocene molecular junction when a bias voltage is applied across the junction. Recall that we have a molecular structure characterized by three unpaired electrons strongly localized in the vanadium atom in which we introduce a local Zeeman field. We show the results of the total magnetization in Fig. 3.5. Panels (a), (b) and (c) correspond to the components M_x, M_y and M_z of the magnetization of the full junction (as indicated by the molecular junction geometry and reference system at the bottom right side of each panel). Each set of data corresponds to a different value of the Zeeman field (ranging from -5 eV to 5 eV) and we plot the evolution of M_α with the voltage bias from -0.3 V to 0.3 V. We also show, as reference, the dashed black line at 3 a.u. that indicates the spin density of the junction at zero bias as given by the initial DFT without self-energies when no Zeeman field is applied. The inset in each panel corresponds to a zoom for the grey shaded area.

The first observation, already anticipated, is that the magnetic moment of vanadocene mainly points in the $\hat{\mathbf{z}}$ direction, as the components of the magnetization in $\hat{\mathbf{x}}$ and $\hat{\mathbf{y}}$

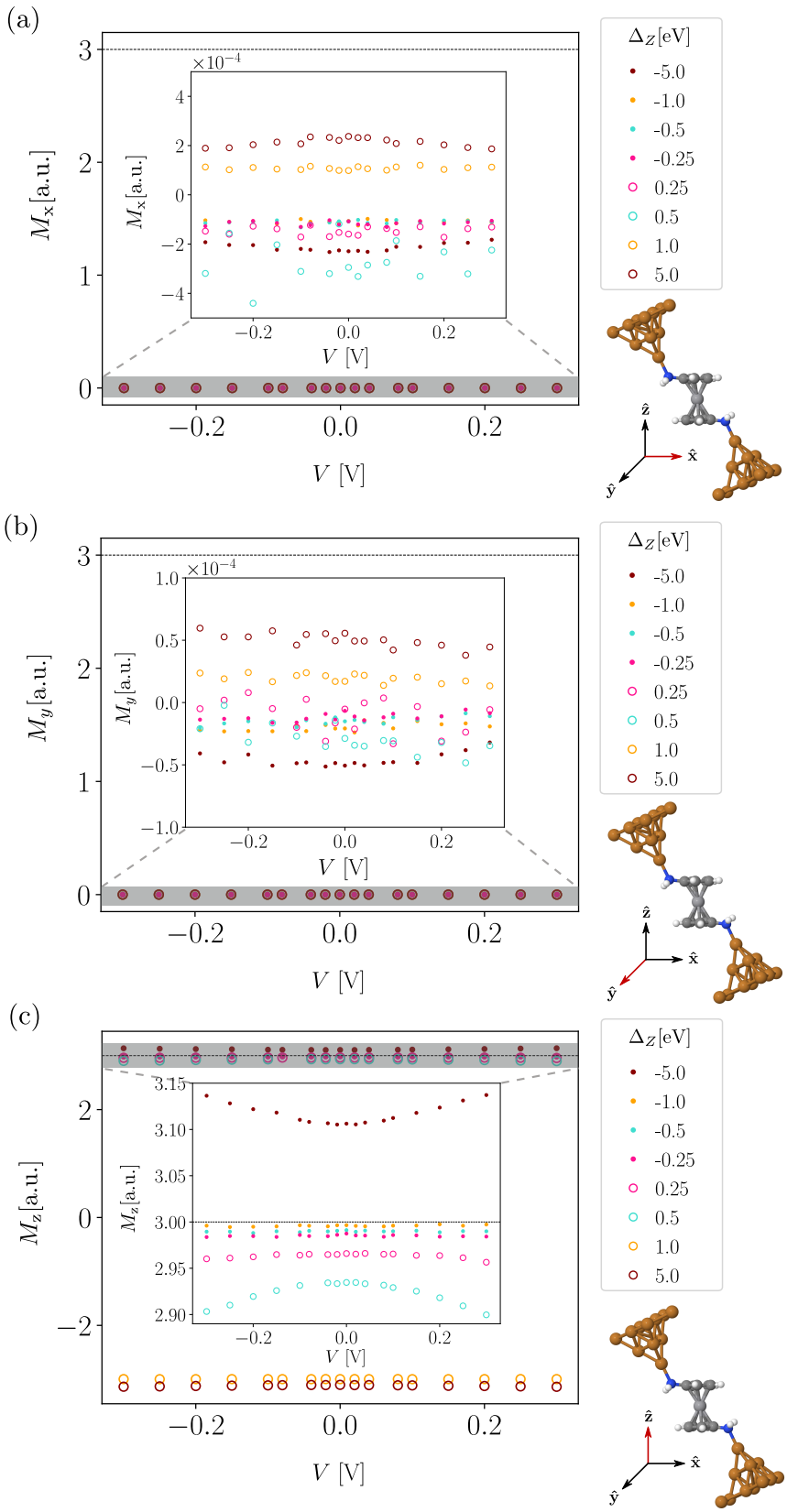

Figure 3.5 – Magnetization of the vanadocene-copper molecular junction for Zeeman fields $\Delta_Z \in [-5.0, 5.0]$ eV as a function of the bias voltage $V_{\text{bias}} \in [-0.30, 0.30]$ V. Each panel corresponds to a different spatial direction: (a) $\hat{\mathbf{x}}$, (b) $\hat{\mathbf{y}}$, (c) $\hat{\mathbf{z}}$, as indicated in red in the reference system close to the molecular junction geometry in the bottom right corner. The inset shows a zoom of the grey area. The horizontal dashed black lines at $M_\alpha = 3.0$ a.u. correspond to the total magnetic moment of reference for the isolated cluster. We find that the magnetization is oriented preferentially on the $\hat{\mathbf{z}}$ direction, as M_z is several orders of magnitude larger than M_x, M_y. For M_z, a small curvature of $\sim 1\%$ is found for different Zeeman fields larger than 0.25 eV; larger local negative Zeeman fields can even invert the magnetization of the whole junction.

directions are 4 and 5 orders of magnitude smaller than M_z. Next, we observe that M_x and M_y respond very weakly to the applied bias voltage and remain almost flat; on the contrary we see that M_z presents a small curvature of $\sim 1\%$ when the current flows through the junction. We attribute this curvature to the transfer of angular momentum of the itinerant electrons from the current to the spins (located mainly at the vanadium atom) mediated by the SO coupling. Note also that, even though the Zeeman term is applied locally in space, the whole junction magnetic properties can be affected due to the hybridization of the metallic orbitals (on which Σ_Z has non-zero value) with the rest of the atomic orbitals in the vanadocene molecule.

Now, we analyze the change of value of the magnetization due to the local Zeeman field and focus on the trends that can be observed in panel (c). We also find that the sign of the magnetization changes from large values of $\Delta_Z > 0$ ($\Delta_Z \in [1.0, 5.0]$ eV for which $M_z < 0$) to $\Delta_Z < 0$ (for which $M_z > 0$). This is easily understood from our implementation of the Zeeman Hamiltonian, whose ground state has opposite spin density direction compared to the ground state of the Kohn-Sham Hamiltonian of the molecular junction. Observe that for $\Delta_Z = -5.0$ eV, the magnetization in the $\hat{\mathbf{z}}$ direction is *larger* than 3.0 a.u.. This can occur if, for example, the large Zeeman energy produces strong shifts in the energy levels of the junction and paired electrons from inner shells promote to empty energy levels. The overall effect is an increase of the magnetization in the direction of the Zeeman field. The spin-flip transition occurs for values between $\Delta_Z = 0.5$ eV and $\Delta_Z = 1.0$ eV; this change starts to be anticipated in the inset of panel (c), where we can appreciate that the curvature of the magnetization with the bias voltage has a negative sign.

3.4.2 Projected magnetization per atomic species

We now proceed to analyze the contribution to the magnetization of each atomic species. In Fig. 3.6 we show the magnetization m_x, panel (a); m_y, panel (b) and m_Z, panel (c) projected on each of the atomic species in the junction. For simplicity, only the Zeeman energies close to the spin-flip transition, $\Delta_Z \in [0.5, 1.0]$ eV, are given in the voltage window $V_{\text{bias}} \in [-0.3, 0.3]$ V. The color code for the atomic species is grey (for carbon), copper (for copper), light-blue (for hydrogen), dark blue (for nitrogen) and green (for vanadium).

As seen in Fig. 3.5, all the atomic species present a magnetization in the $\hat{\mathbf{x}}$ and $\hat{\mathbf{y}}$ directions of a factor $4 - 5$ smaller than the magnetization in the $\hat{\mathbf{z}}$ direction. In the directions perpendicular to the easy magnetization axis, all the atomic species show a similar value for the magnetic moment and, except vanadium and copper, react very weakly to the applied voltage bias. For m_z, as seen in panel (c), the magnetization of vanadium is substantially bigger than the magnetization of any other atomic species, although non-zero magnetization is also carried by the carbon atoms that form the Cp rings. In these case, the magnetization response to the bias is also weak but smooth in V_{bias}, in agreement with Fig. 3.5. For $\Delta_Z = 0.5$ eV, $m_z(V) \sim 2.5$ a.u., not so close to 3 a.u.. This is understood from the fact that the relevant MOs occupied by the 3 unpaired electrons in the junction are shifted by the Zeeman field. When $\Delta_Z = 1.0$ eV, the sign of the magnetization of vanadium is reversed (and points downwards in the $\hat{\mathbf{z}}$ direction), while the spin density in carbon is also reduced so that the value of m_z becomes -3.0 a.u.

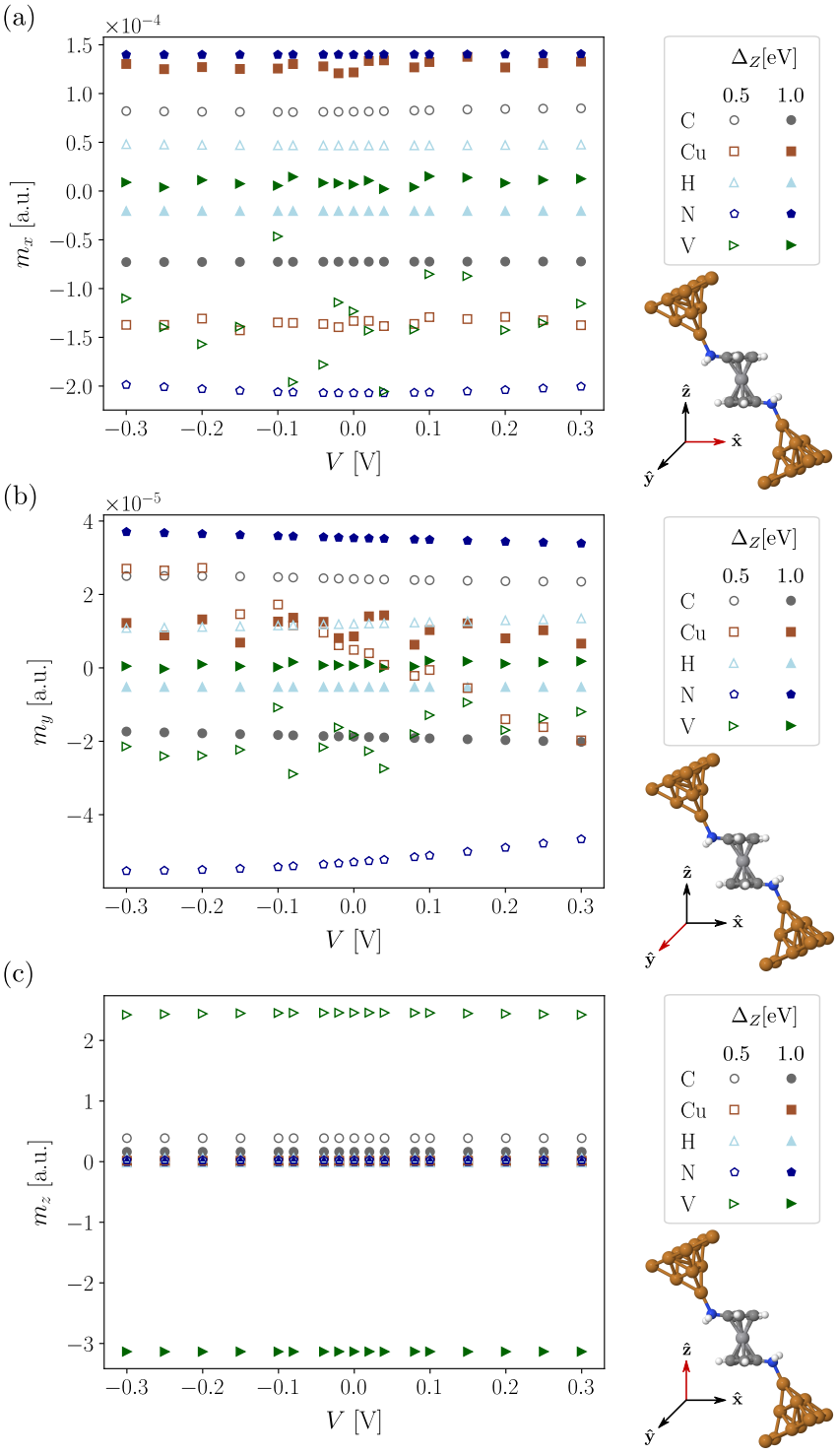

Figure 3.6 – Projected magnetization per atomic species of the vanadocene-copper molecular junction for Zeeman fields $\Delta_Z \in [0.5, 1.0]$ eV as a function of the bias voltage $V_{\text{bias}} \in [-0.3, 0.3]$ V. These values of the Zeeman field correspond to those in which a spin-flip transition occurs at the molecular junction. Each panel corresponds to a different spatial direction; (a) $\hat{\mathbf{x}}$, (b) $\hat{\mathbf{y}}$, (c) $\hat{\mathbf{z}}$ as indicated in red in the reference system close to the molecular junction geometry in the bottom right corner. The different symbols and colors correspond to the atomic species present in the junction (black circles, carbon; copper squared, copper; light blue triangles, hydrogen; dark blue pentagons, nitrogen and green triangles, vanadium). While the magnetization in the $\hat{\mathbf{x}}$ and $\hat{\mathbf{y}}$ directions is small for all atomic species [panels (a) and (b)], the magnetization in the $\hat{\mathbf{z}}$ directions is mostly dominated by the vanadium atom [panel (c)]. In general, the value of the magnetization is reasonably stable as a function of the applied bias, the exception being the vanadium and copper for $\Delta_Z = 0.5$ eV in the directions perpendicular to the easy magnetization axis. These instabilities are attributed to the spin-flip transition that occurs close to that value of the Zeeman field.

We show in Fig. 3.7 the same observable as in Fig. 3.6 but with smaller Zeeman field, $\Delta_Z = -5.0 \cdot 10^{-4}, 5.0 \cdot 10^{-4}$ eV and voltage window $V_{\text{bias}} \in [-0.01, 0.01]$ V. The window of bias voltage is correlated to the Zeeman field, as for larger voltages the magnetization density no longer is a smooth function of V_{bias} because the energy pumped into the system by the current overcomes the stability produced by the local Zeeman field. For small Zeeman fields, no inversion in the magnetization at the vanadium atom is longer obtained.

3.4.3 Local magnetization at the metallic center

Finally, we check in detail the behavior of the magnetization at the vanadium atom in Fig. 3.8. The color code, Zeeman fields and voltage window is the same as the one used in Fig. 3.5; so that immediate comparison can be made. As stated before, the magnetization of the junction in the direction of the easy axis is carried by the vanadium atom and the spin density is reduced after application of a bias voltage across the junction for not small values of Δ_Z. We interpret this smooth change in m_z with V_{bias} as being the consequence of a SOT induced by the SO interaction at the vanadium atom. We focus on its analysis in the next section.

3.5 Spin-orbit torque in vanadocene single-molecule junctions

3.5.1 Spin-orbit torque from *ab initio*

In this last section, we finally present the first calculation of SOT in single-molecule junctions from *first principles*. This calculation compares to the existing *ab initio* calculations of SOT in the literature [69, 65], which are all of them performed for multilayered magnetic heterostructures. Our approach based on a self-consistent DFT-NEGF scheme allows us to go beyond linear response formulations [69] and is applied to atomic non-periodic clusters under a bias voltage. As introduced in Sec. 1.4, we are interested in the response of the magnetization dynamics given by the change of the torque vector, $\mathbf{T} = \dot{\mathbf{S}}$, to the applied bias voltage across the junction. In real space, this quantity is expressed by [69]

$$\delta\mathbf{T} = \int d\mathbf{r}\, \mathbf{M}(\mathbf{r}) \times \delta\mathbf{B}^{xc}(\mathbf{r}) = \int d\mathbf{r}\, \mathbf{B}^{xc}(\mathbf{r}) \times \delta\mathbf{M}(\mathbf{r}), \tag{3.2}$$

so that the torque emerges from the component of $\mathbf{M}$ perpendicular to the exchange field $\mathbf{B}^{xc}(\mathbf{r})$. Note that Eq. (3.2) suggests a trivial decomposition of the torque into a sum of local torque contributions.

Our results for the local SOT at the vanadium atom after applying a bias voltage across the vanadocene-based molecular junction are given in Fig. 3.9. Each panel (a), (b) and (c), corresponds to each of the torque components δt_x, δt_y and δt_z expressed in eV. In (a) and (b) δt_x and δt_y are the so-called out-of-plane components with respect to the magnetization direction, m_z, where most of the local spin density of the vanadium atom is oriented, while δt_z corresponds to the so-called in-plane component. As in Sec. 3.4, the inset displays the geometry employed in our calculations and we highlight by red arrows and boxes the direction of the component as well as the local position at which the SOT has been computed. We find that the torque appearing due to the presence of SO

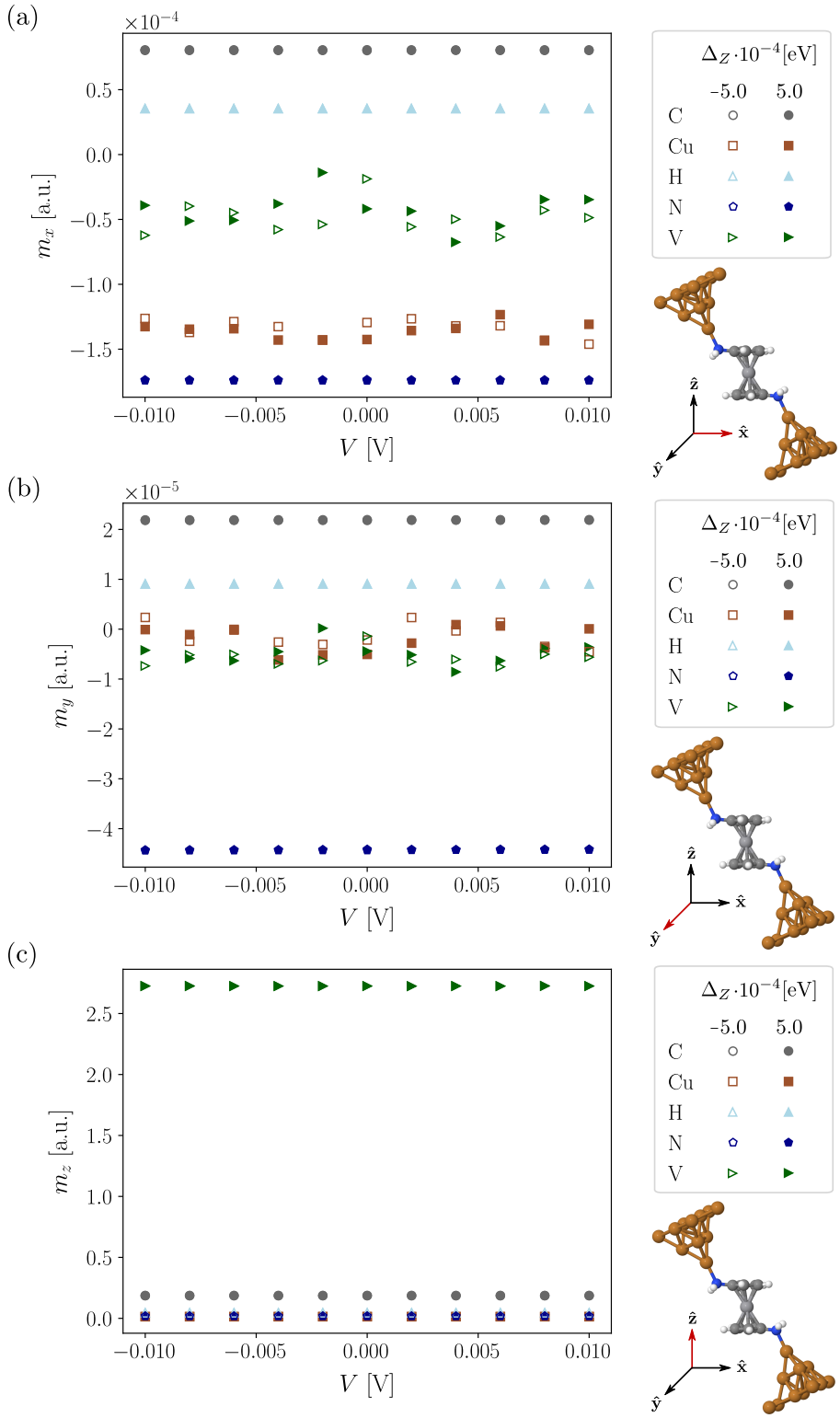

Figure 3.7 – Same as in Fig. 3.6 but for smaller Zeeman fields, $\Delta_Z = -5.0{\cdot}10^{-4}$eV, $5.0{\cdot}10^{-4}$ eV, and different voltage window $V_{\text{bias}} \in [-0.01, 0.01]$ V. For small Zeeman fields applied at the vanadium atom, the projected magnetization is very stable with the bias voltage and no spin-flip transition at the vanadium atom is observed for the $\hat{\mathbf{z}}$ component.

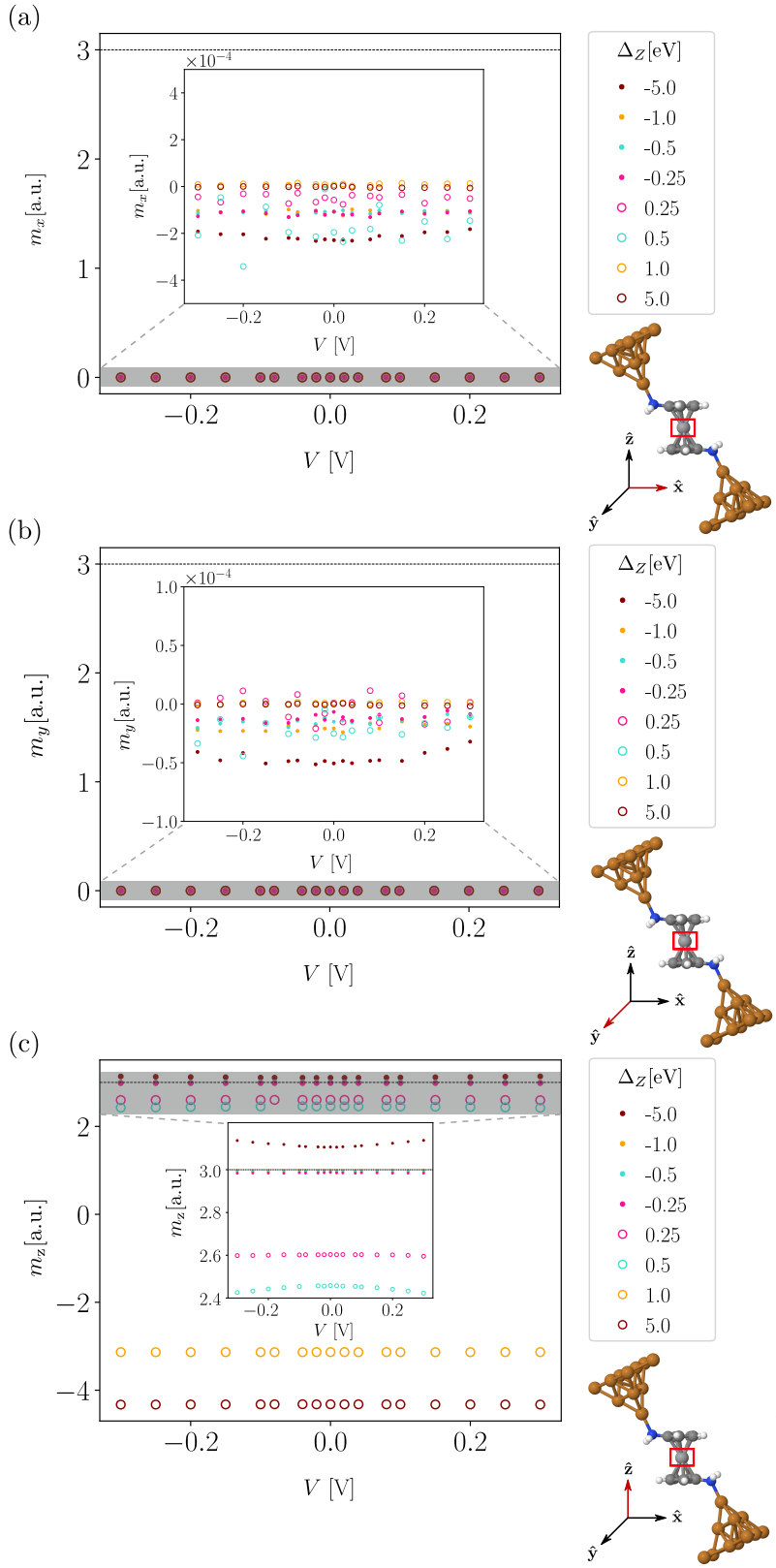

Figure 3.8 – Local magnetization at the vanadium atom for Zeeman fields $\Delta_Z = [-5.0, 5.0]$ eV as a function of the voltage bias $V_{\text{bias}} = [-0.30, 0.30]$ V. Each panel corresponds to a different spatial direction; (a) $\hat{\mathbf{x}}$, (b) $\hat{\mathbf{y}}$, (c) $\hat{\mathbf{z}}$ as indicated in red in the reference system close to the molecular junction geometry in the bottom right corner. The position of the vanadium atom is marked with a red box. The reference value of the magnetization in the $\hat{\mathbf{z}}$ direction, 3.0 a.u., is marked by a horizontal black dashed line. Comparison to Fig. 3.5 shows that the magnetization of the full junction (both the order of magnitude and the behavior with the applied Zeeman field) is essentially dominated by the magnetization at the vanadium atom. We therefore recover that the magnetization $m_z \gg m_x, m_y$ by several orders of magnitude and that a spin-flip transition occurs in the vicinity of $\Delta_Z \sim 0.5$ eV with almost total inversion for $\Delta_Z \sim 1.0$ eV.

interaction is mostly dominated by the out-of-plane components. Both have typical order of magnitude of 10^{-6} eV for δt_x and similarly 10^{-6} eV for δt_y. The in-plane component is approximately two orders of magnitude smaller compared to δt_x. Under the assumption that the exchange field is not strongly anisotropic, this result is consistent with the fact that the magnetization in the easy axis has much larger value compared to any magnetization component on a hard axis.

The response of the torque to the bias voltage is, in general, odd under bias reversal. This behavior is similar to the current voltage traces (see Fig. 3.4) and it can be understood considering the junction similar to a heterostructure. In this scenario, we draw the attention to a simple Rashba model with magnetization employed in Ref. [88]. There it has been shown that the torque induced by the SO interaction is proportional to the current flowing in the system. We therefore would expect a similar behavior here. For values of the voltage $V_{\text{bias}} \lesssim 0.1$ V, the torque presents an approximately linear relation with the applied voltage, while for $V_{\text{bias}} > 0.1$ V non-linearities start to appear. Note that the range of voltages for which the torque vector changes linearly with the bias voltage does not necessary coincide with the voltage interval for which current and voltage also have a linear dependence.

3.5.2 Comparison to torkance calculations

We now compare our results with previous works to get an intuition of the correctness of our calculations of the SOT. We note that the available physical systems that we can use for the comparison are heterostructures, while our calculations are in single-molecule junctions. Nevertheless we can get a feeling of how well the impact of SO interaction is taken into account in the non-equilibrium spin properties. Therefore, we turn our attention to the SOT calculation in magnetic layers of Co/Pt(111) performed in Ref. [69]. These are linear response calculations, using the Kubo formalism, where the torque emerges from the application of a weak external electric field $\mathbf{E}$, $\mathbf{T} = \bar{\bar{t}}\mathbf{E}$, and it is characterized by the linear response tensor $\bar{\bar{t}}$ ("torkance"). In their case, it can be shown that due to symmetry considerations some of the components of the torkance tensor vanish. Here we will assume for simplicity that the tensor can be replaced by an scalar (the direction of the torque coincides with that of the applied electric field). In our junction, we can estimate the electric field for small bias V_{bias} by considering the structure to be a capacitor with the insulating layer corresponding to the molecule. Within this picture, the constant electric field, $\mathbf{E}$, is generated from the voltage drop across the junction length. Therefore, $E \sim V_{\text{bias}}/L$, where V_{bias} is the external bias voltage applied and $L \sim 0.68\text{Å} \sim 13a_0$ (a_0 is the Bohr's radius) is the NH_2-Cp_2V-NH_2 length of the molecule measured between the two anchor groups. From Fig. 3.9, we estimate the linear response regime to be characterized by the voltage window with $V_{\text{bias}} \sim 0.04\,\text{V}$, the associated electric field is $E \sim 3 \cdot 10^{-3}\text{V}/a_0$. Therefore, the torkance estimated from $t = T/E$ with δt_x is $t \sim 3 \cdot 10^{-4}\ ea_0$. From Fig. 3 of Ref. [69], we observe that the typical values of the torkance is $t \sim 0.1\ ea_0$.

We now assume that, at lowest order, the SOT has a linear relation with the SO interaction strength[5]. The typical energy splitting associated to the SO interaction of

5. This relation is exact for certain model Hamiltonians [88, 16] such as the Rashba model. Here, since there is only a single atom with relevant SO interaction at the metal-insulator interface (vanadium), the torque has to be linear with the SO interaction strength at lowest order, similar to the isolated atom.

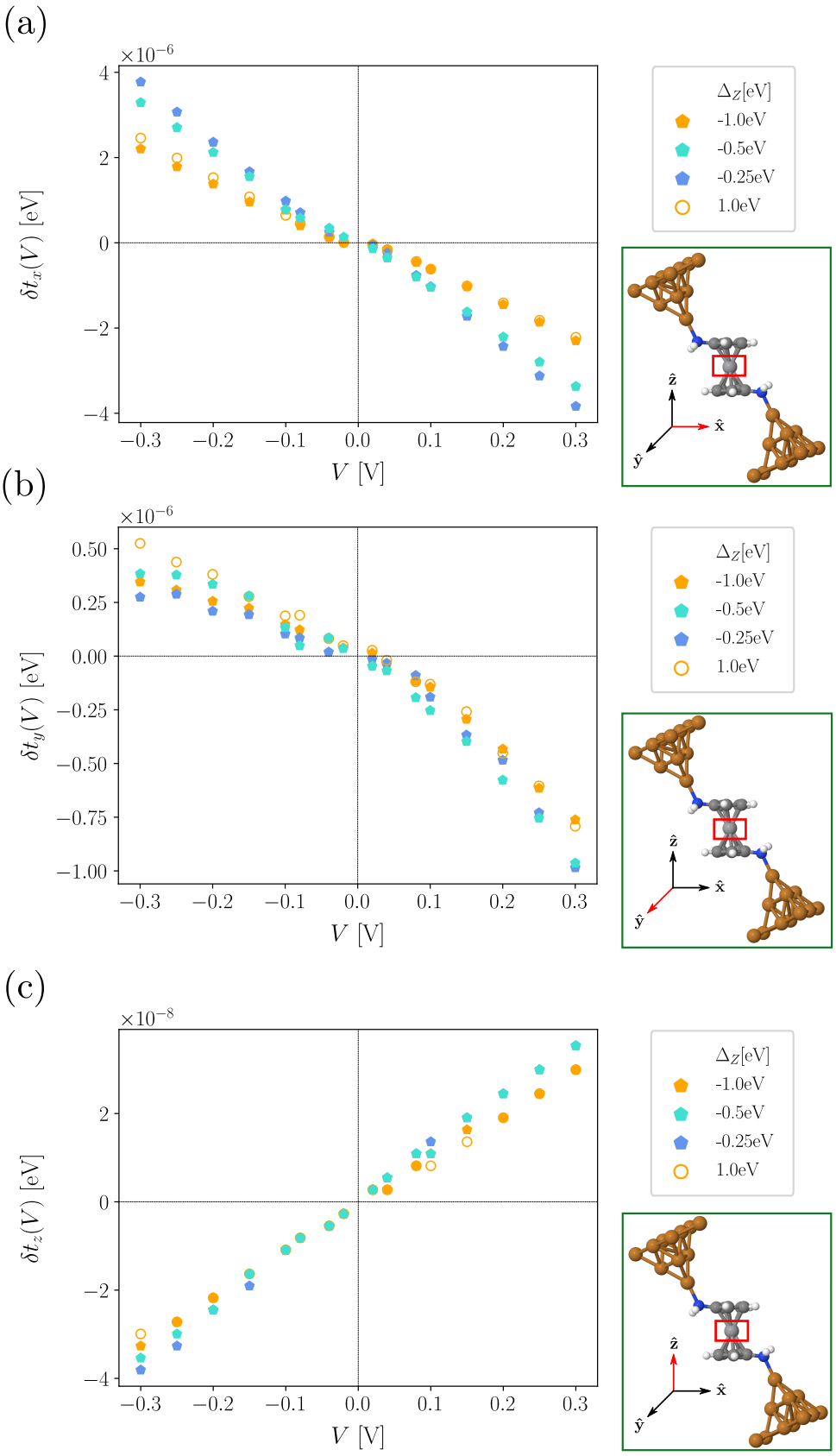

Figure 3.9 – Components of the local SOT exerted at the vanadium atom in the three relevant spatial directions [(a) δt_x, (b)δt_y and (c) δt_z]. The inset for each panel shows the geometry of the full junction as well as the position and direction for which the local SOT has been calculated marked by the red box and the red arrow respectively. The SOT is an odd function of the voltage with a small window of linear regime in the range $V_{\text{bias}} \in [-0.04, 0.04]$ V. The torque exerted in the $\hat{\mathbf{x}}$ and $\hat{\mathbf{y}}$ directions is at least an order of magnitude larger compared to the torque exerted in the $\hat{\mathbf{z}}$ direction, $\delta t_z \gg \delta t_x, \delta t_y$ in agreement with the fact that m_z shows the biggest changes as a function of V_{bias}.

a hydrogen-like atom [121, 122] is $\zeta \sim 0.123$ eV (Co). For the vanadocene molecule, we consider as an analogous quantity the typical level splitting due to SO interaction $\Delta E \sim 0.001$ eV (see Table 3.1). We now define the following ratios, $\xi_{\mathrm{Co}} = t_{\mathrm{Co}}/\zeta$ and $\xi_{\mathrm{V}} = t_{\mathrm{V}}/\Delta E$, which normalize the torque to the SO interaction strength of each system. We find $\xi_{\mathrm{Co}} \sim 1.25 a_0/V$ while $\xi_{\mathrm{V}} \sim 0.3 a_0/V$. The qualitative comparison is actually very good (factor of 4). We attribute the quantitative difference in the ratios to interface effects, not accounted in this estimation, functional dependencies and the approximations performed in the SC calculations indicated in chapter 2. We also observe that SOT in the vanadocene-based junction is not sufficiently large to produce a switch in the magnetization direction of the spin-density in the vanadium atom for a range of voltages between $V_{\mathrm{bias}} \in [-0.3, 0.3]$ V.

Finally, we also estimate the coercitive magnetic field, $\mathbf{B}_c$, which is the magnetic field that has to be applied in order to generate an effect equivalent to that torque in the magnetization $\mathbf{M}$, similarly as in Ref. [69]. It can be calculated as $\mathbf{B}_c = (\mathbf{T} \times \hat{\mathbf{M}})/\mu_s$, where $\hat{\mathbf{M}}$ is the direction of the initial magnetization and μ_s denotes the total spin magnetic moment in the cluster or unit cell. For a typical value of the torque $\sim 10^{-6}$ eV found in our molecular junction, we estimate $B_c \sim 0.001$ mT, oriented in the XY-plane of the vanadocene (parallel to the Cp rings) because its magnetization is oriented mainly in the $\hat{\mathbf{z}}$ direction. This quantity, B_c, gives the magnetic field necessary to generate the same effect on the magnetization of this molecular junction as the SOT. The number obtained is very small (of the order of the Earth magnetic field [124]), in agreement with the small torques calculated.

3.6 Summary of this chapter

In this chapter, we have shown the first calculation of SOT in a single-molecule junctions. As a test case, we have presented the vanadocene molecular junction connected to copper leads. By introducing a local Zeeman field that sets a preferential magnetization axis, we show that the magnetization at the vanadium atom can be controlled by application of an external voltage bias in the junction. The changes of the magnetization are attributed to the SOT, which is exerted on the spin density through the exchange of angular momentum with the current by means of SOC. The SOT computed by following the method introduced in chapter 2 has also been compared to the SOT obtained in magnetic heterostructures. We find that, in spite of the strong approximations taken here in the SC cycle, the normalized ratios of the torkance to the SO interaction strength are in qualitatively good agreement. Discrepancies are attributed to geometrical details at the interface, functional dependencies or, also, to the methodology approximations. In addition, we provide an estimation of the magnetic field that would be needed to produce an equivalent local torque in the vanadocene junctions. We find that for $t_x \sim 10^{-6}$eV, we need a magnetic field of ~ 0.001 mT (smaller than the Earth magnetic field). We also conclude that, under the conditions in which the calculation has been performed, SOT is not sufficiently large to produce a switch in the magnetization direction of the spin density in the vanadium atom.

Chapter 4

Mechanically-tunable quantum interference in ferrocene-based molecular junctions

A part of the material covered in this chapter can be found in the preprint:

M. Camarasa–Gómez[†], D. Hernangómez–Pérez[†], M. S. Inkpen, G. Lovat, E–Dean Fung, X. Roy, L. Venkataraman, and F. Evers, *Mechanically-tunable quantum interference in ferrocene-based molecular junctions*, chemRxiv.12252059.v1, 2020. [†: equally contributing authors]. Ref. [125]. Adapted with permission from *Nano Letters*, submitted for publication. Unpublished work copyright 2020 American Chemical Society.

In this chapter, we perform a theoretical study of quantum transport properties of ferrocene-based single-molecule junctions. We analyze the charge transfer mechanism and discuss the origin of the low conductance properties of these junctions (two orders of magnitude smaller than the conductance of molecules of comparable length). The low conductance is explained in terms of destructive quantum interference, which manifest in the transmission function by Fano-like anti-resonances close to the Fermi energy. These antiresonances are consequence of the hybridization of the localized d-orbitals of the metallic atom with the extended π-systems of the carbon-based ligand groups. The low energy cost of rotation of the organic rings against each other allows for mechanical control of the hybridization (and therefore the quantum interference). Consequently, the conductance can change upon rotation in the junction by orders of magnitude in a controlled manner. Our theoretical calculations confirmed experimental observations performed in L. Venkataraman's group.

4.1 Why quantum interference in ferrocene?

As introduced in section 3.3, metallocenes are organometallic compounds that consist of a dimer made of two five-member carbon rings (cyclopentadienyl, Cp) that "sandwich" a transition metal atom. When the metal is iron, the molecule is called ferrocene. Ferrocene is a very interesting compound, both from the chemical (see molecular orbital diagram in Fig. 4.1) and structural point of view [126]. Indeed, it was discovered only a few years

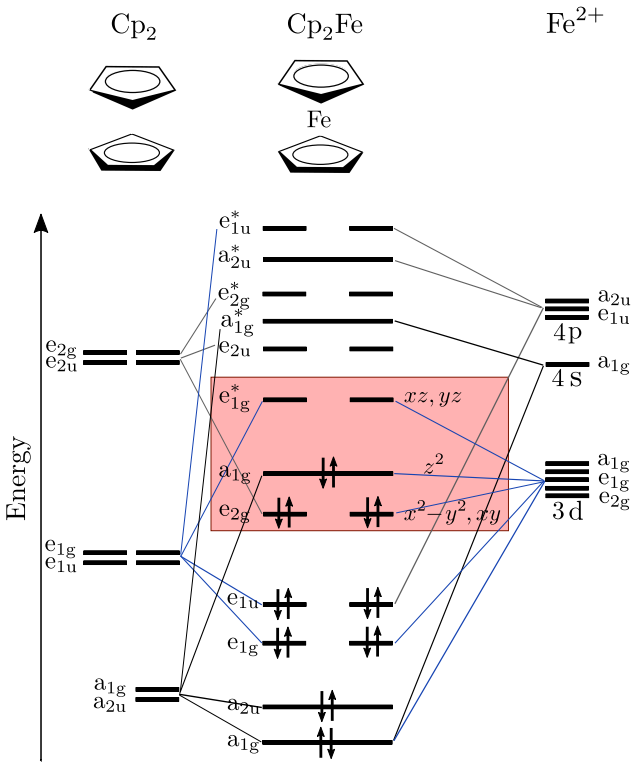

Figure 4.1 – Qualitative molecular orbital (MO) diagram of the pristine ferrocene molecule. The nomenclature and *d*-orbital symmetry being the same as in Fig. 3.2. On the left hand side, the energy levels and chemical structure of the two *naked* cyclopentadienyl rings (Cp) is shown.On the right hand side, the energy levels of the Fe^{2+} are also represented. As a result of hybridization, we find the electronic structure of the (staggered) pristine ferrocene molecule detailed in the central column. Ferrocene is an octahedral closed-shell organometallic complex whose *d*-electrons are distributed as shown in the red shaded area of the MO diagram.

after its synthesis [127] that ferrocenes could be employed as a molecular conformational switch, since the two Cp rings can easily rotate against each other thanks to a low energy barrier (of the order of tens of meV) [127, 128]. The easy mechanical degree of freedom given by the near rotation of the Cp rings against each other (the "scissor mode") may allow for adsorption of different conformations of metallocenes close to a metal surface. These different geometries come from having several local energy minima in the conformational space. Therefore, the metallocene can have different adsorption geometries to local defects, steps or islands. This can occur either for self-assembled monolayers [129, 130] or at the single-molecule [131, 132].

Even though single metallocenes moieties have been employed, since the pioneering work of Getty *et al.* [133], as key pieces for molecular devices (such as spin-filters [116], rectifiers [134, 135, 136] or switches [137, 138])for already a decade, the possible role of the scissor mode on charge transport was not fully understood. Only some works have studied the impact of the rotational flexibility on charge-transfer properties of metallocene single-molecule junctions. Recent computational studies [131, 139, 140, 141, 142] have tried to give an explanation to the large variations of the conductance that can be measured in metallocene-based molecular junctions. In particular, the conductance does not decay monotonically with the system length and the values are low compared to molecules of similar length. This behavior was attributed to the variation in the Fermi level alignment [142] for different conformations of the molecule in the junction or to the sensitivity of the conductance to the binding geometry [140].

In this chapter, we propose that the origin of the low conductance features (compared to cross- or linearly-conjugated molecules of similar length) appearing in ferrocene-based single-molecule junctions is quantum interference. We perform a detailed investigation of

the quantum transport properties and show that the soft rotational degree of freedom can be employed to manipulate the degree of destructive quantum interference (DQI) - and therefore the conductance - in these junctions by mechanical means. The origin of this phenomenon lies on the peculiarities of the hybridization of the metallic d-states with the delocalized π-orbitals of the Cp rings. Our theoretical predictions were key to interpret experimental measurements performed in L. Venkataraman's group.

4.2 Transport simulations in ferrocene-based junctions

4.2.1 *Ab initio*-based transport characteristics

The chemical structure of the molecules studied in this chapter are shown in Fig. 4.2 (a). We consider the $1,1$'-Fe and $1,3$-Fe derivatives. Both molecules have the same ferrocene core in which the iron unit has oxidation state Fe^{2+}. The difference between them lies on the position of the substituent phenyl ligands: for 1,1' each phenyl ligand is attached to a different Cp ring while for 1,3 both phenyl ligands are attached to the same Cp ring. For comparison, due to its similar length, we also consider $1,4$ phenylene or terphenyl (P_3). The main difference is that the central phenyl does not have a "side group" as it can be considered the metallic unit and one of the Cp rings in the ferrocene derivatives. The phenyl rings in P_3 can also rotate along the main molecular symmetry axis but the molecule is more rigid, it does not bend easily.

To analyze the transport properties of our molecular junctions, we calculate the non-self-consistent transmission functions employing the non-equilibrium Green's function formalism. For technical details, we refer the reader to appendix D. The transmission functions of the DFT-optimized geometries Fig. 4.2 (b) are shown in Fig. 4.2 (c). First, we observe that the transmission for P_3 is dominated by Breit-Wigner resonances produced by the HOMO and LUMO orbitals of the molecule. The curve also shows evident signs of constructive quantum interference (QI). This can be attributed to the configuration of the phenyl ligands connected to the benzene ring [143] and it is also understood from selection rules valid for planar cross-conjugated aromatic molecules [21, 144]. In comparison, the transmission functions of the ferrocene-based derivatives $1,1$'-Fe and $1,3$-Fe present deep and sharp anti-resonances of the Fano-type. These anti-resonances are clear indication of DQI. The anti-resonances are located close to the Fermi energy, therefore, they lead to the suppression of zero-bias conductance and can explain the low conductance values that these molecules have in the single-molecule junction context.

4.2.2 Conductance control by ferrocene ring rotation

We now focus on the study of the DQIs features of $1,1$'-Fe (our basic conclusions carry over to $1,3$-Fe as well as the other metallocenes studied in chapter 5) and analyze the impact of the "scissor mode" in the interference properties.

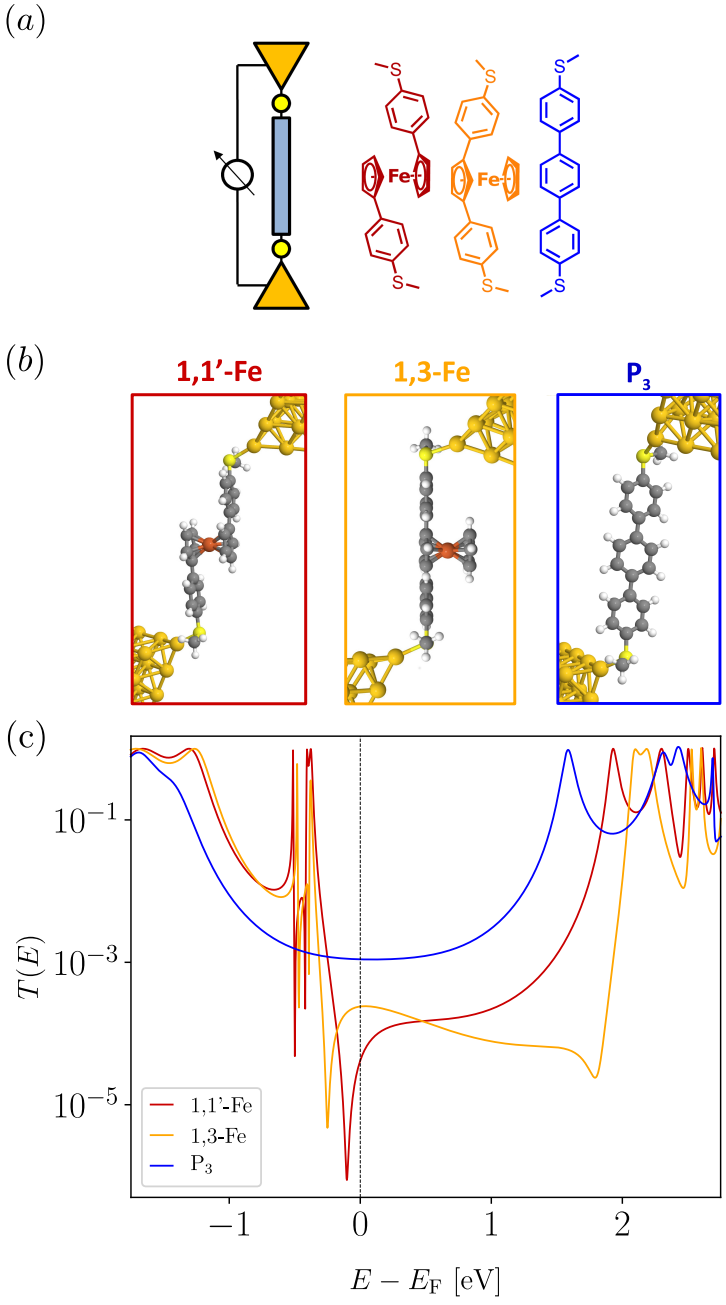

Figure 4.2 – (a) Scheme of STM-BJ setup and chemical structure of 1, 1'-Fe, 1, 3-Fe and P_3 (b) DFT-optimized molecular geometries. (c) Non-self-consistent transmission spectra for the single-molecule junctions 1, 1'-Fe, 1, 3-Fe and P_3. The curves for 1, 1'-Fe, 1, 3-Fe present strong DQI effects close to the Fermi energy compared to P_3. Adapted with permission from [125].

Energetics of ring rotation of gas-phase 1,1'-Fe

As we mentioned in section 4.1, metallocenes have a rotational degree of freedom, with rotation taking place at low energy cost for the pristine ferrocene [127, 128, 132]. The rotation is parametrized with the angle φ, see Fig. 4.3.

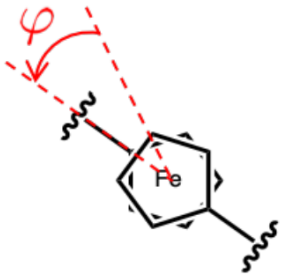

Figure 4.3 – Sketch that represents the rotation of the Cp rings against each other in 1,1'-Fe ("scissor mode"). We denote by φ the rotation angle. Adapted with permission from [125].

We examine now the energy landscape related to rotation of the gas-phase 1,1'-Fe molecule at zero temperature. In Fig. 4.4, we show the energy of the molecule (normalized to the energy of the relaxed gas-phase molecule) for different rotation angles φ. The landscape possesses several local minima and maxima: the minima correspond to the so-called eclipsed configuration of the ferrocene moiety (characterized by mirror symmetry with respect to a plane parallel to the Cp rings containing the iron atom) while the maxima correspond to the so-called staggered conformation (characterized by inversion symmetry with respect to the iron atom). The energy barrier between both conformations of 1,1'-Fe is around $\Delta \simeq 33.5\,\text{meV}$. When the anchor groups, SMe, are close to each other, the height of the energy barrier increases ~ 10 times due to the electrostatic repulsion between lone electron pairs at the thiol groups. In view of the low energy cost for the 1,1'-Fe, the "scissor mode" can produce several geometries, which can be explored in a realistic setup in the formation of the junction.

Evolution of transmission under ring rotation

We now investigate the transport features associated to the different rotation angles φ in order to elucidate the impact of the "scissor mode" on the charge transfer properties. In Fig. 4.5 (a) we show several geometry configurations of the 1,1'-Fe molecule obtained after applying a rigid rotation to the relaxed structure of $\varphi \in \{\pi/6, \pi/2, 2\pi/3\}$. Note that here $\varphi = 0$ is chosen as reference for the relaxed conformation and does not correspond to the angle between the phenyl arms (which is closer to $5\pi/6$) [1].

For each φ, we perform a NEGF transport calculation. The result is shown in Fig. 4.5 (b) in the form of a two-dimensional plot in which the variation of the non-self-consistent

1. The molecular geometries have been obtained starting from a fully-relaxed optimized geometry. As our goal here is to study the effect of the rotational degree of freedom in the interference features, we choose to constrain the phenyl linker and the SMe anchor group to be in the same plane. We have also performed additional calculations given in appendix D, where the impact on transmission of relaxing this constraint is analyzed and seen to be quantitatively small.

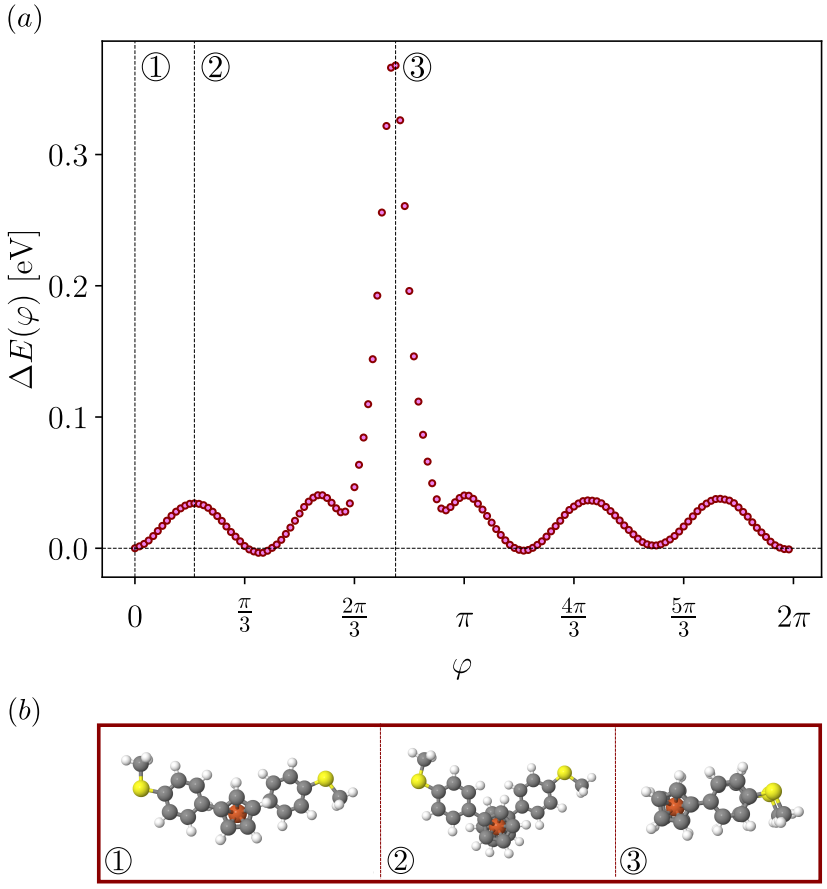

Figure 4.4 – (a) Energy landscape for the scissor mode in 1, 1'-Fe. The energy is normalized with respect to the energy of the optimized gas-phase molecule. (b) Selection of the molecular structures for the energies marked with dashed lines in panel (a). ① corresponds to the so-called eclipsed configuration, ② shows a so-called staggered configuration and ③ represents the extreme case where the SMe anchor groups are on top of each other. The energy barrier created by the minimization of the SMe-SMe distance is $\Delta_{1\to3} \simeq 365.0\,\text{meV}$, this large barrier arises due to Coulomb repulsion of the lone electron pairs in the S atoms. The energy landscape shows that transitions between configurations due to rotation easily occurs since $\Delta_{1\to2} \simeq 33.5\,\text{meV}$. Adapted with permission from [125].

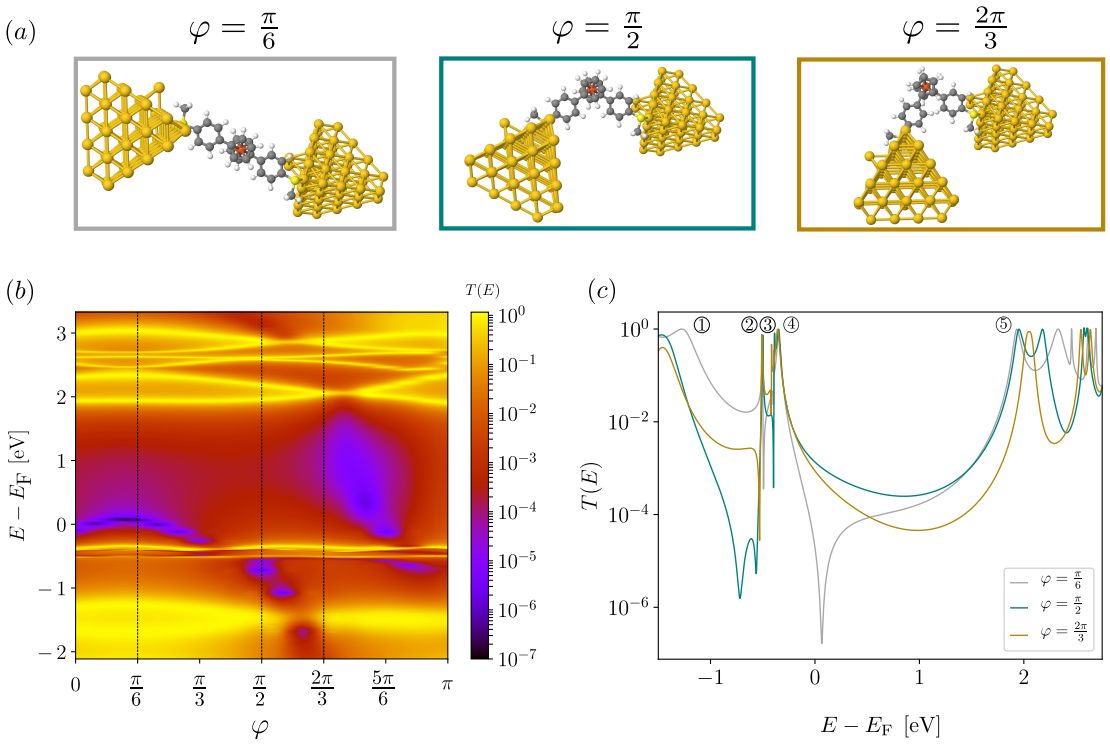

Figure 4.5 – (a) Selection of geometries representing the scissor mode for 1, 1'-Fe molecular junction. The optimized geometry obtained from the *ab initio* DFT calculation gives the reference angle, $\varphi = 0$. (b) Two-dimensional transmission plot that results from the rotation applied to 1, 1'-Fe molecular junction. (c) Selection of transmission curves corresponding to the three geometries shown in (a) marked in the two-dimensional map, in (b) with dashed lines. The rotation of the Cp rings against each other produces strong changes in the DQI features. For $\varphi = \pi/6$ the antiresonance appears in the HOMO-LUMO gap, while in the case of $\varphi = \pi/2$ emerges again for lower values (between HOMO-3 and HOMO). For $\varphi = 2\pi/3$, the dip almost disappears under the HOMO resonance. The gas-phase orbitals, which can be identified in the molecular junction, are labeled by ① (HOMO−3), ② (HOMO−2), ③ (HOMO−1), ④ (HOMO) and ⑤ (LUMO), and yield the yellow traces in panel (b). Adapted with permission from [125].

transmission $T(E)$ with the rotation angle φ is shown. The black vertical lines correspond to the transmission corresponding to the geometries shown in (a), which we replot for clarity in Fig. 4.5 (c). The position of the relevant orbitals involved (derived from gas-phase HOMO-3 to LUMO) is labeled from ① to ⑤. The associated transmission resonances are depicted in yellow in Fig. 4.5 (b). HOMO- and LUMO-based resonances correspond to the horizontal lines at $E - E_F \simeq -0.5$ eV and $E - E_F \simeq 2$ eV. Thus, the HOMO-LUMO gap is the red band occupying the central part of the plot. The two purple areas inside the band correspond to spectral intervals where the transmission is strongly suppressed (between 10^{-4} and 10^{-7} G_0). The sharper purple areas, also appearing at $0 < \varphi < 2\pi/3$, are the consequence of DQI between molecular orbitals. We also note that these areas "flow" in the map when the Cp ring is rotated. The purple region located at $\varphi > 2\pi/3$ has a different origin: it results from the direct tunneling between the phenyl anchors when the two are very close to each other. Direct tunneling through space (and not through the ferrocene moiety) also reduces the transmission. As a consequence, the areas do not flow with the angle φ. The conclusion of these calculation is thus twofold: (i) DQI close to the

Fermi energy strongly suppresses the conductance at zero-bias and (ii) the conductance can be tuned by orders of magnitude (through tuning the interference properties) by rotation of the Cp rings.

Orbital analysis: origin of quantum interference

We now analyze the contribution of the different Kohn-Sham (scattering) states to the quantum interference in 1, 1'-Fe. In Fig. 4.6 (a) we show the molecular orbitals ranging HOMO−3 (top row) to LUMO (bottom row) for the geometries corresponding to the rotation angles $\varphi = \pi/2, \pi/6, 2\pi/3$. First, we observe that HOMO−2 and HOMO−1 are mainly localized in the ferrocene moiety and they do not hybridize with the contact atoms, independently of the rotation angle. As a consequence, in the non-self-consistent transmission function, they manifest as very narrow Fano resonances, corresponding to ② and ③.

To understand the strong localization of these two orbitals at the ferrocene moiety, we analyze the symmetries of the $d-$states derived from the iron core involved. We start with HOMO−2, which at the metal atom presents d_{z^2} spatial symmetry, see Fig. 4.6 (b). This orbital couples with σ-type bonding to the π-system of the carbon ring because it has most of its weight in regions where the π-system of the Cp ring has none. Next, we analyze the localization mechanism for HOMO−1. The symmetry of this orbital at the iron atom is d_{xy} and this leads to δ-type bonding with the ligand π-system. This bond results in such a way that it locates a node at the carbon which connects with the phenyl anchor. Consequently, the hybridization with the contacts remains weak.

We now turn to the analysis of the HOMO−3, HOMO and LUMO Kohn-Sham states, which are significantly more extended across the junction. Consequently, the corresponding resonances in the transmission function are broader, due to larger hybridization with the contacts. These scattering states produced the dominating transport resonances and are labeled as ①, ④ and ⑤ in Fig. 4.6 (b). We can also proceed with the analysis of the d-state symmetries as for the localized orbitals, see Fig. 4.6 (b). Specifically, we observe that the d-state symmetries are d_{yz} (HOMO−3), $d_{x^2-y^2}$ (HOMO) and d_{xz} (LUMO). The delocalization of the HOMO is easily explained reasoning in a similar way than for HOMO−1. Here, the $d_{x^2-y^2}$ orbital overlaps with the π-system of the phenyl arms when d_{xy} for HOMO−1 does not. For HOMO−3 and LUMO the hybridization is a consequence of the partial overlap of the lobes which come from the d_{yz} and d_{xz} orbitals and the π-system at the Cp ring.

To understand the origin of the changes in the quantum interference properties, it is crucial the observation that the nodal structure of the orbitals depend on φ. This change in the nodal structure manifests in a phase-shift of the wavefunctions at the linker groups. For example, we see easily in Fig. 4.6 (a) that HOMO−3 alters the phase of the wavefunction at the linkers upon rotation between $\varphi = \pi/2$ and $\varphi = 2\pi/3$. Similarly, HOMO also alters its nodal structure upon rotation, as can be inferred from the scattering states shown in the first two panels of the fourth row: the wavefunction changes a node upon rotation from $\varphi = \pi/6$ to $\varphi = \pi/2$. These changes of the nodal structure are reproduced at the level the isolated molecule in Fig. 4.7 for selected angles of HOMO−3, HOMO and LUMO. Note that the underlying mechanism that produces these states, and consequently

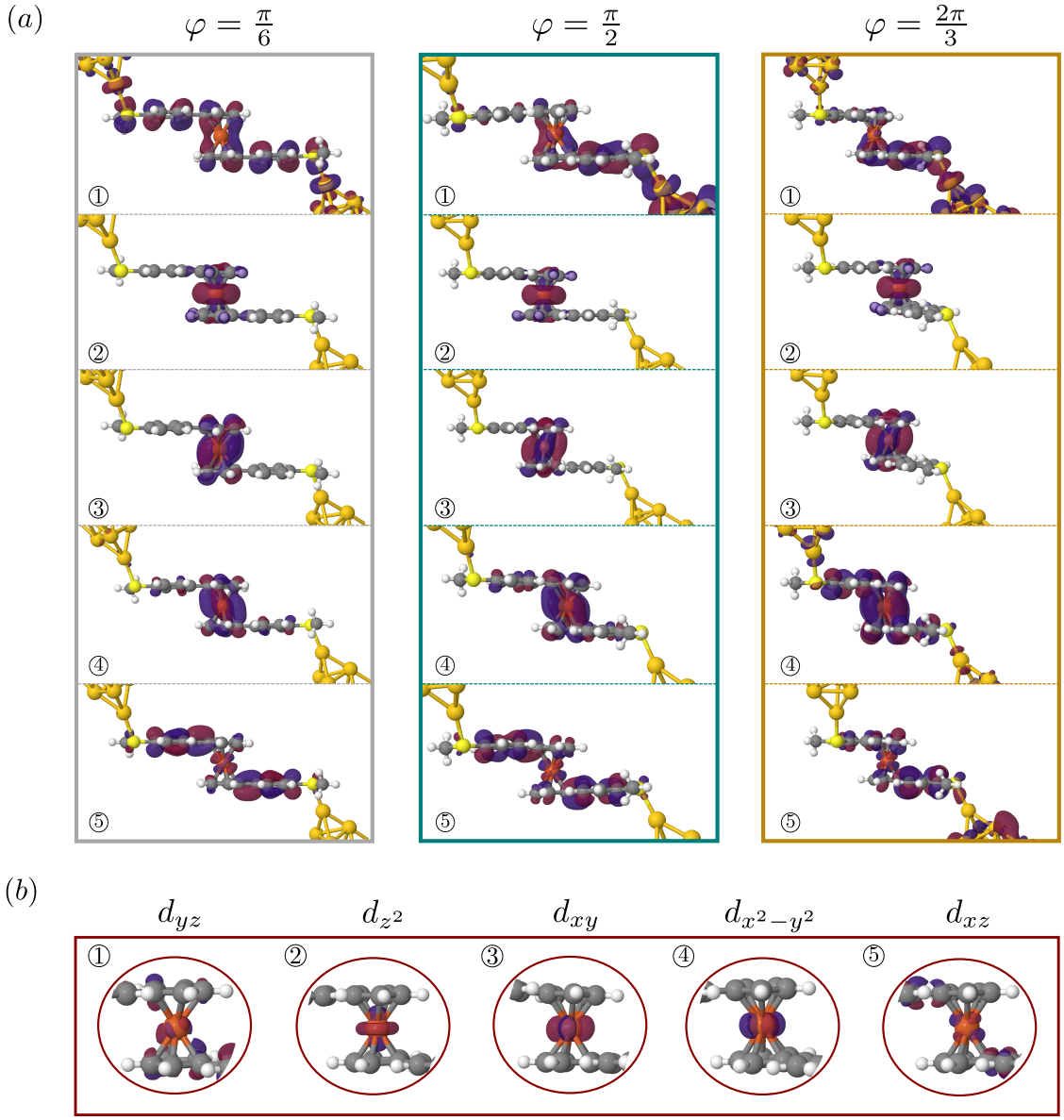

Figure 4.6 – (a) Isosurface plots of the relevant transport orbitals in the 1,1'-Fe junction for the rotation angles $\varphi \in \{\pi/6, \pi/2, 2\pi/3\}$. The orbitals are labeled according to Fig. 4.5 (c), ① (HOMO−3), ② (HOMO−2), ③ (HOMO−1), ④ (HOMO) and ⑤ (LUMO). (b) Zoom of the states showing the d-orbital symmetry of the Kohn-Sham states of panel (a) at $\varphi = \pi/2$. Adapted with permission from [125].

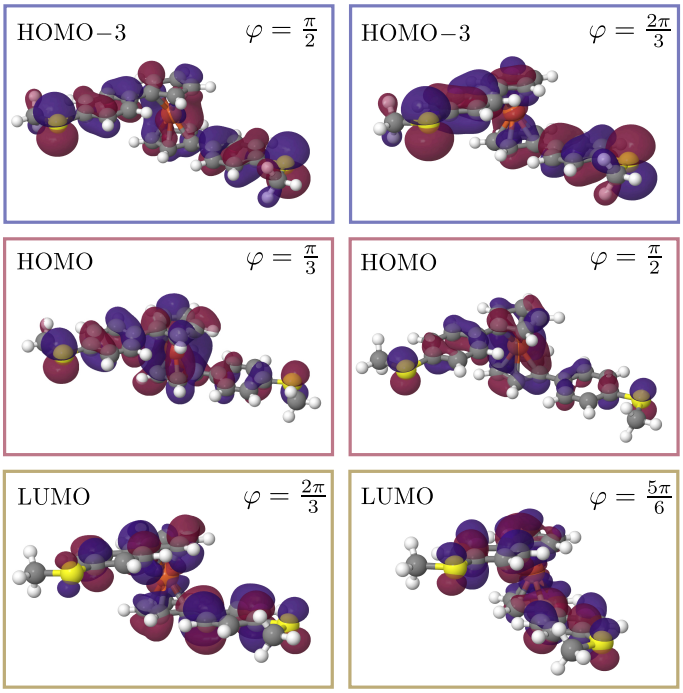

Figure 4.7 – Change in the nodal structure of selected gas-phase Kohn-Sham states under "scissor mode" rotation of the ferrocene core. We show only the states for which a change in the nodal structure has occurred, marked with a rectangle in Table 4.1. Adapted with permission from [125].

the quantum interference features, is not exclusive to 1,1'-Fe. Our analysis also applies to other metallocenes of the same family and even to the bare ferrocene molecule (see appendix E).

4.3 Model-based analysis of quantum interference

To rationalize the quantum transport calculations, we perform an analysis of the interference properties using the Meir-Wingreen trace formula. In the absence of degenerate orbitals, the discussion is straightforward. First, we introduce the basic idea by employing a generalization of the two-level system discussed in Ref. [145] and afterwards we apply the concepts to the three-level model to further understand the result of our *ab initio* calculations.

4.3.1 Interference terms in transmission trace formula

The transmission function, $T(E)$, can be written using Eq. (1.42), where we recall that the anti-Hermitian part of the self-energies is given by $\hat{\Gamma}_\alpha = \hat{\Gamma}_\alpha(E) = -i[\hat{\Sigma}_\alpha(E) - \hat{\Sigma}_\alpha^\dagger(E)]$, and that $\hat{G} = \hat{G}(E)$ represents the (retarded) Green's function of the extended molecule (*i.e.* molecule and part of the contact atoms, see section 1.2). Considering the one-dimensional model geometry shown in Fig. 4.8 (where the contact to the leads happens at

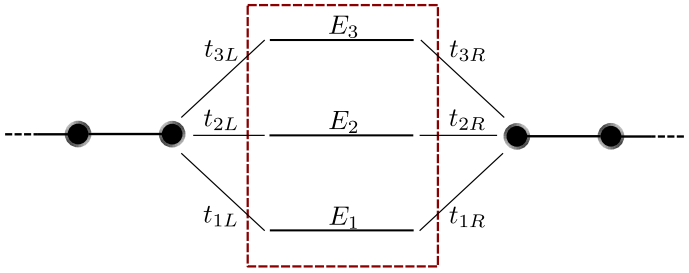

Figure 4.8 – Sketch of the minimal model. We consider three non-interacting molecular levels which connect to the same single-atom of the contacts through hopping parameters $t_{i\alpha}$.

a single site), we can write the self-energy as

$$\hat{\Sigma}_\alpha(E) = \mathbf{t}_\alpha^\dagger g_\alpha(E) \mathbf{t}_\alpha, \tag{4.1}$$

where $\mathbf{t}_\alpha = (t_{1\alpha}, t_{2\alpha}, \ldots)$ is a vector that contains the hopping matrix elements connecting the central (molecular) part to the contact site and $g_\alpha(E)$ represents the Green's function of the reservoir evaluated at the contact site. The Green's function is related to the local density of states at the site by the relation $\rho_\alpha(E) = -\mathrm{Im}\left[g_\alpha(E)\right]/\pi$.

For the coupled system, the Green's function is defined in the usual way, $\hat{G}(E) = [E\mathbb{1} - \hat{H}_0 - \hat{\Sigma}_\mathrm{L}(E) - \hat{\Sigma}_\mathrm{R}(E)]^{-1}$, with $\hat{H}_0$ being the Hamiltonian of the isolated molecule. This object can be expressed in terms of left $[\chi^{(\mathrm{l})} = \chi^{(\mathrm{l})}(E)]$ and right eigenvectors $[\chi^{(\mathrm{r})} = \chi^{(\mathrm{r})}(E)]$ [146]

$$\hat{G}(E) = \sum_i \frac{\chi_i^{(\mathrm{r})}(E) \cdot \chi_i^{(\mathrm{l})\dagger}(E)}{E - z_i(E)}, \tag{4.2}$$

where

$$\begin{aligned} \left[\hat{H}_0 + \hat{\Sigma}_\mathrm{L}(E) + \hat{\Sigma}_\mathrm{R}(E)\right] \chi_i^{(\mathrm{r})} &= z_i \chi_i^{(\mathrm{r})}, \\ \chi_i^{(\mathrm{l})\dagger} \left[\hat{H}_0 + \hat{\Sigma}_\mathrm{L}(E) + \hat{\Sigma}_\mathrm{R}(E)\right] &= z_i \chi_i^{(\mathrm{l})\dagger}. \end{aligned} \tag{4.3}$$

Using this representation, we can express the transmission function as a sum over poles, indeed it is easy to check that the transmission can be written as

$$T(E) = \left|\tau_\mathrm{LR}\right|^2, \tag{4.4}$$

where τ_LR are the transmission coefficients. We can write them explicitly as

$$\tau_{\alpha\beta}(E) = \sum_i \frac{v_{i\alpha} v_{i\beta}^*}{E - z_i}, \tag{4.5}$$

with $i = 1, \ldots, \dim(\hat{H}_0)$. Here, the residue coefficients, $v_{i\alpha}$, and the functions, $z_i(E)$, are energy dependent. The residues can be written as $v_{i\alpha} = \sqrt{2\pi\rho_\alpha}\mathbf{t}_\alpha \chi_i^{(\mathrm{r})}$, and $v_{i\beta}^* = \sqrt{2\pi\rho_\beta}\chi_i^{(\mathrm{l})\dagger}\mathbf{t}_\beta^\dagger$, while the poles appear as the roots of the denominator $E - z_i$. As long as the molecule is weakly coupled to the electrodes, $z_i(E)$ have values close to the eigenenergies E_i of $\hat{H}_0$. In other words, the self-energies are small.

The transmission function in Eq. (4.4) can be decomposed as the sum of two terms,

$$T(E) = \sum_i T_i(E) + \sum_{i<j} T_{ij}(E). \tag{4.6}$$

The first term represents the single-orbital contribution to the transmission function. In the wide-band limit, since z_i is independent of the energy (as the self-energy is), we can write $z_i{=}E_i{+}i(\gamma_{i\mathrm{L}}{+}\gamma_{i\mathrm{R}})/2$ and $T_i(E)$ has a Lorentzian shape

$$T_i(E) \simeq \frac{\gamma_{i\mathrm{L}}\gamma_{i\mathrm{R}}}{(E-E_i)^2 + \left(\dfrac{\gamma_{i\mathrm{L}}+\gamma_{i\mathrm{R}}}{2}\right)^2}. \tag{4.7}$$

This expression corresponds to the Breit-Wigner resonances characteristic of single transport levels. It is characterized by three parameters (per resonance), $E_i, \gamma_{i\mathrm{L}}, \gamma_{i\mathrm{R}}$.

The second term in (4.6) corresponds to the pairwise interference between the transport levels. Following Ref. [145] this term can be written using the following parametrization for the transmission coefficients as

$$\tau_{\alpha\beta}(E) = \sum_i e^{i[\psi_i - \theta_i(E)]} |T_i(E)|^{1/2}, \tag{4.8}$$

where $\psi_i \coloneqq \arg[v_{i\mathrm{L}} v_{i\mathrm{R}}^*]$ and $\theta_i \coloneqq \arg[E{-}z_i]$ as

$$T_{ij}(E) \simeq 2\cos(\psi_{ij} - \theta_{ij}) |T_i(E)|^{1/2} |T_j(E)|^{1/2}. \tag{4.9}$$

Here $\psi_{ij} = \psi_i{-}\psi_j$ and $\theta_{ij} = \arg[(E{-}z_i)/(E{-}z_j)]$. The angles ψ_{ij} and θ_{ij} determine the constructive or destructive nature of the quantum interference. If the cosine is negative, a destructive interference is produced while if the cosine is positive, we have constructive interference. The phase-shift observed in the molecular orbitals at the contacts is the fourth parameter per resonance and it determines the shape of $T(E)$ shape. Note that for weakly coupled systems, the coefficients $v_{i\alpha}$ have a small imaginary part because the anti-hermitian part of the self-energies, Γ_α, is also small by definition. This means that the angles ψ_i are either close to π or to 0. Which one of these two possibilities is realized can be seen by visual inspection of the Kohn-Sham state associated to the resonance at E_i. For example, for HOMO-3 at $\varphi = \pi/6$ the phase-shift is π, see Fig. 4.6.

Finally, we point out that interference can be easily identified in a given energy window between two well-defined Lorentzian resonances. For energies E between both resonances, $E_i < E < E_j$, we have, according to its definition, $\theta_{ij} \simeq \pi$. As a result, constructive interference will appear if the pair of orbitals present a phase-shift of $\psi_i - \psi_j = \pi$. On the contrary, if the phase-shift that they show is the same $\psi_i \simeq \psi_j$, destructive interference occurs. Note that this model implies that for any pair of (extended) orbitals identified in the *ab initio* calculations at the gas-phase, we can determine their phase-shift and predict the type of quantum interference that we would expect in a transport calculation performed in the weak-coupling limit without the need of actually making this calculation.

4.3.2 Effective three-level model for ferrocene junctions

We now develop an effective model to discuss the main features in the ferrocene-based transmission functions from Fig. 4.5 (c). Because HOMO$-$2 and HOMO$-$1 are

State \ φ	0	$\pi/6$	$\pi/3$	$\pi/2$	$2\pi/3$	$5\pi/6$
HOMO−3	π	π	π	π	0	0
HOMO	0	0	0	π	π	π
LUMO	0	0	0	0	0	π

Table 4.1 – Phase-shifts ψ_i of the Kohn-Sham states at the contact points with the leads. The phase-shift value is obtained from inspection of the orbitals in Figs. 4.7 and D.3. The boxes indicate angles at which changes in the nodal structure have occurred. As explained in the text, this results in switching between destructive and constructive interference induced by the rotation.

strongly localized (and therefore they lead to very narrow resonances that barely change with φ), this model invokes the three states: HOMO−3, HOMO and LUMO. These are states delocalized across the junction and dominate the transport features. A graphical representation of this model is shown in Fig. 4.8.

In this type of models, one usually first fixes the model parameters $E_i, t_{i\alpha}$ employing, for instance, *ab initio* calculations and later computing the transmission function. Here, however, we proceed in a different way and read directly these parameters (resonance positions, broadenings) from the *ab initio* transmission function. From the position and width of the Lorentzian-shaped isolated resonances in Fig. 4.5 (c) (which are characteristic of a weakly coupling scenario) can be employed to extract the parameters E_i, γ_i. We further consider a symmetric coupling situation [see Figs. 4.5 (a)], in consistency with the fact that the resonance acquires a maximum value close to unity.

The fourth parameter (phase-shifts) is directly obtained from the Kohn-Sham states of the isolated molecule and not reconstructed from the *ab initio* transmission function. We can summarize the shift for each angle, ψ_i, in a table (see Table 4.1) for a selected number of relevant angles φ. This table has been constructed from Fig. D.3 provided in the appendix.

We now proceed with the analysis of our model results. In Fig. 4.9 (a) we show the *ab initio* transmission and the model result for $\varphi = \pi/6$. The position of the antiresonance between HOMO and LUMO states is well-reproduced in the model transmission function. Note that obtaining a quantitative agreement for the position of the antiresonance between the model and the *ab initio* calculations is actually not guaranteed as small deviations can occur here because the poles z_i and the residues $\tau_{\alpha\beta}$ have been chosen to be energy independent.

In Fig. 4.9 (b) the model-based transmission is shown for several rotational angles $\varphi \in \{\pi/6, \pi/2, 2\pi/3\}$. We remind the reader that these angles correspond to the geometries and *ab initio* traces shown in Fig. 4.5 (a) and (c). For each trace, the parameters $\{z_i(\varphi), \psi_i(\varphi)\}$ are separately determined from the *ab initio* results[2]. We find that the model reproduces qualitatively the shape of the transmission functions and, importantly,

2. We provide the numerical parameters obtained by fitting the *ab initio* traces in Table D.1.

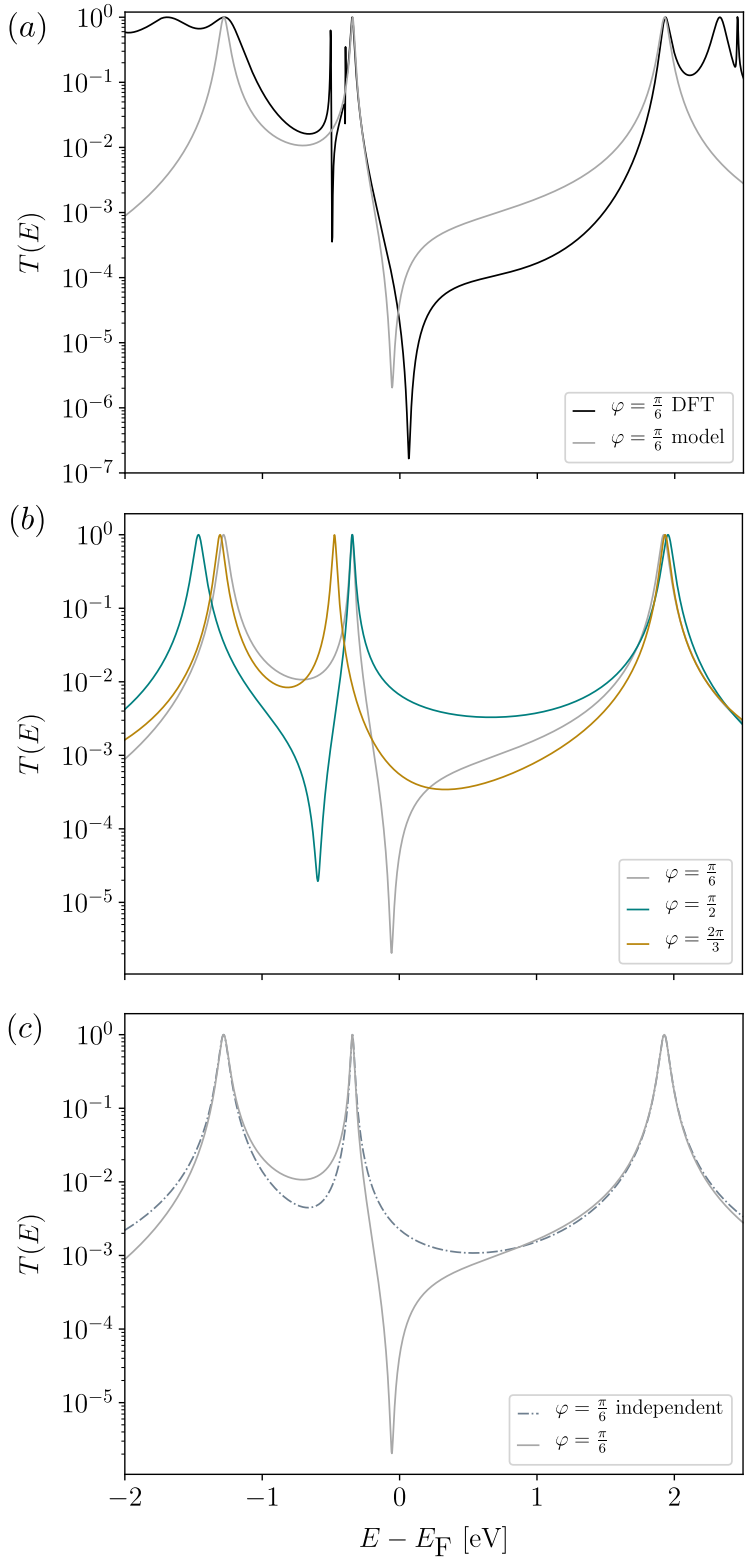

Figure 4.9 – Transmission curves, $T(E)$, obtained for different rotation angles, φ, in the effective three-level model. (a) Comparison between the effective three-level model transmission function and the *ab initio* transmission for $\varphi = \pi/6$. (b) Model transmission function $T(E)$ obtained for the three rotation angles shown in Fig. 4.5. The model clearly predicts the switching between constructive and destructive QI. (c) Comparison between the first term in Eq. (4.6) and the full transmission function $T(E)$ to highlight the importance of the quantum interference contribution.

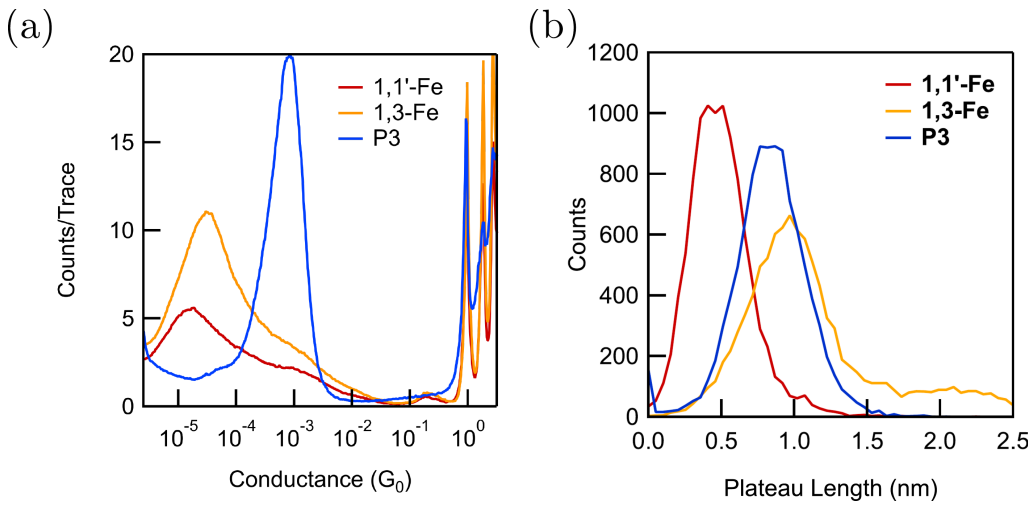

Figure 4.10 – (a) One-dimensional conductance histograms for molecular junctions of 1,1'-Fe, 1,3-Fe and P_3 obtained in L. Venkataraman's group. The histograms are obtained without data selection. The bias voltages $V_{\text{bias}} = 450\,\text{mV}$, for 1,1'-Fe and 1,3-Fe, and $V_{\text{bias}} = 230\,\text{mV}$ for P_3 are employed. (b) Plateau length one-dimensional histogram obtained from the two-dimensional conductance-displacement histograms for each molecular species. Adapted with permission from [125].

the position of the antiresonances associated to DQI. From our results, we therefore arrive to the important conclusion: the phase-shift angle difference, $\psi_{ij}(\varphi) = \psi_i(\varphi) - \psi_j(\varphi)$, is the crucial parameter that controls the quantum interference between two (extended) orbitals.

Finally, we highlight the importance of the interference terms Fig. 4.9 (c). We show, for $\varphi = \pi/6$, the comparison of the first term in Eq. (4.6) and the full expression (4.6). We find that in HOMO-LUMO gap region, DQI only appears if the interference term is considered. Interestingly, the region in the energy window $E_1 < E < E_2$ also shows interference features as the conductance increases when employing Eq. (4.6) compared to the independent-channel transmission. This is due to constructive quantum interference, which happens due to the fact that HOMO-3 and HOMO have different phase-shift.

4.4 Relation to experimental measurements

4.4.1 Conductance and displacement measurements

We are now in a position to discuss the experimental measurements performed in L. Venkataraman's group based on our theoretical insights. These measurements have been obtained using the scanning tunneling microscope-based break junction technique and we refer the curious reader to appendix F for a brief discussion of this method.

In Fig. 4.10 (a) we show the result of the room-temperature conductance measurements of the molecules under study.

Looking at the experimental conductance values of the two ferrocene moieties, we see

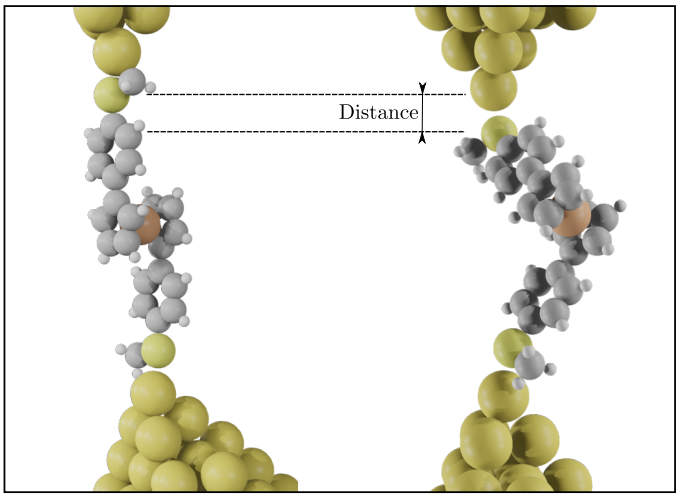

Figure 4.11 – Artistic sketch of the compression and elongation mechanism induced by ring rotation proposed in the theoretical calculations. The compression and elongation of the full junction can happen easily by profiting from the conformational flexibility of 1,1'-Fe. Adapted with permission from [125].

that both present a low typical conductance value, $G \simeq 2 \cdot 10^{-5} G_0$ (1, 1'-Fe) and $G \simeq 3.3 \cdot 10^{-5} G_0$ (1, 3-Fe). This values are substantially smaller compared to the conductance a species with similar length, as it is the case for P_3, for which $G \simeq 10^{-3} G_0$. We also note that the conductance histogram peaks for the ferrocene derivatives are very broad and show an additional "shoulder" at $G \simeq 10^{-3} G_0$. This secondary local maximum does not show in the P_3 histogram. We will discuss the physics associated to this signal in section 5.4.

By comparing at the experimental data and the *ab initio* calculations, we observe that the trends in both are the same. 1, 1'-Fe has the lowest value for the conductance, followed by 1, 3-Fe, and finally, the largest conductance values are for P_3. The experimental value of the conductance for the ferrocene derivatives was smaller (by a factor of 26 and 48 for 1, 1'-Fe and 1, 3-Fe, respectively) as compared to the conductance of P_3. In the computational simulations this result is in qualitative agreemeent with respect to the experiments, being a factor of 50 for 1, 3-Fe and 28 1, 1'-Fe.

We attribute the low conductance values of ferrocene moieties to their DQIs properties. The broader histograms are explained thanks to the flexibility of the "scissor mode", which allows for many stable configurations at low energy cost. The shoulder at higher conductance values is related to direct metal-electrode binding, see section 5.4.

Finally, we note that a crucial point in our argument is that the DQIs features have to be located close to the Fermi energy level, E_F, to have a suppression of the conductance. The precise position of the antiresonance can change since, due to intrinsic DFT errors, the energy level alignment is not completely accurate [21, 25]. Despite the possible DFT artifacts, we can rely on the theoretical findings due to the following: First, the nodal structure of our Kohn-Sham orbitals is robust at the DFT-level; second, the DFT simulations show that the molecule remains neutral and the Fermi energy does not change. Even if the possible discrepancies in the level alignment can then be up to ~ 1 eV, the

transmission would be suppressed even if the DQI anti-resonances lies in a (wide) energy window close to the Fermi energy.

4.4.2 Pull-push measurements

With the idea of mechanically tuning the quantum interference properties guided by the theoretical calculations, the pull-push measurements were carried out in L. Venkataraman's group. We show an artistic representation of this experiment in Fig. 4.11, the junction is elongated to the $\varphi = \pi/6$ geometry (full-elongation) and compressed by reducing the tip-substrate distance by 2.4 Å. While doing so, the conductance is recorded. Similar experiment was carried out for P_3. The experimental measurements are summarized in Fig. 4.12. It is found that for 1,1'-Fe the conductance changes by a factor of almost 7, while performing the pull-push measurements for P_3, the conductance changes just by a factor of ~ 3. Of course, there can be many reasons why the conductance of the junction can be modulated while moving the electrodes in this way. For example, the gold atoms at the tip can reorganize, the SMe-electrode binding can change or the through-space contribution to the conductance be modified due to the fact that the gap between the electrodes is modulated. Importantly, all these reasons apply both to 1,1'-Fe and P_3. Therefore, we believe that changes in the molecular conformation in 1,1'-Fe due to the soft rotational degree of freedom, together with its impact on the interference properties, is the predominant reason for the largest conductance modulation observed here.

4.5 Summary of this chapter

In this chapter, we have studied quantum transport properties of ferrocene-based single-molecule junctions. We have shown that ferrocene-derivatives, 1, 1'-Fe and 1, 3-Fe which have different substitution patterns, present important DQI effects. These are produced by the interplay of several localized and delocalized orbitals derived from d-orbitals at the iron core. We have proposed that DQI occurring close to E_F determine the transmission characteristics and result in a reduced value for the low-bias conductance (compared to the conductance of molecules of comparable length). We have also explained how the flexibility of the Cp ring allows to alter the interference properties of the molecular junction. Since rotation alters the nodal structure of the relevant transport orbitals, the interference properties can change from destructive to constructive. If that change occurs close to the Fermi energy, the conductance can change by orders of magnitude. Our calculations have been crucial to provide explanation of transport experiments performed in L. Venkataraman's group.

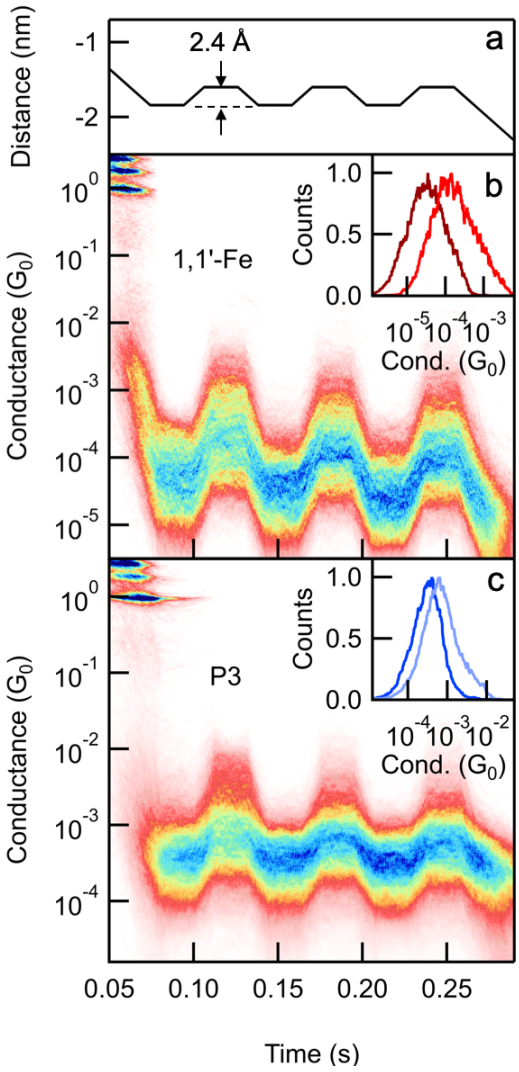

Figure 4.12 – Data obtained in L. Vankataraman's group. (a) Modulation of the distance between the tip and the substrate as a function of time. (b) Two-dimensional conductance histogram of the 1,1'-Fe molecular junction obtained during the modulation. The conductance recorded in the junction decreases when the distance between the substrate and the tip gets increases. Upon modulation of the tip-sample distance, the conductance changes by a factor of ~ 7. The inset shows the number of counts collected for the conductance obtained at the maximal (dark red) and minimal (light red) junction length. (c) Same as in (b) but for P_3. Here, we find that the conductance changes by a factor of ~ 3 only. Reprinted with permission from [125].

Chapter 5

Molecular insulators

A part of the material covered in this chapter has been published in:

H. Li[†], T. A. Su[†], M. Camarasa–Gómez[†], D. Hernangómez–Pérez, S. E. Henn, V. Pokorný, C. D. Caniglia, M. S. Inkpen, R. Korytár, M. L. Steigerwald, C. Nuckolls, F. Evers, and L. Venkataraman, *Silver makes better electrical contacts to thiol-terminated silanes than gold*, Angew. Chem. Int. Ed. **56**, 14145 (2017) [†: equally contributing authors]. (Ref. [147], covered in Sec. 5.2).

T. Fu, S. Smith, M. Camarasa–Gómez, X. Yu, J. Xue, C. Nuckolls, F. Evers, L. Venkataraman, and S. Wei *Enhanced coupling through π-stacking in imidazole-based molecular junctions*, Chem. Sci. **10**, 9998-10002 (2019) - Published by The Royal Society of Chemistry. (Ref. [148], covered in Sec. 5.3).

The chapter also contains unpublished material of the manuscript in preparation:

M. S. Inkpen, G. Lovat, M. Camarasa–Gómez, D. Hernangómez–Pérez, F. Evers, X. Roy, and L. Venkataraman, *Metallocene-electrode contacts in single-molecule junctions* (Ref. [149], covered in Sec. 5.4).

We present in this chapter three transport studies with molecular insulators in the single-molecule junction context. In the first part of the chapter, we present a transport study of single-molecule junctions formed with σ-conjugated silicon-based molecular wires (silanes) attached to leads of different metals. When terminated by thiol, these wires have larger conductance for silver (Ag) contacts compared to gold (Au) ($G_{\mathrm{Ag}} > G_{\mathrm{Au}}$). This result contradicts the expectations based on simple arguments that rely on the metal work functions trends. However, we recover the expected trend ($G_{\mathrm{Au}} > G_{\mathrm{Ag}}$) when considering amine-terminated silanes. We provide an explanation of these findings based on ab initio transport calculations, taking into consideration the important role of the anchor group in the conductance properties. In the second part of the chapter, we present a study of the conductance properties of single-molecule junctions made of alkane wires connected with imidazole linker groups to gold leads. We investigate how the imidazole terminations can also form $\pi - \pi$ stacked dimers with high through-space conductance, opening the possibility to simultaneously bind more than one molecular wire in a molecular junction.

In the third part of the chapter, we study how metallocenes can bind to metal leads by metal-electrode bonds. We investigate the impact of the substitution of the metal atom in the transport properties of these junctions.

5.1 Why molecular insulators?

In a very simplified picture, a single-molecule junction can be seen as a one-dimensional tunnel barrier, with the molecule playing the role of the insulating layer between the two metallic contacts, as shown in Fig. 1. With this picture in mind, the electronic transport in the single-molecule junction occurs due to transmission of electrons/holes across the tunnel barrier [45]. The transmission probability in this model shows an exponential decay with the barrier length and is characterized by a decay constant, β, estimated as $\beta \sim \sqrt{2mV_{\text{barrier}}/\hbar}$.

Carbon-based molecular wires are archetypical examples of molecular insulators [7, 21, 150, 151, 152, 153, 154, 155, 156, 157]. It has been observed that, in the coherent off-resonant regime, the conductance of these wires normally decreases exponentially when the length of the wire increases by adding the new units to the molecular backbone (methylene units in the case of alkanes) [150, 152, 153, 155]. The variation of the conductance with the wire length [150, 152, 153, 155] can be used to extract an empirical β parameter by fitting $G = G_c \exp[-\beta L]$, where L is the length of the molecule and G_c, a prefactor related to the inverse of the contact resistance. This parameter provides information about the molecular backbone and can be related to the electronic band-gap in the limit $L \to +\infty$ [158]. In other words, the β parameter might be used to interpret the metallic or insulating character of the wire [1]. For alkanes [2], $\beta = 0.8 - 1.01\,\text{Å}^{-1}$ [161, 162], so that the conductance is easily suppressed and the wire clearly acts as a molecular insulator. For this reason, alkanes have been considered to be the standard (molecular) insulators in molecular electronics.

It is therefore very tempting to speculate if analogue of these wires can be made of different elements. This has been achieved only recently, with silicon-based [29, 163] and germanium-based [155, 162] wires. Although we might think that these novel wires possess similar physical properties to alkanes, both can reveal interesting and novel physical properties. For example, as we already mentioned in the Introduction of the thesis, it has been reported [29] that a complete suppression of the electron transmission occurs for silicon molecular wires when the Si-Si bonds are locked in *cis*-dihedral configuration. As a consequence, the conductance drops to a value smaller than conductance obtained from through-space tunneling, (*i.e.*, tunneling directly through vacuum) if the Si-Si bond would be broken for distances smaller than 1 nm. This is interesting for obtaining ideal insulators when electronic devices are miniaturized, as in nanogaps electron tunneling processes normally occur.

As a result of our close collaboration with the experimental group of L. Venkataraman's in Columbia University, we have been motivated to investigate other molecular insulators leading to several side projects that we present in this chapter.

1. We note that this parameter must be used with care for the case of conjugated wires that possess strong odd-even effects. In this case, β might lose its meaning if the wire has a complete metallic character, $\beta = 0$ and can become even positive due to solvent interface effects [152].
2. For the beta values of other molecules, we refer the reader to Refs. [159] and [160].

5.2 Silane-based single-molecule junctions

5.2.1 Motivation

As we have already mentioned in the previous section 5.1, silicon-based molecules with *cis*-configuration for the Si-Si bond act as ideal molecular insulators. These molecular wires completely suppress the electronic transmission [29]. As a consequence, they present a conductance value smaller than a equivalent vacuum layer of the same width as the molecule. There are other silicon-based wires such as siloxanes, which also present good insulating properties [163]. Silanes, with *trans*-configuration, are more conductive due to their strong σ-conjugated backbone. They present both fundamental and technological interest as components of silicon-based molecular nanoelectronics, similar to the wires in conventional electronics [30]. We thus ask ourselves the question of how does charge transfer occurs in silanes at the molecular level.

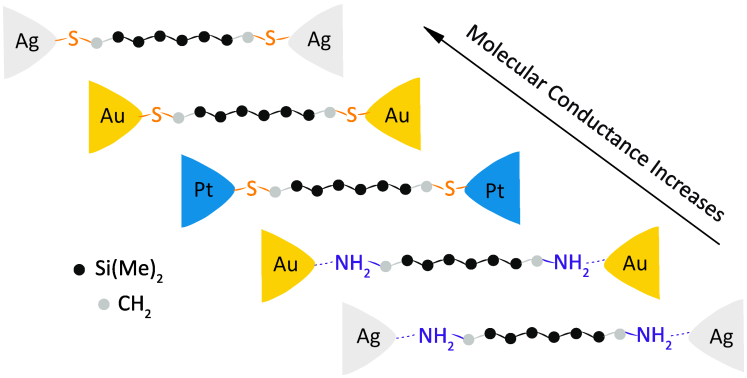

Figure 5.1 – Sketch of the silane single-molecule junctions studied in this section. For a given backbone length, the conductance of the thiol-terminated silanes is larger than the conductance of the diamine-terminated ones. For the thiol-terminated wires, the conductance is larger when the molecule is attached to Ag contacts compared to Au and Pt ($G_{\mathrm{Ag}} > G_{\mathrm{Au}} > G_{\mathrm{Pt}}$); the situation is however reversed when considering amine-terminated wires ($G_{\mathrm{Ag}} < G_{\mathrm{Au}}$). From [147].

Traditionally, single-molecule junctions have been mainly formed using gold (Au) as the primary material for the electrodes. This material presents many advantages, such as inertness and malleability in ambient conditions, being as well able to form stable junctions with a huge variety of molecules. Recently, some stable junctions have been formed using as electrical contacts other materials. Specifically, metals like silver (Ag) [164, 165, 166, 167], platinum (Pt) [168, 169, 170] or palladium (Pd) [170, 171, 172] have become increasingly popular. Employing different metallic electrodes in a junction allows us to explore new physical properties of silane single-molecule junctions, as well as to obtain a deeper understanding of the role of metal-molecule coupling through anchor groups. For

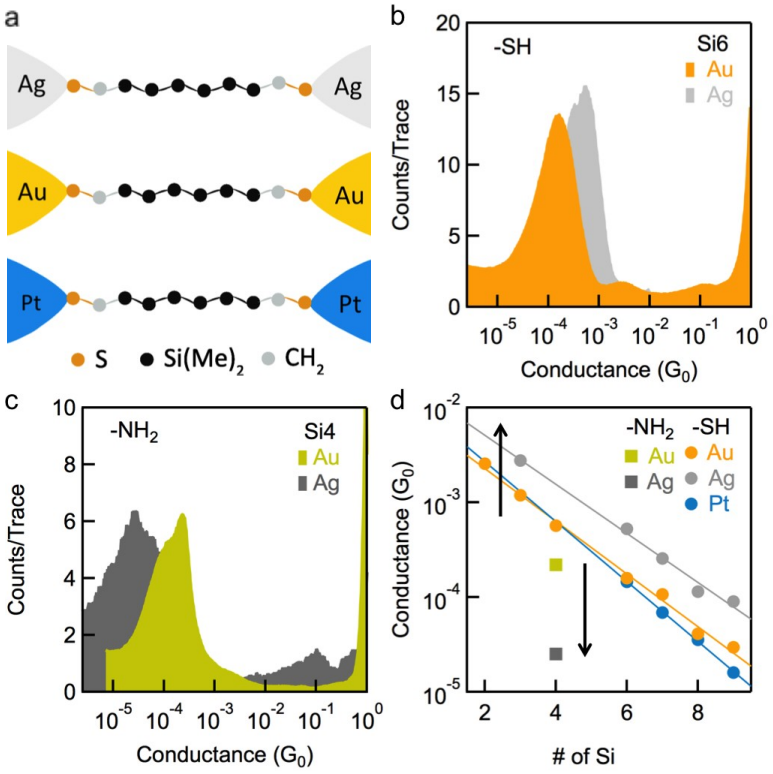

Figure 5.2 – (a) Sketch of thiol-terminated Si_6 silanes attached to Ag, Au and Pt contacts. (b) Logarithmically binned one-dimensional (1D) conductance histograms for Au and Ag junctions for Si_6 wires with thiol linkers. (c) Logarithmically binned 1D conductance histograms for Au and Ag junctions of Si_4 wires bound with amine linkers. (d) Experimental values for the conductance (in logarithmic scale) plotted against the number of silicon units in the molecular backbone. The fitted exponential decay for each data set is shown by straight lines. The arrows indicate that for SH anchor groups $G_{Ag} > G_{Au}$ while for NH_2, $G_{Ag} < G_{Au}$. From [147]. Copyright © 2017 Wiley-VCH Verlag GmbH & Co. KGaA, Weinheim. Reproduced with permission.

example, relativistic effects present in heavy elements, such as spin-orbit (SO) coupling or corrections to the kinetic energy (described in section 1.3.1), can also influence the metal-molecule interaction and affect the charge transfer properties of molecular junctions [173, 174].

In this section, we analyze theoretically the quantum transport properties of a series of methylthiol- (Si_N-SH) and methylamino- (Si_N-NH_2) terminated silicon-based permethyl wires. The experimental measurements were performed in the group of Latha Venkataraman in Columbia University. The experiments were carried out using Au, Ag and Pt as contact materials, see sketch in Fig. 5.1. The experimental procedure (STM-BJ) used to measure the conductance in these single-molecule junctions at room temperature is described in appendix F.

The experiment has been repeated using different metallic contacts (Pt) or anchor groups between the molecule and the electrodes, see Fig. 5.2 (a), (b) and (c). The resulting value of the conductance represented against the number of silicon atoms in the backbone of the wire is shown in Fig. 5.2 (d). We observe that increasing the backbone length of the

molecule yields to the exponential suppression of the conductance. This phenomenology is typical of a (coherent) tunneling mechanism for charge transport. Fitting the data with an exponential $G = G_c \exp(-\beta N)$ for the SH-Si_N-SH junctions the values of the attenuation parameter $\beta_{Au} = 0.64 \pm 0.02$ N^{-1}, $\beta_{Ag} = 0.60 \pm 0.03$ N^{-1} and $\beta_{Pt} = 0.73 \pm 0.02$ N^{-1} are found (here N is the number of units in the wire). A crucial observation concerns the dependency of the conductance trends on (i) the anchor group and (ii) the material of the contacts. For NH_2-Si_4-NH_2, it is found that the value of the conductance is substantially lower compared to SH-Si_4-SH. Importantly, the anchor group significantly alters the charge transport properties depending on the metal to which it connects in the electrode: for NH_2-Si_4-NH_2, the conductance for Ag electrodes is smaller compared to Au. This situation is reversed for SH-Si_N-SH junctions for which the conductance for Au electrodes is smaller compared to Ag. This is a surprising result because one would expect that always $G_{Ag} < G_{Au}$ looking at the trends from the metal work function of the different metals (Ag: 4.64 eV; Au: 5.47 eV; Pt: 5.84 eV [175]) [3].

5.2.2 Transport calculations for silane junctions

In order to understand the non-trivial experimental results and the underlying charge transfer properties of these single-molecule junctions, we turn to *ab initio* quantum transport simulations based on DFT. We consider the test cases of a silane wire terminated with thiol and amine linker groups, attached to Au and Ag contacts. For technical details on how these calculations are performed, we refer the reader to appendix G.

The geometries and the resulting non-self-consistent transmission functions are shown in Fig. 5.3, where we have considered silanes with backbone lengths of $N = 4$ (for amine) and $N = 7$ (for thiol). We note that the charge transfer is dominated in both cases by the HOMO level, with the conductance determined by its width and alignment with the Fermi energy of the metal. Nevertheless, several differences are found between thiol- and amine-terminated silanes wires, which clearly emerge from the transmission curves. In Fig. 5.3 (a), we plot the transmission function for NH_2-Si_4-NH_2 with Au and Ag electrodes. We observe that in both cases resonances produced by the HOMO and LUMO orbitals are rigidly shifted by ~ 0.4 eV. This shift can be understood from the dative (weak) chemical nature of the lead-linker chemical bond. As such, the shift in the transmission function is consistent with the mismatch found between the experimental values of the work function, ~ 0.6 eV, for the metals [175, 178].

For thiol-terminated silanes the situation is drastically altered. We show the corresponding transport calculations for SH-Si_7-SH in Fig. 5.3 (b). First, as compared to the diamine anchor case, we find that the conductance is enhanced even if the wire is substantially longer (almost twice as long in silicon atom units). For Ag electrodes, the enhancement is larger (by roughly a factor of 5) as compared to Au (roughly a factor of

3. In what follows, we shall focus our theoretical analysis on the Au and Ag contacts only since, as shown in Ref. [147], the conductance plateau for Pt is not so well defined due to the lack of a sharp conductance drop following the rupture of the metallic contact. It is nevertheless surprising that the experimental results for Pt are characterized by lower conductance compared to Au or Ag since previous theoretical studies on benzenedithiol [176, 177] and experimental measurements on alkane-dithiol junctions [170] seem to suggest larger values of the conductance are found for Pt leads when compared to others (Au, Ag).

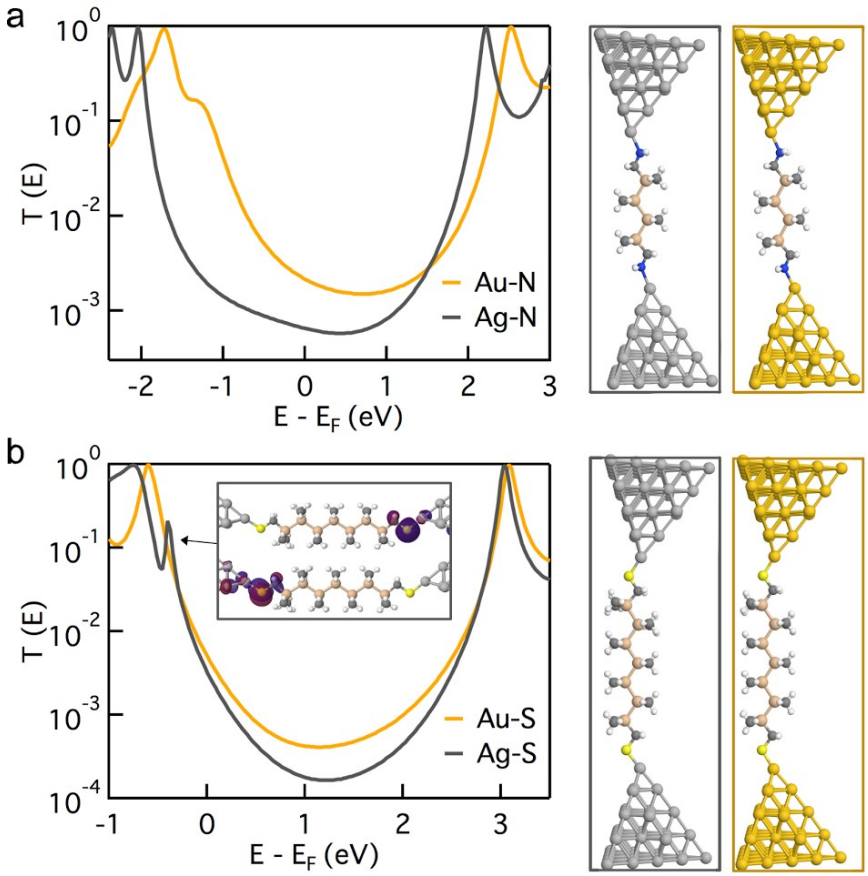

Figure 5.3 – (a) [Left] non-self-consistent transmission function, $T(E)$, calculated for the junction NH_2-Si_4-NH_2 with Au and Ag contacts. [Right] corresponding relaxed geometries employed in the calculation. (b) [Left] Non-self-consistent transmission functions, $T(E)$, calculated for the junction SH-Si_7-SH with Au and Ag contacts. The inset shows the isosurface of the gateway states, which produce an additional resonance for Ag and Au electrodes. The gateway state is clearly separated from the HOMO resonance width and close to E_F for the molecular junction made with Ag, contributing to the conductance enhancement. [Right] Relaxed geometries used in the transport calculation. From [147]. Copyright © 2017 Wiley-VCH Verlag GmbH & Co. KGaA, Weinheim. Reproduced with permission.

4). The overall increase in the conductance can be understood from the better alignment of the relevant transport orbitals with the Fermi energy of the metals. We also note that after replacing the amines with thiols, the relative shift of the HOMO and LUMO peaks is substantially smaller (~ 0.1 eV), and significantly reduced (by a factor of 6) when comparing with the work function difference for the bulk metal. We understand this difference as being a consequence of the covalent nature of the lead-linker bond.

In addition, we see an additional resonance in the transmission function appearing for Ag at around 400 meV below the Fermi energy. This resonance is attributed to a so-called "gateway" state: a state mainly located at the anchor group S. These states come by pairs, see inset in Fig. 5.3. Because for Ag the (narrow) gateway resonance is placed close of the Fermi level and outside of the width of the HOMO peak, the gateway state can significantly enhace the transmission function at the Fermi energy compared to Au.

Note that in Au-based junctions, these states *also* exist but they are closer to the HOMO resonance and therefore cannot be identified as a separate resonance. Consequently, they take a reduced role in the charge transfer properties.

Finally, a word of caution: we note that the general trends seen in experiments can be reliably reproduced with our DFT-based transport calculations at a qualitative level but we can not predict the relative order of the conductance as seen in the experiments (reversal of the conductance order between amine and thiol linkers when attached to Ag and Au leads). We attribute the discrepancy between theory and experiment to difficulties in the description of relative level alignment of energy levels inherent to Kohn-Sham transport calculations. Moreover, in the present situation we cannot rely upon cancelation of errors in the exchange-correlation functionals as relativistic corrections of the kinetic energy and SO interaction has larger contribution for the Au molecular junctions than in Ag [151].

5.2.3 Impact of relativistic kinetic energy corrections on transmission

As we mentioned in section 1.3.1, in heavy atoms, like Au, it is necessary to also consider in the *ab initio* calculations relativistic corrections. These relativistic effects involve corrections to the scalar kinetic energy or SO interaction. In this subsection, we benchmark two implementations of the scalar corrections to the kinetic energy: (i) the so-called zero-th order regular approximation (ZORA) as implemented in FHI-aims and (ii) the effective core potential (ECP) correction as implemented in TURBOMOLE. *A priori*, the ZORA has been designed to provide an efficient relativistic description of the valence and outer core electrons, however, it might lead to inaccuracies for deep levels of heavy atoms [55]. To check the impact of such inaccuracies in our calculations, we have compared non-self-consistent transmission functions obtained using FHI-aims and TURBOMOLE [4].

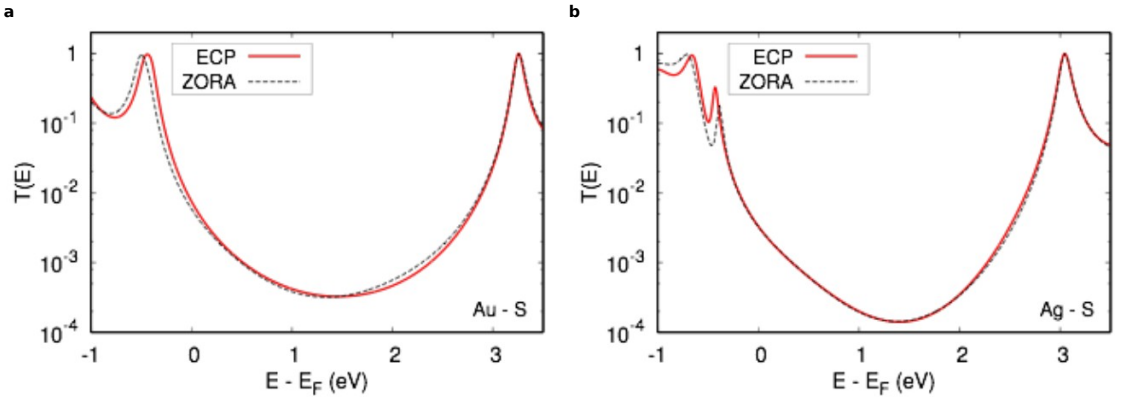

Figure 5.4 – Transmission function for a SH-Si_7-SH silane molecular junction with (a) Au and (b) Ag contacts. In each panel, a calculation with ZORA (from FHI-aims) and ECP (TURBOMOLE) scalar relativistic corrections to the kinetic energy in the non-self-consistent transmission function are compared. From [147]. Reproduced with permission.

In Fig. 5.4 we show both relativistic calculations. We see that the differences in the relativistic treatment do not lead to either significant or systematic deviations of the trans-

4. Calculations employing TURBOMOLE have been performed in the group of Dr. Richard Korytár at Charles University in Czech Republic.

mission curves. In both calculations, the same geometry and exchange-correlation functional are employed together with similar basis set (triple-zeta basis for TURBOMOLE, roughly equivalent to FHI-aims "tight" settings). The embedding self-energy used in both calculations was also identical. There is a small deviation in the height of the HOMO resonances (about 80 meV bigger for ECP as compared to ZORA). Because of this shift, the conductance of the Au-linked junction differs by 25% between ZORA and ECP. For the Ag gateway state, the deviations between ZORA and ECP are of the order of $\sim 2\%$, which is negligible once possible errors due to different basis sets are taken into account. Importantly, the order of the transmissions is not altered between both ZORA and ECP and therefore, it confirms our interpretation of the transport calculations as detailed above.

5.2.4 Impact of spin-orbit coupling on transmission

We now briefly discuss the importance of considering SO interaction. In Fig. 5.5 we show the calculations performed for the geometries provided in Fig. 5.3. The geometries and DFT parameters are the same, the only difference is that SO corrections are not considered here. Although in panel (a), the non-self-consistent transmission functions for NH_2-Si_4-NH_2 attached to Ag or Au in the absence of SO coupling do not present significant differences to the SO coupled case, this is not the case for the non-self-consistent transmission functions of SH-Si_7-SH for Ag and Au electrodes. We note that for SH-Si_7-SH, the work function mismatch in the absence of SO coupling increases and also that the gateway states located close to chemical potential for the Ag lead do not enhance the conductance as much as in the calculation with SO coupling. We therefore clearly see that SO coupling can induce differences in the transmission and that relativistic effects thus should be taken into account when comparing different materials in the electrodes.

5.2.5 Summary of this section

To conclude, we have shown that the conductance of silane molecular wires depend on different electrode materials and anchor groups for the same molecular bridge on a non-trivial way. When amine-terminated wires are attached to Au contacts, the conductance is higher than Ag. The situation is reversed when thiol-terminated wires are considered (higher conductance for Ag electrodes compared to Au electrodes). This difference in the transport characteristics cannot be explained by looking at bulk properties of the contacts (*i.e.* metal work function) only and our calculations highlight the crucial nature of the chemical bond between the contact and the anchor on charge transfer. Our theoretical study suggests that the level alignement and the presence of additional (and difficult to predict) resonances produced by gateway states are key to explain the experimental results. We have also studied the impact of SO interaction and relativistic effects on the non-self-consistent transmission. These corrections induce an enhancement on the conductance of the molecular junction when heavy elements, such as Au, are present and produce larger shifts of the frontier orbital resonances. Therefore, the relativistic corrections can be highly relevant, especially when comparing different materials for the electrodes with the same molecular bridge.

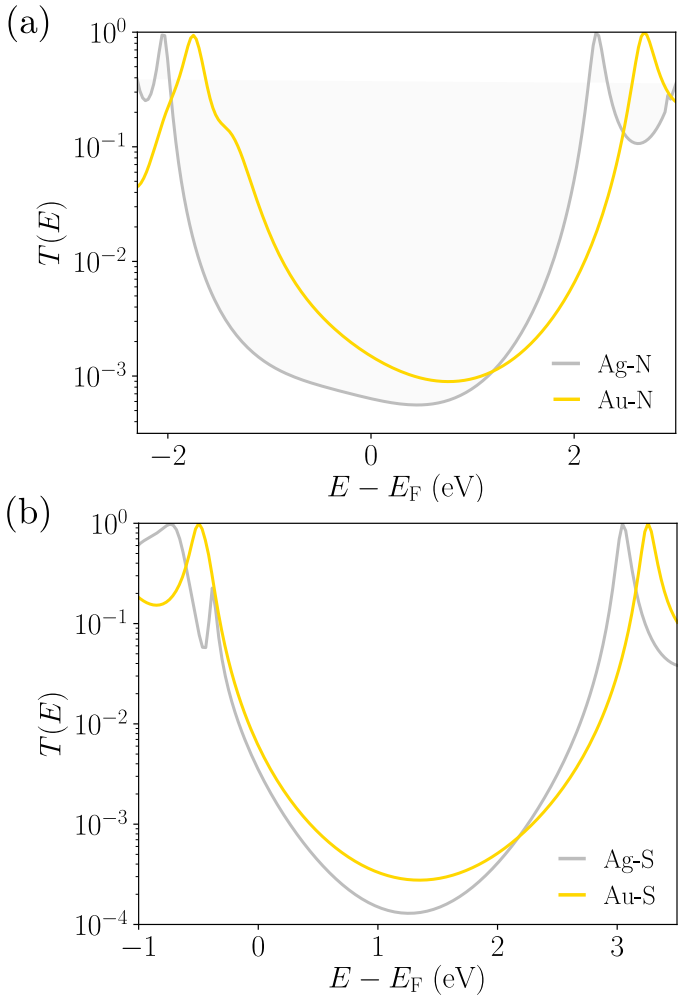

Figure 5.5 – Transmission characteristics (and corresponding relaxed geometries) for the two silane-based molecular junctions studied in this chapter. (a) Non-self-consistent transmission function, $T(E)$, of the junction NH_2-Si_4-NH_2 with Au and Ag contacts, where no SO coupling has been included in the calculation. (b) Same as in (a) but with thiol anchors and a longer wire, SH-Si_7-SH.

5.3 Imidazole-based single- and stacked-molecular junctions

5.3.1 Imidazole as an anchor group

As we have seen in the first part of this chapter, the type of anchor group and the metal-linker interaction play an important role on the charge transfer of single-molecule junctions. With an eye on bio-nanoelectronic applications, it is interesting to bind biochemical molecular wires to metallic leads. However, biochemical compounds are in general difficult to bind to metal electrodes. One way to solve this difficulty is the use of precursors as linkers. Since precursors are part of other (larger) biochemical complexes it is interesting to use them to bind the (bio)molecule to the metallic contacts. For this reason, we turn our attention to imidazole.

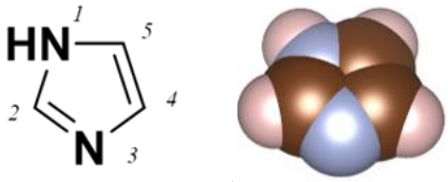

Figure 5.6 – Structural formula and geometry of imidazole following the IUPAC labeling. From [148] - Published by The Royal Society of Chemistry. Copyright CC BY-NC 3.0.

Imidazole is a heterocyclic organic compound (see Fig. 5.7) which consists of a planar five-member carbon-based ring with two nitrogen substitutions. Its chemical formula is $C_3N_2H_4$. The two nitrogens have different chemical nature, one is pyrrole-like (N_1) and donates electrons to the aromatic ring, while the other one is pyridine-like (N_3) and has a lone electron pair. These electrons are located in a sp^2 orbital and are responsible for the coordination with other metals (similar to the amine-metal dative bond of section 5.2.2). Imidazole is also an electron-rich functional group, and thus, it allows for non-covalent intermolecular interactions between π orbitals or hydrogen bonding. This gives imidazole a broad functionality in different contexts: For instance, in biochemistry, it can be used as a precursor group of the aminoacid histidine or participate in redox reactions of superoxide dismutases [179, 180]. Even though it has been used before in material science in some metal-organic frameworks [181] up to now imidazole had not been considered in the context of molecular electronics. We investigate here how the binding with the metallic lead occurs, how imdazole binds to molecular wires made of σ-bonded carbon atoms (alkanes) and how the transport properties of alkanes change due to the use of imidazole as linker.

To that purpose, the group of Latha Venkataraman performed conductance measurements of four imidazole-terminated alkanes with different backbone lengths [im-N-im, where $N = 3 - 6$ is the number of carbon atoms in the backbone of the alkane wire, see Fig. 5.7 (a)]. These measurements are done following standard procedures described in appendix F. The resulting 1D logarithmically binned histograms are shown in Fig. 5.7 (b). We observe in these histograms a peak at $\sim 1G_0$, which is a clear indication of the formation of a Au point contact between the substrate and the tip. The conductance peaks corresponding to the molecule bridging the gap between the substrate and the tip correspond to maxima at about $10^{-4}G_0$ and $10^{-6}G_0$, where the peak with the smallest (resp. larger) conductance value corresponds to the im-6-im (resp. im-4-im) molecular junction.

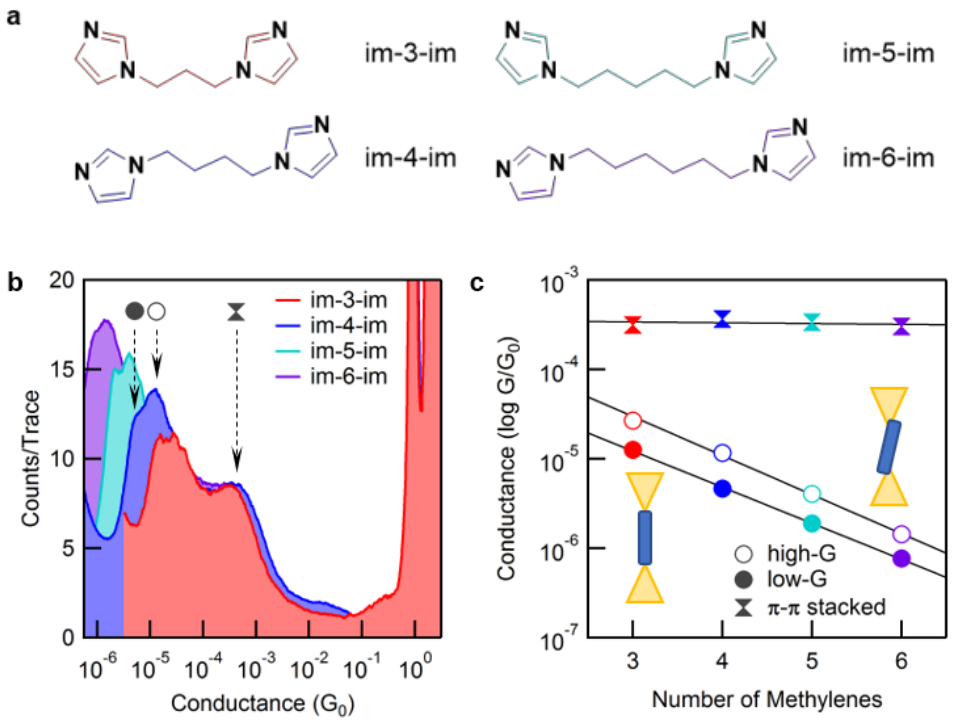

Figure 5.7 – (a) Chemical structure of a series of imidazole-terminated alkanes, im-N-im with $N = 3, 4, 5, 6$. (b) 1D conductance histogram (logarithmically binned) for the series of im-N-im molecules. For all wire lengths, we observe three peaks in the conductance histogram corresponding to the low conductance (low-G) configuration, high conductance (high-G) configuration and the $\pi - \pi$ stack dimer marked by a black circle, a white circle and a black hourglass, respectively. (c) Logarithm of the normalized conductance, G/G_0, obtained from the histograms shown in (b) as a function of the number of methylene units in the alkyl chain. We show each of the three possible configurations of the molecule in the junction (straight, tilted and stack as indicated in the inset). The attenuation parameter, β, obtained from fitting the experimental results to an exponential function is $\beta = 0.93$ N^{-1} and $\beta = 1.01$ N^{-1} for low- and high-G junctions, respectively. From [148] - Published by The Royal Society of Chemistry. Copyright CC BY-NC 3.0.

As expected for molecular insulators in which coherent tunneling occurs, the value of the conductance increases while decreasing the backbone length of the alkane wire. Furthermore, there is also an additional feature ("shoulder") in every histogram at around $10^{-3}G_0$, which point towards the formation of smaller complexes. In L. Venkataraman's group it has been hypothesized that these are intermolecular $\pi - \pi$ stacked complexes between two of the imidazole linkers [182, 183, 184, 185, 186, 187].

A closer inspection of the molecular conductance peaks reveals that at each peak there are actually two local maxima, similar to what has been observed for pyridine-based linkers [188, 189, 190]. In L. Venkataraman's group it has been that this double peak feature is related to imidazole linker binding to Au through the pyridine-like nitrogen so that it can form a vertical σ-coupled junction or a tilted σ- and π-coupled junction, as shown in the inset of 5.7 (c). These conformations correspond to a so-called low conductance ("low-G") and high conductance ("high-G") binding configurations. The differences between them have been investigated elsewhere [190, 191] and we focus our investigations primarily on

the low-G case.

In Fig. 5.7 (c) we show the experimental conductance value for each molecule (normalized to the conductance quantum) as a function of the wire length. The solid circles correspond to the low-G configuration, while the hollow circles corresponds to the high-G configuration described above. For both cases, the conductance decreases exponentially with the addition of methylene units to the alkane backbone. To calculate the corresponding attenuation parameter, β, we fit the data with the function $G = G_c e^{-\beta N}$ expected for the tunneling transmission model. We find for the low-G configuration, $\beta = 0.93$ N^{-1}, while for the high-G we obtain $\beta = 1.01$ N^{-1}. These values are in quantitative agreement wih the attenuation parameters obtained for alkyl molecules with thiol or amine linkers [151, 192]. By extrapolation to $N = 0$ (no carbon bridge), we can also compute the contact resistance of the junction which is $1/G_c \sim 65$ MΩ. This quantity serves as an indication of the linker nature: smaller anchors have smaller values of the contact resistance [5]. A comparison to pyridine shows that imidazole is clearly comparable (the contact resistance of pyridine is ~ 23 MΩ, also determined experimentally [189]).

5.3.2 Transport calculations for imidazole-terminated alkanes

In order to rationalize the experimental results, we turn to quantum transport calculations performed in collaboration with the group of Latha Venkataraman. We relegate the technical details to appendix G.2.1. A typical (relaxed) geometry used in our *ab initio* calculations is shown in Fig. 5.8 (a) with the non-self-consistent transmission function for our four im-N-im molecules shown in Fig. 5.8 (b). We see that, although the conductance is overestimated due to intrinsic DFT artifacts [47], the calculated transmission at the Fermi energy, E_F, follows the trend seen in the experimental measurements: we find an exponential decrease of the conductance with the system length as shown in the inset of Fig. 5.8 (b). The β parameter obtained in experiments is 0.93 per methylene unit, close to the theoretical result 1.10 (in collaboration with our experimental colleagues at Columbia University).

To verify that the conclusions from our zero-bias calculation of the transmission function can be applied to the experiments at finite bias, additional checks were performed monitoring the shape of the conductance histogram for different bias voltages. If non-linearities are small, as expected from the fact that the molecule has a large HOMO-LUMO gap and therefore the polarizability of the molecule is also small, then the 1D and 2D histograms have to preserve their shape with the bias voltage. We refer the reader to the Supporting Information of Ref. [148] for the data that supports this reasoning.

An analysis of the frontier orbitals for the low-G non-self-consistent transmission functions shows that the transmission function at the Fermi energy has large contributions from the molecular states HOMO−2 and HOMO−4. The amplitude of these states decays along the molecular backbone as seen in the blue frame of Fig. 5.8 (c). The resonance at $E - E_F = -1.6$ eV is produced by a gateway state derived from the HOMO−8 molecular orbital (green frame). As it happens with the states close to the Fermi energy, it is primarily a σ-based orbital which has most of its weight at one of the anchor groups. Finally,

5. For instance, -SMe: ~ 0.27 MΩ and -NH_2: ~ 0.37 MΩ [192].

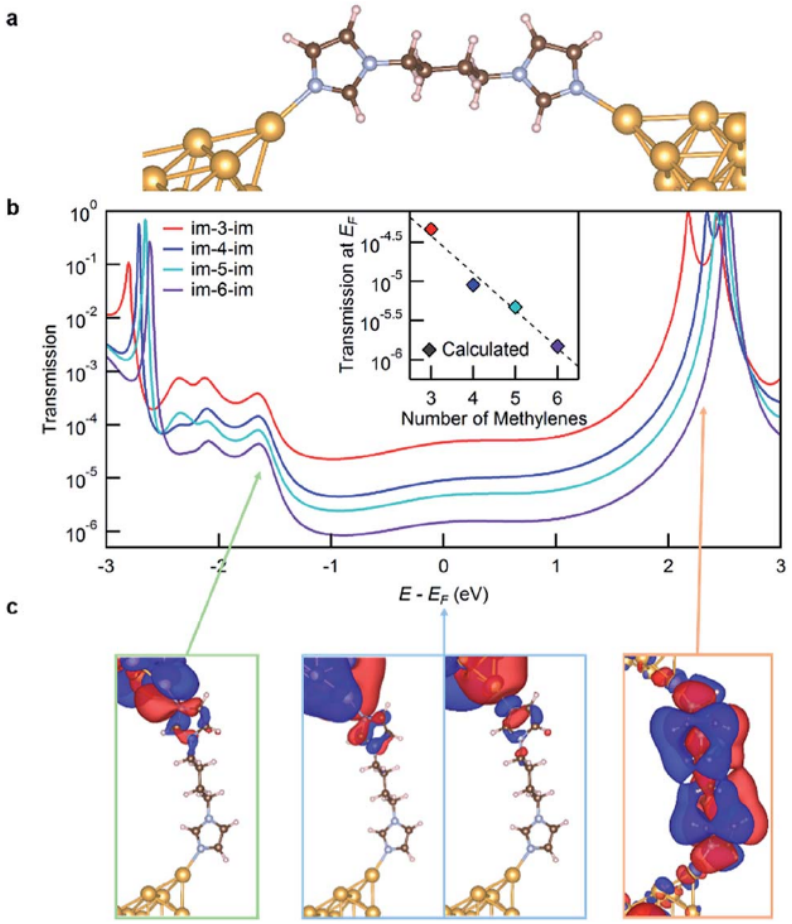

Figure 5.8 – (a) Geometry obtained from DFT calculations and employed for the theoretical transport calculation of the non-self-consistent transmission function for im-4-im junctions. Similar geometries for the series of alkyl chains are used with longer alkyl chain. (b) Transmission function calculated for the series of im-N-im, where $N = 3, 4, 5, 6$. The inset shows the value of the non-self-consistent transmission at Fermi energy plotted against the number of methylene units in the backbone of the alkyl chain. The continuous line together with the linear fit to extract β. (c) Isosurface of the scattering states for im-4-im producing the resonance (gateway state) at ~ -1.6 eV from the Fermi energy (green rectangle), LUMO-based resonance at ~ 2 eV (orange rectangle) as well as the resonances (gateway states) at E_{F} (blue rectangle). From [148] - Published by The Royal Society of Chemistry. Copyright CC BY-NC 3.0.

at $E - E_F = 2.3$ eV we show the resonance produced by the weakly hybridized π-based LUMO orbital (orange frame).

We turn now to the analysis of the "shoulder" peak identified in the conductance histograms at $\sim 10^{-3}G_0$ in Fig. 5.7 (b) for all molecules in the series. Our experimental colleagues suggest that this peak is created by the formation of $\pi - \pi$ stacked dimers, as represented in the geometries from Fig. 5.9 (a) and (b). The dimers can occur thanks to the fact that the pyrrole nitrogen of the imidazole increases the electronic density of the π orbitals of the aromatic ring, thus enhancing the intermolecular $\pi - \pi$ interactions. This is similar to what happens in aniline derivatives with pyrrole-like nitrogens [193].

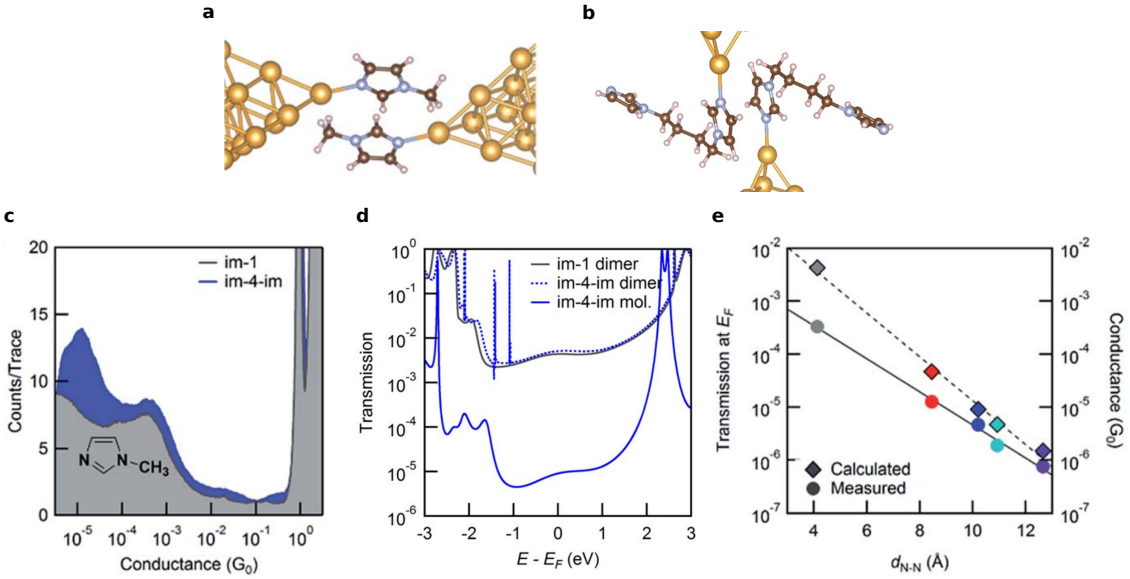

Figure 5.9 – (a) Geometry of the $\pi - \pi$ dimer used in the theoretical calculations of im-1. (b) Model of the im-4 stacked dimer. (c) 1D logarithmically binned conductance histogram of im-1 and im-4-im molecular junctions. The peak at $\sim 10^{-3}G_0$ is attributed in both cases to the formation of the dimer structure. (d) Transmission plot of im-1 (black line) and im-4-im (blue dotted line) molecular junctions. In order to compare the conductance to the imidazole linked alkyl wires, the non-self-consistent transmission plot for im-4-im is also shown (blue solid line). Although the conductance is similar for the two stacked dimers, the non-self-consistent transmission function for the im-4-im dimer presents additional Fano resonances due to the presence of the side alkyl chains. (e) Experimental (red, blue, green and purple diamonds) and theoretical (red, blue, green and purple circles) values for the low-bias conductance (in units of G_0) of the im-N-im junctions as a function of the molecule length. Also shown is the conductance of the im-1 $\pi - \pi$ stack dimer (grey diamond and grey circle). Modified from Fig. 4 (main paper) and Fig. S4 (supplementary information) of Ref. [148] - Published by The Royal Society of Chemistry. Copyright CC BY-NC 3.0.

To corroborate this hypothesis, the single-molecule conductance of a im-1 was measured in the group of L. Venkataraman. This molecule only has an imidazole anchor group binding to the metal electrode and, therefore, the only possibility it has is to form a $\pi - \pi$ stacked dimer with more each imidazole group bound to different contacts. We show the resulting 1D conductance histogram in Fig. 5.9 (c) overlaid to the histogram of im-4-im. The peak at $\sim 10^{-3}G_0$ of the im-4-im junctions overlaps with the peak at $\sim 10^{-3}G_0$ of the im-1 junctions.

In order to give theoretical support to this hypothesis, in collaboration with Latha Venkataraman's group, we have performed *ab initio* quantum transport calculations using Van der Waals interaction at the Tkatchenko and Scheffler level [194]. The relaxed geometry used for the calculations of im-1 is shown in Fig. 5.9 (a). From the DFT calculations, we find that the molecular stack is a stable configuration in which the distance between the imidazole centroids is ~ 3.3Å and that has 0.41 eV of binding energy. As comparison, benzene $\pi - \pi$ stacked dimers have a binding energy of 0.15 eV. The difference in the binding energy is attributed to the chemical nature of the nitrogens in the imidazole. The pyrrole-like nitrogen with an excess of local negative charge is opposed to the pyridine-like nitrogen with excess local positive charge. Therefore, the structure tends to enhance the binding due to electrostatic interactions. The non-self-consistent transmission function for this single-molecule junction is given in 5.9 (d). We find that the transmission function at the Fermi energy is two orders of magnitude larger than for the im-4-im junction, as observed in the experimental results.

The conductance of im-1 (black solid trace) is found to have a similar value to the conductance of im-4-im (blue dotted trace). This results from the fact that the additional alkyl side chains only produce very narrow Fano resonances far from the Fermi energy. Finally, we show in Fig. 5.9 (f) the measured and calculated conductance as a function of the junction length (defined as the distance between the nitrogen atoms of the imidazole linkers that bind to the Au leads) for im-1 and im-N-im. The conductance of the $\pi - \pi$ stacked dimer is found to follow the trend of the conductances of the im-N-im molecules. This suggests that for this type of dimers, as opposed to what is found in other weakly bound stacks [23], the conductance is similar to that of a non-stacked junction of longer length.

5.3.3 Summary of this section

In this section, we have studied how the imidazole molecule can be used as an anchor group in single-molecule junctions made with Au leads. Since this molecule is a precursor of several biologically relevant molecules, this work paves the way to the study of electronic properties of biological systems containing imidazole. Imidazole has been used to bind alkane wires; we have found that the conductance trend as a function of the length of the alkane is consistent with the trend found when alkane is bound to contacts by different anchor groups. Finally, we have also proven that $\pi - \pi$ stacked imidazole dimers are robust functional groups that can bind directly to gold electrodes.

5.4 Metallocene-based linkers in single-molecule junctions

5.4.1 Metallocenes as linkers

Other interesting group of molecules which can act as linkers are metallocenes. Different properties of these organometallic compounds have been already studied in chapters 3 and 4. We briefly remind that they consist of two cyclopentadienyl (Cp) rings (five-member carbon rings) "sandwiching" a metallic atom. Since the ferrocene discovery (where the metal center is iron) seventy years ago [126, 195], many similar organometallic complexes

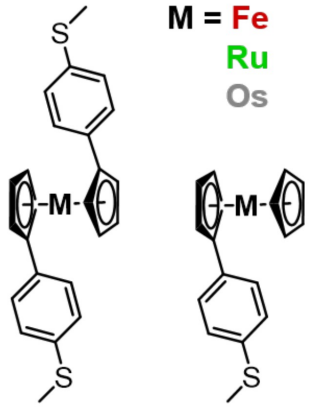

Figure 5.10 – Chemical structure of the metallocenes studied in this section, where M = Fe, Ru, Os corresponds to different metallic centers. (Left) 1,1'-M structure with two phenyl arms, each of them attached to a different Cp ring. (Right) 1-M structure with only one phenyl arm connected to a single Cp ring. Reproduced with permission.

have been synthesized and studied [15, 196, 197], but never, to the best of our knowledge, they have been considered as linker groups in single-molecule electronics. Normally, anchor groups bind to the electrodes using elements from the p-block of the periodic table (N, S or P, for instance). Metallocenes can bind to the gold electrode through the metallic center. This fact opens the possibility of using them to connect (or disconnect) the molecular bridge by changing the oxidation state of the metallic center of metallocene by means of a bias voltage. In other words, for specific values of the bias voltage the molecular bridge is connected to the leads, while for others do not, by using *in situ* reactions [6].

In this part of the chapter, we investigate how metallocenes with different metallic center of group 8 (Fe, Ru, Os) , see Fig. 5.10 bind to the electrodes. We also study how the binding and the transport properties of these molecules change due to the substitution of the "sandwiched" metallic atom. We show that 1-M and 1,1'-M molecular junctions can bind directly through the metal (M = Fe, Ru, Os) atom to the contacts and study by means of *ab initio* calculations, the quantum transport properties of both types of molecular junctions. Our theoretical findings corroborate the experimental results obtained in Latha Venkataraman's group in Columbia University.

The experimental conductance for the metallocene series was measured using the STM-BJ technique (see appendix F). The resulting one-dimensional histograms are shown in Fig. 5.11. In panel (a), we see the histograms corresponding to the 1,1'-M molecular junctions. We observe for all junctions a predominant peak at $\sim 10^{-5}G_0$ and a secondary one at $\sim 10^{-3}G_0$. We also find small differences between the metallocenes: the low-conductance peak for 1,1'-Os is lower in height compared to 1,1'-Fe and 1,1'-Ru, together with a shift to lower conductance values. For the high-conductance "shoulder", we find that the 1,1'-Fe maximum is slightly smaller compared to 1,1'-Ru and 1,1'-Os. A plausible hypothesis proposed by our experimental colleagues for the existence of the secondary peak in the molecular junctions is a direct metal-gold bond. For this reason, in Columbia University the conductance of the series of alternative molecules (1-M) was also measured [see Fig. 5.11 (b)]. We find the conductance for this set of molecules to be $\sim 10^{-3}G_0$; strengthening our hypothesis for direct metal-gold binding. Moreover, this hypothesis is experimentally reinforced by looking at the 2D-conductance histograms, see Fig. G.2 in appendix G, where the corresponding maxima are related to junctions lengths that differ by a factor $2-4$.

6. Private communication from Dr. Michael S. Inkpen.

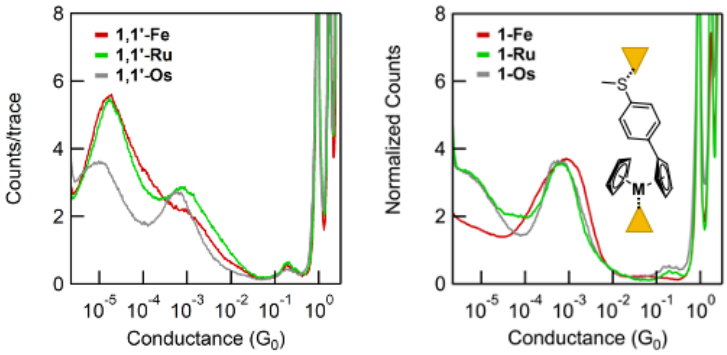

Figure 5.11 – (a) 1D logarithmically binned conductance histograms for metallocene-based $1,1'$-M junctions, where the metal M = Fe (red trace), Ru (green trace), Os (grey trace). In all the three cases the histrogram has two local maxima: a predominant peak at $\sim 10^{-5}G_0$ and a less predominant peak located $\sim 10^{-3}G_0$. (b) 1D logarithmically binned conductance histograms of 1-M junctions with M = Fe (red trace), Ru (green trace), Os (grey trace). The conductance obtained for all 1-M molecules is $\sim 10^{-3}G_0$, similar to the high-conductance maxima for the 1,1'-M junctions in panel (a). Experimental data obtained in Prof. L. Venkataraman's group. Reproduced with permission.

5.4.2 Theoretical analysis of binding and transport properties

In order to provide theoretical support for the proposed hypothesis of direct metal-electrode binding, as well as to understand the low-conductance features of this family of molecules, we perform DFT-based quantum transport calculations (see computational details in appendix G.3.2). We show in Fig. 5.12 (a), the non-self-consistent transmission functions for the 1,1'-M configuration (the inset shows the relaxed geometry for the 1,1'-Fe junction). The transmission of the three molecular species presents sharp anti-resonances close to the Fermi energy, which are responsible of the low conductance features. An in-depth analysis of the origin of these anti-resonances will be made in chapter 4. Despite the fact the theoretical value for the conductance is overestimated roughly by one order of magnitude due to well-known artifacts in the approximations of the exchange-correlation functional [25, 47], the experimental conductance trends are in agreement with our theory calculations $G_{\mathrm{Fe}} \sim G_{\mathrm{Ru}} > G_{\mathrm{Os}}$. In fact, the conductance of 1,1'-Fe and 1,1'-Ru is $\sim 2 \cdot 10^4 G_0$, roughly a factor of two larger than the conductance for Os ($G \sim 1 \cdot 10^{-4}G_0$). The result is quantitatively in agreement with the experimental conductance ratio between $G_{\mathrm{Fe}}/G_{\mathrm{Ru}}$ and G_{Os} for the 1,1'-M configuration.

We analyze now the high-conductance peak at $10^{-3}G_0$ present in all molecular junctions in this series. As we mentioned before, the presence of the peak suggests that 1,1'-M metallocenes bind to the metallic electrode by an additional mechanism that we hypothesize to be direct metal-electrode binding (see inset in the right panel of Fig. 5.11). In order to provide theoretical support for this hypothesis, we calculate the transmission function for a series of 1-M molecular junctions. The results are shown in Fig. 5.12 (b) with examples of relaxed geometries for 1-Fe and 1-Ru given in the inset. Our first observation is that the transmission at Fermi energy reproduces the trend in the conductance obtained in the experiment $G_{\mathrm{Fe}} > G_{\mathrm{Ru}} > G_{\mathrm{Os}}$, although there is a small deviation in the ratio between the conductances of each molecular junction. Our second observation is that there is a discrep-

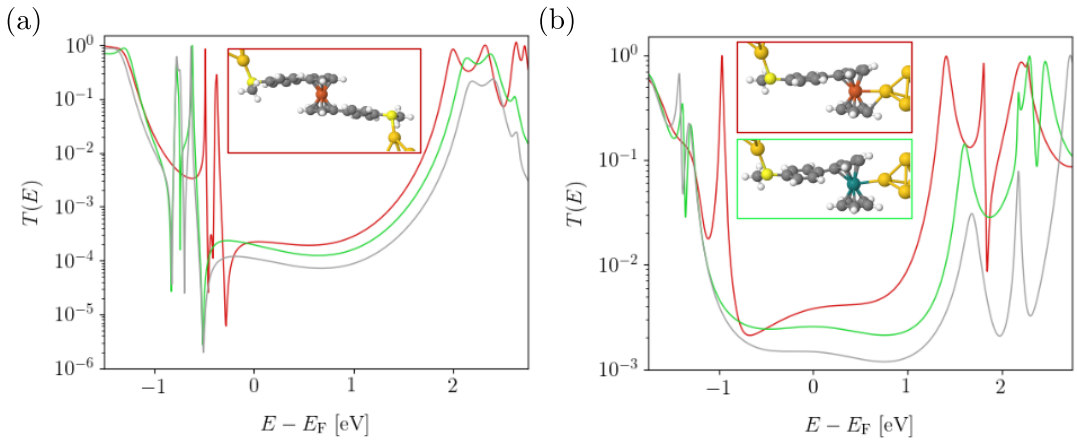

Figure 5.12 – (a) Transmission functions for the 1,1'-M junctions, M = Fe (red), Ru (green), Os (grey). The theoretical conductance trend, obtained from the non-self-consistent transmission at Fermi level for the different metallocene traces, agrees with the experimental conductance trends. Inset: relaxed geometry used for the Fe-1,1' molecular junction.(b) Same as in (a) but for 1-M junctions. Again, the trend that results from the value of the transmission at the Fermi energy for different metals qualitatively reproduces the experimental trend; a larger value of the conductance also supports our interpretation of direct binding between the metal atom and the electrode.

ancy of approximately one order of magnitude between the experimental and theoretical calculations. As before, this is attributed to well-known artifacts in the approximations of the exchange-correlation functional [47, 25]. We also observe that the transmission for 1-Fe system has a larger resonance at $E - E_F = -1$ eV and an anti-resonance at $E - E_F = 1.8$ eV, compared to Ru and Os. Note that the latter present the same features at lower energies. The presence of the stronger resonance can be explained due to a possible overbond of the electrode apex to the Cp rings of the metallocene. This can happen because the pitch is larger in the double decker for Os and Ru (3.64 and 3.65 Å) while smaller for the Fe (3.29 Å).

We note that, in principle, we cannot discard alternative binding geometries where the electrode binds to the Cp ring and not the metal center. In order to explore this possibility, we calculate the non-self-consistent transmission function, as well as the binding energies for the configurations shown in Fig. 5.13 (a) and (b). We observe that, the transmission at E_F is very similar for the three possible geometries considered here (bottom panel). Furthermore, the binding energies for the configurations shown in (a), 1.17 eV, and (b), 1.25 eV, are comparable to the binding energy of the direct binding to the metallic atom 1.22 eV. Because the peak in the one-dimensional histogram in Fig. 5.11 (b) is wide, all the possible binding configurations might be contributing to the high-conductance peak.

Finally, we note that transport calculations alone cannot explain the difference in the height of the conductance peak at $10^{-3}G_0$ between the different metal centers. However, from the chemical point of view, Lewis theory applied to transition metals [198] indicates that for heavy atoms, such as ruthenium and osmium, there is a preference to bind to metallic atoms such as gold and not to carbon. This argument is strengthened by looking at the binding energies for 1-Fe, 1-Ru and 1-Os (1.22 eV, 1.43 eV, 1.57 eV, respectively). Note that if a C-Au bond is produced, the binding energies would not be strongly affected by substituting the metallic center and therefore, we would expect the high-conductance

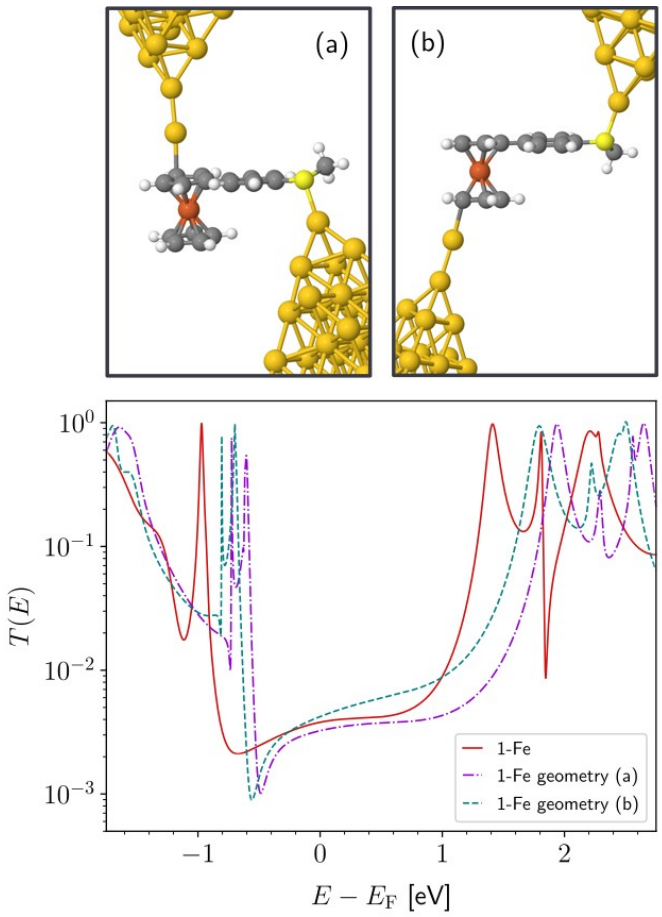

Figure 5.13 – Alternative binding configurations for the 1-Fe molecule connected to Au electrodes. In (a) the electrodes are both connected to the upper part of the molecule while in (b) one electrode is connected to the lower Cp ring, with the second linked to the SMe anchor at the phenyl group. In both cases there is also one additional uncoordinated Au atom in one of the electrodes for stability reasons. Bottom panel: Comparison between the non-self-consistent transmission functions for the alternative geometries in (a), (b) and the transmission from Fig. 5.12.

peak in Fig. 5.12 (a) to be the same for all metals. In addition, the pitch of the double-decker structure for osmocene (3.64 Å) and ruthenocene (3.65 Å) is larger compared to ferrocene (3.29 Å), Therefore, the possibility of bond formation between the metallic center of the metallocene and the gold electrode is larger for osmocene- and ruthenocene-based molecular junctions than for ferrocene which can explain the difference in the height of the high-conductance maxima.

5.4.3 Summary of this section

In this section, we have shown that the metallocene series 1,1'-M, M = Fe, Ru, Os, can bind to gold electrodes either through the two thiol anchor groups or by a direct metal-electrode bond. In the first case, we have demonstrated that the impact of substituting the metallic atom of the 1,1'-M metallocenes on the conductance is relatively small: the

value of the conductance in Fe and Ru is roughly a factor of two larger (and correlated with the larger HOMO-LUMO gap). We have seen that the metallocene can act itself as an anchor group. Although from transport measurements/calculations we cannot discard, in principle, direct bonding to the carbons of the Cp-ring, arguments based on Lewis theory as well as the larger pitch of 1-Ru and 1-Os (compared to 1-Fe) support the direct metal-electrode binding.

Summary and conclusions

This thesis has three parts: one is devoted to spin-orbit (SO) torque, another covers quantum interference (QI) effects and a last one investigates molecular insulators. In the following, we summarize the conclusions from each part.

Spin-orbit torque. An idea underlying molecular spintronics is the manipulation and control of the spin degree of freedom of molecules for technological purposes. This has been typically addressed by applying external magnetic fields. An alternative idea would be exploiting intrinsic spin-orbit (SO) coupling to achieve control of the spin in a single-molecule device by means of SO torque (SOT).

In order to study SOT, in this thesis, we have extended the existing transport code AITRANSS to incorporate SO interaction. In the previous versions of this code, the NEGF was implemented, but SO was not considered. To calculate out-of-equilibrium physical effects, AITRANSS was previously interfaced with FHI-aims to perform self-consistent (SC) calculations. These account for the redistribution of charge in the presence of large bias voltages in non-periodic systems. We have used the AITRANSS module, which incorporates SO coupling, in the SC cycle for the calculation of the SOT. To the best of our knowledge, this is the only code for calculating SOT self-consistently in non-periodic systems.

As a first application of the implementation, we have chosen a vanadocene-based single-molecule junction (whose molecular bridge has vanadium as metallic center). Vanadocene presents an open-shell electronic structure with magnetic moments localized at the vanadium atom. We investigate whether SOT is large enough to manipulate the local magnetic moments. We find, for this system, that the SOT values are of the order of $\delta t_x \sim 10^{-6}$ eV, $\delta t_y \sim 10^{-6}$ eV and $\delta t_z \sim 10^{-8}$ eV. The small values of SOT are due to the small SO interaction of the vanadium atom. Our results are compatible with previous calculations of the SOT based on the Kubo formula in metallic heterostructures.Our investigations suggest that a switching in the spin direction of vanadocene is not possible for bias voltages $|V_{\text{bias}}| \leq 0.3$ V across the junction.

We point out that these results are obtained under the following set of conditions: First, FHI-aims is a collinear DFT code and SO coupling is applied in a post-processing step after the SC solution of the Kohn-Sham equation is obtained. Therefore, our calculation

is not fully SC. Because of the collinearity, we are forced to neglect the off-diagonal blocks and the imaginary part of the coefficients in the density matrix during the SC cycle. Second, the spin is easily rotated so in order to perform right SC calculations we have introduced a local Zeeman field in the vanadium atom inducing a splitting in the energy levels ($\Delta_Z \in [-1.0, 1.0]$ eV). We observe that the value of the torque components is fairly robust with the Zeeman field changing by at most by a factor of $2-3$ when the Zeeman field changes sign. Ideally the Zeeman field has to be zero and due to the difficulty of the calculations this work will be done in future calculations.

Quantum interference. Metallocenes, such as the aforementioned vanadocene, are molecules with a sandwich structure where a metal atom is embedded between two carbon-based rings, *i.e.* an iron atom in the case of ferrocenes. They present a molecular orbital structure with $d-$states localized near the metallic center and ligand $\pi-$systems of the carbon rings (Cp). Also, ferrocenes exhibit a low activation barrier for the rotation of the Cp rings. Therefore, ferrocenes are very interesting candidates to study quantum interference -induced by $d-$orbitals- which intriguingly might be mechanically controllable by using the rotational degree of freedom. This degree of freedom has never been considered as a tuning parameter to control the quantum interference properties of molecules. The idea of this project is to explore this degree of freedom to mechanically control QI in ferrocenes.

We have performed DFT-based transport calculations, employing the NEGF as implemented in AITRANSS and FHI-aims. As it turned out, these calculations were instrumental to interpret experiments in L. Venkataraman's group on ferrocene-based molecular junctions (the manuscript is currently under review in *Nano Letters* [125]).

We observe in the transmission function destructive quantum interference features that strongly affect the electronic transport in the junction. As expected, the destructive quantum interference of the Fano-type appears as a consequence of the hybridization of the d-orbitals at the iron core with the delocalized π-system of the carbon-based ligands. Due to the low energy barrier for conformational changes in the molecule, the hybridization of the orbitals can be modified at low energy cost. If the change alters the nodal structure of the orbitals the interference properties are also altered. When the phase shift difference of the two orbitals at the contact point with the leads is zero, destructive QI arises. The current is suppressed across the junction and, accordingly, the value of the conductance is low. When the phase shift difference is π, the interference is constructive and the conductance increases. These changes in conductance can be revealed by mechanically elongating and compressing the junction due to the deep connection between geometrical properties and interference. We have proposed a model that generalizes previous ideas to understand QI: we put forward a perspective according to which by inspection of any pair of orbitals the type of QI associated with them can be predicted from just a gas phase calculation.

Molecular-insulators. In these close collaborations with experimental groups several side projects arose around the topic of molecular insulators. These are molecules completely the electronic transmission and, therefore, their conductance is smaller than the conductance expected from tunneling through a vacuum layer. Even if carbon-based

wires, such as alkanes, or siloxanes (silicon-based wires with oxygen substituents) were considered good molecular insulators, their conductance was always larger than the associated conductance of the vacuum layer of the same dimension [29]. It has been observed in L. Venkataraman's group that a silicon-based wire in a *cis*-dihedral silicon bond configuration acts as a molecular insulator due to quantum interference effects. These molecules suppress strongly the current and can be used at the nanoscale as insulators [29].

In this thesis, we have looked at the conductance properties of linear silicon-based molecular insulators in a *trans*-configuration. They present both fundamental and technological interest since understanding the charge transport through silicon molecular wires is crucial in the quest of miniaturization of silicon-based electronic components up to the molecular level, as anticipated by Aviram and Ratner [2]. It has been observed in L. Venkataraman's group that the conductance of these wires is larger when attached to silver electrodes by thiol anchors than the conductance when they are attached to gold contacts with the same linker. The trend is reversed to what one would expect based on the work function difference. The opposite trend is observed in equivalent carbon-based wires and in silicon wires when amine anchor groups are employed.

These contraintuitive results are explained by performing DFT-based transport calculations with FHI-aims and AITRANSS. We have shown that the trend reversal is produced by the presence of localized molecular orbitals at the anchor groups that appear close to the Fermi energy (in the case of silver electrodes, thus enhancing the current), the SO coupling and the chemical nature of the metal-anchor bonds thiol-covalent vs. amine-dative (this work has been published in *Angewandte Chemie* [147]).

Applications in bio-nanoelectronics require binding macromolecular insulators to metallic leads [199]. These biochemical complexes are difficult to bind to gold contacts. One possibility to overcome this difficulty is to use precursors, which are naturally part of these molecules, and that also act as anchor groups binding to the electrodes.

For this reason, we focus our attention on imidazole. This is an organic molecule composed of a carbon ring with two nitrogen substituents. It acts as precursor of numerous biochemical compounds, and therefore it is very attractive to use it as anchor group to bind (biochemical) molecules to gold. Open questions are how this binding occurs, how do other molecules bind to imidazole and how does this anchor affect their transport properties.

We have analyzed transport features of imidazole anchoring alkane chains to Au electrodes and to alkane chains (carbon-based molecular insulators). Using FHI-aims and AITRANSS, in collaboration with members of L. Venkataraman group, we have performed part of the transport calculations. We have theoretically shown that in imizadole the simultaneously binding occurs thanks to the different nature (electron-donor and acceptor) of the two nitrogen atoms present in its chemical structure. In addition, two imidazoles can form a $\pi - \pi$ stacked dimer with increased through-space coupling compared to molecular bonding. We show that this dimer can simultaneously bind more than one molecular wire inducing Fano-type resonances in the transmission function (this work has been published in *Chemical Science* [148]).

Interestingly, other molecules that might take the role of linkers in molecular junctions are metallocenes. These can also directly bind to the metallic leads through the metal center. This type of bonds can be found in bulk systems (alloys) but are less common in

single-molecule junctions. Normally, single-molecules are connected to leads by bonding between metal and atom-based groups of species belonging to the p-block of the periodic table, such as N, S or P. It is significantly interesting to extend the available library of contact moieties because the metal-metal bonding offers the possibility of controlling the binding through the oxidation state of the metal in the molecule *in situ*. In other words, the oxidation state of the metallic center in metallocenes is controlled by the bias voltage applied across the junction, binding the molecule to the lead for specific voltages and remaining detached for other values of the bias voltage.

Then, we focus once more our attention on ferrocenes and also on metallocenes with substituted metal atom by ruthenium and osmium. Open questions are how this binding occurs and how the metal substitution affects both binding and transport features.

We have theoretically studied (with FHI-aims and AITRANSS) the transport properties of different substitued metallocenes. We find that heavier metallocenes bind stronger to gold contacts. This results from the larger distance (pitch) between the Cp rings of osmocene and ruthenocene compared to ferrocene. Transport calculations show that the conductance of ferrocene is larger compared to ruthenocene/osmocene due to the smaller HOMO-LUMO gap. These calculations are key to interpret experimental results obtained in L. Venkataraman's group (this manuscript is in preparation).

Outlook

We now discuss, in the following, the possible future directions that our work presented here opens up.

In order to cure the limitations of the density functional theory (DFT) code for the calculation of spin-orbit torque (SOT) (approximations at the level of the density matrix) we plan to interface our transport code with a non-collinear DFT package. Indeed, we collaborate with the group of Dr. Richard Korytár in Charles Prague University to build an interface with the package TURBOMOLE. From a numerical perspective, this new interface would come with two advantages: First, we can test our approximations made for the vanadocene junction against a full self-consistent calculation. Second, we could also investigate other molecules with larger SO interaction. Interesting candidates are other sandwich compounds with heavier metal center. If one sandwich compound is considered, this system is a voltage-controlled (through the SOT) molecular bit. As an application, more than one sandwich molecule can be connected in a chain and we can think of molecular logic gates in which the local magnetic moments can be manipulated by voltage.

In addition, our implementation is ready to include spin-transfer torque (STT) effects, with spin-polarized currents. In this way, we can investigate which mechanism (STT vs SOT) is better suited to produce a switch of the magnetization.

One can think about the possibility of performing SOT calculations for functionalized carbon-based systems. For instance, graphene has attracted a lot of attention for technological applications in spintronic devices. Pristine graphene is well-known for having small SO coupling. Distortions, defects or ad-atoms in graphene flakes and nanoribbons produce a local enhancement of the effective SO coupling [58]. In the case of hydrogenic adsorbates, the enhancement has been attributed to a sp_3 hybridization of the carbon lattice with the hydrogen atom. Also, other adsorbates, like fluorine or metals (such as copper, which also carries intrinsic SO coupling) can induce a local enhancement of the effective SO interaction. If these adsorbates carry local magnetic moments they can be manipulated by means of the SOT when a current is applied. It might be interesting to study SOT for small arrays or islands of atoms which are magnetically active embedded in the graphene flakes. The controlled manipulation of the local magnetic moments by means of SOT could be exploited for the design of memory devices using normal metals as contacts instead of ferromagnetic leads, as reviewed in Ref. [200]. The reading of the memory can be achieved with the same currents used for encoding the information into the local moments but this

time with a ferromagnetic contact.

Also interference effects might be studied in the context of molecular spintronics. The introduction of impurities, both magnetic or non-magnetic (for instance, hydrogenic adsorbates), induces complex interference patterns in graphene nanoribbons and flakes [27]. To the best of our knowledge it is unknown how these patterns affect the local SOT (or STT) or how sensitive they are to the possibly large value of the local currents.

We have planned improvements of the AITRANSS module. From the computational aspects, beyond the OpenMP thread parallelization employed through the module, we plan to incorporate MPI parallelization. This allows for the computation of SOT in supercomputers and computer clusters distributing the tasks in several nodes, while OpenMP restricts the computation to a single node. Depending on the availability of nodes and CPU cores, MPI parallelization may be best suited to improve the computational speed in the self-consistent cycle. In addition, we have taught, together with other current and former members of F. Evers's group, AITRANSS to the experimental groups of L. Venkataraman (Columbia University), M. Kamenetska (Boston University) and O. Tal (Weizmann Institute of Science). These teaching events have made us realize that a more-friendly user interface of the module is desirable. For this reason, the present interface is planned to be improved in the near future.

To conclude this thesis, we just want to state that there is still room for much investigation in molecular (spin/elec)tronics. We hope that, with the results and the theoretical tools developed in this thesis, we are a little bit closer to the ideas that Richard Feynman had in mind when he gave his lecture in the American Physical Society meeting in 1959.

Appendices

Appendix A

Structure of the transport module and computational performance

In this appendix we provide information of the AITRANSS module extension in which spin-orbit (SO) interaction has been included.

A.1 Scheme of the code structure of the AITRANSS module with spin-orbit coupling

In Fig. A.1, we present the general code structure for the module with SO coupling has been included. The light orange modules reconstruct the Kohn-Sham Hamiltonian obtained from density functional theory (DFT). The optional Zeeman term is also introduced in this branch, and employed in chapter 3. The code has two main branches: In light blue, open quantum systems are treated, while in the pink branch isolated systems are considered. In the light branch, the self-energies are estimated. The non-equilibrium density matrix can also be computed (and write into a text file to be read by the DFT code), as well as the magnetization, SO torque and the transmission function. In the pink branch, we can reconstruct a density matrix for an isolated system and write it out into a text file to be read by the DFT code.

A.2 Computational performance of AITRANSS module with spin-orbit coupling

In order to speed up the calculations, we have parallelized the AITRANSS module using OpenMP. We point out that the DFT code in the self-consistent cycle works only with a single thread. All the calculations have been run in the Athene cluster of the University of Regensburg.

In Fig. A.2 we show a sample benchmark of the computational performance (CPU

Threads	Walltime (h:m:s) Σ computation	Walltime (h:m:s) E_{F} computation
8	29 : 57 : 46	09 : 01 : 11
12	23 : 54 : 03	04 : 54 : 34
16	21 : 20 : 00	04 : 23 : 34
24	17 : 47 : 22	03 : 50 : 03

Table A.1 – Benchmark of the walltime needed for the self-consistent calculations shown in Fig. A.2 for a fixed number of threads.

time) against the number of iteration steps for 8, 12, 16 and 24 threads. We consider as geometry the vanadocene-based single-molecule junction from chapter 3 and the parameters indicated in section C.2. Panel (a) displays the CPU time needed for each iteration of the self-consistent loop during the computation of the self-energy. The spikes are produced due to the greedy algorithm employed in the calculation of the self-energy. For more than 100 iterations, the most efficient choice for the algorithm is 12 threads. Panel (b) shows the CPU time needed for the calculation of the chemical potential when $\mathrm{V_{bias}} = 0.3$ V is applied across the junction. We find again that 12 threads is the most sensible choice with respect to the optimization of the CPU time.

In Table A.1 we give a benchmark of the total walltime needed for the calculations in panels (a) and (b) of Fig. A.2. As opposed to Fig. A.2, we see that the wall-time decreases with the number of threads. This suggests that I/O is the bottleneck in the self-consistent loop, as the CPU time of the AITRANSS computational time alone does not always decrease by increasing the number of threads.

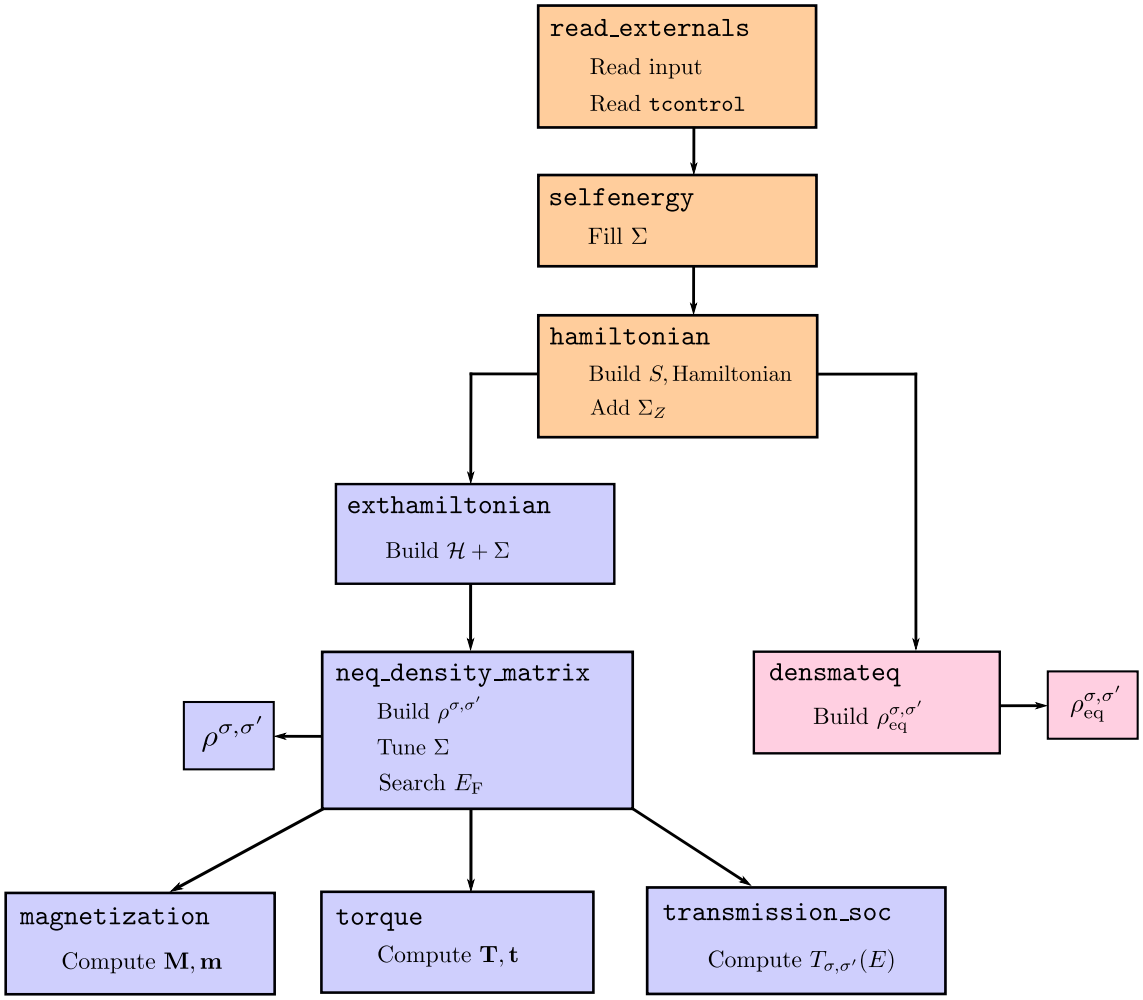

Figure A.1 – Code structure of the AITRANSS extension in which SO has been incorporated. Only the main modules are shown. Modules in light orange reconstruct the Kohn-Sham Hamiltonian. The blue modules are used to calculate non-equilibrium physical quantities (magnetization, torque, transmission and density matrix). The pink modules are employed to obtain the density matrix of the isolated system.

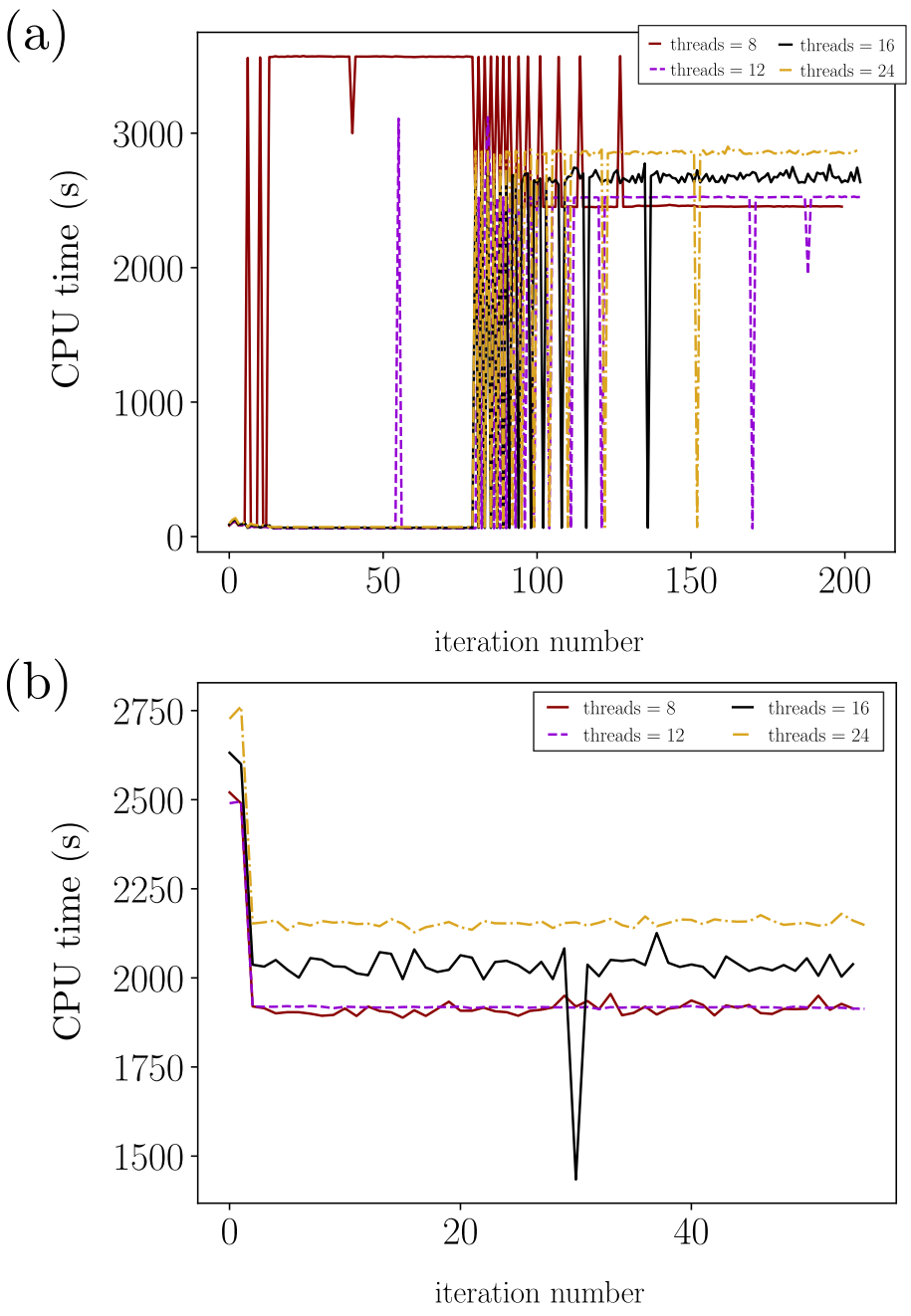

Figure A.2 – CPU time represented against the number of iterations for a fixed number of threads. (a) CPU time needed to compute the real part of the self-energy, using the parameters given in section C.2 and appendix C. The computation has been done for 8, 12, 16 and 24 threads. The spikes in the plot are due to the greedy algorithm employed in the computation of the real part of the self-energy. (b) Sample of CPU time needed to obtain the optimal value of the chemical potential (in this case, for a bias-voltage $V_{bias} = 0.3$ V) considering 8, 12, 16 and 24 threads.

Appendix B

Practical guide for spin-orbit dependent calculations with FHI-aims and AITRANSS

In this appendix, we describe the procedure to perform SOT calculations, following the scheme in Fig. 2.1. In addition to SOT, we also provide the keywords and instructions to perform self-consistent and non-selfconsistent transmission calculations in the presence of SO interaction. The calculations generalize the scheme presented in Refs. [49, 71].

B.1 Step 0: Optimization of the molecular junction geometry

The first step in the calculation is the optimization of the junction geometry. We refer the reader to the manual of FHI-aims for further explanations on how to perform this calculation.

B.2 Step 1: Parametrization of the self-energy

We now specify the keywords needed for the parametrization of the self-energy in the presence of SO interaction. The calculation is controlled by a shell script together with the auxiliary code[1] that transforms the density matrix files from plain text into ELSI-readable format (`a2e_real.x`).

This calculation requires two control files. For the DFT code, we include the standard (mandatory) keywords as described in the manual as well as

```
output aitranss
include_spin_orbit
output soc_eigenvectors 1
```

1. Provided by Victor Wen-zhe Yu from the group of Assoc. Prof. Volker Blum.

```
output soc_aitranss
```

The latter keywords [2] allow for the basis, as well as the real and imaginary parts of the eigenvectors, to be printed in separate plain text files. These files can be directly read by AITRANSS. The output keyword `soc_aitranss` has been incorporated to the DFT code during this PhD work *ex profeso*.

The transport module AITRANSS has been modified to incorporate SO interaction. The compulsory files and basic keywords are the same as for the spinless case (see manual). We only point out here that the basis, overlap and eigenvector files must have the following names:

```
basis-indices.soc.out
omat.aims.soc
soc.mos.dn.im
soc.mos.dn.re
soc.mos.up.im
soc.mos.up.re
```

and must be located in the same folder as the `tcontrol` file. The name of the files are self-explanatory.

The calculation of the self-energy is performed in the transport code. For this purpose, in addition to the compulsory AITRANSS keywords, the following ones need to be included in the `tcontrol` file:

`$ecp off`
`$densmat_cycle on` → flags to start the self-consistent loop
`$densmat` → flags to start the self-consistent loop
    `charge.dens file=dmat`
    `spin.dens file=smat`
`$bias 0.0`
`$dmix` *value* → percentage of mixing parameter for the density matrices
`$efsearch` → flags for searching the chemical potential
    `nelconv` *value*
    `nclstmo` *value*
    `maxiter` *value*
`$densconv` *value* → density convergence criterium
`$ldos off`
`$transmission off`
`$ener undefined`
`$estep undefined`
`$eend undefined`
`$eta 1.0d-10`
`$testing off`
`$expert on` → flag to calculate self-energy and chemical potential
`$fixed_efermi off` → flag to the average chemical potential to float
`$tcontrol_efermi_update off` → flag to update the Fermin in `tcontrol`

2. `soc_eigenvectors` provided by Dr. William P. Huhn from the group of Assoc. Prof. Volker Blum.

`$adjust_rsigma on` → flag to adjust the real part of the self-energy (see, i.e. [71])
    `rfactor` *value*
    `rguess` *value*
    `nelcnv` *value*
    `iterlimit` *value*
`$s1r` *value* → initial guess for the real part of the self-energy
`$s1i` *value* → imaginary part of the self-energy for the outermost layer
`$s2r` *value* → analogue to `s1r`
`$s2i` *value* → analogue to `s1i`
`$s3r` *value* → analogue to `s1r`
`$s3i` *value* → analogue to `s1i`
`$efermi` *value* → initial guess for the Fermi energy

In addition, we have implemented a Zeeman term that can be applied locally to a given element described in the geometry file. This effect can be achieved using the flag `$zeeman element` *value*.

B.3 Step 2: Finite bias calculation

After the parametrization of the real part of the self-energy, we can apply a bias voltage to the system. The calculation requires the files detailed in section B.2 as well as to include the following additional flags in the `tcontrol` file

```
$bias value
$efsearch
    nelconv value
    nclstmo value
    maxiter value
$expert off
$fixed_efermi off
$tcontrol_efermi_update on
$adjust_rsigma off
```

A calculation at zero-bias is first required to fine-tune the chemical potential, then the finite bias calculation proceeds with the flags detailed above.

B.4 Step 3: Spin density, spin-orbit torque, transmission function

After convergence of the self-consistent field cycle from section B.3, we can proceed with post-processing to compute different observables at finite bias employing the AITRANSS package. We remind the reader that, as a general rule, the standard DFT files are required together with the output files from previous steps. The specific flags for each available observable are detailed in the next subsections.

B.4.1 Spin-orbit torque and magnetization

In order to compute the magnetization density and the SOT response for a given voltage, the following non-mandatory keywords must be specified in the `tcontrol` file

```
$densmat_cycle off
$sot_changedens on
$output_sot on
```

Note that, as explained in chapter 2, that to prevent spurious contributions at equilibrium for observables that have non-zero expectation value only due to the response to the bias, we must substract the density matrix at zero bias. For this purpose, the code is prepared to provide as an output the density matrix saved in the files `dens.orth.real` (real part of the matrix elements) and `dens.orth.imag` (imaginary part of the matrix elements). Similarly, the Kohn-Sham Hamiltonian is also stored (in files labeled as `ham.orth.real` and `ham.orth.imag`) once the keywords above are employed. For the finite bias calculation, we use the updated chemical potentials as well as these files of the Hamiltonian and the density matrix.

After the calculation finishes, the following files are generated:

— `magnetization` containing the spin density per atom and spatial direction.

— `sot.local.out` containing the SOT per atom and spatial direction [see Eq. (1.61)].

B.4.2 Transmission function

As detailed in the main text, we can also perform self-consistent transmission function calculations at finite bias in the presence of SO coupling by including the following self-explanatory flags in the `tcontrol` file

```
$densmat_cycle off
$transmission_soc on
$ener value
$estep value
$eend value
```

The result is a plain text file `.dat` with the σ, σ' components of the transmission function as defined in Eq. (1.42).

B.4.3 Current

For a calculation of the electric current at zero-temperature and finite bias V_{bias} using Eq. (1.24), the following keywords are also mandatory:

```
$output_mag_and_trans on
$ener value
$estep value
$eend value
```

where the energy window has to be defined taking into account the chemical potential and the bias voltage.

B.5 Non-self consistent transmission with spin-orbit coupling

As we explained in chapter 2, when the size of the electrodes is large enough, it is possible to perform non-self-consistent calculations at zero-bias without the need to include the real part of the self-energy. We have implemented for this thesis also the possibility to perform this type of one-shot transmission calculations into AITRANSS. For this purpose, first we need to include the non-mandatory keywords in the DFT control as detailed in section B.2. Second, in the AITRANSS `tcontrol` file we must have the mandatory keywords (see AITRANSS manual) as well as the following input files:

```
$basis file=basis-indices.soc.out
$read_omat file=omat.aims.soc
$scfmo file=mos.aims
$self_energy file=self.energy.in
```

At the time of writing this manual, only an all-electron calculation of the transmission function is available and we must also include the keyword `$ecp off`.

Appendix C

Sample input files and parameters for spin-orbit torque calculations

In this appendix, we provide additional parameters not specified through chapter 2 and chapter 3.

C.1 Parameters for figures in chapter 2

For Figs. 2.4 and 2.5, we employ the following `tcontrol` file:

```
$aims_input on
$coord file=geometry.in
$natoms 42
$basis file=basis-indices.soc.out
$read_omat file=omat.aims.soc
$scfmo file=mos.aims
$nsaos 1440
$ecp off
$lsurc 16
$lsurx 18
$lsury 21
$rsurc 5
$rsurx 7
$rsury 10
$nlayers 2
$densmat_cycle on
$densmat
    charge.dens file=dmat
    spin.dens file=smat
$nelectr 1820
```

```
$bias 0.0
$dmix 0.01
$efsearch
   nelconv 1.0d-7
   nclstmo 2
   maxiter 15
$densconv 3.0d-4
$output_charges on
$ldos off
$transmission off
$ener undefined
$estep undefined
$eend undefined
$output file=TE.dat
$eta 1.0d-10
$testing off
$expert on
$fixed_efermi off
$tcontrol_efermi_update off
$self_energy file=self.energy.in
$adjust_rsigma on
   rfactor 0.90
   rguess 0.15
   nelcnv 0.10D-04
   iterlimit 60
$s1r 0.059708250065321044620
$s1i 0.050000000000000002776
$s2r 0.029854125032660522310
$s2i 0.025000000000000001388
$efermi -0.17455929564032102
$end
```

For Fig. 2.7, the following DFT parameters have been used:

```
sc_iter_limit 700
xc pbe
charge 0.0
spin none
relativistic atomic_zora scalar
occupation_type gaussian 0.1
mixer pulay
n_max_pulay 10
charge_mix_param 0.2
density_update_method density_matrix
sc_accuracy_rho 1E-6
sc_accuracy_eev 1E-4
sc_accuracy_etot 1E-7
```

For Fig. 2.8, the following parameters were employed:

DFT parameters:

```
sc_iter_limit 1
postprocess_anyway .true.
elsi_restart read
xc pbe
charge 0.0
spin collinear
default_initial_moment 0.0
relativistic atomic_zora scalar
occupation_type gaussian 0.0001
charge_mix_param 0.01
density_update_method density_matrix
sc_accuracy_rho 1E-6
sc_accuracy_eev 1E-4
sc_accuracy_etot 1E-7
output aitranss
```

The active part when the self-consistent SOC part is included needs:

```
include_spin_orbit
output soc_eigenvectors 1
output soc_aitranss
```

The following parameters are needed in the transport part for the calculations that include a real part of the self-energy, as well as for the non-equilibrium calculation finite bias. In the non self-consistent calculation, the values of the imaginary part were changed accordingly. We employ the corresponding flags in the `tcontrol` for each case, as indicated in appendix B:

```
$dmix 0.05
$efsearch
nelconv 1.0d-7
nclstmo 2
maxiter 60
$densconv 3.0d-7
$eta 1.0d-10
$adjust_rsigma off
    rfactor 0.90
    rguess 0.15
    nelcnv 0.10D-05
    iterlimit 60
$s1r -0.013903905359006870496
$s1i 0.010000000000000000208
```

```
$efermi -0.161662995638
```

C.2 Parameters for figures in chapter 3

In the following we indicate the parameters employed for the calculations of the magnetization and the SOT in chapter 3.

Parameters needed for the calculation of the self-energy:

DFT parameters:

```
sc_iter_limit 1
postprocess_anyway .true.
elsi_restart read
xc pbe
charge 0.0
spin collinear
default_initial_moment 0.0
relativistic atomic_zora scalar
occupation_type gaussian 0.0001
mixer linear
charge_mix_param 0.01
density_update_method density_matrix
sc_accuracy_rho 1E-6
sc_accuracy_eev 1E-4
sc_accuracy_etot 1E-7
output aitranss
include_spin_orbit
output soc_eigenvectors 1
output soc_aitranss
```

`tcontrol` file for the AITRANSS module

AITRANSS parameters:

```
$aims_input on
$coord file=geometry.in
$natoms 47
$basis file=basis-indices.soc.out
$read_omat file=omat.aims.soc
$scfmo file=mos.aims
$nsaos 1882
$ecp off
$lsurc 44
$lsurx 47
$lsury 42
$rsurc 6
$rsurx 8
```

```
$rsury 11
$nlayers 1
$densmat_cycle on
$densmat
charge.dens file=dmat
spin.dens file=smat
$nelectr 747
$bias 0.0
$dmix 0.05
$efsearch
nelconv 1.0d-7
nclstmo 2
maxiter 60
$densconv 3.0d-6 (maximal value to obtain SOT)
$eta 1.0d-10
$testing off
$expert on
$adjust_rsigma on
    rfactor 0.90
    rguess 0.15
    nelcnv 0.10D-04
    iterlimit 60
$output_charges on
$ldos off
$transmission off
$ener undefined
$estep undefined
$eend undefined
$output file=TE.dat
$zeeman v 0.001837466D+00 (sample value for the Zeeman term)
$s1r 0.04998462981604150784
$s1i 0.050000000000000000021
$efermi -0.135237500000 (Guess for the calculation of the chemical potential)
```

Appendix D

Additional calculation details for ferrocene-based molecular junctions

A part of the material covered in this appendix can be found in the preprint:

M. Camarasa–Gómez[†], D. Hernangómez–Pérez[†], M. S. Inkpen, G. Lovat, E–Dean Fung, X. Roy, L. Venkataraman, and F. Evers, *Mechanically-tunable quantum interference in ferrocene-based molecular junctions*, chemRxiv.12252059.v1, 2020. [†: equally contributing authors]. Ref. [125]. Adapted with permission from *Nano Letters*, submitted for publication. Unpublished work copyright 2020 American Chemical Society.

In this appendix we provide additional ab initio details to reproduce and explain the results shown in chapter 4.

D.1 Computational details for *ab initio* calculations

Our *ab initio* calculations are carried out with density functional theory as implemented in FHI-aims [34]. We consider the non-empirical generalized gradient-corrected approximation (PBE) for the exchange-correlation functional [42]. We also incorporate scalar relativistic corrections to the kinetic energy at the level of the atomic zeroth-order regular approximation (ZORA) [201]. The Kohn-Sham orbitals were represented using an optimized all-electron numeric atom-centered basis "tight" computational settings for the molecule and "light" for the gold atoms of the contacts). The convergence criteria used in the density functional theory self-consistent cycle for the difference in the particle density are 10^{-5} electrons/Å^3, for total energy 10^{-6} eV and 10^{-4} eV, for the sum of Kohn-Sham eigenvalues.

The relaxed structures for the molecular junctions were obtained using the a two-step procedure: First, the position of the atoms of the molecule and the tip of the contact were optimized using the Broyden-Fletcher-Shanno-Goldfarb algorithm [34]. The pyramidal gold clusters used for this geometry optimization contain up to 11 gold atoms per pyramid. We also fix the S-Me dihedral angle so that the methyl group lies and the functionalized phenyl rings are in the same plane. Second, we fix the molecular and tip geometries and add layers of gold atoms (up to 55 atoms per gold cluster) to the most external planes of

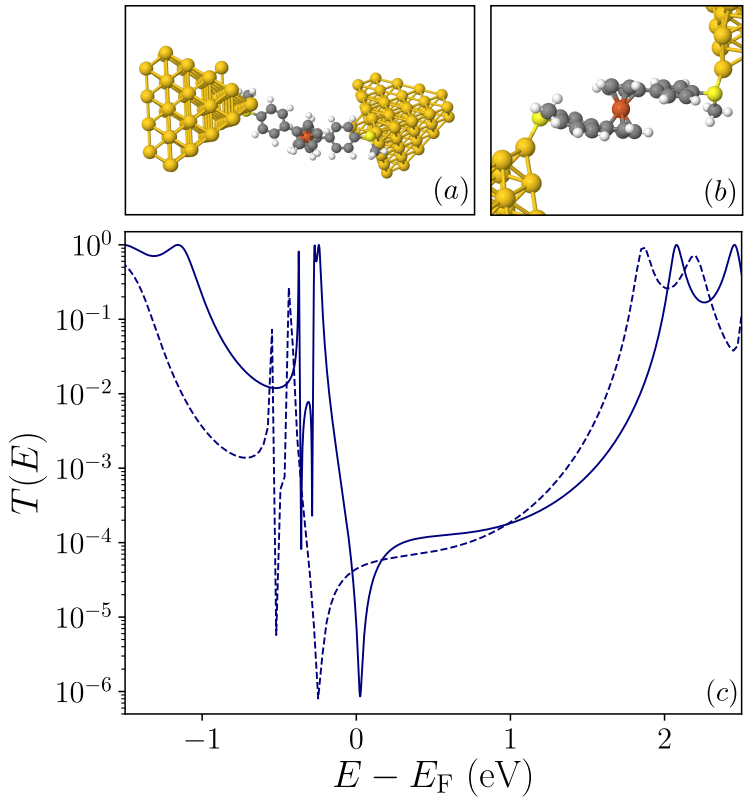

Figure D.1 – (a) Top view of the 1,1'-Fe optimized geometry. (b) Side view of the 1,1'-Fe optimized geometry. Phenyl arms here are not constrained to the plane of the Cp π-system. Anchor groups SMe are neither constrained to the aforementioned plane. (c) Comparison between transmission curves obtained with geometries in (a) (solid blue line) and (b) (dashed blue line). Both transmissions correspond to the angle shown in (a). The orientation of the dihedral angle determine by the anchor group and the Au tip does not change qualitatively the transmission. It shifts the position of the resonances and antiresonances by 250 meV away with respect to the Fermi energy.

the electrode tips. This is done in order to ensure the screening of the excess charge in the transmission function calculations. We considered that the geometries were structurally relaxed when the force component per atom is below the value of 10^{-2} eV/Å.

The transmission function is computed using the non-equilibrium Green's function formalism (NEGF) as implemented in AITRANSS [26, 49]. The self-energy of the reservoirs was parametrized by the energy-independent spatially local function, $\Sigma(\mathbf{r}, \mathbf{r}') = i\eta(\mathbf{r})\delta(\mathbf{r} - \mathbf{r}')$ with non-zero values only in the subspace associated to the outermost layers of the finite cluster. The absorption rate, $\eta(\mathbf{r})$, is chosen to ensure that the electronic transmission does not change under small variations of $\eta(\mathbf{r})$.

D.2 Impact on transmission of the functionalized linker rotations

In section 4.2.2 we have studied the evolution of the transmission under ring rotation under the constraint that the Cp ring, the functionalized linker and the anchor group all

lie in the same plane. Here, the impact of removing this constraint is explored. To that purpose, the following DFT-NEGF calculation is performed: First, the phenyl linkers and the SMe anchor group are left unconstrained and a geometry optimization of the model junction following section D.1 is carried out. The resulting geometry is shown in Fig. D.1 (a), (b). In a second step, the transmission function is computed. We show the results in Fig. D.1 (c) (dashed blue trace). For comparison, the transmission function for the constrained 1,1'-Fe model junction with the same rotation angle φ, (solid blue curve) is shown. We find that changes in the dihedral angle between the phenyl ring and the SMe anchor group do not alter qualitatively the shape of the transmission curve. We observe a rigid shift of the resonances by 250 meV with respect to the Fermi energy, and a decrease in the value of the transmission at the resonances produced by the localized orbitals (HOMO−2 and HOMO−1). However, the interference properties remain unchanged and hence the constraint used does not alter the conclusions presented regarding interference features of ferrocene-based molecular junctions.

D.3 Isosurface plots of relevant gas-phase orbitals

We show in Fig. D.2 the Kohn-Sham states where the rotation angle is such that there is an energy barrier in the energy landscape associated to the "scissor-mode".

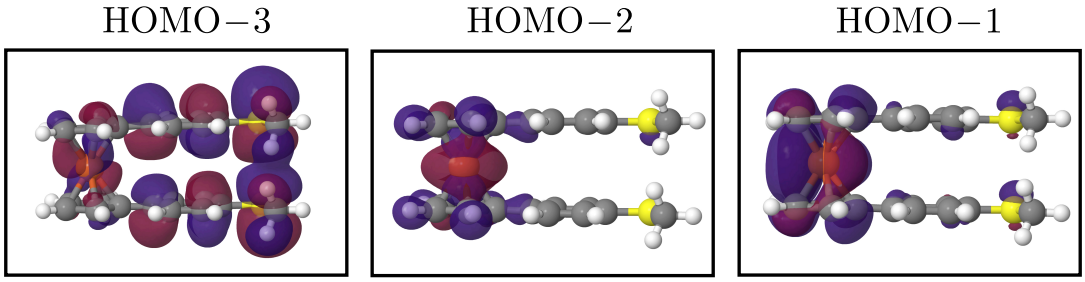

Figure D.2 – HOMO−3, HOMO−2 and HOMO−1 of gas-phase 1,1'-Fe for the rotation angle $\varphi \simeq 5\pi/6$. The distance between SMe-SMe is minimal. HOMO−3 shows strong overlap between the anchor groups and the phenyl arms. Reprinted with permission from [125].

In Fig. D.3 we display the relevant orbitals (in gas-phase) used to obtain the phase shift which enters into the three-level model. This phase-shift directly affects the presence/absence of DQI. Therefore, as we mentioned in chapter 4, we only need to analyze the gas-phase Kohn-Sham states to determine what type of quantum interference occurs, without performing a transport calculation.

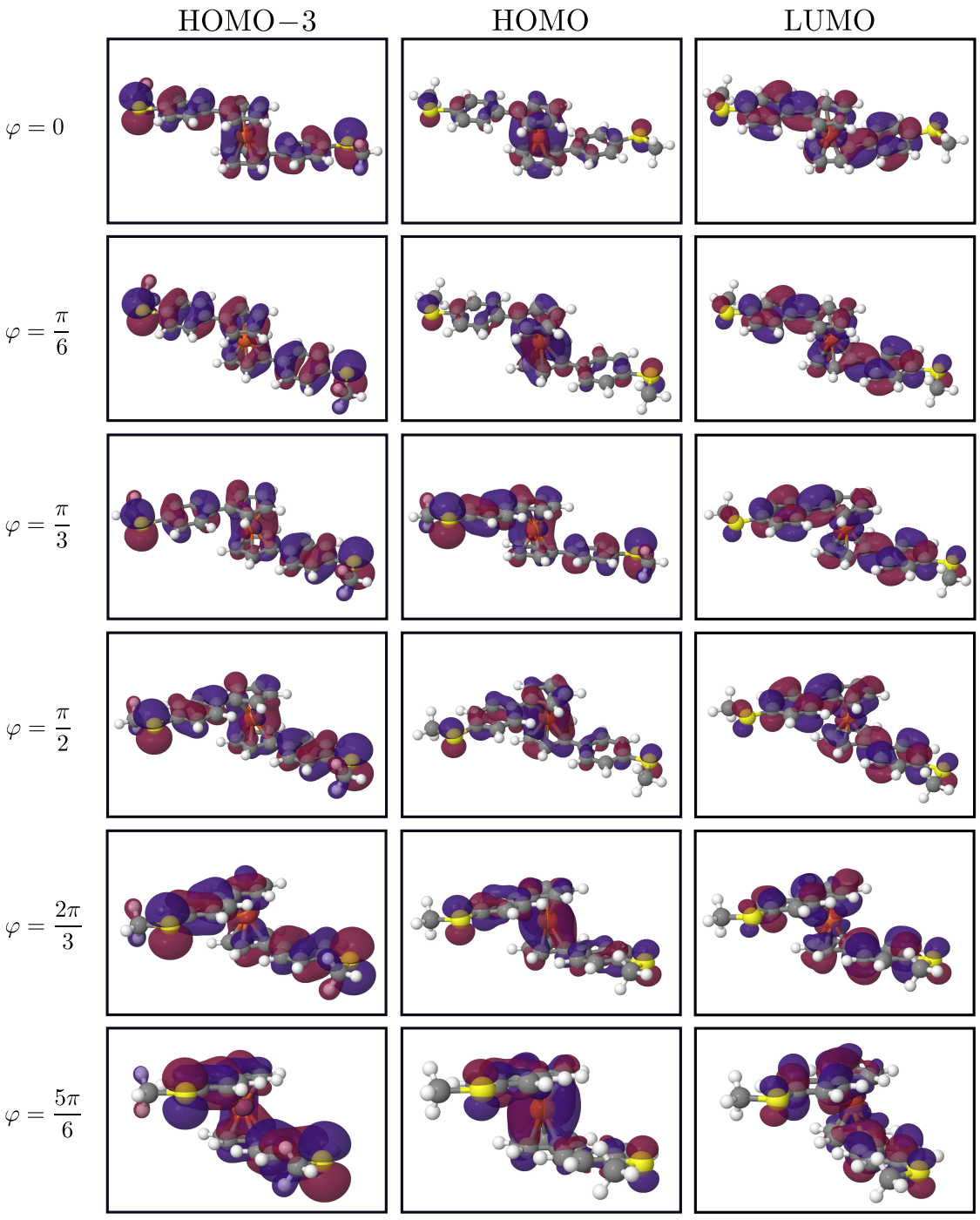

Figure D.3 – Isosurface plots of HOMO−3, HOMO and LUMO orbitals of the gas-phase 1,1'-Fe for several rotation angles φ. The phase shift at the linker groups is incorporated as parameter in the effective model in chapter 4. Adapted with permission from [125].

D.4 Model parametrization

Param. \ φ	$\pi/3$	$\pi/2$	$2\pi/3$
$E_{\text{HOMO-3}}$ [eV]	-5.971	-6.155	-5.927
E_{HOMO} [eV]	-5.033	-5.035	-5.094
E_{LUMO} [eV]	-2.763	-2.734	-2.685
E_{F} [eV]	-4.690	-4.692	-4.622
γ_{HOMO} [eV]	0.012	0.014	0.015
γ_{LUMO} [eV]	0.033	0.035	0.029

Table D.1 – Numerical data obtained from the *ab initio* transport calculation and employed in the effective three-level model for the plots in Fig. 4.9.

Appendix E

Quantum interference in ferrocene molecular junctions

In this appendix we study the quantum transport properties of ferrocene single-molecule junctions. We show that mechanically tunable quantum interference is already inherent to ferrocene moieties due to the hybridization of the d-states of the iron atom with the π-system of the Cp rings of the molecule in a similar manner as discussed in chapter 4 for 1,1'-Fe.

E.1 Energetics of ring rotations of gas-phase SMe-Fe

As mentioned in section 4.2.2, metallocenes possesses a soft mechanical degree of freedom ("scissor mode") with low conformational energy cost. We explore the energy landscape of this degree of freedom in SMe-Fe isolated molecules. Our results are summarized in Fig. E.1: local maxima correspond to staggered configurations; the local minima to eclipsed configurations. The energy barrier between different eclipsed configurations depends on the rotation angle, with typical value of $\Delta \lesssim 20\,\text{meV}$. This barrier is $\sim 30\%$ lower compared to 1,1'-Fe. Furthermore, compared to the energy landscape of isolated 1,1'-Fe, the impact of the SMe linkers here seems to be larger. Indeed, the energy landscape is distorted enough so that the global energy minimum occurs for a eclipsed conformation in which SMe linkers are not inversion-symmetric. Finally, as in 1,1'-Fe, there is still a large energy barrier produced by the Coulomb interaction between the two thiol anchor groups ($\Delta \simeq 180.0\,\text{meV}$), which can be understood as a consequence of repulsion between lone electron pairs from the SMe anchor groups.

E.2 Conductance control by ring rotation

In the main text, we have presented a theoretical study of transport properties of single-molecule metallocene molecular junctions (1,1'-Fe and 1,3-Fe). Fundamental principles behind the transmission characteristics are expected to be universal for all metallocene

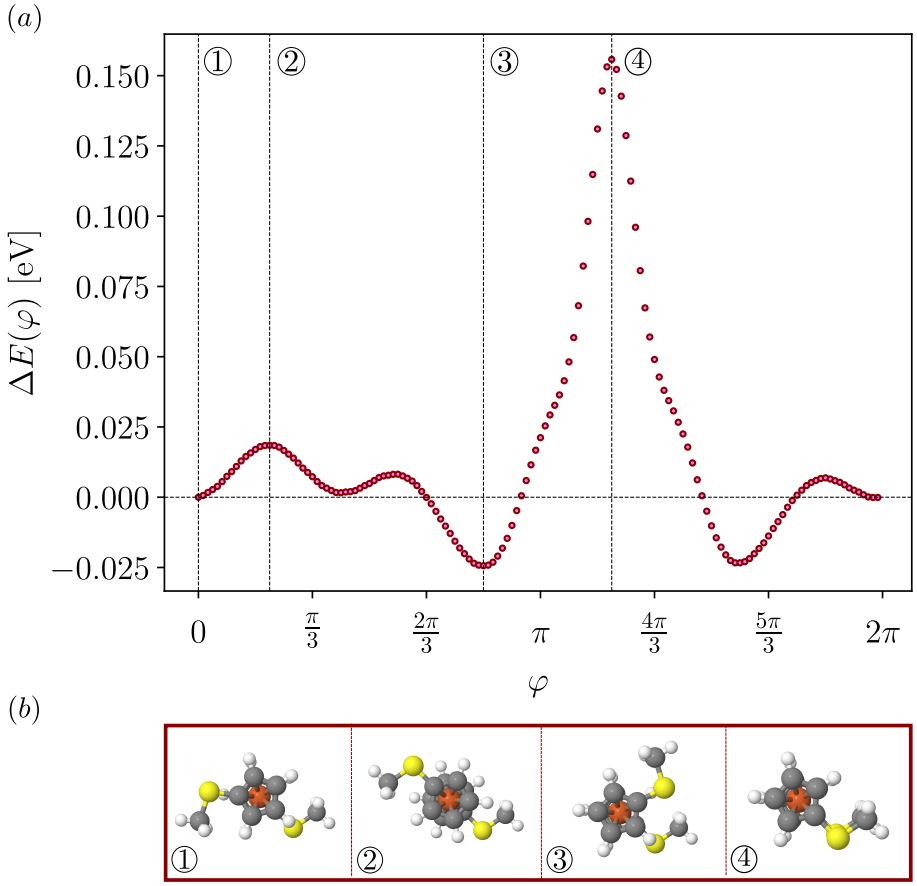

Figure E.1 – (a) Energy landscape of the SMe-Fe molecule due to rotation of the Cp rings with the "scissor mode" explained in Chapter 4. The rotation energies are normalized with respect to the total energy of the relaxed gas-phase SMe-Fe molecule. (b) Selection of the geometries corresponding to the energies marked in (a) with dashed line. ① and ③ are in the so-called eclipsed configuration, while ② represents a staggered conformation. ④ points to the situation in which the distance SMe-SMe is minimal. Similar to what has been presented in chapter 4, the distance minimization between the anchor groups induces a large energy barrier of $\Delta_{3\to4} \simeq 180.0\,\text{meV}$ due to lone electron pair repulsion. Transitions between eclipsed and staggered configurations (from ① to ②) can be produced at room temperature since $\Delta_{1\to2} \simeq 18.5\,\text{meV}$.

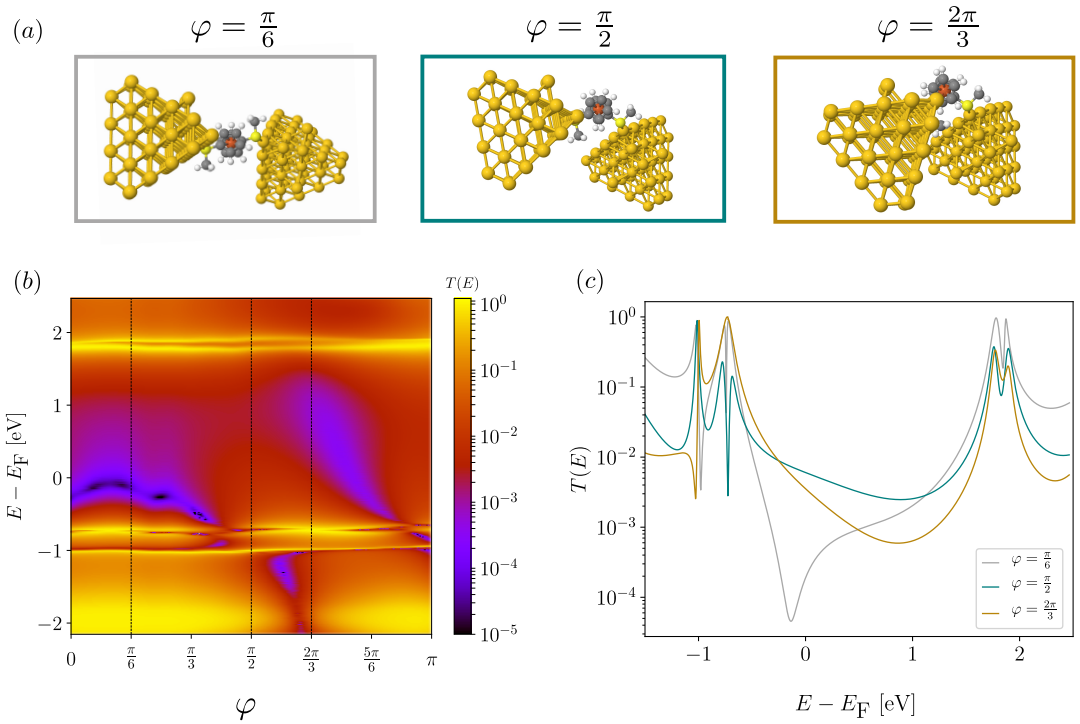

Figure E.2 – (a) Selection of geometries showing the "scissor mode" rotation for SMe-Fe. $\varphi = 0$ corresponds to the optimized geometry of the molecular junction given by DFT. (b) Two-dimensional transmission plot of SMe-Fe. The yellow traces correspond to resonances produced by orbitals which can be identified in single-molecule in gas-phase. The purple regions correspond to areas where the transmission is strongly suppressed. As it happens for 1,1'-Fe (see chapter 4) the origin of both regions is different. The sharp purple area is due to DQI, while the broader purple areas are due to the tunneling between the linker groups SMe. (c) Selection of transmission curves corresponding to the geometries in (a). These curves are marked in (b) by black vertical dashed lines.

species with a single central-unit because transport properties depend on the *d*-orbital coupling to the Cp π-system already present there. To prove this, we have calculated the *ab initio*-based transmission characteristics of SMe-Fe for different rotation angles, φ, between the two Cp rings. Our results are shown in Fig. E.2, a figure analogous to Fig. 4.5 in chapter 4. The phenomenology observed in Fig. E.2 is the same to that already described for 1,1'-Fe: broad regions of strongly suppressed transmission due to quantum interference appear for certain rotation angles together with sharp features corresponding to localized Fano-type resonances. Observe that compared to Fig. 4.5 (a), the antiresonances produced by the quantum interferences are not as deep, presumably due of the smaller size of the molecular junction.

E.3 Impact of the anchor group in the quantum interference

We now investigate the role in the transport properties of the anchor group. To that purpose, we compare the transmission functions of two ferrocene-based molecular junctions with (i) SMe and (ii) NH_2 anchors. The latter, has recently been studied both

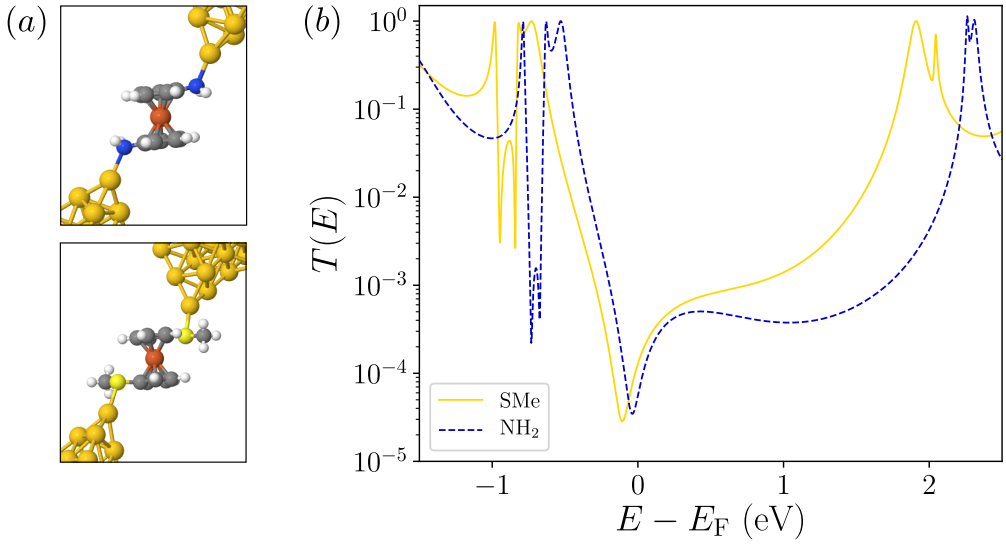

Figure E.3 – (a) Optimized molecular geometries for NH_2-Fe (top) and SMe-Fe junctions made of Au. (b) Transmission curves for the geometries in (a). The change in the anchor group has a reduced impact in the transmission characteristics, except for small shifts on the molecular energy levels. Therefore, we expect similar transmission maps for NH_2-Fe, as those shown in Fig. E.2.

experimentally and theoretically [140]. These previous DFT-based calculations have suggested substantial sensitivity of the transmission to the binding geometry but no signature of quantum interference. In Fig. E.3 panel (a), the optimized junction geometries (left, SMe-Fe; right, NH_2-Fe) are shown. We show in panel (b) the transmission characteristics for both molecular junctions. As expected, we obtain a clear antiresonance dip consequence of DQI.

Appendix F

The scanning tunneling microscope-based break junction technique

In this appendix we give a brief introduction to how measurements of the conductance are obtained with the scanning tunneling microscope-based break junction method. This technique has been employed to obtained the experimental data shown in this thesis in the group of L. Venkataraman.

In this thesis, the scanning tunneling microscope-based break junction (STM-BJ) method [7] has been the experimental method employed to make the molecular junctions and obtain the conductance measurements. We briefly introduce here the basic mechanism of this method. An ensemble of molecules with anchor groups (linkers), one of which will form the junction bridge, are put in a solution that is dropped onto the substrate (metallic layer) of the STM. The tip of the cantilever approaches the substrate and smashes the appex onto the substrate. Only afterwards it retracts until it forms a point contact characterized by a conductance G_0, where $G_0 = 2e^2/h$ is the quantum of conductance. After that, the tip continues to be retracted and, hopefully, one of the molecules in the solution will bridge the broken point contact to form a junction. A scheme of how this technique works is shown in Fig. F.1. The probabilistic nature of the junction formation, as well as the fluctuating geometries of the molecules bridging the gap from one sample to another, requires a statistical analysis to extract values for the conductance of the molecular junction. Therefore, typically 1D histograms (see Fig. F.1) are recorded with the maxima associated to the most probable (optimal) molecular configurations. More ellaborated 2D-conductance histograms [32] can be obtained by combining the data from the 1D histogram (counts/conductance) with the electrode-electrode displacement recorded in the experiment to obtain information about the length of the molecular bridge.

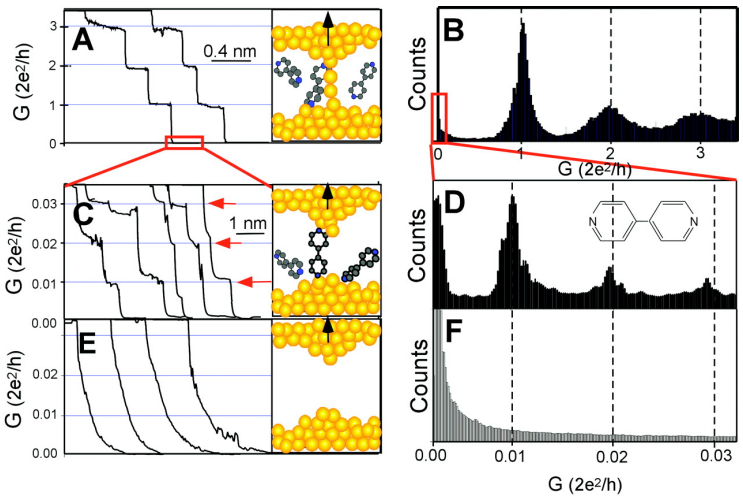

Figure F.1 – (a), (c) and (e) Conductance steps arising from the pull-up mechanism of the STM tip while forming the molecular junction with bipyridine molecule. Each panel corresponds with the formation stage indicated in the inset. (b), (d), (f) 1D-histograms of counts recorded for each process of the molecular junction formation. From [7]. Reprinted with permission from AAAS.

Appendix G

Theoretical calculation details for silane, imidazole and metallocene-based molecular junctions

A part of the material covered in this appendix has been published in:

H. Li[†], T. A. Su[†], M. Camarasa–Gómez[†], D. Hernangómez–Pérez, S. E. Henn, V. Pokorný, C. D. Caniglia, M. S. Inkpen, R. Korytár, M. L. Steigerwald, C. Nuckolls, F. Evers, and L. Venkataraman, *Silver makes better electrical contacts to thiol-terminated silanes than gold*, Angew. Chem. Int. Ed. **56**, 14145 (2017) [[†]: equally contributing authors]. Copyright © 2017 Wiley-VCH Verlag GmbH & Co. KGaA, Weinheim. The material is reused with permission (Ref. [147], covered in Sec. G.1).

T. Fu, S. Smith, M. Camarasa–Gómez, X. Yu, J. Xue, C. Nuckolls, F. Evers, L. Venkataraman, and S. Wei *Enhanced coupling through π-stacking in imidazole-based molecular junctions*, Chem. Sci. **10**, 9998-10002 (2019) - Published by The Royal Society of Chemistry. Copyright CC BY-NC 3.0 (Ref. [147], covered in Sec. G.2).

The appendix also contains unpublished material of the manuscript in preparation:

M. S. Inkpen, G. Lovat, M. Camarasa–Gómez, D. Hernangómez–Pérez, F. Evers, X. Roy, and L. Venkataraman, *Metallocene-electrode contacts in single-molecule junctions* (Ref. [149], covered in Sec. G.3).

In this appendix we provide the technical computational details for the results shown in chapter 5.

G.1 Silane-based molecular junctions

G.1.1 Computational details

Our DFT-based quantum transport calculations are performed using the DFT implementation of FHI-aims [34]. We use an all-electron localized basis set (tier1 - "light" settings, which are equivalent to double-ζ quality) with convergence criteria for the difference in the ground state total energy (10^{-6} eV), particle density ($10^{-5}/\text{Å}^3$) and forces

(10^{-4} eV/Å). As exchange-correlation functional, we employ PBE [42] and include (i) scalar relativistic corrections to the kinetic energy at the ZORA (zeroth order regular approximation) level and (ii) spectral effects of SO interaction included non-self-consistently [55]. In order to obtain the optimized geometries for the transport calculations, we first find the geometry of the molecular wire from a gas-phase relaxation. Then, we simultaneously optimize the position of the tip of the electrodes (up to 11 atoms) and the molecular atoms. In every geometry optimization we use the enhanced Broyden-Fletcher-Shanno-Goldfarb algorithm, until the residual forces per atom are below the threshold value of 10^{-2} eV/Å. Afterwards, we fix the resultant geometry and new layers are added to the external planes of the electrodes to ensure the proper screening of the excess charge in the transport calculations. The electrodes contain 37 atoms and are cut from a (111) face-centered crystal with interatomic distance of 2.88 Å (for Au) and 2.89 Å (for Ag). Transport calculations are performed non-selfconsistently with the package AITRANSS [26, 49], which implements the standard non-equilibrium Green's function method as detailed in section 1.2.

G.1.2 Relevant scattering states involved in charge transport

We show in this section the isosurface plots of the scattering states producing the relevant transport resonances in the transmission plots from Fig. 5.3. We depict the HOMO and LUMO-based orbitals for Au and Ag contacts, both with thiol and amine linkers.

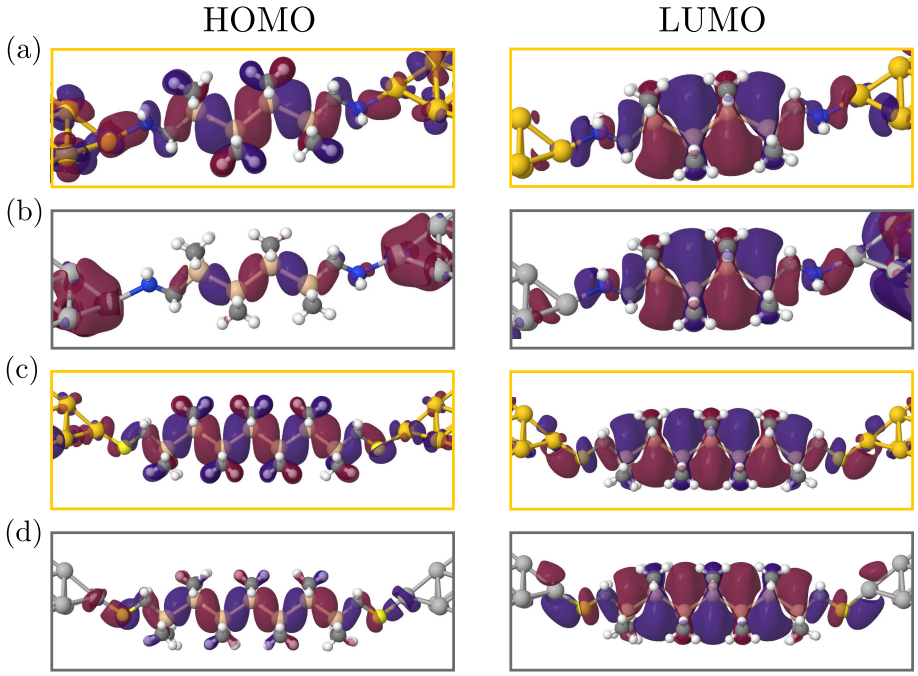

Figure G.1 – (a) Molecular orbitals producing HOMO and LUMO resonances for the molecular junction with NH_2-Si_4-NH_2 and Au contacts. (b) Molecular orbitals producing HOMO and LUMO resonances for the molecular junction with NH_2-Si_4-NH_2 and Ag contacts. (c) Molecular orbitals producing HOMO and LUMO resonances for the molecular junction with SH-Si_7-SH and Au contacts. (d) Molecular orbitals producing HOMO and LUMO resonances for the molecular junction with SH-Si_7-SH and Ag contacts.

G.2 Imidazole-based molecular junctions

G.2.1 Computational details

Our DFT calculations shown in section 5.3 use the Kohn-Sham formulation implemented in the package FHI-aims [34, 202]. The convergence criteria used were 10^{-6} eV for the difference in the ground state total energy, 10^{-5} electrons/Å^3 for the particle density, 10^{-3} eV for the sum of the eigenenergies and 10^{-2} eV/Å for the residual force per atom and direction. The exchange-correlation functional employed was PBE [42] and the transmission function was calculated using non equilibrium Green's function technique as implemented in AITRANSS [26, 49] 1.2. The electrodes of the molecular junction were modeled by pyramidal clusters of 55 atoms, with closest interatomic distance of 2.88 Å and cut from a face-centered crystal grown in the (111) direction. For the DFT calculations we used the FHI-aims "light" quality of the basis set (roughly equivalent to double-ζ quality). To determine if this basis set quality was enough, we checked for the im-4-im and im-1 dimer junctions that the transmissions functions were unaffected by using the FHI-aims "tight" settings on the lighter atoms (H, C, N, and O). For the geometry optimizations, the set of im-N-im molecules were fully relaxed in *anti* conformation gas phase configuration using the enhanced Broyden-Fletcher-Shanno-Goldfarb algorithm, until the residual forces per atom are below the threshold value of 10^{-2} eV/Å. We find the optimized contact angle between the gold atom of the pyramidal apex by a subsequent fully relaxation with a single Au atom of the complex Au_{apex}-im-N-im-Au_{apex}. Subsequently, additional gold layers are added to build up the full gold electrodes and the quantum transport calculations are performed.

G.3 Metallocene-based linkers in single-molecule junctions

G.3.1 Experimental two-dimensional conductance-displacement histogram of 1,1'-M metallocenes

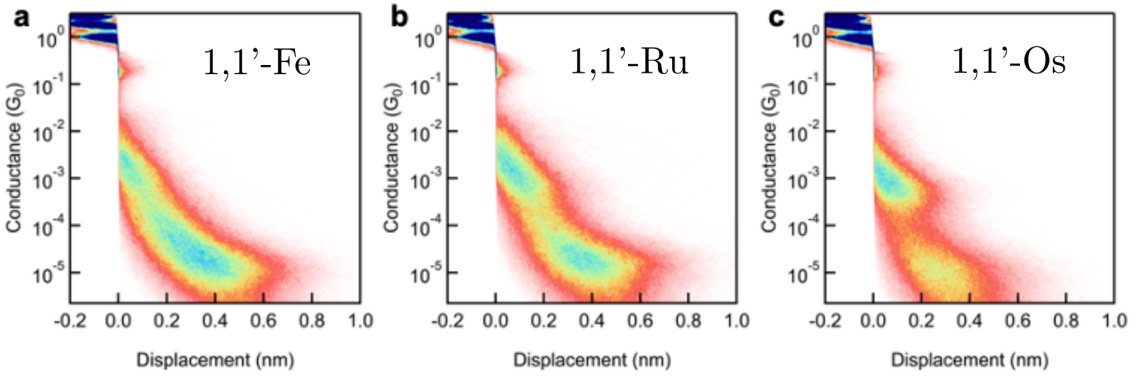

Figure G.2 – Two-dimensional conductance-displacement length histograms of the corresponding 1,1'-Fe (a), 1,1'-Ru (b) and 1,1'-Os (c) molecular junctions. The blue islands indicate the displacement where a larger number of counts have been collected. The red areas correspond to the minimal amount of counts are obtained. Experimental data obtained in Prof. L. Venkataraman's group. Adapted with permission.

G.3.2 Computational details

Our theory calculations are done using DFT with the all-electron implementation in FHI-aims package [34] and the computation of the transmission function is done using our home-made AITRANSS code [26, 49], in which we use the Kohn-Sham states from the DFT together with the non-equilibrium Green's functions formalism. The self-energy is energy independent and included following an empirical model as in chapters 1. The transmission is calculated at $V_{\text{bias}} = 0$ since all the experiments are performed in the linear response regime.

We use as exchange-correlation functional PBE [42]. We also include scalar relativistic corrections to the kinetic energy at the level of the zeroth-order regular approximation (ZORA) of all atoms. The basis set employed is equivalent to double-zeta plus polarization for the molecular atoms and double-zeta for metallic heavy atoms of the leads. The electrodes are modeled as pyramidal clusters with (111) direction growth. The clusters include a total amount of 55 atoms, in 6 layers, with closest interatomic distance 2.88 Å to ensure the screening of the electric charge at the boundaries of the metallic cluster. The ground state state is obtained by imposing the following convergence criteria: 10^{-5} electrons/Å^3 for the difference in the particle density, 10^{-6} eV for the difference in the total energy and 10^{-3} eV for the sum of the eigenvalues of the Kohn-Sham orbitals. The geometry optimization in order to get the ground state is obtained using the Broyden-Fletcher-Shanno-Goldfarb algorithm [34]. The relaxation of the molecular junction is achieved when the absolute value of the components of the residual force per atom is below 10^{-2} eV/Å. In order to optimize the geometry we proceed as follows: first we realize an optimization of the molecule in gas phase and then we add and relax the electrode to get the right contact angle.

Bibliography

[1] Feynman, R. P., *Engineering and Science*, 1960, **23**(5), 22–36.

[2] Aviram, A. and Ratner, M. A., *Chemical Physics Letters*, 1974, **29**(2), 277 – 283.

[3] Binnig, G.; Rohrer, H.; Gerber, C. and Weibel, E., *Phys. Rev. Lett.*, 1982, **49**, 57–61.

[4] Reed, M. A.; Zhou, C.; Muller, C. J.; Burgin, T. P. and Tour, J. M., *Science*, 1997, **278**(5336), 252–254.

[5] van der Zant, H. S. J.; Kervennic, Y.-V.; Poot, M.; O'Neill, K.; de Groot, Z.; Thijssen, J. M.; Heersche, H. B.; Stuhr-Hansen, N.; Bjørnholm, T.; Vanmaekelbergh, D.; van Walree, C. A. and Jenneskens, L. W., *Faraday Discuss.*, 2006, **131**, 347–356.

[6] Zhou, C.; Muller, C. J.; Deshpande, M. R.; Sleight, J. W. and Reed, M. A., *Applied Physics Letters*, 1995, **67**(8), 1160–1162.

[7] Xu, B. and Tao, N. J., *Science*, 2003, **301**(5637), 1221–1223.

[8] Schmaus, S.; Bagrets, A.; Nahas, Y.; Yamada, T. K.; Bork, A.; Bowen, M.; Beaurepaire, E.; Evers, F. and Wulfhekel, W., *Nature Nanotechnology*, 2011, **6**, 185–189.

[9] Ballmann, S.; Härtle, R.; Coto, P.; Elbing, M.; Mayor, M.; Bryce, M.; Thoss, M. and Weber, H. B., *Phys. Rev. Lett.*, 2012, **109**, 056801.

[10] Guedon, C.; Valkenier, H.; Markussen, T.; Thygesen, K.; Hummelen, J. and van der Molen, S., *Nat. Nanotechnol.*, 2012, **7**, 305.

[11] Bogani, L. and Wernsdorfer, W., *Nature Materials*, 2008, **7**, 179–186.

[12] Sanvito, S., *Chem. Soc. Rev.*, 2011, **40**, 3336–3355.

[13] Guo, L.; Gu, X.; Zhu, X. and Sun, X., *Advanced Materials*, 2019, **31**(45), 1805355.

[14] Gobbi, M.; Novak, M. A. and Del Barco, E., *Journal of Applied Physics*, 2019, **125**(24), 240401.

[15] Long, N. J., *Metallocenes: An Introduction to Sandwich Complexes*, Wiley-Blackwell, 1 ed., 1998.

[16] Manchon, A.; Železný, J.; Miron, I. M.; Jungwirth, T.; Sinova, J.; Thiaville, A.; Garello, K. and Gambardella, P., *Rev. Mod. Phys.*, 2019, **91**, 035004.

[17] Aharonov, Y. and Bohm, D., *Phys. Rev.*, 1959, **115**, 485–491.

[18] Yoshizawa, K.; Tada, T. and Staykov, A., *Journal of the American Chemical Society*, 2008, **130**(29), 9406–9413.

[19] Tada, T. and Yoshizawa, K., *Phys. Chem. Chem. Phys.*, 2015, **17**, 32099–32110.

[20] Hansen, T.; Solomon, G. C.; Andrews, D. Q. and Ratner, M. A., *The Journal of Chemical Physics*, 2009, **131**(19), 194704.

[21] Evers, F.; Korytár, R.; Tewari, S. and van Ruitenbeek, J. M., *arXiv:1906.10449*, 2019.

[22] Vazquez, H.; Skouta, R.; Schneebeli, S.; Kamenetska, M.; Breslow, R.; Venkataraman, L. and Hybertsen, M., *Nature Nanotechnology*, 2012, **7**, 663–667.

[23] Frisenda, R.; Janssen, V. A. E. C.; Grozema, F. C.; van der Zant, H. S. J. and Renaud, N., *Nature Chemistry*, 2016, **8**, 1099–1104.

[24] Stefani, D.; Weiland, K. J.; Skripnik, M.; Hsu, C.; Perrin, M. L.; Mayor, M.; Pauly, F. and van der Zant, H. S. J., *Nano Letters*, 2018, **18**(9), 5981–5988.

[25] Thoss, M. and Evers, F., *The Journal of Chemical Physics*, 2018, **148**(3), 030901.

[26] Arnold, A.; Weigend, F. and Evers, F., *J. Chem. Phys.*, 2007, **126**(17), 174101.

[27] Walz, M.; Wilhelm, J. and Evers, F., *Phys. Rev. Lett.*, 2014, **113**, 136602.

[28] Pal, A. N.; Li, D.; Sarkar, S.; Chakrabarti, S.; Vilan, A.; Kronik, L.; Smogunov, A. and Tal, O., *Nature Communications*, 2019, **10**, 5565.

[29] Garner, M. H.; Li, H.; Chen, Y.; Su, T. A.; Shangguan, Z.; Paley, D. W.; Liu, T.; Ng, F.; Li, H.; Xiao, S.; Nuckolls, C.; Venkataraman, L. and Solomon, G. C., *Nature*, 2018, **558**(7710), 415–419.

[30] Su, T. A.; Li, H.; Klausen, R. S.; Kim, N. T.; Neupane, M.; Leighton, J. L.; Steigerwald, M. L.; Venkataraman, L. and Nuckolls, C., *Accounts of Chemical Research*, 2017, **50**(4), 1088–1095.

[31] Hohenberg, P. and Kohn, W., *Phys. Rev.*, 1964, **136**, B864–B871.

[32] Martin, C. A.; Ding, D.; Sørensen, J. K.; Bjørnholm, T.; van Ruitenbeek, J. M. and van der Zant, H. S. J., *Journal of the American Chemical Society*, 2008, **130**(40), 13198–13199.

[33] Kohn, W. and Sham, L. J., *Phys. Rev.*, 1965, **140**, A1133–A1138.

[34] Blum, V.; Gehrke, R.; Hanke, F.; Havu, P.; Havu, V.; Ren, X.; Reuter, K. and Scheffler, M., *Computer Physics Communications*, 2009, **180**(11), 2175 – 2196.

[35] Furche, F.; Ahlrichs, R.; Hättig, C.; Klopper, W.; Sierka, M. and Weigend, F., *WIREs Computational Molecular Science*, 2014, **4**(2), 91–100.

[36] Balasubramani, S. G.; Chen, G. P.; Coriani, S.; Diedenhofen, M.; Frank, M. S.; Franzke, Y. J.; Furche, F.; Grotjahn, R.; Harding, M. E.; Hättig, C.; Hellweg, A.; Helmich-Paris, B.; Holzer, C.; Huniar, U.; Kaupp, M.; Marefat Khah, A.; Karbalaei Khani, S.; Müller, T.; Mack, F.; Nguyen, B. D.; Parker, S. M.; Perlt, E.; Rappoport, D.; Reiter, K.; Roy, S.; Rückert, M.; Schmitz, G.; Sierka, M.; Tapavicza, E.; Tew, D. P.; van Wüllen, C.; Voora, V. K.; Weigend, F.; Wodyński, A. and Yu, J. M., *The Journal of Chemical Physics*, 2020, **152**(18), 184107.

[37] Giannozzi, P.; Baroni, S.; Bonini, N.; Calandra, M.; Car, R.; Cavazzoni, C.; Ceresoli, D.; Chiarotti, G. L.; Cococcioni, M.; Dabo, I.; Dal Corso, A.; de Gironcoli, S.; Fabris, S.; Fratesi, G.; Gebauer, R.; Gerstmann, U.; Gougoussis, C.; Kokalj, A.; Lazzeri, M.; Martin-Samos, L.; Marzari, N.; Mauri, F.; Mazzarello, R.; Paolini, S.; Pasquarello,

A.; Paulatto, L.; Sbraccia, C.; Scandolo, S.; Sclauzero, G.; Seitsonen, A. P.; Smogunov, A.; Umari, P. and Wentzcovitch, R. M., *Journal of Physics: Condensed Matter*, 2009, **21**(39), 395502.

[38] Blaha, P.; Schwarz, K.; Sorantin, P. and Trickey, S., *Computer Physics Communications*, 1990, **59**(2), 399 – 415.

[39] Ceperley, D. M. and Alder, B. J., *Phys. Rev. Lett.*, 1980, **45**, 566–569.

[40] Burke, K., *The Journal of Chemical Physics*, 2012, **136**(15), 150901.

[41] Perdew, J. P.; Ruzsinszky, A.; Tao, J.; Staroverov, V. N.; Scuseria, G. E. and Csonka, G. I., *The Journal of Chemical Physics*, 2005, **123**(6), 062201.

[42] Perdew, J. P.; Burke, K. and Ernzerhof, M., *Phys. Rev. Lett.*, 1996, **77**, 3865–3868.

[43] Kim, K. and Jordan, K. D., *The Journal of Physical Chemistry*, 1994, **98**(40), 10089–10094.

[44] Stephens, P. J.; Devlin, F. J.; Chabalowski, C. F. and Frisch, M. J., *The Journal of Physical Chemistry*, 1994, **98**(45), 11623–11627.

[45] Cuevas, J. C. and Scheer, E., *Molecular Electronics: An Introduction to Theory and Experiment*, World Scientific, 2 ed., 2010.

[46] Di Ventra, M., *Electrical Transport in Nanoscale Systems*, Cambridge University Press, 1 ed., 2008.

[47] Koentopp, M.; Burke, K. and Evers, F., *Phys. Rev. B*, 2006, **73**, 121403.

[48] Evers, F. and Arnold, A., In *CFN Lectures on Functional Nanostructures - Vol. 2, Lecture Notes in Physics*, Röthig, C.; Schön, G. and Vojta, M., Eds., Springer, 2011; Vol. 820; pages 27–53.

[49] Bagrets, A., *J. Chem. Theory Comput.*, 2013, **9**(6), 2801–2815.

[50] Walz, M.; Bagrets, A. and Evers, F., *Journal of Chemical Theory and Computation*, 2015, **11**(11), 5161–5176.

[51] Landauer, R., *IBM Journal of Research and Development*, 1957, **1**(3), 223–231.

[52] Büttiker, M.; Imry, Y.; Landauer, R. and Pinhas, S., *Phys. Rev. B*, 1985, **31**, 6207–6215.

[53] Fisher, D. S. and Lee, P. A., *Phys. Rev. B*, 1981, **23**, 6851–6854.

[54] Dirac, P. A. M. and Fowler, R. H., *Proceedings of the Royal Society of London. Series A, Containing Papers of a Mathematical and Physical Character*, 1928, **117**(778), 610–624.

[55] Huhn, W. P. and Blum, V., *Phys. Rev. Materials*, 2017, **1**, 033803.

[56] Weissbluth, M., *Atoms and Molecules*, Academic Press, 1978.

[57] Winkler, R., *Spin-Orbit Effect in Two-Dimensional Electron and Hole Systems*, Springer Tracts in Modern Physics, Springer Berlin Heidelberg, 2003.

[58] Wilhelm, J.; Walz, M. and Evers, F., *Phys. Rev. B*, 2015, **92**, 014405.

[59] Frank, T.; Högl, P.; Gmitra, M.; Kochan, D. and Fabian, J., *Phys. Rev. Lett.*, 2018, **120**, 156402.

[60] van Lenthe, E.; Snijders, J. G. and Baerends, E. J., *The Journal of Chemical Physics*, 1996, **105**(15), 6505–6516.

[61] Peng, D.; Middendorf, N.; Weigend, F. and Reiher, M., *The Journal of Chemical Physics*, 2013, **138**(18), 184105.

[62] Armbruster, M. K.; Weigend, F.; van Wüllen, C. and Klopper, W., *Phys. Chem. Chem. Phys.*, 2008, **10**, 1748–1756.

[63] Löwdin, P., *The Journal of Chemical Physics*, 1950, **18**(3), 365–375.

[64] Haney, P.; Duine, R.; Núñez, A. and MacDonald, A., *Journal of Magnetism and Magnetic Materials*, 2008, **320**(7), 1300 – 1311.

[65] Nikolić, B. K.; Branislav, K.; Dolui, K.; Petrović, M. D.; Plecháč, P.; Markussen, T. and Stokbro, K., In *Handbook of Materials Modeling: Applications: Current and Emerging Materials*, Andreoni, W. and Yip, S., Eds., Springer International Publishing, 2018; pages 1–35.

[66] Vignale, G. and Rasolt, M., *Phys. Rev. B*, 1988, **37**, 10685–10696.

[67] Ullrich, C. A., *Phys. Rev. B*, 2018, **98**, 035140.

[68] Papior, N.; Lorente, N.; Frederiksen, T.; García, A. and Brandbyge, M., *Computer Physics Communications*, 2017, **212**, 8–24.

[69] Freimuth, F.; Blügel, S. and Mokrousov, Y., *Phys. Rev. B*, 2014, **90**, 174423.

[70] Géranton, G.; Freimuth, F.; Blügel, S. and Mokrousov, Y., *Phys. Rev. B*, 2015, **91**, 014417.

[71] Schnaebele, P. Electronic transport in atomistic nanostructures: electrochemical effects and non-equilibrium forces Master's thesis, Karlsruhe Institute of Technology.

[72] Hasan, M. Z. and Kane, C. L., *Rev. Mod. Phys.*, 2010, **82**, 3045–3067.

[73] Haney, P. M.; Waldron, D.; Duine, R. A.; Núñez, A. S.; Guo, H. and MacDonald, A. H., *Phys. Rev. B*, 2007, **76**, 024404.

[74] Tsoi, M.; Jansen, A. G. M.; Bass, J.; Chiang, W.-C.; Seck, M.; Tsoi, V. and Wyder, P., *Phys. Rev. Lett.*, 1998, **80**, 4281–4284.

[75] Tsoi, M.; Jansen, A. G. M.; Bass, J.; Chiang, W.-C.; Seck, M.; Tsoi, V. and Wyder, P., *Nature*, 2000, **406**, 46–48.

[76] Katine, J. A.; Albert, F. J.; Buhrman, R. A.; Myers, E. B. and Ralph, D. C., *Phys. Rev. Lett.*, 2000, **84**, 3149–3152.

[77] Albert, F. J.; Emley, N. C.; Myers, E. B.; Ralph, D. C. and Buhrman, R. A., *Phys. Rev. Lett.*, 2002, **89**, 226802.

[78] Pufall, M. R.; Rippard, W. H. and Silva, T. J., *Applied Physics Letters*, 2003, **83**(2), 323–325.

[79] Kiselev, S. I.; Sankey, J. C.; Krivorotov, I. N.; Emley, N. C.; Schoelkopf, R. J.; Buhrman, R. A. and Ralph, D. C., *Nature*, 2003, **425**, 380–383.

[80] Myers, E. B.; Ralph, D. C.; Katine, J. A.; Louie, R. N. and Buhrman, R. A., *Science*, 1999, **285**(5429), 867–870.

[81] Grollier, J.; Cros, V.; Jaffres, H.; Hamzic, A.; George, J. M.; Faini, G.; Ben Youssef, J.; Le Gall, H. and Fert, A., *Phys. Rev. B*, 2003, **67**, 174402.

[82] Stiles, M. D. and Zangwill, A., *Phys. Rev. B*, 2002, **66**, 014407.

[83] Ralph, D. and Stiles, M., *Journal of Magnetism and Magnetic Materials*, 2008, **320**(7), 1190 – 1216.

[84] Misiorny, M. and Barnaś, J., *Phys. Rev. B*, 2007, **75**, 134425.

[85] Misiorny, M. and Barnaś, J., *Phys. Rev. B*, 2008, **77**, 172414.

[86] Liu, L.; Pai, C.-F.; Li, Y.; Tseng, H. W.; Ralph, D. C. and Buhrman, R. A., *Science*, 2012, **336**(6081), 555–558.

[87] Gaudenzi, R.; Misiorny, M.; Burzurí, E.; Wegewijs, M. R. and van der Zant, H. S. J., *The Journal of Chemical Physics*, 2017, **146**(9), 092330.

[88] Gambardella, P. and Miron, I. M., *Philosophical Transactions of the Royal Society A: Mathematical, Physical and Engineering Sciences*, 2011, **369**(1948), 3175–3197.

[89] Be, C.; Sato, N. and Wang, S. X. In *Advances in Non-Volatile Memory and Storage Technology (Second Edition)*, Magyari-Köpe, B. and Nishi, Y., Eds., Woodhead Publishing Series in Electronic and Optical Materials; Woodhead Publishing, 2 ed., 2019; chapter "6 - Spin-orbit torque magnetoresistive random-access memory (SOT-MRAM)", pages 203 – 235.

[90] Prenat, G.; Jabeur, K.; Di Pendina, G.; Boulle, O. and Gaudin, G. In *Spintronics-based Computing*, Zhao, W. and Prenat, G., Eds.; Springer, Cham, 2015; chapter "Beyond STT-MRAM, Spin Orbit Torque RAM SOT-MRAM for High Speed and High Reliability Applications", pages 145–157.

[91] Honjo, H.; Nguyen, T. V. A.; Watanabe, T.; Nasuno, T.; Zhang, C.; Tanigawa, T.; Miura, S.; Inoue, H.; Niwa, M.; Yoshiduka, T.; Noguchi, Y.; Yasuhira, M.; Tamakoshi, A.; Natsui, M.; Ma, Y.; Koike, H.; Takahashi, Y.; Furuya, K.; Shen, H.; Fukami, S.; Sato, H.; Ikeda, S.; Hanyu, T.; Ohno, H. and Endoh, T. In "First demonstration of field-free SOT-MRAM with 0.35 ns write speed and 70 thermal stability under 400°C thermal tolerance by canted SOT structure and its advanced patterning/SOT channel technology", *2019 IEEE International Electron Devices Meeting (IEDM)*, pages 28.5.1–28.5.4, 2019.

[92] Sato, N.; Xue, F.; White, R. M.; Bi, C. and Wang, S. X., *Nature Electronics*, 2018, **1**, 508–511.

[93] Seo, Y.; Kwon, K.-W. and Roy, K., *IEEE Electron Device Letters*, 2016, **37**, 982–985.

[94] Bhatti, S.; Sbiaa, R.; Hirohata, A.; Ohno, H.; Fukami, S. and Piramanayagam, S., *Materials Today*, 2017, **20**(9), 530 – 548.

[95] Rocha, A. R.; García-suárez, V. M.; Bailey, S. W.; Lambert, C. J.; Ferrer, J. and Sanvito, S., *Nature Materials*, 2005, **4**, 335–339.

[96] Slonczewski, J., *J. Magn. Magn. Mater.*, 1996, **159**(1), L1–L7.

[97] Berger, L., *Phys. Rev. B*, 1996, **54**, 9353–9358.

[98] Chernyshov, A.; Overby, M.; Liu, X.; Furdyna, J. K.; Lyanda-Geller, Y. and Rokhinson, L. P., *Nature Physics*, 2009, **5**, 656–659.

[99] Miron, I. M.; Garello, K.; Gaudin, G.; Zermatten, P.-J.; Costache, M. V.; Auffret, S.; Bandiera, S.; Rodmacq, B.; Schuhl, A. and Gambardella, P., *Nature*, 2011, **476**, 189–193.

[100] Dolui, K.; Petrović, M. D.; Zollner, K.; Plecháč, P.; Fabian, J. and Nikolić, B. K., *Nano Letters*, 2020, **20**(4), 2288–2295.

[101] Choi, G.-M.; Oh, J. H.; Lee, D.-K.; Lee, S.-W.; Kim, K. W.; Lim, M.; Min, B.-C.; Lee, K.-J. and Lee, H.-W., *Nature Communications*, 2020, **11**, 1482.

[102] Braatas, A.; Bauer, G. E. W. and Kelly, P. J., *Phys. Rep.*, 2006, **427**, 157.

[103] Wruss, E.; Prokopiou, G.; Kronik, L.; Zojer, E.; Hofmann, O. T. and Egger, D. A., *Phys. Rev. Materials*, 2019, **3**, 086002.

[104] Mugarza, A.; Robles, R.; Krull, C.; Korytár, R.; Lorente, N. and Gambardella, P., *Phys. Rev. B*, 2012, **85**, 155437.

[105] Atxabal, A.; Ribeiro, M.; Parui, S.; Urreta, L.; Sagasta, E.; Sun, X.; Llopis, R.; Casanova, F. and Hueso, L. E., *Nature Communications*, 2016, **7**, 13751.

[106] Matoko-Ngouma, J.; Malonda-Boungou, B.; Raji, A.; Moussounda, P. and M'Passi-Mabiala, B., *Journal of Molecular Structure*, 2020, **1211**, 128034.

[107] Siegert, B.; Donarini, A. and Grifoni, M., *Beilstein Journal of Nanotechnology*, 2015, **6**, 2452–2462.

[108] Tabata, K.; Sasaki, T. and Yamamoto, Y., *Applied Physics Letters*, 2013, **103**(4), 043301.

[109] Giovannetti, G.; Brocks, G. and van den Brink, J., *Physical review B: Condensed matter and materials physics*, 2008, **77**, 035133/1–035133/8.

[110] Stepanow, S.; Lodi Rizzini, A.; Krull, C.; Kavich, J.; Cezar, J. C.; Yakhou-Harris, F.; Sheverdyaeva, P. M.; Moras, P.; Carbone, C.; Ceballos, G.; Mugarza, A. and Gambardella, P., *Journal of the American Chemical Society*, 2014, **136**(14), 5451–5459.

[111] Herper, H.; Brena, B.; Puglia, C.; Bhandary, S.; Wende, H.; Eriksson, O. and Sanyal, B., *Molecular Nanomagnets: Fundamental Understanding*, Springer Briefs in Applied Sciences and Technology, Springer Singapore, 1 ed., 2020.

[112] Nawa, K.; Kitaoka, Y.; Nakamura, K.; Akiyama, T. and Ito, T., *Journal of Applied Physics*, 2015, **117**(17), 17E131.

[113] Tokár, K.; Derian, R.; Mitas, L. and Štich, I., *The Journal of Chemical Physics*, 2016, **144**(6), 064303.

[114] Wang, J.; Zhang, X.; Schleyer, P. v. R. and Chen, Z., *The Journal of Chemical Physics*, 2008, **128**(10), 104706.

[115] Miyajima, K.; Nakajima, A.; Yabushita, S.; Knickelbein, M. B. and Kaya, K., *Journal of the American Chemical Society*, 2004, **126**(41), 13202–13203.

[116] Zhou, L.; Yang, S.-W.; Ng, M.-F.; Sullivan, M. B.; Tan, and Shen, L., *Journal of the American Chemical Society*, 2008, **130**(12), 4023–4027.

[117] Wang, P.; Jiang, X.; Hu, J.; Huang, X.; Zhao, J. and Ahuja, R., *Journal of Physics: Condensed Matter*, 2017, **29**(43), 435802.

[118] Mokrousov, Y.; Atodiresei, N.; Bihlmayer, G.; Heinze, S. and Blügel, S., *Nanotechnology*, 2007, **18**(49), 495402.

[119] Zhang, X.; Wang, J.; Gao, Y. and Zeng, X. C., *ACS Nano*, 2009, **3**(3), 537–545.

[120] Prins, R. and Voorst, J., *The Journal of Chemical Physics*, 1968, **49**(10), 4665–4673.

[121] Bransden, B.; Joachain, C. and Plivier, T., *Physics of Atoms and Molecules*, Pearson Education, Prentice Hall, 2003.

[122] Bendix, J.; Brorson, M. and Schaffer, C. E., *Inorganic Chemistry*, 1993, **32**(13), 2838–2849.

[123] García, A.; Papior, N.; Akhtar, A.; Artacho, E.; Blum, V.; Bosoni, E.; Brandimarte, P.; Brandbyge, M.; Cerdá, J. I.; Corsetti, F.; Cuadrado, R.; Dikan, V.; Ferrer, J.; Gale, J.; García-Fernández, P.; García-Suárez, V. M.; García, S.; Huhs, G.; Illera, S.; Korytár, R.; Koval, P.; Lebedeva, I.; Lin, L.; López-Tarifa, P.; Mayo, S. G.; Mohr, S.; Ordejón, P.; Postnikov, A.; Pouillon, Y.; Pruneda, M.; Robles, R.; Sánchez-Portal, D.; Soler, J. M.; Ullah, R.; Yu, V. W.-z. and Junquera, J., *The Journal of Chemical Physics*, 2020, **152**(20), 204108.

[124] Finlay, C. C.; Maus, S.; Beggan, C. D.; Bondar, T. N.; Chambodut, A.; Chernova, T. A.; Chulliat, A.; Golovkov, V. P.; Hamilton, B.; Hamoudi, M.; Holme, R.; Hulot, G.; Kuang, W.; Langlais, B.; Lesur, V.; Lowes, F. J.; Lühr, H.; Macmillan, S.; Mandea, M.; McLean, S.; Manoj, C.; Menvielle, M.; Michaelis, I.; Olsen, N.; Rauberg, J.; Rother, M.; Sabaka, T. J.; Tangborn, A.; Tøffner-Clausen, L.; Thébault, E.; Thomson, A. W. P.; Wardinski, I.; Wei, Z. and Zvereva, T. I., *Geophysical Journal International*, 2010, **183**(3), 1216–1230.

[125] Camarasa-Gómez, M.; Hernangómez-Pérez, D.; Inkpen, M. S.; Lovat, G.; Fung, E.-D.; Roy, X.; Venkataraman, L. and Evers, F., *chemrXiv:10.26434/chemrxiv.12252059.v1*, 2020.

[126] Kealy, T. J. and Pauson, P. L., *Nature*, 1951, **168**, 1039.

[127] Haaland, A. and Nilsson, J.-E., *Chem. Commun. (London)*, 1968, pages 88–89.

[128] Nemnes, G. A. and Nicolaev, A., *Phys. Chem. Chem. Phys.*, 2014, **16**, 18478–18482.

[129] Tegenkamp, C.; Schmeidel, J. and Pfnür, H., *Surface Science*, 2011, **605**(3), 267 – 271.

[130] Müller-Meskamp, L.; Karthäuser, S.; Waser, R.; Homberger, M.; Wang, Y.; Englert, U. and Simon, U., *Surface Science*, 2009, **603**(4), 716 – 722.

[131] Bredow, T.; Tegenkamp, C.; Pfnür, H.; Meyer, J.; Maslyuk, V. V. and Mertig, I., *The Journal of Chemical Physics*, 2008, **128**(6), 064704.

[132] Meyer, J.; Bredow, T.; Tegenkamp, C. and Pfnür, H., *The Journal of Chemical Physics*, 2006, **125**(19), 194705.

[133] Getty, S. A.; Engtrakul, C.; Wang, L.; Liu, R.; Ke, S.-H.; Baranger, H. U.; Yang, W.; Fuhrer, M. S. and Sita, L. R., *Phys. Rev. B*, 2005, **71**, 241401.

[134] Nijhuis, C. A.; Reus, W. F. and Whitesides, G. M., *Journal of the American Chemical Society*, 2010, **132**(51), 18386–18401.

[135] Nerngchamnong, N.; Yuan, L.; Qi, D.-C.; Li, J.; Thompson, D. and Nijhuis, C. A., *Nature Nanotechnology*, 2013, **8**, 113.

[136] Matsuura, Y., *The Journal of Chemical Physics*, 2013, **138**(1), 014311.

[137] Liu, R.; Ke, S.-H.; Baranger, H. U. and Yang, W., *Nano Letters*, 2005, **5**(10), 1959–1962.

[138] Liu, R.; Ke, S.-H.; Yang, W. and Baranger, H. U., *The Journal of Chemical Physics*, 2007, **127**(14), 141104.

[139] Morari, C.; Rungger, I.; Rocha, A. R.; Sanvito, S.; Melinte, S. and Rignanese, G.-M., *ACS Nano*, 2009, **3**(12), 4137–4143.

[140] Kanthasamy, K.; Ring, M.; Nettelroth, D.; Tegenkamp, C.; Butenschön, H.; Pauly, F. and Pfnür, H., *Small*, 2016, **12**(35), 4849–4856.

[141] Zhao, X.; Kastlunger, G. and Stadler, R., *Phys. Rev. B*, 2017, **96**, 085421.

[142] Zhao, X. and Stadler, R., *Phys. Rev. B*, 2019, **99**, 045431.

[143] Li, Y.; Buerkle, M.; Li, G.; Rostamian, A.; Wang, H.; Wang, Z.; Bowler, D. R.; Miyazaki, T.; Xiang, L.; Asai, Y.; Zhou, G. and Tao, N., *Nature Materials*, 2019, **18**(4), 357–363.

[144] Stuyver, T.; Fias, S.; De Proft, F.; Geerlings, P.; Tsuji, Y. and Hoffmann, R., *The Journal of Chemical Physics*, 2017, **146**(9), 092310.

[145] Géranton, G.; Seiler, C.; Bagrets, A.; Venkataraman, L. and Evers, F., *J. Chem. Phys.*, 2013, **139**(23), 234701.

[146] Farid, B. In *Electron Correlation in the Solid State*, March, N. H., Ed.; Imperial College Press, 1999; chapter "Ground and Low-Lying Excited States of Interacting Electron Systems: a Survey and Some Critical Analysis", pages 103–261.

[147] Li, H.; Su, T. A.; Camarasa-Gómez, M.; Hernangómez-Pérez, D.; Henn, S. E.; Pokorný, V.; Caniglia, C. D.; Inkpen, M. S.; Korytár, R.; Steigerwald, M. L.; Nuckolls, C.; Evers, F. and Venkataraman, L., *Angewandte Chemie International Edition*, 2017, **56**(45), 14145–14148.

[148] Fu, T.; Smith, S.; Camarasa-Gómez, M.; Yu, X.; Xue, J.; Nuckolls, C.; Evers, F.; Venkataraman, L. and Wei, S., *Chem. Sci.*, 2019, **10**, 9998–10002.

[149] Inkpen, M. S.; Lovat, G.; Camarasa-Gómez, M.; Hernangómez-Pérez, D.; Evers, F.; Roy, X. and Venkataraman, L. to be submitted, 2020.

[150] Akkerman, H. B. and de Boer, B., *Journal of Physics: Condensed Matter*, 2007, **20**(1), 013001.

[151] Li, C.; Pobelov, I.; Wandlowski, T.; Bagrets, A.; Arnold, A. and Evers, F., *Journal of the American Chemical Society*, 2008, **130**(1), 318–326.

[152] Gunasekaran, S.; Hernangómez-Pérez, D.; Davydenko, I.; Marder, S.; Evers, F. and Venkataraman, L., *Nano Letters*, 2018, **18**(10), 6387–6391.

[153] Su, T. A.; Neupane, M.; Steigerwald, M. L.; Venkataraman, L. and Nuckolls, C., *Nature Reviews Materials*, 2016, **1**, 16002.

[154] Klöckner, J. C.; Bürkle, M.; Cuevas, J. C. and Pauly, F., *Phys. Rev. B*, 2016, **94**, 205425.

[155] Su, T. A.; Li, H.; Klausen, R. S.; Kim, N. T.; Neupane, M.; Leighton, J. L.; Steigerwald, M. L.; Venkataraman, L. and Nuckolls, C., *Accounts of Chemical Research*, 2017, **50**(4), 1088–1095.

[156] Cui, X. D.; Primak, A.; Zarate, X.; Tomfohr, J.; Sankey, O. F.; Moore, A. L.; Moore, T. A.; Gust, D.; Harris, G. and Lindsay, S. M., *Science*, 2001, **294**(5542), 571–574.

[157] Haiss, W.; Nichols, R. J.; van Zalinge, H.; Higgins, S. J.; Bethell, D. and Schiffrin, D. J., *Phys. Chem. Chem. Phys.*, 2004, **6**, 4330–4337.

[158] Reuter, M. G., *Journal of Physics: Condensed Matter*, 2016, **29**(5), 053001.

[159] Yamada, R.; Kumazawa, H.; Tanaka, S. and Tada, H., *Applied Physics Express*, 2009, **2**, 025002.

[160] Sedghi, G.; García-Suárez, V. M.; Esdaile, L. J.; Anderson, H. L.; Lambert, C. J.; Martín, S.; Bethell, D.; Higgins, S. J.; Elliott, M.; Bennett, N.; Macdonald, J. E. and Nichols, R. J. a., *Nature Nanotechnology*, 2011, 10.1038/nnano.2011.111, **6**, 517–523.

[161] Tewari, S. *Molecular electronics: controlled manipulation, noise and graphene architecture* PhD dissertation, Leiden University, 2018.

[162] Su, T. A.; Li, H.; Zhang, V.; Neupane, M.; Batra, A.; Klausen, R. S.; Kumar, B.; Steigerwald, M. L.; Venkataraman, L. and Nuckolls, C., *Journal of the American Chemical Society*, 2015, **137**(38), 12400–12405.

[163] Li, H.; Garner, M. H.; Su, T. A.; Jensen, A.; Inkpen, M. S.; Steigerwald, M. L.; Venkataraman, L.; Solomon, G. C. and Nuckolls, C., *Journal of the American Chemical Society*, 2017, **139**(30), 10212–10215.

[164] Kaneko, S.; Nakazumi, T. and Kiguchi, M., *The Journal of Physical Chemistry Letters*, 2010, **1**(24), 3520–3523.

[165] Kim, T.; Vázquez, H.; Hybertsen, M. S. and Venkataraman, L., *Nano Letters*, 2013, **13**(7), 3358–3364.

[166] Peng, Z.-L.; Chen, Z.-B.; Zhou, X.-Y.; Sun, Y.-Y.; Liang, J.-H.; Niu, Z.-J.; Zhou, X.-S. and Mao, B.-W., *The Journal of Physical Chemistry C*, 2012, **116**(41), 21699–21705.

[167] Wang, Y.-H.; Li, D.-F.; Hong, Z.-W.; Liang, J.-H.; Han, D.; Zheng, J.-F.; Niu, Z.-J.; Mao, B.-W. and Zhou, X.-S., *Electrochemistry Communications*, 2014, **45**, 83 – 86.

[168] Kiguchi, M.; Tal, O.; Wohlthat, S.; Pauly, F.; Krieger, M.; Djukic, D.; Cuevas, J. C. and van Ruitenbeek, J. M., *Phys. Rev. Lett.*, 2008, **101**, 046801.

[169] Yelin, T.; Korytár, R.; Sukenik, N.; Vardimon, R.; Kumar, B.; Nuckolls, C.; Evers, F. and Tal, O., *Nature Materials*, 2016, **15**, 444–449.

[170] Ko, C.-H.; Huang, M.-J.; Fu, M.-D. and Chen, C.-h., *Journal of the American Chemical Society*, 2010, **132**(2), 756–764.

[171] Wang, Y.-H.; Zhou, X.-Y.; Sun, Y.-Y.; Han, D.; Zheng, J.-F.; Niu, Z.-J. and Zhou, X.-S., *Electrochimica Acta*, 2014, **123**, 205 – 210.

[172] Wang, Y.-H.; Hong, Z.-W.; Sun, Y.-Y.; Li, D.-F.; Han, D.; Zheng, J.-F.; Niu, Z.-J. and Zhou, X.-S., *The Journal of Physical Chemistry C*, 2014, **118**(32), 18756–18761.

[173] Pyykko, P. and Desclaux, J. P., *Accounts of Chemical Research*, 1979, **12**(8), 276–281.

[174] Adak, O.; Korytár, R.; Joe, A. Y.; Evers, F. and Venkataraman, L., *Nano Letters*, 2015, **15**, 3716–3722.

[175] Hoelzl, J.; Schulte, F. K. and Wagner, H., In *Solid Surface Physics*, Springer-Verlag, 1979; pages 1–150; Springer tracts in modern physics.

[176] Lawson, J. W. and Bauschlicher, C. W., *Phys. Rev. B*, 2006, **74**, 125401.

[177] Geng, W.; Nara, J. and Ohno, T., *Thin Solid Films*, 2004, **464-465**, 379–383.

[178] Skriver, H. L. and Rosengaard, N. M., *Phys. Rev. B*, 1992, **46**, 7157–7168.

[179] Antonyuk, S. V.; Strange, R. W.; Marklund, S. L. and Hasnain, S. S., *Journal of Molecular Biology*, 2009, **388**(2), 310–326.

[180] Tainer, J. A.; Getzoff, E. D.; Richardson, J. S. and Richardson, D. C., *Nature*, 1983, **306**, 415–419.

[181] Park, K. S.; Ni, Z.; Côté, A. P.; Choi, J. Y.; Huang, R.; Uribe-Romo, F. J.; Chae, H. K.; O'Keeffe, M. and Yaghi, O. M., *Proceedings of the National Academy of Sciences*, 2006, **103**(27), 10186–10191.

[182] Wu, S.; González, M. T.; Huber, R.; Grunder, S.; Mayor, M.; Schönenberger, C. and Calame, M., *Nature Nanotechnology*, 2008, **8**, 569–574.

[183] Martín, S.; Grace, I.; Bryce, M. R.; Wang, C.; Jitchati, R.; Batsanov, A. S.; Higgins, S. J.; Lambert, C. J. and Nichols, R. J., *Journal of the American Chemical Society*, 2010, **132**(26), 9157–9164.

[184] Yoshida, K.; Pobelov, I. V.; Zsolt Manrique, D.; Pope, T.; Mészáros, G.; Gulcur, M.; Bryce, M. R.; Lambert, C. J. and Wandlowski, T., *Scientific Reports*, 2015, **5**, 9002.

[185] González, M. T.; Leary, E.; García, R.; Verma, P.; Herranz, M. n.; Rubio-Bollinger, G.; Martín, N. and Agraït, N., *The Journal of Physical Chemistry C*, 2011, **115**(36), 17973–17978.

[186] Hong, W.; Valkenier, H.; Mészáros, G.; Zsolt Manrique, D.; Mishchenko, A.; Putz, A.; Moreno García, P.; Lambert, C. J.; Hummelen, J. C. and Wandlowski, T., *Beilstein Journal of Nanotechnology*, 2011, **2**, 699–713.

[187] Zheng, J.-T.; Yan, R.-W.; Tian, J.-H.; Liu, J.-Y.; Pei, L.-Q.; Wu, D.-Y.; Dai, K.; Yang, Y.; Jin, S.; Hong, W. and Tian, Z.-Q., *Electrochimica Acta*, 2016, **200**, 268 – 275.

[188] Borges, A.; Fung, E.-D.; Ng, F.; Venkataraman, L. and Solomon, G. C., *The Journal of Physical Chemistry Letters*, 2016, **7**(23), 4825–4829.

[189] Kamenetska, M.; Quek, S. Y.; Whalley, A. C.; Steigerwald, M. L.; Choi, H. J.; Louie, S. G.; Nuckolls, C.; Hybertsen, M. S.; Neaton, J. B. and Venkataraman, L., *Journal of the American Chemical Society*, 2010, **132**(19), 6817–6821.

[190] Kim, T.; Darancet, P.; Widawsky, J. R.; Kotiuga, M.; Quek, S. Y.; Neaton, J. B. and Venkataraman, L., *Nano Letters*, 2014, **14**(2), 794–798.

[191] Quek, S. Y.; Kamenetska, M.; Steigerwald, M. L.; Choi, H. J.; Louie, S. G.; Hybertsen, M. S. and Neaton, J. B., *Nature Nanotechnology*, 2009, **4**, 230–234.

[192] Park, Y. S.; Whalley, A. C.; Kamenetska, M.; Steigerwald, M. L.; Hybertsen, M. S.; Nuckolls, C. and Venkataraman, L., *Journal of the American Chemical Society*, 2007, **129**(51), 15768–15769.

[193] Magyarkuti, A.; Adak, O.; Halbritter, A. and Venkataraman, L., *Nanoscale*, 2018, **10**, 3362–3368.

[194] Tkatchenko, A. and Scheffler, M., *Phys. Rev. Lett.*, 2009, **102**, 073005.

[195] Miller, S. A.; Tebboth, J. A. and Tremaine, J. F., *J. Chem. Soc.*, 1952, pages 632–635.

[196] Astruc, D., *European Journal of Inorganic Chemistry*, 2017, **2017**(1), 6–29.

[197] Welker, M. E., *Molecules*, 2018, **23**(7).

[198] Bauer, J.; Braunschweig, H. and Dewhurst, R. D., *Chemical Reviews*, 2012, **112**(8), 4329–4346.

[199] Brisendine, J. M.; Refaely-Abramson, S.; Liu, Z.-F.; Cui, J.; Ng, F.; Neaton, J. B.; Koder, R. L. and Venkataraman, L., *The Journal of Physical Chemistry Letters*, 2018, **9**(4), 763–767.

[200] Han, W.; Kawakami, R. K.; Gmitra, M. and Fabian, J., *Nature Nanotechnology*, 2014, **9**, 794–807.

[201] Lenthe, E. v.; Baerends, E. J. and Snijders, J. G., *J. Chem. Phys.*, 1993, **99**(6), 4597–4610.

[202] Havu, V.; Blum, V.; Havu, P. and Scheffler, M., *Journal of Computational Physics*, 2009, **228**(22), 8367 – 8379.

List of publications

Part of the work presented in this thesis has been published in the following articles:

- M. S. Inkpen, G. Lovat, **M. Camarasa–Gómez**[*],
  D. Hernangómez–Pérez, F. Evers, X. Roy, and L. Venkataraman,
  Metallocene-electrode contacts in single-molecule junctions,
  (in preparation)

- **M. Camarasa–Gómez**[†], D. Hernangómez–Pérez[†], M. S. Inkpen,
  G. Lovat, E–Dean Fung, X. Roy, L. Venkataraman, and F. Evers,
  Mechanically-tunable quantum interference in ferrocene-based molecular junctions,
  chemRxiv.12252059.v1 (under review in *Nano Letters*)

- T. Fu, S. Smith, **M. Camarasa–Gómez**, X. Yu, J. Xue,
  C. Nuckolls, F. Evers, L. Venkataraman, and S. Wei
  Enhanced coupling through π-stacking in imidazole-based molecular junctions,
  Chem. Sci. **10**, 9998-10002 (2019)

- H. Li[†], T. A. Su[†], **M. Camarasa–Gómez**[*,†], D. Hernangómez–Pérez,
  S. E. Henn, V. Pokorný, C. D. Caniglia, M. S. Inkpen, R. Korytár,
  M. L. Steigerwald, C. Nuckolls, F. Evers, and L. Venkataraman,
  Silver makes better electrical contacts to thiol-terminated silanes than gold,
  Angew. Chem. **129**, 14333 (2017)

Publications not included in this thesis:

- **M. Camarasa–Gómez**, A. Di Marco, F. W. J. Hekking,
  C. B. Winkelmann, H. Courtois, and F. Giazotto,
  Superconducting cascade electron refrigerator,
  Appl. Phys. Lett. **104**, 192601 (2014)

[†] joint first author
[*] first theory author

List of programs

The work presented in this thesis has been obtained employing the following programs:

- **FHI-aims**: `https://aimsclub.fhi-berlin.mpg.de`
- **TURBOMOLE**: `https://www.turbomole.org/`
- **AITRANSS**: Developed in the group of Prof. Dr. Ferdinand Evers: `http://www.physik.uni-regensburg.de/forschung/evers/index.phtml`
- **Jmol**: `http://www.jmol.org/`
- **VESTA**: `https://jp-minerals.org/vesta/en/`
- **Matplotlib**: `https://matplotlib.org/`
- **Inkscape**: `https://inkscape.org/`

Acknowledgements

Some things in life arrive after taking an unexpected detour and they turn out into something even better of what we thought. Here, in this very important page, I want to thank all the people I met in this detour and also those who have been always with me. Without them, this work would not have been possible.

First I want to thank my PhD. advisor, Ferdinand Evers: Thanks for giving me the opportunity to work in your group. I will always be grateful to you for your guidance and support, for the inspiring discussions, and for all the things I have learnt over this time. They will be priceless in the forthcoming years.

I also want to thank Latha Venkataraman for the joyful discussions and being a source of inspiration: You showed me that a balance between science and family is possible. Thanks for all the things you have taught me over the past four years.

I am also thankful to Jaroslav Fabian for agreeing to be the second referee of my thesis.

I am also grateful for the financial support from the German Research Foundation (DFG) via the Collaborative Research Center (SFB) 1277–Project ID 314695032 (subproject B01) and the Research Training Group (GRK) 1570.

I cannot forget in these acknowledgements Richard Korytár, Vladislav Pokorný and Héctor Vázquez, who always offered scientific inspiration. Prague was always a joyful place. Thanks for that.

I also want to thank Michael S. Inkpen for his patience answering my multiple questions regarding chemistry.

Thanks to Andrea Donarini, Magda Marganska-Lyzniak, Patrick Gröessing, Nithin Thomas and Ferdinand Evers for proofreading.

Thanks to Matthias Stosiek and Magda Marganska-Lyzniak, again, for making our office the most pleasant place of the whole Chair (at least for me!).

Once more, Magda, thanks for the endless conversations about everything (scientific and personal), for your support, help, friendship and for the wonderful time together. I also want to express my deepest gratitude to you, Andrea, for your incredible support, either scientific and personal, for your patience and help. Thanks for showing me that a healthy family life is also possible in the world of science. Patrick, I will always be in debt with you: you made Germany a home for me. Your friendship is one of the things I will take in my heart. Thanks to you and your sister, Beatrice, for your endless help.

I am thankful to the old and new Evers' gang: Patrick Gröessing, Matthias Stosiek, Nithin Thomas, Felix Weiner and Jan Wilhelm, for the fantastic atmosphere. Without you I would have been lost in the difficult moments of the thesis. I will certainly miss the conversations in the corridor and the office. Thanks for this time together and for your support.

I also want to thank the rest of the members (current and former) of the Chair of Quantum Transport and Dissipation for the great atmosphere: Milena Grifoni, Nico Leumer, Moritz Frankerl, Christoph Rohrmeier, Luca Magazzù, Heng Wang, Michael Niklas, Lars Milz, Michael Kammermeier, Martin Wackerl, Paul Wenk and Ivan Dmitriev. It was always a pleasure to come to work here. Special thanks go to Claudia Zange, Sylvia Hrdina, Alexandra Prem and Doris Meier, who always offered solutions and guidance through the bureaucratic jungle. You always had the door open for help.

I am thankful to Santi. Gracias por ser un gran amigo a pesar de la distancia. Es reconfortante saber que no importa en qué país viva, tú siempre serás una de las constantes de mi vida y sé que siempre estarás ahí para todo, en cualquier momento. Gracias por recordarme las cosas importantes de la vida.

To Marisa, Mariano, Olga, Nieves and Diego. Hace cinco años tuve la enorme fortuna de ganar unos padres y tres hermanos. Porque sois la mejor familia que uno podría desear cuando se une a otra persona. Por el apoyo incondicional, en todo y en cualquier momento, que ha sido fundamental para sobreponerme en los momentos bajos durante el largo camino de la tesis. Gracias por vuestra constante fuente de amor y cariño porque me hacéis sentir como si fuera vuestra hija o hermana.

I am thankful to my father, Javier "Tres Jolis". Por ser el mejor padre que se puede tener. Por estar siempre ahí y hacer lo imposible por mí. Por recorrer media Europa conmigo, incluso con dos gatas si es necesario. Por hacerme reir y por sacarme una sonrisa siempre, sin importar lo oscura que parezca la tormenta. Gracias por enseñarme a disfrutar de cada minuto y del ahora, y proveerme de la correcta perspectiva ante la vida. Gracias por todo tu amor y cariño. Estoy agradecida de ser tu hija. Sin tu apoyo no habría conseguido terminar esta tesis.

I am thankful to my mother, María José "La Petite". Because she taught me the value of being perseverant and patient. Because she made me understand that life is not a sprint, but a long-distance race. Because she encouraged me to fight and be brave and spirited for the things I want. Mom, I wish you could be here with me and see this work done, but I know that, up there (or wherever you are), you are proud of me. Without all the things you taught me, I would have never arrived here.

Last and foremost, I am thankful to Daniel. There are no words for me in English, Spanish or any other language, to express what my soul feels and thank everything you have made for me. Sin ti, no estaría escribiendo estas palabras. Esta tesis te la dedico a ti por tu apoyo incondicional a lo largo de estos años. Porque tú siempre me has transmitido la fuerza que he necesitado. Por enseñarme que no hay fronteras ni límites. Por confiar ciegamente en mí. Por cuidarme. Por tu amor. Por ser tú. Porque en este desvío del camino, la vida me trajo el mejor regalo que podría recibir: a ti, mi "Sambo Norte".